Universidade de Aveiro Departamento de Química

Liliana Adelina Afonso Novo de Almeida Truta

DESENVOLVIMENTO DE BIOSSENSORES PARA DIAGNÓSTICO PRECOCE DE BIOMARCADORES DO CANCRO E APLICABILIDADE EM CÉLULAS FOTOVOLTAICAS

MERGING BIOSENSORS AND PHOTOVOLTAIC CELLS FOR CANCER BIOMARKERS DETECTION

2019

Universidade de Aveiro Departamento de Química

Liliana Adelina Afonso Novo de Almeida Truta

DESENVOLVIMENTO DE BIOSSENSORES PARA DIAGNÓSTICO PRECOCE DE BIOMARCADORES DO CANCRO E APLICABILIDADE EM CÉLULAS FOTOVOLTAICAS

MERGING BIOSENSORS AND PHOTOVOLTAIC CELLS FOR CANCER BIOMARKERS DETECTION

Tese apresentada à Universidade de Aveiro para cumprimento dos requisitos necessários à obtenção do grau de Doutor em Nanociências e Nanotecnologia, realizada sob a orientação científica de Doutora Maria Goreti Ferreira Sales, Professora Adjunta com Agregação do Departamento de Engenharia Química do Instituto Superior de Engenharia do Porto/Politécnico do Porto e de Doutor Tito da Silva Trindade, Professor Catedrático do Departamento de Química da Universidade de Aveiro

Apoio financeiro do European Research Council através da ERC-StG-3P's/2012, GA 311086.

BioMark, Sensor Research
Instituto Superior de Engenharia do Porto

Dedico esta dissertação ao meu marido, Joaquim Alves, pais e irmã por todo o amor, dedicação e, apoio incondicional demonstrado ao longo desta caminhada de 4 anos.

"Aqueles que passam por nós, não vão sós, não nos deixam sós.
Deixam um pouco de si, levam um pouco de nós."

Antoine de Saint-Exupéry (O Principezinho)

o júri
presidente

Professora Doutora Maria Manuel Rocha Teixeira Baptista
Professora Catedrática da Universidade de Aveiro

Professor Doutor Jorge Fernando Jordão Coelho
Professor Catedrático do Departamento de Engenharia Química da Universidade de Coimbra

Professor Doutor Adélio Miguel Magalhães Mendes
Professor Catedrático do Departamento de Engenharia Química da Faculdade de Engenharia da Universidade do Porto

Professor Doutor José Ricardo Ramos Franco Tavares
Professor Auxiliar com Agregação do Departamento de Química da Faculdade de Ciências e Tecnologia da Universidade Nova de Lisboa

Professora Doutora Helena Isabel Seguro Nogueira
Professora Auxiliar do Departamento de Química da Universidade de Aveiro

Professora Doutora Maria Goreti Ferreira Sales
Professora Adjunta com Agregação do Departamento de Engenharia Química do Instituto Superior de Engenharia do Porto/Politécnico do Porto

Agradecimentos

Primeiramente agradeço aos meus orientadores, Professora Doutora Goreti Sales (BioMark, Sensor Research/ISEP) e Professor Doutor Tito Trindade (CICECO/Universidade de Aveiro) pela boa concordância e compreensão entre os dois, e pelo apoio, incentivo e conhecimento científico transmitido ao longo deste trabalho.

Um agradecimento muito especial à Professora Doutora Goreti Sales pela oportunidade concedida para a concretização deste doutoramento no âmbito do projeto 3P's, por todo o esforço no sentido de me transmitir os seus conhecimentos, incentivando à minha constante evolução profissional e, acima de tudo, pela confiança e amizade revelada ao longo de todos os momentos.

Um agradecimento em especial ao Professor Doutor Tito Trindade por ter aceite colaborar neste projeto sem hesitação, assim como, por toda a confiança demonstrada ao longo do desenvolvimento deste projeto. Agradeço, também, aos membros do laboratório associado CICECO, no departamento de Química da Universidade de Aveiro, pela compreensão e apoio demonstrado ao longo deste trabalho e pela disponibilidade de todos os meios necessários para a realização do mesmo.

A todos os membros do grupo BioMark que, direta ou indiretamente, contribuíram para este trabalho. Um agradecimento em especial a Ana Tavares, Felismina Moreira, Helena Gomes e Joana Guerreiro pela amizade, incentivo e compreensão ao longo desta caminhada, assim como, pelos bons momentos em conferências.

Agradeço, também, a todos os meus amigos pela sua sincera amizade, compreensão, paciência com que aceitaram a minha alguma indisponibilidade ao longo deste tempo e incentivo dado em cada um dos momentos especiais e menos bons.

Um agradecimento especial à minha querida irmã de coração e sobrinho e restante família, por todo o carinho, compreensão e incentivo manifestados em todos os momentos.

Por fim, agradeço aos pilares da minha vida, marido, irmã e pais, por serem o meu "porto seguro", por ensinarem a viver um dia de cada vez, a apreciar as pequenas coisas da vida e a estarem sempre do meu lado. A vida é muito melhor quando compartilhada convosco e claro com os membros mais recentes da família, Sininho e Tobias.

Palavras-chave

Cancro, marcadores tumorais, biossensores, polímeros de impressão molecular, células solares sensibilizadas por corante, nanopartículas metálicas.

Resumo

O cancro é uma doença que tem vindo aumentar de forma exponencial em Portugal ao longo dos anos, à semelhança do que acontece no resto da Europa. Deste modo, diversos esforços têm vindo a ser feitos no sentido de mitigar a sua incidência, entre os quais a adesão a comportamentos saudáveis (programas de vacinação e modificação do estilo de vida) e ao diagnóstico precoce da doença. Atualmente, o rastreio da doença é concretizado através de marcadores tumorais (CEA, CA15-3, CA125, CA19-9, PSA, entres outros), não-invasivos, que circulam no organismo, em fluídos como sangue e urina.

Neste sentido, esta tese de doutoramento teve o intuito de desenvolver plataformas sensoras de baixo custo, baseadas em novos biomateriais sensores que facultem o rastreio dos biomarcadores do cancro em amostras biológicas, de forma a serem aplicados num contexto clínico. Para este efeito foram consideradas como moléculas alvo a carnitina (CRT), um potencial biomarcador para o diagnóstico do cancro do ovário, e o antigénio carcinoembrionário (CEA), um marcador tumoral que, apesar de ser indicador de outros tipos de cancro como da mama, do pâncreas e do pulmão, apresenta uma elevada especificidade para o cancro do colorretal.

Para a conceção destes biossensores foram concretizadas duas abordagens distintas que se basearam no desenvolvimento de anticorpos plásticos, recorrendo à síntese de polímeros de impressão molecular, e no reconhecimento anticorpo-antigénio, através da construção de imunossensores para a deteção do biomarcador do cancro do colorretal.

As plataformas sensoras construídas sobre um suporte sólido de vidro condutor (composto por um filme de óxido de estanho dopado com flúor) permitiram avaliar a interação entre o biomarcador e o material sensor através de sinais de natureza elétrica. De modo a possibilitar a portabilidade destes dipositivos para a deteção de marcadores tumorais, neste projeto foi proposta uma nova abordagem que estabeleceu a integração de uma plataforma sensora numa célula fotovoltaica, nomeadamente, numa célula solar sensibilizada por corante (Dye-Sensitized Solar Cell, DSSC), uma vez que estas são, por si só, células capazes de gerar energia eléctrica por conversão da energia solar. Também foram realizados esforços no sentido de melhorar o desempenho geral destas células fotovoltaicas, alterando a sua configuração, através da implementação de nanopartículas metálicas, como as nanopartículas de ouro, na constituição do fotoânodo, ou até mesmo através da funcionalização química do material semicondutor que compõe estes fotoânodos e, posterior, ligação a estas nanopartículas metálicas.

De uma forma geral, os dispositivos sensores desenvolvidos poderão ser uma ferramenta promissora, de baixo custo e portátil, para um diagnóstico precoce, ou para o acompanhamento e a monitorização terapêutica do cancro, de modo não invasivo ou minimamente invasivo, para aplicação num contexto clínico.

Keywords

Cancer, cancer biomarkers, biosensors, molecular imprinting polymers, DSSCs, metallic nanoparticles.

Abstract

Cancer diseases are exponentially growing in Portugal throughout the years, reflecting the same scenario as in Europe. Several efforts have been made to minimize cancer incidence, including adopting a healthier behaviour (as vaccination programs and lifestyle adjustments) and early diagnosis of the disease. Currently, the screening of the disease can be performed by monitoring tumour markers (CEA, CA15-3, CA125, CA19-9, PSA, among others) that circulate in the body fluids, as blood and urine. Thus, the development of new analytical tools for detecting these biomarkers in a clinical context is also of growing interest.

This PhD thesis aimed to develop low-cost sensing platforms based on newly biomaterials to screen cancer biomarkers in biological samples towards on-site application. For the purpose, different analyte targets were presented herein, including CRT, which is a potential biomarker in ovarian cancer, and CEA, a tumor marker that despite being an indicator of other types of cancer such as breast, pancreas and lung, offers high specificity in colorectal cancer.

Distinct approaches were developed for this purpose, based on the design of plastic antibodies by means of molecular imprinting technology, and on antibody-antigen recognition though the development of immunosensors for the detection of colorectal cancer biomarker.

The sensing platforms built on a solid conductive glass support (composed by fluorine-doped tin oxide film (FTO)) allowed understanding the interaction between cancer biomarker and the sensing material through electrical signals. In order to allow the portability of these devices, a new approach was proposed in this project, establishing the integration of a sensing platform in a photovoltaic cell, namely in a DSSC, once these cells are capable of generating electrical energy from solar energy. In addition, efforts were made to improve the overall performance of these photovoltaic cells, modifying the DSSCs configuration by introducing metallic nanoparticles, such as gold nanoparticles, in the composition of photoanodes, or even, by the chemical functionalization of the semiconductor material, followed by the metallic nanoparticles binding.

In general, the emerging biosensing materials and platforms out coming from this project may contribute for the development of new non-invasive or minimally invasive and self-sustained devices suitable for the early diagnosis of cancer biomarkers in a clinical application.

CONTENTS

LIST OF FIGURES

LIST OF TABLES

LIST OF ABBREVIATIONS AND SYMBOLS

Ab-CEA	Anti-CEA antibody
AP	3-Aminophenol
APBA	3-Aminophenylboronic acid monohydrate
APS	Ammonium persulfate
APTES	3-Aminopropyltriethoxysilane
ATR	Attenuated Total Reflectance
BSA	Bovine serum albumin
CA15-3	Cancer antigen 15-3
CA19-9	Cancer antigen 19-9
CA125	Cancer antigen 125
CE	Counter electrode
CEA	Carcinoembryonic antigen
CPE	Constant phase element
Crea	Creatinine
CRT	Carnitine
CV	Cyclic voltammetry
DLS	Dynamic light scattering
DMF	N,N-Dimethylformamide
DSSC(s)	Dye-sensitized solar cell(s)
Dyes N719 and N3	Ruthenium sensitizer dyes
EDAC	N-(3-dimethylaminopropyl)-N'-ethylcarbodiimide hydrochloride
EDS	Energy dispersive spectroscopy
EDOT	3,4-Ethylenedioxythiophen
EGDMA	Ethylene glycol dimethacrylate
EIS	Electrochemical impedance spectroscopy
ELFA	Enzyme linked fluorescent assay
ELISA	Enzyme-linked immunosorbent assay
emf	Electromotive force
FBS	Fetal bovine serum
FTIR	Fourier transform infrared spectroscopy
FTO	Fluorine doped tin oxide

GO	Graphene oxide
hCCI	Homemade conductive carbon ink
HEPES	4-(2-Hydroxyethyl)-1-piperazineethanesulfonic acid
ICP	Inductively coupled plasma
ISE(s)	Ion selective electrode(s)
ITO	Indium doped tin oxide
LLLR	Lower limit of linear range
LOD	Limit of detection
LSPR	Localized Surface Plasmon Ressonance
MES	2-(N-morpholino) ethanesulfonic acid
MIP(s)	Molecularly-imprinted polymer(s)
MOPS	4-Morpholinepropanesulfonic acid, sodium salt
MPAP	Molecular imprinted material based on PAP
NHS	N-Hydroxysuccinimide
NIM	Non-imprinted material
NPAP	Non-imprinting material based on PAP
NP(s)	Nanoparticle(s)
***o*NPOE**	o-Nitrophenyloctyl ether
OSC ink	Organic silver conductive ink
OCP	Open circuit potential
PA	Photoanode
PAP	Poly(aminophenol)
PBS	Phosphate buffer solution
PCE	Power conversion efficiency
PET	Polyethylene terephthalate
pFTO	Pre-treated FTO glass
PIPES	Piperazine-N,N′-bis(2-ethanesulfonic acid)
POC	Point-of-care
TpClPB	Potassium tetrakis(4-chlorophenyl) borate
PSA	Prostate-specific antigen
PV	Photovoltaic cell
PVC	Poly(vinyl chloride)
PVC-COOH	Poly(vinyl chloride) carboxylated

QCM	Quartz crystal microbalance
SAW	Surface acoustic wave
SDS	Sodium dodecyl sulfate (electrophoresis)
SiO_2/SiDTC	Siliceous shells enriched in dithiocarbamate moities
SPAM	Smart polymer antibody material
SSA	4-Styrenesulfonic acid sodium salt
THF	Tetrahydrofuran
pTOAB	p-tetraoctilammonium bromide
TRIS	Hydrochloric acid and tris(hydroxymethyl) aminomethane
VPi	Vinyl pivalate
WE	Working electrode
WHO	World Health Organization

a_i	Activity of the primary ion in the sample
D	Diffusion coefficient of the species
E	Potential difference between two electrodes
η	Energy conversion efficiency
η_c	Charge collection efficiency
F	Faraday's constant
FF	Fill factor
ΔG	Energy change
i	Main ion to which the electrode displays a selective response
I_p	Peak current
j	Interfering ionic species
J_{sc}	Short circuit current density
J-V	Photocurrent density-photovoltage
k	Constant
K_D	Dissociation constant
$K_{i,j}^{pot}$	Selectivity coefficient
n	Number of electrons exchanged
n_i	Number of electrons participating in the reaction
R_g	Universal gas constant (R_g = 8.314 J.mol^{-1}.K^{-1})
R	Resistance

R_s	Resistance of solution
R_{ct}	Resistance of charge transfer
$R_{ct}^{máx}$	Maximum charge transfer density
T	Temperature
t	Time constant
τ_n	Electron lifetime
τ_s	Electron transport time
W	Warburg diffusion element
ω	Angular frequency
V_{oc}	Open-circuit potential
v	Scan-rate of the potential
Z	Impedance
$-Z_{Im}$	Real component of impedance
$-Z_{Re}$	Imaginary component of impedance

CHAPTER 1
Framework

This chapter reports the motivation and the thesis outline, presenting the main objectives of this PhD work, and the list of publications and co-supervising activities accomplished during this project.

1.1. Motivation

Cancer diseases are a leading cause of death worldwide. However, mortality data may be reduced if the disease is detected and treated early. The discovery of cancer biomarkers (as single proteins or protein-based molecular assemblies) has emerged as a crucial evidence that could assist not only cancer diagnosis but also the follow-up of disease progression.

Tumor markers are defined as biomolecules that are produced by the body in response to cancer growth, and can be detected in biological samples as blood, urine or tissues. Thus, biomarkers are a dynamic and a powerful approach to reflect the stage of a disease, at a faster, non-invasive and low-cost way, suitable for an early monitoring of diseases and useful for wide screening programs and applications in point-of-care (POC).

Many advances have been made in this field to use biosensors as an alternative to the conventional methods usually employed in hospitals. In these, the interaction between the biorecognition element and target analyte can be translated through the transducer surface into an analytical optical signal (UV/Vis spectrophotometry, fluorimetry, surface plasmon resonance, Raman spectroscopy, etc.) and/or electrical signal (potentiometry; electrochemical impedance spectroscopy, EIS; square wave voltammetry, SWV; cyclic voltammetry, CV; etc.). Biosensors are a promising tool to obtain a simple and a sensitive device with low cost manufacturing, once they allow detecting and quantifying specific biomarkers present in a disease, as cancer, needing low concentration and low sample volumes. In addition, these may offer portable device versions to carry out tests in POC.

In this PhD research, novel approaches are accomplished aiming to develop new sensing platforms and to attach these with a simple/green strategy and renewable energy platform, as the DSSCs. Thus, it is shown possible to obtain a platform able to detect target analytes, such as cancer biomarkers, supported itself by solar energy and allowing a good portable device performance without high costs, thereby enabling clinical diagnosis in POC

For this purpose, different approaches are targeted, making use of different biorecognition elements, including natural antibodies and plastic antibodies based on molecular imprinting materials, employing molecular imprinting techniques and specific nanomaterials. These approaches are always linked to biosensing platforms of electrical nature.

The devices prepared are further optimized in various aspects of their design, by evaluating their physical/chemical characteristics and their analytical performance. In the end, the sensor materials are integrated into a photovoltaic cell, in which the electrical output signal of the cell changes proportionally with the interference generated by the amount of protein biomarker bound to the cathode. In addition, this work pursues the employment of Au NPs in the construction of the DSSCs photoanodes, in order to improve its performance, as photocurrent and, thus, the power conversion efficiency.

The global results obtained in this PhD work was achieved through five individual works, along 5 years, from which three papers were published: Chapter 3, Chapter 4 and Chapter 6, and two papers are submitted: Chapter 5 and Chapter 7.

1.2. Outline of the thesis

This thesis is organized in 8 chapters.

Chapter 1 contains the motivation of the intended research plans in 3P's project funding this work and describes the framework and the report structure, the list of communications and the publications linked to the PhD research program under the 3P's project.

Chapter 2 presents a brief literature review about the pillars of this work, including the target analytes, the recognition elements and the signal transducers, emphasizing those of special relevance to the present research work. This chapter addresses the relevant issues of cancer biomarkers, describes the advantages of using gold nanoparticles in the performance of a typical DSSC, and highlights the great potential derived by the implementation of a biosensor into a DSSC, in order to obtain a portable and autonomous device.

Chapter 3 to Chapter 7, present the construction, characterization and application of biosensors for the quantification of cancer biomarkers, such as CRT and CEA. Likewise, it is introduced new and simple/green platforms using renewable energies.

Chapter 3 reports a novel smart polymer antibody material (SPAM) nanostructure tailored on graphene oxide (GO) supports with charged monomers for the detection of CRT metabolite in a biological sample, as urine. These materials were successfully introduced in plasticized poly(vinyl chloride) (PVC) membranes for potentiometric transduction made with electrodes of different conductive materials.

The analytical performance of the final devices was evaluated successfully, providing suitable selectivity features for practical application, with fast response and improved the limit of detection (LOD) for this potential biomarker of ovarian cancer.

In order to study a non-invasive protein cancer biomarker directly used in a clinical context, in the second work, **Chapter 4**, the CEA glycoprotein was selected an important biomarker applied in the colorectal cancer screening. A simple and sensitive immunosensor for CEA detection was developed using a sol-gel chemistry, where the link between electrical receptor platform and the antibody acting as biorecognition element was accomplished. The effective analytical features presented by electrochemical techniques suggested that a suitable orientation of the antibody over a conductive glass platform (FTO glass) was successfully achieved. Therefore, the presented approach can be a potential method for screening CEA towards on-site application, due to the simplicity of fabrication, short response time and low cost. Thus, the present work described a different and simpler immunosensor design for CEA detection.

Despite the good sensitivity of this CEA immunosensor device to be applied in the analysis of biological sample, a novel plastic antibody for CEA (**Chapter 5**) was developed by molecularly imprinted technique on a carbon ink film linked by sol-gel strategy to a FTO glass support. Given the good electrical conductivity of carbon nanostructures and their great capability in interacting with a high number of target molecules, it was possible to develop a new approach of designing protein plastic antibody for CEA detection. So, as proof of concept, the electrical biosensor was tailored on top of a disposable conductive glass electrode, following a bottom-up approach for targeting CEA. All construction steps involved a chemical modification of a homemade conductive carbon ink (hCCI) layer and lead to the creation of a biomimetic material with an imprinted matrix of polyaminophenol (MPAP) and an analogous control sensing material, without the presence of CEA (NPAP). Evaluation of the analytical performance through electrochemical measurements: EIS and CV and characterization of the chemical modifications of the sensor surface by FTIR spectroscopy, Raman spectroscopy and confocal Raman microscopy, and scanning electron microscopy (SEM) with energy dispersive spectroscopy (EDS) analysis.

In general, the MPAP device offered simplicity in designing, low-cost and a quick manufacturing, comparing to the conventional or concurrent methodologies described in the literature. Likewise, this device was found a suitable and a promising tool to monitor CEA for clinical applications, presenting a good sensitivity and selectivity, once it could detect CEA concentration levels within the normal physiological values.

Monitoring cancer biomarkers in biological fluids has become a key tool for disease diagnosis, which should be of easy access anywhere in the world while being incorporate into routine clinical care. Merging biosensing technology with photovoltaic cells, such as DSSCs, may lead to the production of self-sustained biosensors, once these cells are able to generate electrical current from light. Thereby, the fourth work, **Chapter 6**, describes an innovative electrochemical immunosensing system using a DSSC as an electrical reading box. Briefly, this work proposed an immunosensor for CEA assembled on FTO glass by means of a bottom-up approach, followed by conventional electrochemical techniques. Briefly, the assembled of this new platform describing the integration of an immunosensor for CEA detection inside a photovoltaic cell was based on the following steps:

i. Synthesis of the organic silver conductive ink (OSC ink);
ii. Modification of conductive glass (FTO glass) with the OSC ink;
iii. Assembly of the immunosensor for CEA detection, applying a bottom-up approach according to an antibody/antigen (Ab-CEA/CEA) affinity reaction on top of the modified WE;
iv. DSSC assembly employing a conventional photoanode composed by TiO_2 anatase and a cathode (CEA immunosensor);
v. Characterization of the sensing material by FTIR and Raman spectroscopies;
vi. And electrochemical evaluation of the CEA immunosensor in a 3-electrode system (EIS and CV), and also as counter electrode of the DSSC.

The resulting biosensor that acted as counter electrode of a DSSCs displayed suitable and sensitive features to monitor different concentrations of CEA within the concentration range of clinical interest and in the analysis of real samples. Overall, the presented approach demonstrated that photovoltaic cells may be employed as an electrical reading box of electrochemical biosensors, yielding a new direction towards autonomous electrochemical biosensing.

In order to improve the overall performance of DSSCs that act as the electrical reading box of a biosensor for CEA diagnosis, a new approach was proposed in the **Chapter 7**, where a suitable and environmentally safe interface between DSSCs and gold nanoparticles (Au NPs) was established. Simple approaches to chemically synthesized colloidal Au NPs, with different particle sizes, and incorporate these in the photoanodes of DSSCs were performed, including a two-stage modification in which the titanium dioxide (TiO_2) nanoparticles were modified with siliceous shells enriched in dithiocarbamate moities (SiO_2/SiDTC), followed by the loading of the colloidal Au NPs with different particles sizes.

For this purpose, several steps were accomplished, as described below:

i. Chemical synthesis of colloidal Au NPs and then their attach to TiO_2 NPs and, also, to TiO_2 surface modified with siliceous shells enriched in dithiocarbamate moieties (SiO_2/SiDTC);

ii. Modification of the photoanodes composed of a conductive glass covered by fluorine doped tin oxide (FTO glass) with films of TiO_2 anatase, and TiO_2@Au NPs (diameter ~4 nm and ~22nm), and TiO_2 chemically functionalized with SiO_2/SiDTC and loaded with colloidal Au NPs, in order to improve the typical energy conversion efficiency of DSSCs;

iii. Immersion of this thin films in a solution of ruthenium sensitizer dye (N719);

iv. Preparation of a platinum counter electrode (cathode), in parallel;

v. Assembly of the typical DSSC sandwich configuration using the photoanode, the counter electrode, and an iodide electrolyte solution (I^-/I_3^-). This allowed the photoexcitation of the sensitizer dye adsorbed on the TiO_2 surface, promoting the transfer of electrons injected into the conduction band of the TiO_2 and reaching the counter electrode through the outer circuit. By electron donation from the I^-/I_3^- redox couple, the photosensitizer dye is regenerated and the circuit is completed via electron migration through the external load;

vi. Electrochemical evaluation of DSSCs performance through EIS analysis and a photocurrent density-photovoltage (*J*-*V*) measurement system under irradiation of a white LED (100 mW/cm^2);

vii. And characterization of the final photoanodes films (with and without Au NPs) by Raman, FTIR and inductively coupled plasma (ICP) spectroscopies and, also, by SEM and transmission electron microscopy (TEM) analysis.

In general, this work demonstrated the beneficial influence of plasmonic Au NPs to the photovoltaic performance, according to different strategies, that allowed the improvement of the visible light adsorption, due to Au NPs surface plasmon effect yielding light harvesting within the visible region and scattering properties.

Chapter 8 ends the thesis with the main conclusions obtained and the future work, in order to make the device completely self-sustained regarding to the electrical source and, also, to the reading box.

1.3. List of publications

1.3.1. Paper published in international scientific journal

(1) Liliana A.A.N.A. Truta, Nádia S. Ferreira, M. Goreti F. Sales, Graphene-based biomimetic materials targeting urine metabolite as potential cancer biomarker: Application over different conductive materials for potentiometric transduction, *Electrochimica Acta*, 2014, 150:99–107, DOI: 10.1016/j.electacta.2014.10.136.

(2) Liliana A.A.N.A. Truta, M. Goreti F. Sales, Sol-Gel Chemistry in Biosensing Devices of Electrical Transduction: Application to CEA Cancer Biomarker, Current Topics in Medicinal Chemistry, 2015, 15:256–261, DOI: 10.2174/1568026614666141229113318.

(3) Liliana A.A.N.A. Truta, Felismina T.C. Moreira, M. Goreti F. Sales, A dye-sensitized solar cell acting as the electrical reading box of an immunosensor: Application to CEA determination, Biosensors and Bioelectronics, 2018, 107:94–102, DOI: 10.1016/j.bios.2018.02.011.

(4) Liliana A.A.N.A. Truta, Sónia Pereira, Carolina Hora, Tito Trindade, M. Goreti F. Sales, Coupling gold nanoparticles to Dye-Sensitized Solar Cells for an increased efficiency (under submittion).

(5) Liliana A.A.N.A. Truta, M. Goreti F. Sales, Carcinoembryonic antigen imprinting by simple electropolymerization on a common conductive glass support and its determination in serum samples (under submittion).

1.3.2. Communications presented in national and international scientific conferences

Oral communications

(1) Liliana A.A.N.A. Truta, M. Goreti F. Sales. The potential of artificial antibodies as biosensing devices for monitoring the Interleukin 2 cancer biomarker, presented at NanoPt 2016 International Conference, Braga, Portugal, February 16-19, 2016.

(2) Liliana A.A.N.A. Truta, M. Goreti F. Sales. The potential of artificial antibodies as biosensing devices for monitoring Ca15-3 cancer biomarker, presented at 5th Graduate Student Symposium on Molecular Imprinting, Porto, Portugal, June 8-9, 2017.

(3) Liliana A.A.N.A. Truta, M. Goreti F. Sales. Modification of TiO_2 with gold nanoparticles: application to Dye-Sensitized Solar Cells, presented at 2017 EMN Meeting on Biomaterials, Milan, Italy, August 14-18, 2017.

Poster presentations

(1) Liliana A.A.N.A. Truta, Nádia S. Ferreira, M. Goreti F. Sales. Host-Tailored Sensors for Carnitine Potentiometric Measurements based on Surface Molecular Imprinting, P10, presented at 5th Graduate Student Symposium on Molecular Imprinting, in Queen's University, Belfast, United Kingdom, August 15-17, 2013.

(2) Liliana A.A.N.A. Truta, Nádia S. Ferreira, M. Goreti F. Sales. Carnitine tailored Sensors on Surface Molecular Imprinting based on Graphene layers, P32, presented at III Jornadas de Electroquímica e Inovação (Electroquímica e Nanomateriais), in Trás-os-Montes e Alto Douro University, Vila Real, Portugal, September 16-17, 2013.

(3) Liliana A.A.N.A. Truta, M. Goreti F. Sales. A disposable glass-based immunosensor for monitoring the cancer biomarker CEA in urine. Poster presentation based on topic Nanobio/Nanomedicine, presented at NanoPT 2014 International Conference, in Portugal, on February 12-14, 2014.

(4) Liliana A.A.N.A. Truta, M. Goreti F. Sales. Sol-gel biomimetic material designed to target CEA cancer biomarker, Poster J3, presented at 1st ASPIC International Congress, in Fundação Calouste Gulbenkian, Lisbon, Portugal, November 25-26, 2014.

(5) Liliana A.A.N.A. Truta, M. Goreti F. Sales. The potential of molecular imprinting as a biosensing device for monitoring the CEA cancer biomarker, P5, presented at 6th Graduate Student Symposium on Molecular Imprinting, in Medway School of Pharmacy, Kent, United Kingdom, August 27-28, 2015.

(6) Carolina Hora, Liliana A.A.N.A. Truta, Ana P. M. Tavares, Manuela F. Frasco, Ana M. Piloto, M. Goreti F. Sales. Integrating biosensors in photovoltaic cells: the 3P's project, Poster 27, presented at iBEM-International Biomedical Engeneering Meeting, in Escola Superior de Estudos Industriais e de Gestão, Porto, Portugal, March 21, 2016.

1.4. Co-Supervision activities

2012-2013: Internship of Catherine HUA (bachelor student from the Department of Chemistry of IUT d'Orsey, France). Development of a scientific work entitled *Paper imprinted with ion-jelly for Carnitine detection*, in BioMark, Sensor Research/CINTESIS/ISEP, School of Engineering, Polytechnic Institute of Porto, Portugal.

2013-2014: Master thesis of Catarina Alexandra Campos Vieira to confer the Master degree in Computer Engineering and Medical Instrumentation. Development of a scientific work entitled *Plastic antibodies development for detection of Cancer biomarkers*, in BioMark, Sensor Research/CINTESIS/ISEP, School of Engineering, Polytechnic Institute of Porto, Portugal.

2014-2015: Master thesis of Joaquim Domingos Lopes Alves to confer the Master degree in Chemical Engineering Energy optimization in the Chemical Industry. Development of a scientific work called *Materials and sensing devices for Norfloxacin detection*, in BioMark, Sensor Research/CINTESIS/ISEP, School of Engineering, Polytechnic Institute of Porto, Portugal.

CHAPTER 2

Literature review

This chapter provides an overview about cancer diseases and the associated tumor markers with important role for clinical applications; biosensors in general (biorecognition elements and transducers); and photovoltaic cells (DSSCs and plasmonic effect in the performance of these cells).

2.1. Cancer diseases

Cancer diseases are a leading cause of death worldwide. According to the most recent *World Cancer Report 2014* published by the WHO, the most common causes of cancer death are lung, liver, stomach, colorectal and breast cancers [1,2]. In addition, and also according to WHO statistics, new cancer cases are expected to rise about 70%, over the next 20 years.

Carcinogenesis consists in the abnormal transformation of cells within the body, which leads to their uncontrolled proliferation and, ultimately, to the invasion of nearby tissues. These cells are able to release growth factors and digestive enzymes that promote their continuous division. The overall process is composed by three stages: tumour initiation, promotion, and progression, in which simultaneous changes on specific molecules and cells occur. The rapid and irreversible initiation stage starts with a genetic alteration leading to abnormal proliferation of a single cell, and then the outgrowth of a population of tumor cells. After, there is a long stage called tumour promotion, involving the active proliferation and accumulation of cancer cells. Lastly, the progression stage comes, including tumour growth, which may have invasive and metastic nature [3,4].

2.1.2. Cancer biomarkers

Cancer diseases are difficult to detect in the initial state, because the morphological alterations in the tissues are not evident. In this context, the discovery of tumor markers emerged as an important factor not only for the diagnosis of cancer but also for monitoring its response during the treatment or recurrence and, more recently, at an early analysis of cancer risk [1,2]. Tumor markers are defined as biomolecules that are produced by the body in response to or along with cancer growth, and that may be detected in biological samples, such as blood, urine or tissues [2]. Thereby, biomarkers are a dynamic and a powerful approach to reflect the stage of a disease, at a faster, non-invasive and low-cost way, useful for over wide screening programs and applications in POC context, and consequently suitable for early monitoring of cancer diseases [1,5]. Ideally, a tumor marker should be highly specific and sensitive to a certain tumor and fulfill certain criteria to avoid false positive results: provide a lead-time over clinical diagnosis, and be able to correlate reliably the levels of markers and the tumor stage, detecting accurately any progression or regression of tumor [6-8].

Currently, numerous tumor markers (CEA, CA15-3, CA125, CA19-9, PSA, among others) are being used clinically to monitor a wide range of cancer types, including colorectal, breast, ovary, uterine, lung, pancreas, liver, and prostate cancer, and among others [2,7]. Amongst the several cancer biomarkers, CRT and CEA were studied herein for their relevance and different features.

CEA is an important tumor marker that has been employed in clinical diagnosis of over 90% colorectal cancers. This is the third most common type of cancer disease and the major cause of the death throughout the world. Such bad scenario accounts the complexity and heterogeneity through the multiple genetic mutations that occurs in the disease [9]. The discovery of novel non-invasive biomarkers, as CEA, and their fast determination at low cost is presently required [10,11]. CEA is a marker that plays an important role for clinical diagnosis and prognosis evaluation of colorectal cancer, providing a follow-up examination during therapy stage of the disease and its monitoring through CEA levels that can be presented in different biological samples, including urine, serum or blood [2,12-16]. In 2011, Nielsen and co-authors determined that CEA marker was an important biomarker for early detection of colorectal cancer. The normal levels of CEA marker in healthy adult's range 2.5 ng/mL (non-smokers)-5.0 ng/mL (smokers) and levels above 5.0 ng/mL may signal the presence of cancer [12]. The high importance and potentiality of tumor markers detection on both disease prevention, and on stratified and individualised patient care have been demonstrated by a variety of techniques employed in these assays [2,17].

The detection of CEA marker in different biological samples has been described in the literature through several analytical techniques, including colorimetric enzyme immunoassay, chemiluminescence immunoassay, radiometry immunoassays, ELISA, colorimetry immunoassay, spectrophotometry, fluoroimmunoassay and electrochemical immunoassay, electrochemical assays based on potentiometry and amperometry, DLS immunoassay [1,18-25,26], and other conventional methods. Despite their effectiveness to monitor CEA in different biological samples, these methods are expensive, complex and time consuming, requiring sophisticated instrumentation and highly qualified personnel [27,28]. In general, all these methods are effective, but unsuitable for POC applications [15,17]. Therefore, as an alternative to immunoassay techniques usually used in clinical context, a new design of biosensors is desired, exhibiting simplicity in the design, fast response, low cost, easy miniaturization, and portability [16,25,29-33]. In fact, the quantification of biological or biochemical processes are of utmost importance for medical, biological and biotechnological applications. However, this is a tricky challenge due to the complexity of interfacing a sensing device with a biological environment, which offers a complex composition [34]. Hence, the emerging of new biosensing materials and platform designs may open new horizons in the medical field.

CRT is a quaternary amine that according to its antioxidant features plays an important role for the transport of long-chain fatty acids into the mitochondrial matrix, and in the normal function of the cells. Thus, it displays a protective effect upon oxidative stress conditions, typically implicated in several diseases such as cardiovascular diseases, diabetes, heart/renal failure, or cancer. In addition, carnitine may also act as a disease biomarker in specific conditions, such as ovarian cancer.

Ovarian cancer is one of the deadliest cancer of all gynecologic tumors due its limited detection. So, its early detection by the screening of specific biomarker compounds would be important for patients. During illness, the tissues can be transformed into several quaternary amines, including carnitine, excreted in urine. Thus, carnitine levels in urine may be correlated to this cancer, making this a potential biomarker for an early diagnosis of ovarian cancer.

Numerous analytical methods have been described in the literature for carnitine detection in different biological samples, associated to distinct diseases. In 2004, Liu et al. described the effluence of CRT and its metabolites (such as acetyl-*L*-CRT) in plasma and brain, rat ambulatory activity, and biomarkers of oxidative stress. This is an essential molecule for the translocation of fatty acids into mitochondrial matrix. Its deficiency caused a disorder in the metabolism, which can be related with myocardial diseases and kidney failure [35,36]. However, Hoppel (2003) reported that therapeutic administration of CRT can be promising in treating of patients with heart failure [36]. Moreover, Engle et al. (2009) described the study on the effect of acetyl-*L*-CRT on ovarian cancer cells, and if this ester of CRT affects the cytotoxicity of standard chemotherapy on ovarian cancer cells. Herein, the authors concluded that CRT metabolite, detectable in a physiological range around 1-5 μM in human plasma, does not interfer in the cytotoxicity assays, which may not cause any adverse response in the treatment of ovarian cancer [37]. More recently, Sahafi et al. (2017) reported a review article on chemotherapy that induce infertility, and the potential protective role of CRT, based on clinical trials, case reports and medical publications. Despite to the promising effect of the therapeutic administration of CRT during a chemotherapy treatment, the reseachers concluded that further studies are required in future [38].

Overall, biomarkers are mostly useful for clinical purposes, especially when there are devices capable of monitoring these an efficient and simple way.

2.2. Biosensors

The discovery of biosensors dates to the early 1960s by Clark and Lyons that reported the first biosensor to monitor glucose in blood through amperometric detection [35]. Since then, many advances have been made in the field, in order to turn biosensors a challenging alternative to the conventional methods (such as ELISA, chromatographic or spectrophotometric methods, among others), once they allow detecting and quantifying specific biomarkers present in a disease, eventually in POC [16,36,37].

Several sensors for cancer disease diagnostic and screening have been reported in the literature. These have been summarized in **Table 2.1**, highlighting the target tumor marker, the (bio)recognition element, the transducer component, the concentration levels and their respective cut-off values.

Table 2.1 showed the relation of CEA biomarker to monitor several cancers. In general, most of analytical methodologies used for CEA detection are based on electrical transducers, using different type of (bio)recognition elements. The electrochemical sensors designed with an antibody-antigen interaction showed a good linear response in the CEA concentration levels between 0.05 ng/mL and 150 ng/mL in serum samples, with LOD values varying from 0.003 ng/mL to 0.4 ng/mL [18-23,39,41]. Similarly, the sensors based on optical transducer showed good performance in the range of CEA concentration levels used for the electrochemical sensors, and, also, lower LOD values [2,40]. Despite to the effective response of these methodologies and also to the ELISA assays, it was necessary to develop new strategies to decrease the costs associated to the use of the conventional analytical techniques. Therefore, sensors based on molecularly imprinted technologies have emerged, mimetizing the natural antibodies [1,24,39]. In general, MIPs based on electric transducers showed better results comparing with the optical sensors and, also, demonstrated good results as electrochemical immunosensors, since they allowed to reach LOD values in the reference range of the physiological levels (non-smokers: 2.5 ng/mL, smokers: 5.0 ng/mL) [39]. In case of the other cancer biomarkers (CA125, CA15-3, PSA and CA19-9), immunosensors are the most methodology applied to monitoring these biomarkers, due to its powerfull and rapid response. However, the MIPs shows to be a promising tool, that can be optimized in order to obtain more sensitivity and lower LOD as those obtained by conventional methods.

Table 2.1. Biosensors for tumor markers with different transducers and their respective detection range described in the literature.

Tumor markers	Form of Cancer	Source	Clinical use	Sensing approach	Transducer	Response range	Limit of detection (LOD)	Reference
Carcinoembryonic antigen (CEA)	Pancreatic	Serum	Early diagnosis; screening	Molecular imprinting (MIP) sensor	Electrochemical (EIS)	0-8.5 ng/mL	0.5 ng/mL	[39]
	Several	Serum	Screening	Label-free amperometric immunosensor	Electrochemical (voltammetry)	0.01-150 ng/mL	0.003 ng/mL	[39]
	Colorectal	Serum	Diagnosis	Chemiluminescence immunosensor	Optical	0.5-50 ng/mL	0.05 ng/mL	[40]
	Several	Serum	Screening	Immunosensor	Electrochemical (voltammetry)	0.5-80 ng/mL	0.05 ng/mL	[39]
	Several	Serum	Screening	Immunosensor	Electrochemical (EIS)	0.5-20 ng/mL	0.1 ng/mL	[39]
	Colorectal	Serum	Diagnosis	Immunosensor	Electrochemical (voltammetry)	0.5-120 ng/mL	0.17 ng/mL	[41]
	Several	Serum	Early diagnosis	Colorimetric immunosensor	Optical	----	0.02 ng/mL	[2]
	Colorectal	Serum	Diagnosis	MIP sensor	Electrochemical (potentiometry)	2.5-250 ng/mL	>8 ng/mL	[1]
	Several	Serum	Early diagnosis	Colorimetric enzyme immunosensor	Optical	0.05-50 ng/mL	0.048 ng/mL	[18]
	Several	Serum	Diagnosis	Immunosensor	Electrochemical (voltammetry; EIS)	0.05-5.0 ng/mL; 5.0-120.0 ng/mL	0.01 ng/mL	[19]

Table 2.1. Biosensors for tumor markers with different transducers and their respective detection range described in the literature (cont.).

Tumor markers	Form of Cancer	Source	Clinical use	Sensing approach	Transducer	Response range	LOD	Reference
Carcinoembryonic antigen (CEA)	Several	Serum	Diagnosis	Immunosensor	Electrochemical (voltammetry; EIS)	0.05-5.0 ng/mL; 5.0-120.0 ng/mL	0.01 ng/mL	[19]
	Several	Serum	Screening	Immunosensor	Electrochemical (voltammetry)	0.5-3.0 ng/mL 3.0-120 ng/mL	0.4 ng/mL	[20]
	Several	Serum	Diagnosis	Amperometric immunosensor	Electrochemical (voltammetry)	0.01–150 ng/mL	0.003 ng/mL	[21]
	Several	Serum	Diagnosis	Amperometric immunosensor	Electrochemical (voltammetry)	0.5-10 ng/mL 10-120 ng/mL	0.2 ng/mL	[22]
	Several	Serum	Screening	Immunosensor	Dynamic Light Scattering (DLS)	0.06-50 ng/mL	0.036 ng/mL	[23]
	Several	----	Diagnosis	MIP sensor	Optical	500-125000 ng/mL	----	[24]
	Several	Serum	Diagnosis	Immunosensor	Electrochemical (voltammetry)	0.50- 80.0 ng/mL	0.27 ng/mL	[25]
	Bladder	Urine; Serum	Early diagnosis	Enzyme immunosensor	ELISA	----	Serum: <3 ng/mL Urine: <30 ng/mL	[42]

Table 2.1. Biosensors for tumor markers with different transducers and their respective detection range described in the literature (cont.).

Tumor markers	Form of Cancer	Source	Clinical use	Sensing approach	Transducer	Response range	LOD	Reference
Carcinoembryonic antigen (CEA)	Several	Serum	Diagnosis	Immunosensor	Electrochemical (voltammetry; EIS)	0.05-5.0 ng/mL; 5.0-120.0 ng/mL	0.01 ng/mL	[19]
	Several	Serum	Screening	Immunosensor	Electrochemical (voltammetry)	0.5-3.0 ng/mL 3.0-120 ng/mL	0.4 ng/mL	[20]
Cancer antigen 125 (CA125)	Ovarian	Serum	Early diagnosis	MIP sensor	Electrochemical (voltammetry)	0.5-400 U/mL	0.5 U/mL	[39]
	Ovarian	Serum	Screening; monitoring	Enzymatic immunosensor	ELISA	----	35 U/mL	[43]
Carbohydrate antigen 15-3 (CA15-3)	Breast	Serum	Diagnosis	Immunosensor	Electrochemical (voltammetry)	0.1–20 U/mL	0.012 U/mL	[39]
	Breast	Serum	Diagnosis	Surface Plasmon Resonance (SPR) sensor	Optical	0.013-160 U/mL	0.025 U/mL	[44]
	Breast	Serum	Diagnosis	MIP sensor	Electrochemical (voltammetry)	0.10-100 U/mL	0.10 U/mL	[45]
	Breast	Serum	Diagnosis	Immunosensor	Electrochemical (voltammetry)	1.0–150 U/mL	0.30 U/mL	[46]
Prostate specific antigen (PSA)	Prostate	Serum	Screening; monitoring	Immunosensor	Electrochemical (voltammetry)	0-1.0 ng/mL	0.25 ng/mL	[39]
	Prostate	Serum	Screening; monitoring	Immunosensor	Electrochemical (voltammetry)	----	0.001 ng/mL	[47]
	Prostate	Serum	Screening	MIP sensor	Electrochemical (potentiometry)	2.0-89.0 ng/mL	2 ng/mL	[45]

Table 2.1. Biosensors for tumor markers with different transducers and their respective detection range described in the literature (cont.).

Tumor markers	Form of Cancer	Source	Clinical use	Sensing approach	Transducer	Response range	LOD	Reference
Prostate specific antigen (PSA)	Prostate	Serum	Screening	MIP sensor	Electrochemical (potentiometry)	2.0-89.0 ng/mL	2 ng/mL	[45]
Carbohydrate antigen 19-9 (CA19-9)	Pancreatic	Serum	Screening; monitoring	Immunosensor	Electrochemical (voltammetry)	2.0×10^{-5}-40 U/mL	1.0×10^{-5} U/mL	[48]
	Pancreatic	Serum	Diagnosis	Immunosensor	Electrochemical (voltammetry)	3.0-20.0 U/mL	2.68 U/mL	[49]
CEA, CA19-9, CA125 and CA15-3	Breast	Serum	Diagnosis	Enzymatic immunoassay	ELISA	----	CEA: 3.0 ng/mL CA19-9: 20 U/mL CA125: 30 U/mL CA15-3: 20 U/mL	[50]
	Lung	Serum	Diagnosis	Enzymatic immunosensor	ELISA	----	CEA: 4.5 ng/mL CA19-9: 16.0 U/mL CA125: 24.5 U/mL CA15-3: 28.8 U/mL	[12]

In general, biosensors combine in a single device biorecognition and transducer elements. These biosensors should be specific, accurate and sensitive, in order to provide few "false positives" and zero "false negatives"; reproducible measuring and possibility of POC analysis are also desired. In addition, these devices must be physically robust and insensitive to environmental interferences, like temperature, pH or ionic strength changes. Under such optimum scenario, these devices can be a perfect tool for molecular screening in a wide range of practical applications (medical, environmental, agricultural, drug detection and food safety) [36,38,51].

2.2.2. Biorecognition elements

The biorecognition element interacts with the intended target molecule, and is typically composed of a biologically-derived compound, such as enzymes, sugars, cells, antibodies, or nucleic acids. The most common biorecognition elements in biosensors are antibodies, which ensure signal selectivity/specificity, regardless their high cost and little stability. Alternative biorecognition elements have synthetic nature, such as aptamers or plastic antibodies (as molecularly-imprinted polymers, MIPs), designed with the purpose of mimicking natural receptors. These synthetic materials have lower cost and higher stability than their natural counterparts, while recent technology in the field is promoting their enhanced selectivity.

This biorecognition layer (**Figure 2.1**) can be constructed using single or group of molecules with a critical importance in a wide range of practical applications. This includes proteins, enzymes, antibodies, cells, tissues, nucleic acids, peptides, aptamers or MIPs, whose detection of binding target to probe in solution is governed by detecting a signal change at a localized surface [17,34,52,53]. The signal change is related to current and/or voltage variations, when electrochemical transducers are considered.

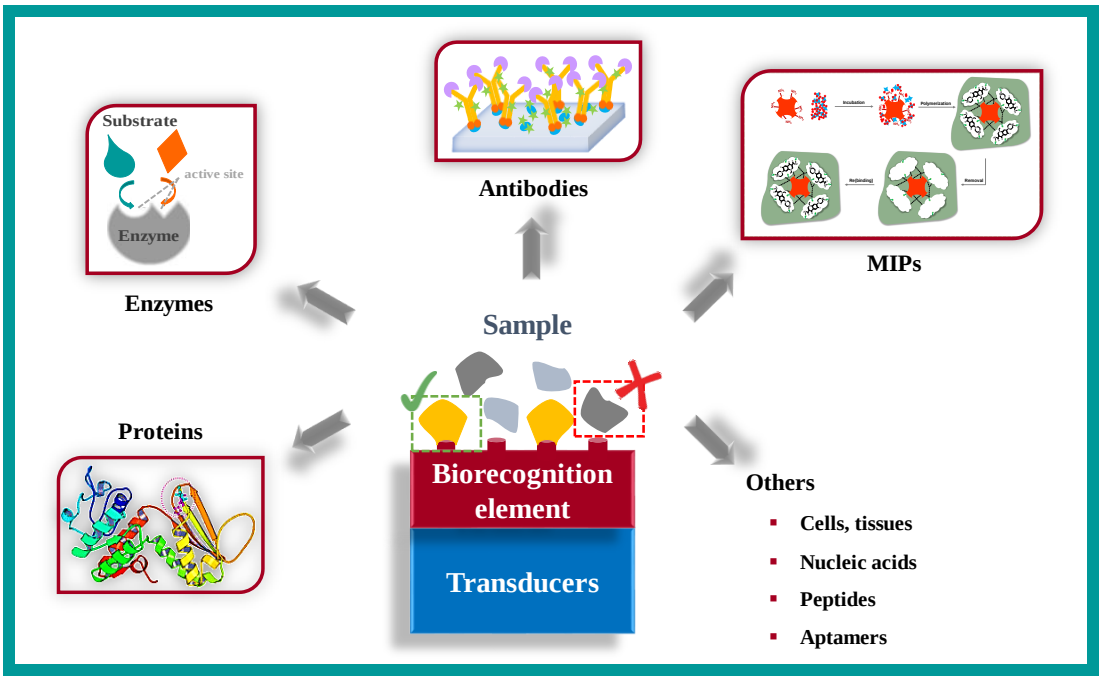

Figure 2.1. Schematic representation of biorecognition elements.

2.2.2.1. Natural antibodies

An antibody is a protein of the immune system that may bind to its target compound, the antigen, with a high level of affinity/specificity [16]. When antibodies are employed as biorecognition element, the biosensor may be named as immunosensor, as it relies in the response of the immune system. In this case, there is a direct interaction between antibody and antigen, and few compounds shall compete for such interaction. But the selective nature of this interaction also justifies their involvement in other conventional methods, like ELISA, fluoroimmunoassay, radiometry immunoassay or even chemiluminescence immunoassay. In general, these methods take a long time to produce a response and do not allow POC use [12], which opens doors towards the use of immunosensors in clinical context. Typically, an immunosensor is assembled by placing either an antibody or an antigen on the transducer surface (**Figure 2.2**) [53,54]. The recognition of the immuno-based interaction may require an appropriate label, which is usually conjugated to a particular component of the immunocomplex, in order to promote a signal alteration after binding [34,52].

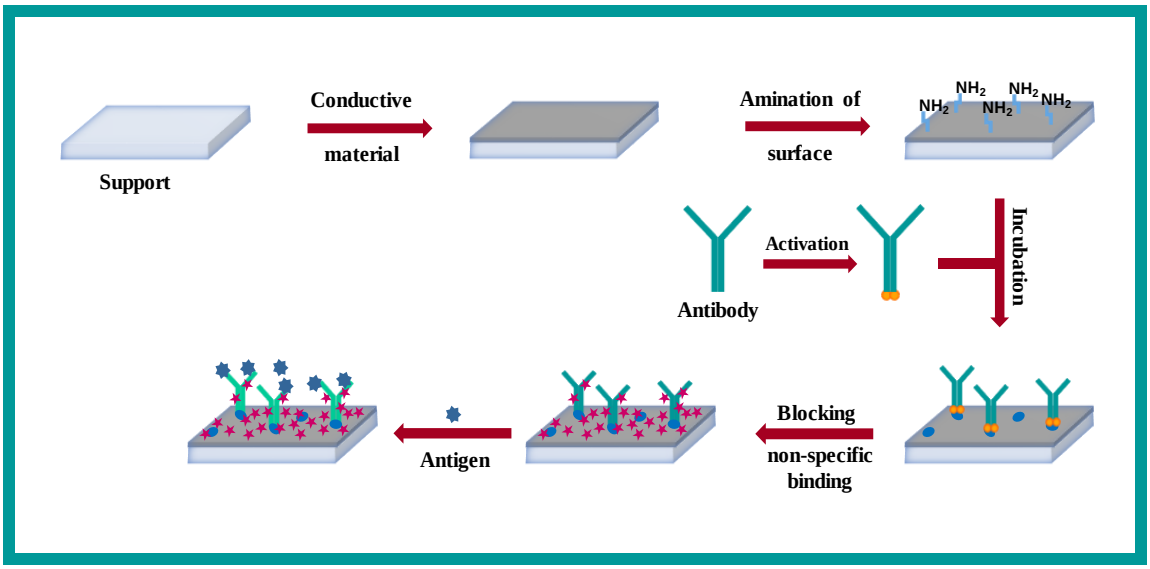

Figure 2.2. Schematic representation of the construction of an immunosensor.

The first antibody based biosensors were introduced by Giaever, Kronick and Little and Tromberg in the early 1970s [55]. Since then, significant progresses have been achieved in the field of immunosensors [52,53]. Many published works may be found in the literature, driven by the detection of biomolecules involved in the disease diagnosis and follow-up. Different configurations are employed for this purpose, which may also imply the use of optical or redox labels [52,56-60]. The analytical features of the resulting devices are typically within the clinical levels of relevance, allowing their application in fluid samples.

2.2.2.2. Plastic antibodies

An interesting alternative to the use of antibodies is the use of the molecular imprinting technique, a fast-growing field allowing the production of a synthetic version of antibodies. This methodology offers several advantages compared to their natural analogues, including greater long-term storage stability, high sensitivity, a potential reusability, robustness, versatility, ease of preparation and low-cost manufacture [36,51,61,62].

MIP-based plastic antibodies are designed by assembling a polymeric material around the target template molecule and removing this target compound after completion of the polymer growth. The template removal allows the generation of selective rebinding sites, ideally allowing a stereochemical fitting of the target compound (**Figure 2.3**) [63,64].

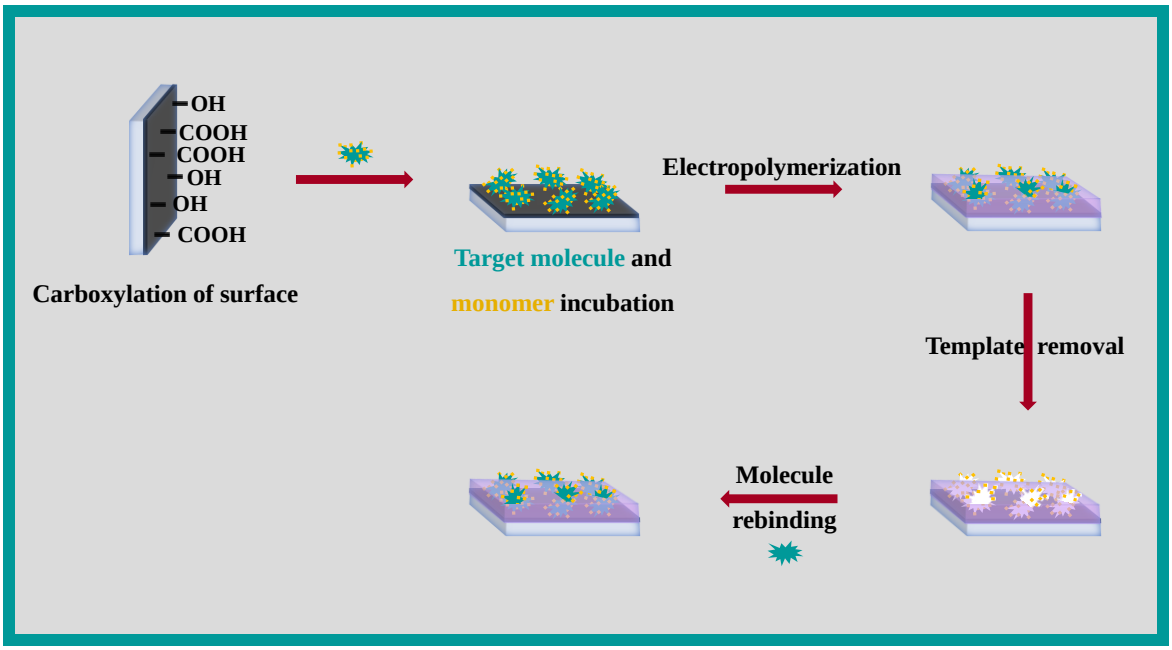

Figure 2.3. Schematic representation of the synthesis of a MIP material on a solid support.

The use of MIP materials in the laboratory stated in the early 1970s, when Wulff and Vesper reported the use of a MIP to separate enantiomers and the Mosbach's group described a MIP to separate amino acid derivatives by liquid chromatography, in stationary phase [64,65]. With the advance of research mostly in the field of nanotechnology, several strategies have been performed to design potential MIP based biosensors, useful for the detection of a wide range of biomolecules. These materials involved the use of gold and silver nanoparticles, carbon nanostructures (e.g. graphene or carbon nanotubes), conductive supports like glass (e.g. fluorine or indium doped tin oxide), and, also, different monomers as aniline [66], pyrrole [30], aminophenol [67,68], phenol [69], *O*-phenylenediamine [70,71] or 3,4-ethylenedioxythiophen (EDOT) [72] by self-assembled monolayers (SAMs) [73,74] and sol-gel [16,75] techniques. Furthermore, different imprinting approaches, such as epitope imprinting, *in situ* polymerization (bulk), surface imprinting, multi-template imprinting, can be employed to the biomimetic sensor construction [76-78].

Overall, the development of a biosensor with good operating features requires that a suitable biorecognition element is immobilized on a suitable receptor surface. However, its successful construction relies not only on the recognition element, but also on the transducing element linked to it [36,51].

2.2.3. Transducers

The transducing element in a biosensor is responsible for reading the physical-chemical change coming from the interaction between the biorecognition element and the analyte. To do so, such change is converted into a detectable signal, which may be of optical, electrochemical, piezoelectric, mechanical, magnetic or thermal nature [36-38,79]. In general, electrical devices allow the production of simple set-ups, thereby allowing portability, just as confirmed by commercial glucose meters. But the detection of a specific analyte through biosensors may combine a given recognition element with different types of transducers (**Figure 2.4**), such as optical, piezoelectric (also called acoustic), thermal or electrochemical based systems [61,80,81].

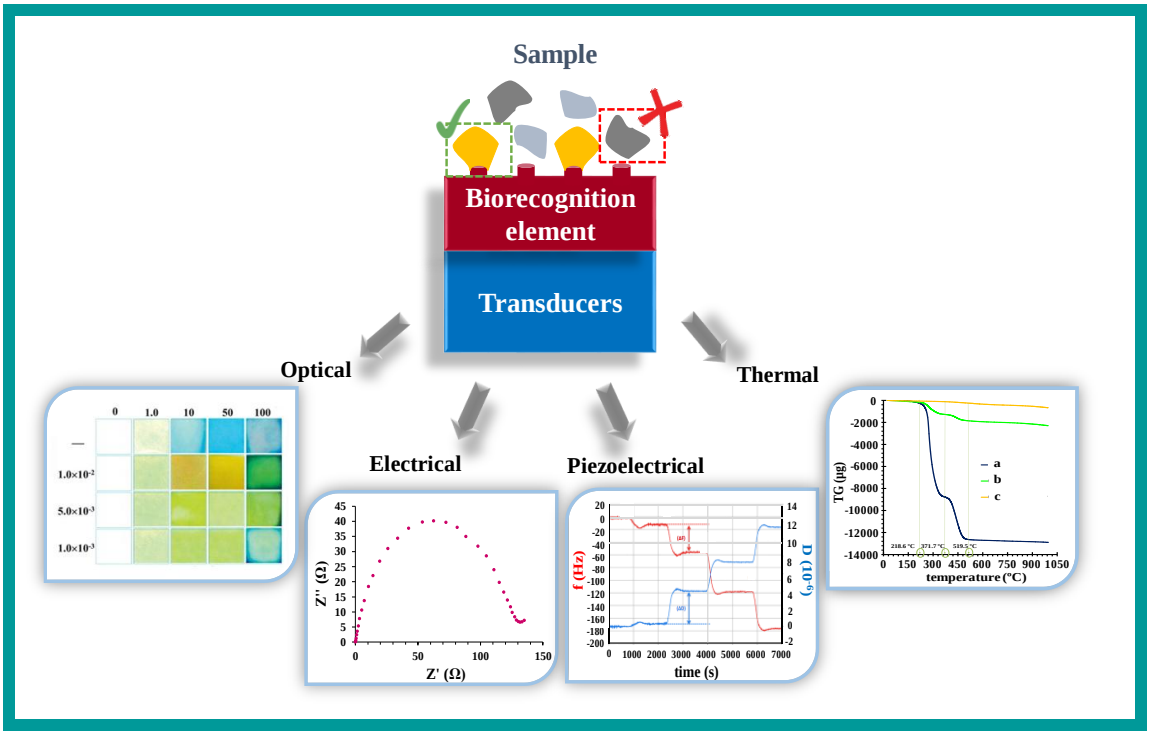

Figure 2.4. Types of transducers that monitor signal changes promoted by the interaction between the target molecule and the biorecognition element.

Thermal transducers exploit the fundamental properties of biological reactions (such as absorption or evolution of heat), which are reflected as a change in the temperature within the reaction medium. Commonly, these devices combine the temperature sensors with enzymes that meet a target analyte, starting the heat reaction of enzymes, where the corresponding signal is measured and calibrated against the analyte concentration [80,82,83]. Numerous applications relating to enzyme activity measurements, clinical monitoring, hybrid sensing, environmental monitoring, among others are described in the literature [59,60,84].

Piezoelectric transducers are devices that use acoustic or mechanical waves as detection system (surface acoustic wave (SAW), quartz crystal microbalances (QCM), or cantilever biosensors). In these transducers, the interaction of the target analyte may cause mechanical or electrical changes yielding variation in mass, conductivity, elasticity and dielectric properties, thereby generating medical, biochemical, and biophysical information [54,82].

Optical transducers have emerged as a good alternative to the previous ones, reflecting the ability of a given analyte to interact with electromagnetic radiation. Optical biosensors can be used in a wide range of different applications, including pharmaceutical research, diagnostic testing, environmental testing, or in life science research [85]. Different approaches may be employed in optical biosensing, such as reflectance measurements, Localized Surface Plasmon Ressonance (LSPR), interferometry, waveguides, and photonic crystals. The selection of an approach for a specific application depends on several factors, including sensitivity, easy fabrication and use, simplicity of readout instrumentation, assay throughput, and compatibility for the integration with fluid handling systems [85].

Electrochemical transducers are amongst the most popular devices in biosensing. Typically, these biosensors signal current or potential changes, providing quantitative data about the analyte present in a given solution [56,86]. Electrochemical biosensors offer rapid, simple, sensitive and inexpensive measurement, compatible with modern miniaturization/microfabrication technologies linked to POC analysis [17,53,57]. Several techniques may be employed for this purpose, including amperometry, voltammetry, potentiometry, capacitance, impedance spectroscopy, and conductivity [28,29,34,52-58,71]. Numerous examples of electrochemical transducers are described in the literature, using a wide range of materials, including nanotubes and nanowires, nanocrystals, polymers, and conventional semiconductors. These materials are expected to improve the overall electrochemical features, which may involve functionalization with appropriate chemical and biological capturing probes [34,52,54,61,84]. Chemical binding at the surface can promote a change in the electrical properties of the original nanomaterials, which may be identified via electrical measurement. Overall, in the electroanalytical field several techniques, including potentiometry, CV, EIS or SWV, among others, are successfully used for the evaluation of the analytical performance of biosensors, as these are simple, selective, involve inexpensive procedures, and require low sample volumes [87,88].

2.2.3.1. Potentiometry

Potentiometry is the field of electroanalytical chemistry that measures a potential difference under conditions of no current flow (or near-zero current), to quantify the analyte of interest [87,89,90]. In general, potentiometric-based methods are versatile, simple, rapid, and inexpensive, allowing the detection of almost any target ion.

Each electrochemical cell is typically composed by an anode and a cathode, and their potential difference results from the energy change (ΔG) that occurs when a chemical reaction proceeds until equilibrium is reached (**Equation 1**). In this equation, n is the number of electrons exchanged, F is *Faraday's* constant (96.485 C.mol^{-1}) and E is the maximum potential difference between two electrodes.

$$\Delta G = n.F.E \qquad \textbf{(Equation 1)}$$

Usually potentiometric measurements not involve electron transfer, but result instead on a potential generated by an ion concentration gradient produced after across a semi-permeable membrane [91]. In this case, the *Nernst* equation (**Equation 2**) should be used to determine the electrochemical potential of cell. In this, E is the potential difference between the two electrodes; E_0 is the cell potential at standard conditions; R_g is the universal gas constant (R_g = 8.314 J.mol^{-1}.K^{-1}); T is the temperature (in *Kelvin*); n_i is the electrical charge of the ion or number of electrons participating in the reaction; F is the *Faraday* constant ($F = 96485\ C.mol^{-1}$); and a_i is the activity of the primary ion in the sample.

$$E = E_0 - 2.303\frac{RT}{n_i F}log(a_i) \qquad \textbf{(Equation 2)}$$

Typically, an ideal analytical ion-selective electrode should be able to detect a single ion in solution, specifically and quantitatively. In such case, the slope of the calibration curve is 59/*n* mV/decade (25 °C), meaning that the potential variation *per decade* concentration (a unit difference among logarithm activities) is equal to 59 mV, dividing by the unit charge of the ionic specifies (positive or negative slopes for positive or negative charges, respectively).
However, the potentiometric probes are rarely specific to a certain ion, being commonly affected by the presence of additional ions in a solution leading to interferences in the system [91].

To determine the influence of an interfering ion against the final potential, the *Nikolsky–Eisenman* equation (**Equation 3**) should be considered, which is an extension of the Nernst equation. In this, $K_{i,j}^{pot}$ is the selectivity coefficient; *j* the interfering ionic species; *i* the main ion to which the electrode displays a selective response; a_j is the activity of the considered ion; and n_j is the electrical charge of the considered ion.

$$E = E_0 - 2.303\frac{RT}{n_i F} log\left(a_i + \sum_{i=1}^{n} K_{i,j}^{pot}(a_j)^{n_i/n_j}\right) \qquad \textbf{(Equation 3)}$$

Ion-selective electrodes (ISEs) are amongst the most common electrode approaches in potentiometry, typically represented by the pH electrodes [89]. ISEs are mostly portable and low-cost devices, suitable for field applications, providing rapid, sensitive, selective, and precise responses over a broad range of concentration of ionic analytes, using a conductive support to enable an easy handling of electrode by suppressing the conventional internal solution [29]. ISEs are characteristically electrodes that exhibit high selectivity for a given ion, once these contain a selective membrane that allows a suitable discrimination towards the targeted ionic species, and, thus, act as a "semi-permeable" membrane. These membranes are linked to an internal reference solution or casted on a solid-contact support, and show low solubility, electrical permittivity and selective interaction with the target analyte [91].

Selective membranes contain three basic components: an ion exchanger/ionophore, a mediator solvent and a polymeric matrix. The first component (exchanger/ionophore) consists in a material responsible for the electrochemical response of the electrode, which may be positively/negatively charged or neutral. The polymeric matrix is the body of the selective membrane, which should display rubbery properties at room temperature, resulting from the presence of the plasticizer solvent, to enable and enhance ion-exchange processes. Most of the ISEs in the literature use PVC membranes.

Selective membranes may be casted over a solid contact of low electrical resistance, providing a simple construction and easy operation, along with longer lifetimes [36,38,91]. In principle, the construction of such device consists of a solid conductive support made of carbon (comprising a mixture of graphite with non-conductive epoxy resin), introduced into a plastic tube and electrically linked to a copper wire. The selective membrane is then applied over the solid carbon support (**Figure 2.5A**). In general, solid contact electrodes present a higher mechanical stability and longer lifetimes than those with an internal reference solution, and offer simpler handling procedures and longer lifetimes. In addition, the electrode body may be recovered or reused for other applications and small amounts of selective membranes are needed to cover the solid conductive support [38,91].

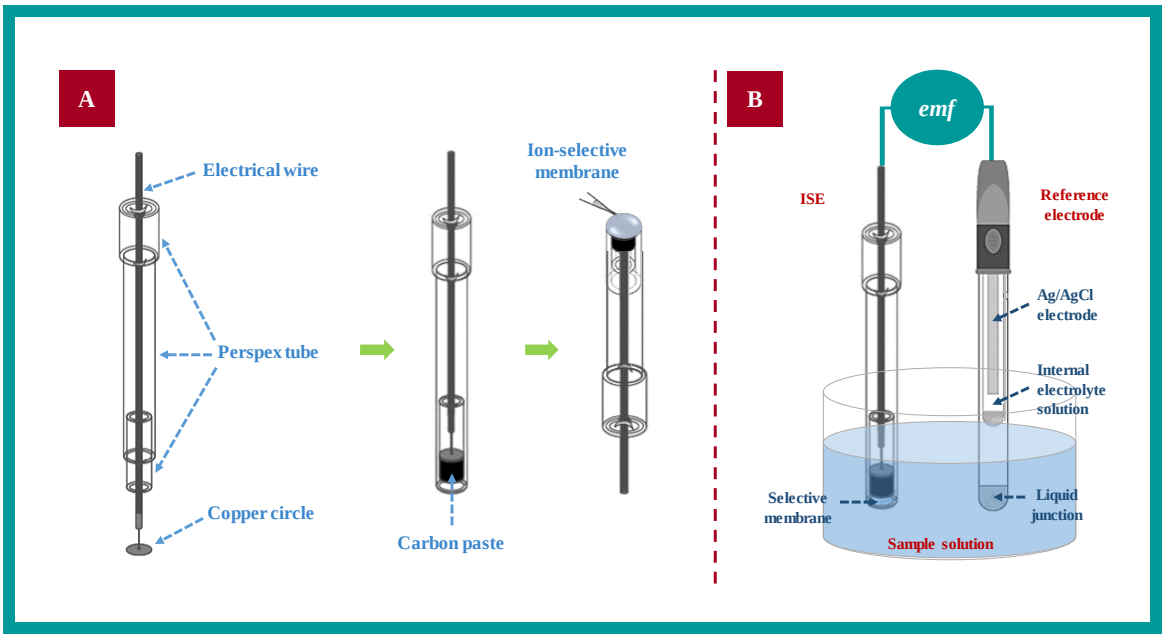

Figure 2.5. Schematic design of **(A)** the ion selective electrode construction and **(B)** electrochemical cell composed by an ion selective electrode and a silver/silver chloride reference electrode.

An ISE provides a stable potential at the interface electrode/solution, combining itself with the reference electrode to form an electrochemical cell and, thus, allowing a difference of the potentials of two electrodes, known as electromotive force (*emf*). Its inability to measure directly the potential of a single electrode creates the need for a reference electrode in the system. Both reference and indicator electrodes are immersed in the test solution and linked through a salt bridge, to measure the *emf* of cell. The reference electrode consists of an aqueous bridge electrolyte in contact with the sample solution via liquid junction, which potential must remain constant, unvarying for the duration of an experiment, with the view to provide a stable potential that is not affected by the environment conditions. The potential of this electrode must be reversible. Commonly, an Ag/AgCl reference electrode is used for this purpose, due to its simplicity, stability and inexpensive design. This electrode contains a silver wire with an electrolytic coating of AgCl chloride, which is immersed in a solution of a known concentration of potassium chloride (**Figure 2.5B**) [36,38]. The potential of this electrode depends of the Ag/Ag^{+} redox system, which in turn depends of the chloride concentration present in the solution, via de formation of AgCl(s), under equilibrium with Ag^{+} and Cl^{-}.

2.2.3.2. Cyclic voltammetry

Cyclic voltammetry (CV) is an electrochemical method where a certain potential (*E*) is applied between working and reference electrodes, varying linearly with time (ν=ΔE/Δt) to produce an electrical current at the electrode surface. This is a simple and fast electroanalytical technique that provides access to qualitative and quantitative information about a given electroactive species (oxidation or reduction reactions) and its reaction mechanisms [87,91].

CV measurements require an electrochemical cell with three-electrodes: working electrode (WE), reference electrode (RE) and counter electrode (CE) [91]. The resulting CV curve depends of the redox species involved in the electrochemical process, leading to the mass transfer of these species and the electron exchange, from the solution to the WE surface (by convection, migration or diffusion) and from the surface of the WE to the contact solution. According to the redox couple features, the system may be classified in reversible, quasi-reversible and irreversible [87]. In a reversible system, the kinetics of the redox couple is fast enough to ensure effective electron transfer and keep the system in equilibrium. In this, the product of the initial oxidation or reduction is fully oxidized or reduced, respectively, when reversing the scan direction. Characteristically, the peak shape of the reductive and reverse oxidative current versus the applied potential presents as shown in **Figure 2.6**.

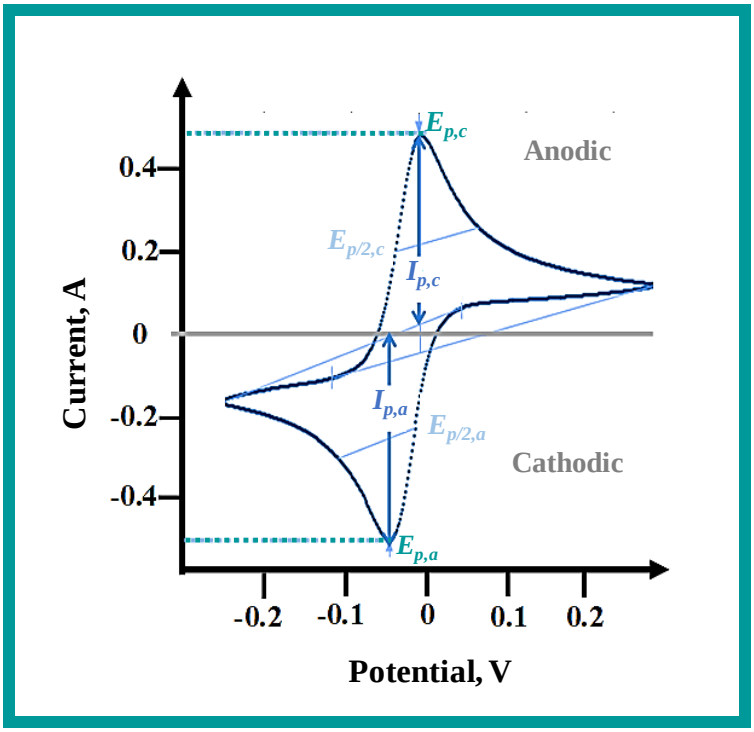

Figure 2.6. Characteristic cyclic voltammogram of a reversible system.

The effect of scan rate upon the peak current (I_p) can be described by *Randle-Sevcik* **equation 4**. In this, I_p corresponds to the peak current (A); the constant k has 2.69×10^5 value; n is the number of electrons involved in the reaction and that are transferred *per* electroactive species; A the area of the electrode surface (cm^2); D the diffusion coefficient of the species (cm^2/s); C the concentration (mol/L); and V the scan-rate of the potential (V/s).

$$I_p = k.n^{\frac{3}{2}}.A.D^{\frac{1}{2}}C.v^{\frac{1}{2}} \qquad \textbf{(Equation 4)}$$

According to this equation, at 25ºC, the I_p parameter is correlated with the scan-rate in order to understand if the electrode reaction is controlled by diffusion, and with the electrode area, to detect the occurrence of surface modifications [87,92].

When the previously mentioned conditions of reversibility do not apply, the system may be considered as quasi-reversible (**Figure 2.7**). In this, the kinetics of the redox reactions occurs simultaneously and the rate of electron transfer becomes comparable to that of the mass transport rate. The system could also be considered as irreversible, if the electron transfer rate is lower than that of the mass transport.

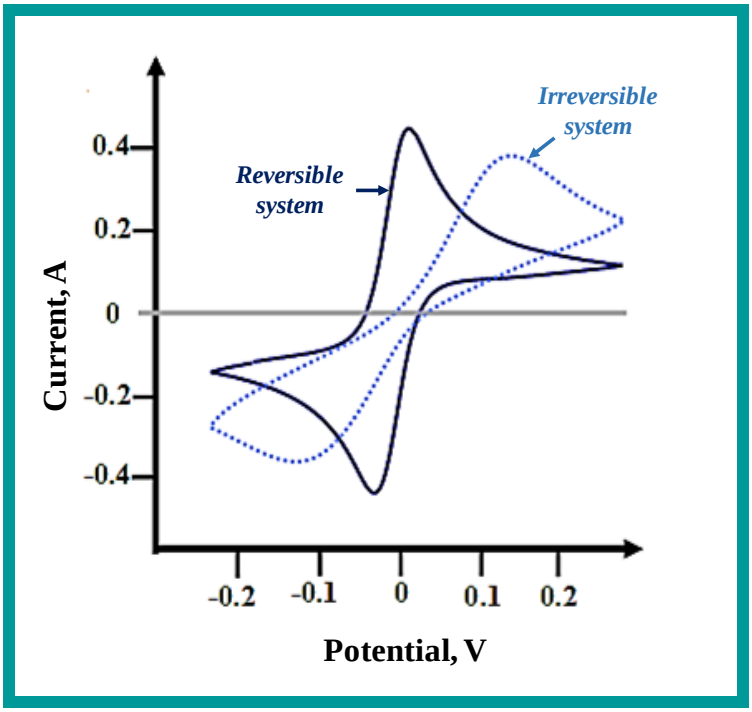

Figure 2.7. Representation of cyclic voltammograms of a reversible and an irreversible electrochemical system.

In general, the electrochemical process reflects the competition between the electrode kinetics and mass transport. Under this condition, the scan-rate increase should yield a greater electrochemical irreversibility and, at the same time, evidence an increased separation between anodic and cathodic peaks [92].

2.2.3.3. Electrochemical impedance spectroscopy (EIS) technique

Electrochemical impedance spectroscopy (EIS) is an electroanalytical technique that measures the impedance of an electrochemical system over a given range of frequencies, evaluating the modifications on the WE surface provided by the electrical transfer changes of a redox system [87,89]. This method allows the determination of several parameters by a fitted model, based on the ratio between the voltage and the current at a specific frequency response of the electrochemical system. By repeatable adsorption and desorption measurements on the WE surface, this electrochemical method gives kinetic and mechanistic information, displaying both resistive and capacitive properties when the system at equilibrium is subjected to a disturbance promoted by a small amplitude sinusoidal excitation [52]. Therefore, electrical response by EIS is defined as the ability of a circuit element to resist at the flow of electrical current, expressed by Ohm's law (**Equation 5**) that defines the resistance (*R*, ohms) in terms of ratio between voltage (*E*, volts) and current (*I*, amps).

$$R(\Omega) = \frac{E(V)}{I(A)} \qquad \textbf{(Equation 5)}$$

While this is a well-known relationship, its use is limited to only one circuit element, the ideal resistor. It also follows several assumptions: i) Ohm's law is valid at all current and voltage levels; ii) its resistance value is independent of the frequency; iii) alternating current (AC) and voltage signals, through a resistor are in phase with each other. Typically, the frequency response data may be characterized by Nyquist plots, which are represented by a real part on the X-axis, where each point corresponds to the impedance at a specific angular frequency (ω), and an imaginary part on the Y-axis of a chart, which is represented by negative values (**Figure 2.8**). These plots allow obtaining qualitative information from the generated semicircle (as shown in **Figure 2.8**), characteristic of a simple equivalent electrical circuit with a single time constant (t), even though some impedance plots could often contain more semicircles.

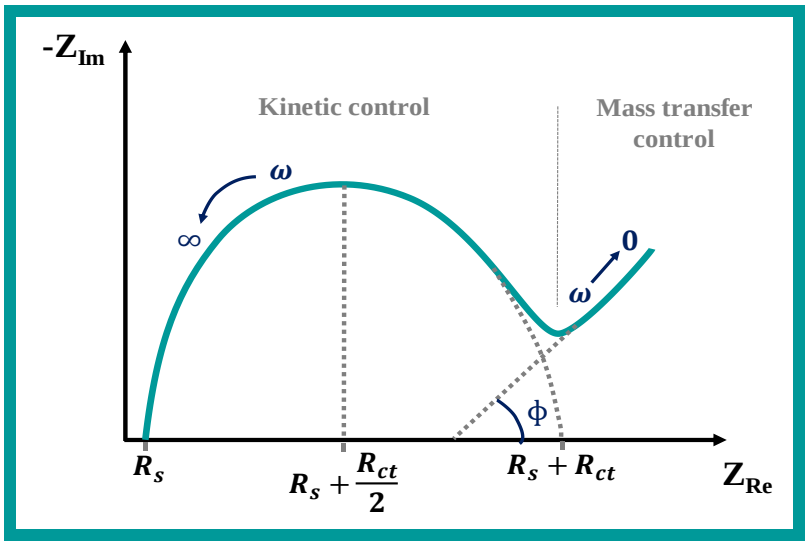

Figure 2.8. Nyquist plot illustrating the real (-Z_{Im}) and imaginary (Z_{Re}) components of the impedance at each angular frequency (ω). R_S: resistance of solution; R_{ct}: resistance of charge transfer and ϕ: phase.

In general, all this process can be translated mainly through **Equation 6**, where the impedance (Z) depends of the applied voltage at a time, $E(t) = E_0.\sin(\omega t)$, and of the intensity of the current, $I(t) = I_0.\sin(\omega t + \phi))$, where E_0 corresponds to the oscillation amplitude of the excitation signal; ω the angular frequency of the sinusoidal excitation (rad.s^{-1}); and I_0 the oscillation amplitude that is different from the current response and shifted in phase (ϕ) relatively to signal, respectively [87,91].

$$Z = \frac{E(t)}{I(t)} = \frac{E_0.\sin(\omega t)}{I_0.\sin(\omega t + \phi)} = Z_0 \frac{\sin(\omega t)}{\sin(\omega t + \phi)} \qquad \textbf{(Equation 6)}$$

Nevertheless, the results of an impedance measurement can, also, be presented through Bode plots, which give additional information from the impedance data, plotting the logarithm of the frequency ($log(\omega)$) on the X-axis and both the absolute values of the logarithm of the impedance ($log(|Z|)$) and the phase angle ($log(\phi)$) on the Y-axis (**Figure 2.9**). The Bode modulus and the Bode phase plots show the frequency values at each point, unlike the Nyquist plot. Moreover, information about the double layer capacitance of the electrochemical cell can be associated to the Bode phase plot behaviour as well as the diffusion coefficient of the system [87,91].

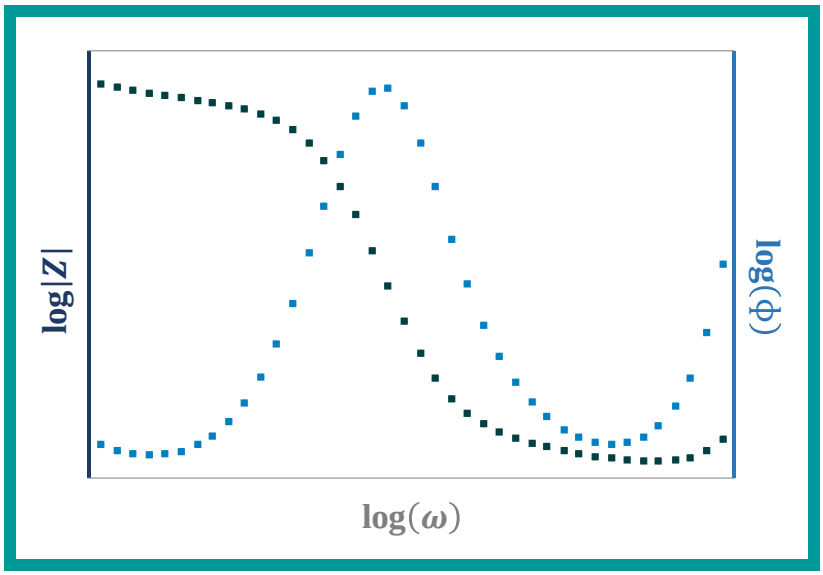

Figure 2.9. Graphic representation of a typical Bode plot: $log(|Z|) = f(log(\omega))$, Bode modulus (left Y-axis), and $log(\phi) = f(log(\omega))$, Bode phase plots (right Y-axis).

Both Nyquist and Bode plots allow evaluating the changes that occur on the conductive surface and blocks the electron transfer. Therefore, it is possible to define equivalent electrical circuit models or process models through developing mathematical formulas based on the kinetics of reactions involved in the system. These models allow fitting the impedance data properly and estimating some parameters (such as resistance of solution, R_s, resistance of charge transfer, R_{ct}, constant phase element, *CPE*, among others), and predicting the behaviour of the system under different conditions [87]. Randle's equivalent circuit is the model commonly adopted to understand the physicochemical process that occurs at a given electrode surface. In this, the elements in the circuit include R_s, R_{ct}, Warburg diffusion element (*W*), and *CPE* or double layer capacitor (C_{dl}), according to the different conditions (resistance when n=0, capacitance if n=1 or Warburg impedance if n=0.5) [93]. Both R_{ct} and capacitance depend of the dielectric and the insulating features at the electrode/solution interface, which can be controlled by the immobilization steps taking place at the electrode surface [94]. In general, EIS is a powerful technique in the development and analysis of materials employed in biosensors, monitoring the changes in the electrical properties of the electrode surface arising from a given chemical modification.

Overall, electrical-based transduction devices are mostly suitable in (bio)sensing. Among the several advantages, the low-cost manufacturing, quick response and portability features, are highlighted. In addition, such devices display suitable features for real-time and *in situ* monitoring, employing non-destructive and label-free analytical approaches, and promoting the production of (bio)layers, surfaces, thin-films, bulk materials or interfaces that may be ideally used to miniaturize and automate biomedical devices [34].

2.3. Photovoltaic cells

Energy is the most consumed resource by human civilization worldwide, and there are many different energies. Renewable sources are of great importance in this context, as these are collected from natural processes, replenished constantly in the human life, as sunlight, wind, rain, waves, and geothermal heat. Other kinds of energy employ non-renewable sources such as fossil fuels, including coal, petroleum, and natural gas, where the carbon represents the main element, and whose supplies can be limited for human lifetimes. With the increase of the global energy consumption along the years, it became crucial to ensure the continuity of the energy supply in order to avoid any energy disruption [95]. An important alternative energy source that has long been recognized is the solar energy abundantly available in the earth throughout the year, for energy conversion and consumption [95,96].

Recent advances in the solar cell technologies, like photovoltaic devices, have played a crucial role in the field of renewable energy, allowing efficient conversions of solar energy into electricity. Different photovoltaic cells have been developed so far, with more or less complexity, with higher or lower efficiencies. Still, the ones that are closer to nature are DSSCs, inspired in the respiration of plants and its system of converting light energy into an electron flow that sustains the cell operation.

2.3.2. Dye-Sensitized Solar Cells (DSSCs)

DSSCs were invented by Brian O'Regan and Michael Grätzel in 1988 [97] and have been the focus of intensive research activity since then, due to their great advantages. Some of these include easy manufacturing and high solar energy conversion efficiency at low fabrication cost, and eco-friendly approach/fabrication [95,96,98-102].

DSSCs make use of a coloured dye to absorb light and excite electrons; these electrons are injected into the valence band of a semiconductor and travel outside towards another electrode system, to reach the dye and regenerate its initial form.

The schematic representation of a DSSC may be seen in **Figure 2.10**. It is composed by a WE (also named photoanode) containing a nanocrystalline TiO_2 film modified with a ruthenium complex as sensitizer dye. This film is produced on a transparent conducting oxide (TCO) film (e.g. fluorine doped tin oxide, FTO, or indium doped tin oxide, ITO) deposited on top of a glass substrate; an iodide electrolyte solution composed by a I^-/I_3^- redox couple, and a platinum (Pt) CE, also known as cathode [96,99,100]. The photoexcitation of the sensitizer dye adsorbed on the TiO_2 surface from the ground state to the excited state promotes the transfer of electrons and their injection into the conduction band of the TiO_2, reaching the CE through the external circuit. These electrodes are collected by the iodide/triiodide (I^-/I_3^-) redox couple and transferred back to the photosensitizer oxidized dye, regenerating this component back to the ground state [95,99].

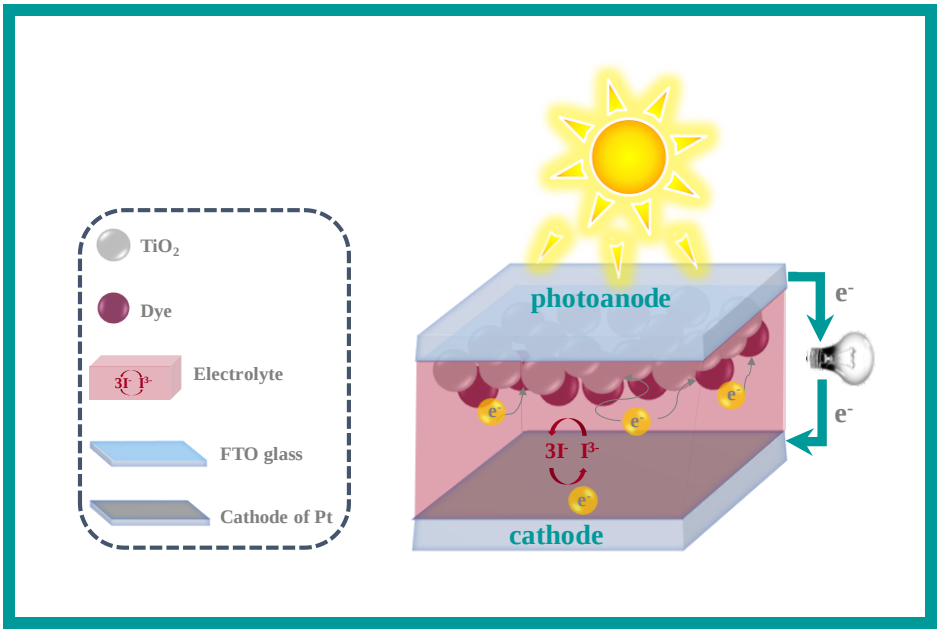

Figure 2.10. Schematic representation of a DSSC during the conversion of solar energy into electric energy.

Despite the high conversion efficiency levels already achieved by DSSCs described in the literature, numerous efforts have been made to improve the generated photocurrent and, consequently, the conversion efficiency of these cells.

Several approaches have been tried in the past decades, including the optimization of nanocrystalline TiO_2 layer thickness, the addition of a scattering layer on top of TiO_2 layer used in the conventional photoanode (such as TiO_2-Rutile or ZrO_2), novel electrolytes, or the synthesized new dyes [100,103,104].

In addition, metal nanoparticles have been embedded into the titanium dioxide layer to enhance the light absorption. This includes the use of Au NPs, Au nanorods or Ag NPs, whose resonant oscillations known as LSPR can be adjusted in the visible-near infrared region of electromagnetic spectrum [98,100,105-107].

2.3.3. Plasmonic effect in DSSCs

Colloidal metals nanoparticles are of great interest in different research fields, accounting their optical and/or electrical properties, and their easy biofunctionalization and high surface area. Overall, this research field has given rise to novel materials with interesting electronic, chemical and spectral properties [2,108,109].

Among the several metals, Au NPs have attracted more attention and were widely studied in several research areas, mostly due to their high conductivity, thermal and chemical stability [110,111,112]. Their optical properties have attracted great interest as signal transducers in bioassays for diagnostic and monitoring of specific target, avoiding the use of expensive and/or sophisticated equipment [109,112-115]. The plasmonic behaviour of these nanoparticles, in which the LSPR band is detected in the visible region of electromagnetic spectrum, shows a high sensitivity for interparticle interactions, particle size and shape, and easy surface chemistry handling [106,112]. In addition, recent advances have revealed the Au NPs sensitivity with dielectric materials and their ability to enhance the performance of photovoltaic devices, like DSSCs, causing alterations in the electron charging effects that, consequently, increase the photocurrent and photovoltage of these solar cells [108,113,114]. Several studies have been described in the literature for this purpose. Derkacs and co-authors (2006) reported the incorporation of Au NPs in an amorphous silicon solar cell, to enhance its photocurrent and, thus, its power conversion efficiency [116]. Brown and co-authors (2011) reported the integration of $Au@SiO_2$ core–shell nanoparticles into the TiO_2 paste in DSSCs, leading to significant improvements in photocurrent and efficiency [117].

Choi et al. (2012) compared the plasmonic and electron charging effects of DSSCs composed with TiO_2-capped Au@SiO_2 and TiO_2-capped Au@TiO_2 nanoparticles, and the best DSSC performance was achieved when TiO_2 had Au@SiO_2 as neighbor [118]. Other works have reported similar conclusions, incorporating Au NPs to enhance the performance of DSSCs, as described in **Table 2.2**.

Table 2.2. Performance characteristics of DSSCs produced with different photoanodes under 100 mW.cm^{-2}.PA: Photoanode; CE: Counter electrode; J_{SC}: Short circuit current density; V_{OC}: Open-circuit potential; *FF*: Fill Factor; η: Energy conversion efficiency; FTO: fluorine-doped tin oxide; NPs: nanoparticles.

Working electrode	J_{SC} (mA/cm^2)	V_{OC} (mV)	*FF* (%)	η (%)	References
PA: N719/TiO_2/FTO	11.90	770.0	63.99	5.84	[101], 2013
PA: N719/TiO_2@AuNPs,15nm/FTO	12.26	780.0	65.65	6.27	
PA: N719/TiO_2@AuNPs,25nm/FTO	12.84	780.0	66.74	6.69	
PA: N719/TiO_2/FTO	11.36	771.3	58.42	5.12	[104], 2016
PA: N719/TiO_2@AuNPs/FTO	12.00	737.3	70.66	6.23	
PA: N719/TiO_2/FTO	12.83	820.0	61.71	6.54	[105], 2016
PA: N719/TiO_2@AuNPs/FTO	12.34	826.7	60.60	6.27	
PA: N719/TiO_2/FTO	10.04	750.0	43.00	4.34	[110], 2014
PA: N719/TiO_2@Au 0.50 mol%/FTO	12.48	780.0	42.00	5.40	
PA: N719/TiO_2@Au 1.0 mol%/FTO	13.06	780.0	44.00	5.52	
PA: N719/TiO_2@Au 2.0 mol%/FTO	8.27	770.0	56.00	4.13	
PA: N719/TiO_2@Au 3.0 mol%/FTO	7.02	770.0	39.00	3.33	
PA: N719/TiO_2/FTO	2.14	740.0	66.00	1.05	[117], 2011
PA: N719/TiO_2@Au-SiO_2/FTO	3.37	760.0	76.00	1.95	
PA: N719/TiO_2/FTO	18.28	729.0	69.70	9.29	[118], 2012
PA: N719/TiO_2@AuNPs/FTO	18.28	771.0	69.40	9.78	
PA: N719/TiO_2@Au-SiO_2/FTO	20.31	727.0	69.10	10.21	
PA: N719/TiO_2/FTO	12.60	700.0	56.00	5.00	[119], 2012
PA: N719/TiO_2@AuNPs/FTO	13.20	740.0	61.00	6.00	

According to the results demonstrated on the previous table, most of control photoanodes (N719/TiO_2/FTO) presented the worst DSSCs performance [101,104,117,118,119] comparatively with the photoanodes composed by Au NPs, once the energy conversion efficiency values varied between 1.95 and 9.29% in the control cells, and 3.33 and 9.78% in the plasmonic DSSCs. Also, as abovementioned, the authors of the works published in 2011 [117] and 2012 [118], described that the included of Au-SiO_2 nanoparticles caused a significant improvement in photocurrent and efficiency of DSSCs. However, Dao et al. (2016) reported that a conventional DSSC, composed only with TiO_2, had better J_{SC}, FF and and efficiency values comparing with the performance of DSSCs composed by photoanodes with Au NPs. Moreover, **Table 2.2**. demonstrates a work of Ninsonti et al. (2014), in which different amounts of Au NPs with an average diameter of 50–100 nm in the DSSC photoanodes composition were employed. The authors studied 0.50, 1.0, 2.0 and 3.0 mol% of Au-loaded TiO_2 in the photoanodes composition, and concluded that the DSSCs with up to 1.0 mol% Au-loaded TiO_2 leading to an enhancement of the performance by localized surface plasmon effect and scattering property. Different sizes of nanoparticles between 15 nm and 25 nm of Au NPs were studied by Zhang et al. (2013) and the best DSSC was achieved with the photoanodes composed by 25 nm sized Au NPs, once exhibited an efficiency of 6.69%, which was 7% and 15% higher than the DSSCs with 15 nm sized Au NPs and control DSSCs, respectively.

Overall, the plasmonic effect of Au NPs yielded good progresses in the performance of DSSCs. There are numerous compositions of CEs (cathodes) already described in the literature, like Pt (the cathode that is commonly used in DSSCs), carbon nanomaterials and conducting polymers, some of these with metal NPs. Such wide range of different publications and approaches also confirms that DSSCs may turn out a promising technique to become the electrical source of a portable device and to carry out tests in POC, targeting the detection of a large range of biomarkers, such as cancer biomarkers.

2.4. Final considerations

Overall, the brief review of the current methods and technologies employed for the assessment of cancer biomarkers presented in this chapter showed the need to develop new strategies for an early diagnosis of cancer biomarkers towards on-site application. For this purpose, there are several recognition elements that may be used for the new design of biosensors, with special emphasis for plastic antibodies. Different electrochemical configurations may also be employed, including glass supports that may be integrated later in another suitable device.

In general, it is important that a given biosensor has the ability to discriminate the target analyte among other compounds and that the electrochemical configuration is suitable for a quick and low cost analysis, especially in POC conditions.

Regarding electrochemical biosensors, the electrical power requirement is the main limitation to a full autonomy, and this may be achieved by coupling this into a system providing electrical current form a renewable source. In this regard, no other work was found in the world combining photovoltaic cells and biosensors published in the literature, apart from the work to be developed herein. Overall, this opens doors for a self-sustained biosensor and, thus, the possibility to have miniaturized and automated biomedical devices that are suitable for the routine screening of the desired targets.

References

[1] Y. Wang, Z. Zhang, V. Jain, J. Yi, S. Mueller, J. Sokolov, Z. Liu, K. Levon, B. Rigas, and M. H. Rafailovich, 'Potentiometric sensors based on surface molecular imprinting: Detection of cancer biomarkers and viruses', *Sensors Actuators B Chem.*, vol. 146, no. 1, pp. 381–387, 2010.

[2] Y. Yin, Y. Cao, Y. Xu, and G. Li, 'Colorimetric immunoassay for detection of tumor markers', *Int. J. Mol. Sci.*, vol. 11, no. 12, pp. 5077–5094, 2010.

[3] S. Ramos, 'Cancer chemoprevention and chemotherapy: Dietary polyphenols and signalling pathways', *Mol. Nutr. Food Res.*, vol. 52, no. 5, pp. 507–526, 2008.

[4] G. M. Cooper and R. E. Hausman, 'The Cell: A molecular approach', fourth edition, 2007.

[5] R. Mayeux, 'Biomarkers: potential uses and limitations', *NeuroRx*, vol. 1, no. 2, pp. 182–188, 2004.

[6] S. Sharma, 'Tumor makers in clinical practice: General principles and guidelines', *Indian J. Med. Res.*, vol. 30, no. 1, pp. 1–8, 2009.

[7] D. W. Mercer and R. B. Herberman, 'Tumor Markers in Cancer Diagnosis and Prognosis'.

[8] N. L. Henry and D. F. Hayes, 'Cancer biomarkers', *Mol. Oncol.*, vol. 6, no. 2, pp. 140–146, 2012.

[9] V. I., T. D., and B. N.L., 'Cancer prevention: State of the art and future prospects', *J. Prev. Med. Hyg.*, vol. 56, pp. 21–27, 2015.

[10] J. Ferlay, I. Soerjomataram, R. Dikshit, S. Eser, C. Mathers, M. Rebelo, D. M. Parkin, D. Forman, and F. Bray, 'Cancer incidence and mortality worldwide: Sources, methods and major patterns in GLOBOCAN 2012', *Int. J. Cancer*, vol. 136, no. 5, pp. E359–E386, 2015.

[11] I. Ewing, J. J. Hurley, E. Josephides, and A. Millar, 'The molecular genetics of colorectal cancer', *Frontline Gastroenterol.*, vol. 5, no. 1, pp. 26–30, 2014.

[12] I. Ghosh, D. Bhattacharjee, A. K. Das, G. Chakrabarti, A. Dasgupta, and S. K. Dey, 'Diagnostic role of tumour markers CEA, CA15-3, CA19-9 and CA125 in lung cancer', *Indian J. Clin. Biochem.*, vol. 28, no. 1, pp. 24–29, 2013.

[13] M. A. A. Hamed, S. A. A. Ahmed, and H. M. Khaled, 'Efficiency of diagnostic biomarkers among colonic schistosomiasis egyptian patients', *Mem. Inst. Oswaldo Cruz*, vol. 106, no. 3, pp. 322–329, 2011.

[14] M. Hall, S. Bryant, M. Jackson, J. T. Johnson, H. Schultze, W. Cooksey, S. D. Manceva, R. Crowell, S. Johnson, T. Sims-Davis, K. L. Beason, S. R. Clinton, D. Fortenberry, C. Bright, H. Hua, J. Ying, and P. Sykes, 'A comparison of CA242 with twelve other tumor antigens for the serodiagnosis of pancreatic, gastric, and other gastrointestinal cancers', *Chemist*, vol. 86, no. 2, pp. 1–16, 2013.

[15] Y. Li, W.-K. Yang, M.-Q. Fan, and A. Liu, 'A sensitive label-free amperometric CEA immunosensor based on graphene-nafion nanocomposite film as an enhanced sensing platform', *Anal. Sci.*, vol. 27, no. 7, pp. 727-731, 2011.

[16] L. A. A. N. A. Truta and M. G. F. Sales, 'Sol-Gel Chemistry in Biosensing Devices of Electrical Transduction: application to CEA Cancer Biomarker', *Curr Top Med Chem.*, vol. 15, no. 3, pp. 256–261, 2015.

[17] I. Zaccari, A. G. Davies, C. Walti, and S. X. Laurenson, 'Label-free electrochemical biosensors for clinical diagnostic', *2014 Cairo Int. Biomed. Eng. Conf.*, pp. 15–18, 2014.

[18] M. Liu, C. Jia, Q. Jin, X. Lou, S. Yao, J. Xiang, and J. Zhao, 'Novel colorimetric enzyme immunoassay for the detection of carcinoembryonic antigen', *Talanta*, vol. 81, no. 4–5, pp. 1625–1629, 2010.

[19] J. C. Kemmegne-Mbouguen, E. Ngameni, P. G. Baker, T. T. Waryo, B. Kgarebe, and E. I. Iwuoha, 'Carcinoembryonic antigen immunosensor developed with organoclay nanogold composite film', *Int. J. Electrochem. Sci.*, vol. 9, no. 1, pp. 478–492, 2014.

[20] F. Tan, F. Yan, and H. Ju, 'A designer ormosil gel for preparation of sensitive immunosensor for carcinoembryonic antigen based on simple direct electron transfer', *Electrochem. commun.*, vol. 8, no. 12, pp. 1835–1839, 2006.

[21] W. Shi and Z. Ma, 'A novel label-free amperometric immunosensor for carcinoembryonic antigen based on redox membrane', *Biosens. Bioelectron.*, vol. 26, no. 6, pp. 3068–3071, 2011.

[22] P. Lv, L. Min, R. Yuan, Y. Chai, and S. Chen, 'A novel immunosensor for carcinoembryonic antigen based on poly(diallyldimethylammonium chloride) protected prussian blue nanoparticles and double-layer nanometer-sized gold particles', *Microchim. Acta*, vol. 171, no. 3, pp. 297–304, 2010.

[23] X. Miao, S. Zou, H. Zhang, and L. Ling, 'Highly sensitive carcinoembryonic antigen detection using Ag@Au core-shell nanoparticles and dynamic light scattering', *Sensors Actuators B Chem.*, vol. 191, pp. 396–400, 2014.

[24] B. J. Casey and P. Kofinas, 'Selective binding of carcinoembryonic antigen using imprinted polymeric hydrogels', *J. Biomed. Mater. Res. - Part A*, vol. 87, no. 2, pp. 359–363, 2008.

[25] Y. Fu, R. Yuan, Y. Chai, Y. Zhang, and Y. Peng, 'Electrochemical immunoanalysis for carcinoembryonic antigen based on multilayer architectures of gold nanoparticles and polycation biomimetic interface on glassy carbon electrode', *Electroanalysis*, vol. 18, no. 24, pp. 2451–2457, 2006.

[26] S. Hammarström, 'The carcinoembryonic antigen (CEA) family: structures, suggested functions and expression in normal and malignant tissues.', *Semin. Cancer Biol.*, vol. 9, no. 2, pp. 67–81, 1999.

[27] D. Das, D. M. Kim, D. S. Park, and Y. B. Shim, 'A glucose sensor based on an aminophenyl boronic acid bonded conducting polymer', *Electroanalysis*, vol. 23, no. 9, pp. 2036–2041, 2011.

[28] W. Wang, G. Xu, X. T. Cui, G. Sheng, and X. Luo, 'Enhanced catalytic and dopamine sensing properties of electrochemically reduced conducting polymer nanocomposite doped with pure graphene oxide', *Biosens. Bioelectron.*, vol. 58, pp. 153–156, 2014.

[29] L.A.A.N.A. Truta, N. S. Ferreira, and M. G. F. Sales, 'Graphene-based biomimetic materials targeting urine metabolite as potential cancer biomarker: Application over different conductive materials for potentiometric transduction', *Electrochim. Acta*, vol. 150, pp. 99–107, 2014.

[30] F. T. C. Moreira, M. J. M. S. Ferreira, J. R. T. Puga, and M. G. F. Sales, 'Screen-printed electrode produced by printed-circuit board technology. Application to cancer biomarker detection by means of plastic antibody as sensing material', *Sensors Actuators B Chem.*, vol. 223, pp. 927–935, 2016.

[31] H. Yu, F. Yan, Z. Dai, and H. Ju, 'A disposable amperometric immunosensor for α-1-fetoprotein based on enzyme-labeled antibody/chitosan-membrane-modified screen-printed carbon electrode', *Anal. Biochem.*, vol. 331, no. 1, pp. 98–105, 2004.

[32] S. Teixeira, R. S. Conlan, O. J. Guy, and M. G. F. Sales, 'Label-free human chorionic gonadotropin detection at picogram levels using oriented antibodies bound to graphene screen-printed electrodes', *J. Mater. Chem. B*, vol. 2, no. 13, pp. 1852, 2014.

[33] G. Cabral-Miranda, E. H. G. Yamashiro-Kanashiro, M. Gidlunda, and M. G. F. Sales, 'Specific label-free and real-time detection of oxidized low density lipoprotein (oxLDL) using an immunosensor with three monoclonal antibodies', *Gold Bull.*, vol. 3, no. 1, pp. 1–5, 2014.

[34] D. Grieshaber, R. Mackenzie, J. Vörös, and E. Reimhult, 'Electrochemical Biosensors -Sensor Principles and Architectures', *Sensors*, vol. 8, pp. 1400–1458, 2008.

[35] S. F. Clarke and J. R. Foster, 'A history of blood glucose meters and their role in self-monitoring of diabetes mellitus', vol. 69, no. 2, pp. 83–93, 2012.

[36] F. Teixeira and C. Moreira, 'Fast screening for diagnostic of heart ischemic episodes', 2013.

[37] E.H. Yoo and S.Y. Lee, 'Glucose Biosensors: An Overview of Use in Clinical Practice', *Sensors*, vol. 10, pp. 4558–4576, 2010.

[38] R. B. Queirós, 'Biosensors for the detection and quantification of aquatic bacterial contamination in waters for human use', 2013.

[39] X. Luo, J.J. Davis, 'Electrical biosensors and the label free detection of protein disease biomarkers', *Chem. Soc. Rev.*, vol. 42, pp. 5944-5962, 2013.

[40] X. Yang, Y. Guo, A. Wang, 'Luminol/antibody labeled gold nanoparticles for chemiluminescence immunoassay of carcinoembryonic antigen', *Analytica Chimica Acta*, vol. 666, pp. 91–96, 2010.

[41] Y. Li, W.K. Yang, M.Q. Fan, A. Liu, 'A sensitive label-free amperometric CEA immunosensor based on graphene-nafion nanocomposite film as an enhanced sensing platform', *Analytical Sciences*, vol. 27, pp. 727-731, 2011.

[42] G.M, Saied, W.H. El-Metenawy, M.S. Elwan, N.R. Dessouki, 'Urine carcinoembryonic antigen levels are more usefulthan serum levels for early detection of Bilharzial and non-Bilharzial urinary bladder carcinoma: Observations of 43 Egyptian cases', *World J. Surg. Oncol.*, vol. 5, no. 4, 2007.

[43] L.J. Havrilesky, C.M. Whitehead, J.M. Rubatt, R.L. Cheek, J. Groelke, Q. He, D.P. Malinowski, T.J. Fischer, A. Berchuck, 'Evaluation of biomarker panels for early stage ovarian cancer detection and monitoring for disease recurrence', *Gynecol. Oncol.*, vol. 110, pp. 374–382, 2008.

[44] C.C. Chang, N.F. Chiu, D.S. Lin, Y. Chu-Su, Y.H. Liang, C.W. Lin, 'High-Sensitivity Detection of Carbohydrate Antigen 15-3 Using a Gold/Zinc Oxide Thin Film Surface Plasmon Resonance-Based Biosensor', *Anal. Chem.*, vol. 82, pp. 1207–1212, 2010.

[45] J.A. Ribeiro, C.M. Pereira, A.F. Silva, M.G.F. Sales, 'Disposable electrochemical detection of breast cancer tumour marker CA 15- 3 using poly(Toluidine Blue) as imprinted polymer receptor', *Biosens Bioelectron*, vol. 30, pp. 246-254, 2018.

[46] J. Amani, A. Khoshroo, M. Rahimi-Nasrabadi, 'Electrochemical immunosensor for the breast cancer marker CA 15–3 based on the catalytic activity of a CuS/reduced graphene oxide nanocomposite towards the electrooxidation of catechol', *Microchim. Acta*, vol. 185, no. 79, 2018.

[47] X. Chen, G. Zhou, P. Song, J. Wang, J. Gao, J. Lu, C. Fan, X. Zuo, 'Ultrasensitive Electrochemical Detection of Prostate-Specific Antigen by Using Antibodies Anchored on a DNA Nanostructural Scaffold', *Anal. Chem.*, vol. 86, pp. 7337−7342, 2014.

[48] S. Zhang, C. Sun, W. Zhou, 'Electrochemical Immunoassay Determination of a Cancer Biomarker (CA19-9) by Horseradish Peroxidase', *Int. J. Electrochem. Sci.*, vol. 12, pp. 8447 – 8456, 2017.

[49] D. Du, F. Yan, S. Liu, H. Ju, 'Immunological assay for carbohydrate antigen 19-9 using an electrochemical immunosensor and antigen immobilization in titania sol–gel matrix', *J. Immunol. Methods*, vol. 283, no. 1-2, pp. 67–75, 2003.

[50] W. Wang, X. Xu, B. Tian, Y. Wang, L. Du, T. Sun, Y. Shi, X. Zhao, J. Jing, 'The diagnostic value of serum tumor markers CEA, CA19-9, CA125, CA15-3, and TPS in metastatic breast cancer', Clinica Chimica Acta, vol. 470, pp. 51-55, 2017.

[51] B. R. Eggins, 'Chemical Sensor and Biosensor', *Anal. Tech. Sci.*, pp. 125–168, 2004.

[52] B. Piro, S. Reisberg, 'Recent Advances in Electrochemical Immunosensors – review', *Sensors*, vol. 17, no. 794, 2017.

[53] A. P. F. Malhotra, D. Bansi, A.P.F. Turner, 'Advances in Biosensors: perspectives in biosensors', 2003.

[54] D. Li, 'Encyclopedia of Microfluidics and Nanofluidics', vol. 53, 2013.

[55] K.R. Rogers, 'Principles of Affinity-Based Biosensors', *Methods in Biotechnology: Affinity Biosensors*, vol 7, pp. 3-18, 1998.

[56] X. Zhang, H. Ju, J. Wang, 'Electrochemical Sensors, Biosensors and their Biomedical Applications', 2008.

[57] A. Syahir, K. Usui, K. Tomizaki, K. Kajikawa, H. Mihara, 'Label and Label-Free Detection Techniques for Protein Microarrays', *Microarrays*, vol. 4, no. 2, pp. 228–244, 2015.

[58] B. Mattiasson, M. Hedström, 'Capacitive biosensors for ultra-sensitive assays', *TrAC Trends in Analytical Chemistry*, vol. 79, pp. 233-238, 2016.

[59] S. Vigneshvar, C.C. Sudhakumari, B. Senthilkumaran, H. Prakash, 'Recent Advances in Biosensor Technology for Potential Applications – An Overview', *Front. Bioeng. Biotechnol.* vol. 4, no. 11, 2016.

[60] S. S. Z. Hindi, 'Recent advances in potential applications of biosensors', *BioElectronics Applications Journal*, vol. 1, no. 2, pp. 1-16, 2016.

[61] H. K. Hunt, A. M. Armani, 'Label-free biological and chemical sensors', *Nanoscale*, vol. 2, no. 9, pp. 1544–1559, 2010.

[62] D. Yin, M. Ulbricht, 'Protein-selective adsorbers by molecular imprinting via a novel two-step surface grafting method', *J. Mater. Chem. B*, vol. 1, no. 25, pp. 3209, 2013.

[63] T.J. Li, P.Y. Chen, P.C. Nien, C.Y. Lin, R. Vittal, T.R. Ling, K.C. Ho, 'Preparation of a novel molecularly imprinted polymer by the sol-gel process for sensing creatinine', *Anal. Chim. Acta*, vol. 711, pp. 83–90, 2012.

[64] G. Vasapollo, R. Del Sole, L. Mergola, M. R. Lazzoi, A. Scardino, S. Scorrano, G. Mele, 'Molecularly imprinted polymers: Present and future prospective', *Int. J. Mol. Sci.*, vol. 12, no. 9, pp. 5908–5945, 2011.

[65] K. Balamurugan, K. Gokulakrishnan, T. Prakasam, 'Preparation and evaluation of molecularly imprinted polymer liquid chromatography column for the separation of Cathine enantiomers', *Saudi Pharmaceutical Journal*, vol.20, pp. 53-61, 2012.

[66] A.K. Roy, V.S. Nisha, C. Dhand, B.D. Malhotra, 'Molecularly imprinted polyaniline film for ascorbic acid detection', *J. Mol. Recognit.*, vol. 24, no. 4, pp. 700–706, 2011.

[67] M.A.R. Khan, F.T.C. Moreira, J. Riu, M.G.F. Sales, 'Plastic antibody for the electrochemical detection of bacterial surface proteins', *Sensors Actuators B Chem.*, vol. 233, pp. 697–704, 2016.

[68] F.T.C. Moreira, R.A.F. Dutra, J.P.C. Noronha, M.G.F. Sales, 'Electrochemical biosensor based on biomimetic material for myoglobin detection', *Electrochim. Acta*, vol. 107, pp. 481–487, 2013.

[69] D. Cai, L. Ren, H. Zhao, C. Xu, L. Zhang, Y. Yu, Y. Lan, M.F. Roberts, J. Chuang, M.J. Naughton, T.C. Chiles, 'A molecular imprint nanosensor for ultrasensitive detection of proteins', vol. 5, no. 8, pp. 597–601, 2011.

[70] A. Mathur, S. Blais, C.M.V Goparaju, T. Neubert, H. Pass, K. Levon, 'Development of a Biosensor for Detection of Pleural Mesothelioma Cancer Biomarker Using Surface Imprinting', *PLoS One*, vol. 8, no. 3, pp. 1–8, 2013.

[71] Y. Wang, Y. Zhou, J. Sokolov, B. Rigas, K. Levon, M. Rafailovich, 'A potentiometric protein sensor built with surface molecular imprinting method', *Biosens. Bioelectron.*, vol. 24, no. 1, pp. 162–166, 2008.

[72] A.P.M. Tavares, N.S. Ferreira, L.A.A.N.A. Truta, M.G.F. Sales, 'Conductive Paper with Antibody-Like Film for Electrical Readings of Biomolecules', *Sci. Rep.*, vol. 6, pp. 26132, 2016.

[73] M.C. Blanco-López, M.J. Lobo-Castañón, A.J. Miranda-Ordieres, P.Tuñón-Blanco, 'Electrochemical sensors based on molecularly imprinted polymers', *TrAC - Trends Anal. Chem.*, vol. 23, no. 1, pp. 36–48, 2004.

[74] F.T.C. Moreira, S. Sharma, R.A.F. Dutra, J.P.C. Noronha, A.E.G. Cass, M.G.F. Sales, 'Smart plastic antibody material (SPAM) tailored on disposable screen printed electrodes for protein recognition: Application to myoglobin detection', *Biosens. Bioelectron.*, vol. 45, no. 1, pp. 237–244, 2013.

[75] F.T.C. Moreira, A.P. Moreira-Tavares, M.G.F. Sales, 'Sol-Gel-Based Biosensing Applied to Medicinal Science', *Curr Top Med Chem*, vol.15, no. 3, pp. 245–255, 2015.

[76] S.A. Piletsky, E.V. Piletska, B. Chen, K. Karim, D. Weston, G. Barrett, P. Lowe, A.P.F. Turner, 'Chemical grafting of molecularly imprinted homopolymers to the surface of microplates. Application of artificial adrenergic receptor in enzyme-linked assay for β-agonists determination', *Anal. Chem.*, vol. 72, no. 18, pp. 4381–4385, 2000.

[77] O.Y.F. Henry, S.A. Piletsky, D.C. Cullen, 'Fabrication of molecularly imprinted polymer microarray on a chip by mid-infrared laser pulse initiated polymerisation', *Biosens. Bioelectron.*, vol. 23, no. 12, pp. 1769–1775, 2008.

[78] M.M. Titirici, B. Sellergren, 'Thin Molecularly Imprinted Polymer Films via Reversible Addition−Fragmentation Chain Transfer Polymerization', *Chem. Mater.*, vol. 18, no. 4, pp. 1773–1779, 2006.

[79] E. Lahiff, C. Lynam, N. Gilmartin, R. O'Kennedy, D. Diamond, 'The increasing importance of carbon nanotubes and nanostructured conducting polymers in biosensors', *Anal. Bioanal. Chem.*, vol. 398, no. 4, pp. 1575–1589, 2010.

[80] K. Ramanathan, M. Rank, J. Svitel, A. Dzgoev, B. Danielsson, 'The development and applications of thermal biosensors for bioprocess monitoring', *Trends Biotechnol.*, vol. 17, no. 12, pp. 499–505, 1999.

[81] G. Liu, Y. Wan, Z.Y. Zou, S.Z. Ren, C.H. Fan, 'Deoxyribonucleic acid molecular design for electrochemical biosensors', *Fenxi Huaxue/ Chinese J. Anal. Chem.*, vol. 39, no. 7, pp. 953–962, 2011.

[82] B.E. Rapp, F.J. Gruhl, K. Länge, 'Biosensors with label-free detection designed for diagnostic applications', *Anal. Bioanal. Chem.*, vol. 398, no. 6, pp. 2403–2412, 2010.

[83] K. Ramanathan, B. Danielsson, 'Principles and applications of thermal biosensors', *Biosens. Bioelectron.*, vol. 16, no. 6, pp. 417–423, 2001.

[84] C. Zhu, G. Yang, H. Li, D. Du, Y. Lin, 'Electrochemical Sensors and Biosensors Based on Nanomaterials and Nanostructures', *Anal. Chem.*, vol. 87, no. 1, pp. 230–249, 2015.

[85] F. Breu, S. Guggenbichler, J. Wollmann, 'Label-free biosensors techniques and applications', *Cambridge University Press*, 2009.

[86] M. Pohanka, P. Skládal, 'Electrochemical Biosensors-Principles and Applications', 2016.

[87] C. Brett, A. Brett, 'Electrochemistry: principles, methods, and applications', *Springer*, pp. 427, 1993.

[88] H.J. Chen, Z.H. Zhang, D. Xie, R. Cai, X. Chen, Y.N. Liu, S.Z. Yao, 'Surface-imprinting sensor based on carbon nanotubes/graphene composite for determination of bovine serum albumin', *Electroanalysis*, vol. 24, no. 11, pp. 2109–2116, 2012.

[89] M.F. Frasco, L.A.A.N.A. Truta, M.G.F. Sales, F.T.C. Moreira, 'Imprinting Technology in Electrochemical Biomimetic Sensors', *Sensors*, vol. 17, no. 3, pp.523, 2017.

[90] X. Shen, L. Zhu, N. Wang, L. Ye, H. Tang, 'Molecular imprinting for removing highly toxic organic pollutants', *Chem. Commun.*, vol. 48, no. 6, pp. 788–798, 2012.

[91] C.G. Zoski, 'Handbook of Electrochemistry', 2007.

[92] D.A.C. Brownson, C.E. Banks, 'The Handbook of Graphene Electrochemistry', 2014.

[93] U.P. Morales, E.V. Lopez, C.O. Otalora, 'Basic Aspects in the Interpretation of the Diagrams of Electochemical Impedance', *Dyna*, pp. 13–19, 2010.

[94] M. Billah, H.C.W. Hays, P.A. Millner, 'Development of a myoglobin impedimetric immunosensor based on mixed self-assembled monolayer onto gold', *Microchim. Acta*, vol. 160, no. 4, pp. 447–454, 2008.

[95] A. Yella, H.W. Lee, H.N. Tsao, C. Yi, A.K. Chandiran, M.K. Nazeeruddin, E.W.G. Diau, C.Y. Yeh, S.M. Zakeeruddin, M. Gratzel, 'Porphyrin-Sensitized Solar Cells with Cobalt (II/III)-Based Redox Electrolyte Exceed 12 Percent Efficiency', *Science*, vol. 334, no. 6056, pp. 629–634, 2011.

[96] C.C. Chou, K.Y. Tsao, C.C. Wu, H. Yang, C.M. Chen, 'Improved power conversion efficiency for dye-sensitized solar cells using a subwavelength-structured antireflective coating', *Appl. Surf. Sci.*, vol. 328, pp. 198–204, 2015.

[97] B. O'Regan, M. Grätzel, 'A low cost, high-efficiency solar cell based on dye-sensitized colloidal TiO_2 films', *Nature*, vol. 353, no. 6346, pp. 737–740, 1991.

[98] H.K. Jun, M.A. Careem, A.K. Arof, 'Plasmonic Effects of Quantum Size Gold Nanoparticles on Dye-sensitized Solar Cell', *Mater. Today Proc.*, vol. 3, pp. S73–S79, 2016.

[99] T. Asano, T. Kubo, Y. Nishikitani, 'Electrochemical properties of dye-sensitized solar cells fabricated with PVDF-type polymeric solid electrolytes', *J. Photochem. Photobiol. A Chem.*, vol. 164, no. 1–3, pp. 111–115, 2004.

[100] N. Chander, A.F. Khan, E. Thouti, S.K. Sardana, P.S. Chandrasekhar, V. Dutta, V.K. Komarala, 'Size and concentration effects of gold nanoparticles on optical and electrical properties of plasmonic dye sensitized solar cells', *Sol. Energy*, vol. 109, pp. 11–23, 2014.

[101] D.W. Zhang, M. Wang, G. Brolo, J. Shen, X.D. Li, S.M. Huang, 'Enhanced performance of dye-sensitized solar cells using gold nanoparticles modified fluorine tin oxide electrodes', *J. Phys. D-Applied Phys.*, vol. 46, pp. 8, 2013.

[102] D. Kozanoglu, D.H. Apaydin, A. Cirpan, E.N. Esenturk, 'Power conversion efficiency enhancement of organic solar cells by addition of gold nanostars, nanorods, and nanospheres', *Org. Electron. physics, Mater. Appl.*, vol. 14, no. 7, pp. 1720–1727, 2013.

[103] J.R. Durrant S.A. Haque, *Solar Cells*, vol. 2, 2003.

[104] M.A.K.L. Dissanayake, J.M.K.W. Kumari, G.K.R. Senadeera, C.A. Thotawatthage, 'Efficiency enhancement in plasmonic dye-sensitized solar cells with TiO_2 photoanodes incorporating gold and silver nanoparticles', *J. Appl. Electrochem.*, vol. 46, no. 1, pp. 47–58, 2016.

[105] V.D. Dao H.S. Choi, 'Highly-Efficient Plasmon-Enhanced Dye-Sensitized Solar Cells Created by Means of Dry Plasma Reduction', *Nanomaterials*, vol. 6, no. 4, pp. 70, 2016.

[106] J.T. Park, W.S. Chi, H. Jeon, J.H. Kim, 'Improved electron transfer and plasmonic effect in dye-sensitized solar cells with bi-functional Nb-doped TiO_2/Ag ternary nanostructures', *Nanoscale*, vol. 6, no. 5, pp. 2718–29, 2014.

[107] A. Brolo, 'Plasmonics for future biosensors', *Nat. Photonics*, vol. 6, pp. 709–713, 2012.

[108] Y.H. Jang, Y.J. Jang, S.T. Kochuveedu, M. Byun, Z. Lin, D. H. Kim, 'Plasmonic dye-sensitized solar cells incorporated with Au-TiO_2 nanostructures with tailored configurations', *Nanoscale*, vol. 6, no. 3, pp. 1823–32, 2014.

[109] S. Jongjinakool, K. Palasak, N. Bousod, S. Teepoo, 'Gold nanoparticles-based colorimetric sensor for cysteine detection', *Energy Procedia*, vol. 56, pp. 10–18, 2014.

[110] H. Ninsonti, W. Chomkitichai, A. Baba, N. Wetchakun, W. Kangwansupamonkon, S. Phanichphant, K. Shinbo, K. Kato, F. Kaneko, 'Au-Loaded Titanium Dioxide Nanoparticles Synthesized by Modified Sol-Gel/Impregnation Methods and Their Application to Dye-Sensitized Solar Cells', *Int. J. Photoenergy*, vol. 2014, pp. 1–8, 2014.

[111] S.O. Pereira, 'Chapter 11: Inorganic nanoparticles in new upcoming biomedical application' in book: Controlled Release Systems: Advances in Nanobottles and Active Nanoparticles, Pan Stanford, 2015.

[112] S.O. Pereira, A. Barros-Timmons, T. Trindade, 'Biofunctionalisation of colloidal gold nanoparticles via polyelectrolytes assemblies', *Colloid Polym. Sci.*, vol. 292, no. 1, pp. 33–50, 2014.

[113] X. Wang, C.E. Egan, M. Zhou, K. Prince, D.R.G. Mitchell, R.A. Caruso, 'Effective gel for gold nanoparticle formation, support and metal oxide templating', *Chem. Commun.*, vol. 104, no. 29, pp. 3060-3062, 2007.

[114] A. Kudo, T. Fujita, X.Y. Lang, L.Y. Chen, M.W. Chen, 'Enhanced Electrochemical Performances of Nanoporous Gold by Surface Modification of Titanium Dioxide Nanoparticles', *Mater. Trans.*, vol. 51, no. 9, pp. 1566–1569, 2010.

[115] V. Guieu, C. Ravelet, S. Perrier, Z. Zhu, S. Cayez, E. Peyrin, 'Aptamer enzymatic cleavage protection assay for the gold nanoparticle-based colorimetric sensing of small molecules', *Anal. Chim. Acta*, vol. 706, no. 2, pp. 349–353, 2011.

[116] D. Derkacs, S.H. Lim, P. Matheu, W. Mar, E.T. Yu, 'Improved performance of amorphous silicon solar cells via scattering from surface plasmon polaritons in nearby metallic nanoparticles', *Appl. Phys. Lett.*, vol. 89, no. 9, pp. 1–4, 2006.

[117] M.D. Brown, T. Suteewong, R.S.S. Kumar, V. D'Innocenzo, A. Petrozza, M.M. Lee, U. Wiesner, H.J. Snaith, 'Plasmonic dye-sensitized solar cells using core-shell metal-insulator nanoparticles', *Nano Lett.*, vol. 11, no. 2, pp. 438–445, 2011.

[118] H. Choi, W.T. Chen, P.V Kamat, 'Know Thy Nano Neighbor. Plasmonic versus Electron Charging Effects of Metal Nanoparticles in Dye-Sensitized Solar Cells', *ACS Nano*, 2012.

[119] S. Muduli, O. Game, V. Dhas, K. Vijayamohanan, K.A. Bogle, N. Valanoor, S.B. Ogale, 'TiO_2-Au plasmonic nanocomposite for enhanced dye-sensitized solar cell (DSSC) performance', *Sol. Energy*, vol. 86, no. 5, pp. 1428–1434, 2012.

CHAPTER 3

Graphene-based biomimetic materials for Carnitine detection as potential cancer biomarker

This chapter is based on the work titled *Graphene-based biomimetic materials targeting urine metabolite as potential cancer biomarker: application over different conductive materilas for potentiometric transduction* published in the journal Electrochimica Acta, 150:99-107, 2014. Herein, a Smart Polymer Antibody Material (SPAM) nanostructure assembled on a graphene oxide support for the detection of carnitine metabolite in urine is described.

3.1. Introduction

Ovarian cancer is also called the “silent killer” because it is hardly detected and the deadliest of all gynecologic cancers. Early detection may be achieved by early screening of specific biomarker compounds bearing a predictive value. Because ovarian tissues can be transformed into several quaternary amines [1], the presence of carnitine (CRT) in urine may be correlated to ovarian cancer [1,2]. CRT is a quaternary amine, with a fundamental role in the mitochondrial β-oxidation of long-chain fatty acids by enabling their transport into the mitochondrial matrix [3]. It also acts as an antioxidant, contributing to maintain the normal function of the cells and protect cells from oxidative stress conditions related to cardiovascular diseases, heart and renal failure [4] and diabetes [5]. Furthermore, CRT is an inhibitor of cisplatin-induced injury of the kidney and small intestine and, hence, it may have therapeutic potential in cancer [6].

Numerous analytical methods have been described in the literature to determine CRT in different biological samples such as chromatography [7,8,9,10,11], radiometry assays [9], electrophoresis [12,13,14], fluorimetry and spectrophotometry [15,16], electrochemical assays with potentiometric [17,18,19], and amperometric [20] or QCM transduction [21]. Overall, these methods are effective but unsuitable for point-of-care applications, where response time, portability and cost are critical. In clinical context, immunoassays are today dominant for ensuring highly selective readings of the target biomolecule. This high selectivity accounts the use of antibodies as bioreceptor material, but this is also coupled to slow and expensive procedures [22]. An alternative to conventional immunoassays, such as ELISA, could be the development of a biomimetic material, acting as plastic antibody, and its use in the construction of a biosensor device.

The production of plastic antibodies makes use of molecular imprinting technology, where a biomolecule is imprinted within a polymeric network. In general, the resulting biomimetic nanostructures display good sensitivity/selectivity for the target compound, while ensuring high mechanical strength, robustness, low cost, reusability, and low response time. Surface imprinting is the technique of choice for avoiding hindered diffusion of the imprinted template from the polymeric matrix [23,24]. The inclusion of charged binding sites to create Smart Polymer Antibody Material (SPAM) surfaces is a recent and successful approach, where the binding positions are complementary to the template both in shape and in charge [25]. Since these sites are designed in a neutral network environment, the affinity/selectivity of the template for its binding/charged site becomes enhanced.

Graphene is a single-layer sheet of sp^2 hybridized carbon atoms arranged in a two-dimensional nanostructure [32], bearing outstanding electrical properties, as well as thermal stability and mechanical strength [32,33]. The easy functionalization of graphene is also a key facture for its compatibility in bio/nano interfaces, justifying its intensive and emerging use [33].

Moreover, the association of plastic antibodies to ion-selective electrodes (ISEs) has been proven an advantageous approach in electrical transduction, not only for the detection of small biomolecules [34], but also for high dimension bio-structures such as protein biomarkers [30]. ISEs are portable and low-cost devices for field applications, providing selective, precise, rapid and sensitive responses over a broad range of concentration of ionic analytes [35]. The use of conductive solid support has shown a successful approach for preparing ISE, enabling an easy handling of the electrode by eliminating its conventional internal solution. In this context, it would be interesting to understand the changes arising by replacing the regular graphite-base conductive support by conductive glass/plastic. These are today low-cost materials, readily available in the market, and could allow replacing the conventional "pen" configuration of ISEs by flat transparent surfaces were half area is electrically active.

Thus, this work describes for the first time a SPAM nanostructure assembled on graphene oxide for the detection of CRT metabolite in urine. This material was created by growing a neutral cross-linked polymer by radical polymerization of vinyl pivalate (VPi) cross-linked with ethylene glycol dimethacrylate (EGDMA). The charged positions were signed with (vinylbenzyl)trimethylammonium (VBTMA) chloride and 4-styrenesulfonic acid (SSA) sodium salt. The obtained materials were included in plasticized PVC selective membranes to act as ionophore in potentiometric transduction, using different conductive solid supports.

Several membrane compositions were produced to ensure that the device would display suitable analytical features. The overall analytical performance was evaluated, and the membrane composition optimized, leading ultimately to a successful application of the device to the analysis of CRT in biological samples.

3.2. Experimental

3.2.1. Equipment and Materials

All electromotive force (emf) measurements were made at room temperature and under constant stirring in a Crison pH-meter, GLP21, decimilivoltammeter (±0.1mV sensitivity) connected to a reference electrode, also from Crison, 5240, or to double-junction combined glass electrode Consort. A Sonorex digitec sonicater from Bandelin, and/or a vortex from Citomed (C 1301B-230V) were used to promote the dissolution of the solids and homogenization of the solutions/suspensions.

Solid materials were characterized by Fourier Transform Infrared Spectrometry (FTIR), using a Nicolet iS10 FTIR spectrometer, from Thermo Scientific, equipped with an Attenuated Total Reflectance (ATR) sampling accessory of diamond contact crystal, also from Nicolet. The same solids were also analyzed by Raman Spectroscopy, using the Confocal Raman Microscope a300M+ from WITec GmbH, equipped with an objective 50× Zeiss NA=0.70 and operating in single spectrum mode, at 532 nm laser.

Indium tin oxide (ITO) coated PET (polyethylene terephthalate), surface resistivity 60 Ω/sq, and Fluorine doped (FTO) tin oxide coated glass slide, surface resistivity ~7 Ω/sq, were purchased from Sigma-Aldrich, cut in pieces (~1×1cm) for electrical wiring and selective membrane deposition.

3.2.2. Reagents and solutions

All chemicals were of analytical grade and deionised water (conductivity <0.1 $\mu S.cm^{-1}$) was employed. CRT hydrochloride, 4-(2-Hydroxyethyl)-1-piperazineethanesulfonic acid (HEPES), bovine serum albumin (BSA), Graphite powder, Piperazine-N,N′-bis(2-ethanesulfonic acid) (PIPES) and VPi were obtained from Sigma-Aldrich; Creatinine (Crea), N-(3-dimethylaminopropyl)-N'-ethylcarbodiimide hydrochloride (EDAC), N-Hydroxysuccinimide (NHS), *o*-Nitrophenyloctyl ether (*o*NPOE), Poly(vinylchloride) (PVC) of high molecular weight and Potassium tetrakis(4-chlorophenyl) borate (TpClPB) from Fluka; Tetrahydrofuran (THF), Ascorbic acid and Sodium phosphate dibasic dihydrate ($Na_2HPO_4.2H_2O$) from Riedel-de-Häen; Hydrochloric acid and tris(hydroxymethyl) aminomethane (TRIS), Potassium di-hydrogenphosphaste (KH_2PO_4) and Sodium chloride (NaCl) were from Panreac, *p*-Tetraoctilammonium bromide (*p*TOAB) and VBTMA chloride 97% to Acrös Organics; 4-Morpholinepropanesulfonic acid, Sodium salt (MOPS) to AppliChem.

Ammonium persulfate (APS) was obtained from JVP; SSA sodium salt and 2-(N-morpholino) ethanesulfonic acid (MES) from Alfa Aesar; Glacial Acetic acid from Carlo Erba; Dextrose anhidrous (Glucose) from Fisher BioReagents. EGDMA and sodium dodecyl sulfate (electrophoresis) (SDS) were obtained from TCI; Potassium nitrate (KNO_3) from Pronalab; Hydrogen peroxide and potassium chloride (KCl) from Merck; Sulphuric acid (H_2SO_4) from Scharlau; Potassium permanganate ($KMnO_4$) from BDH; and Urea was produced from Fagron.

The phosphate buffered saline (PBS) solution, with pH adjusted to 7.4, was prepared by the dissolution of 6.8×10^{-2} mol/L NaCl, 1.4×10^{-3} mol/L KCl, 3.3×10^{-3} mol/L $Na_2HPO_4.2H_2O$ and 8.8×10^{-4} mol/L KH_2PO_4 in deionised water.

3.2.3. Synthesis of SPAM material for CRT

3.2.3.1. Graphene oxide production

The first stage of the SPAM synthesis consisted in the preparation of graphene oxide (GO) by direct exfoliation of graphite powder (**Figure 3.1**). This was made by the modified Hummers method, in which 2.0 g of natural graphite powder, 2.0 g of KNO_3 and 6.0 g of $KMnO_4$ were added slowly to 40 mL of concentrated H_2SO_4, immersed in an ice bath at 0 °C, under vigorous stirring. The obtained mixture was kept under stirring for 1 h, below 35 °C. After that, 160 mL of deionised water was added drop wise to dilute the solution and the temperature increased to ~95 °C and kept at this temperature for 15 min. The resulting mixture was poured into 240 mL of ultrapure water and then, 16 mL of 30% H_2O_2 was added to this solution, giving rise to a yellow-brown suspension, with colloidal GO material and flocculating graphite oxidized particles.

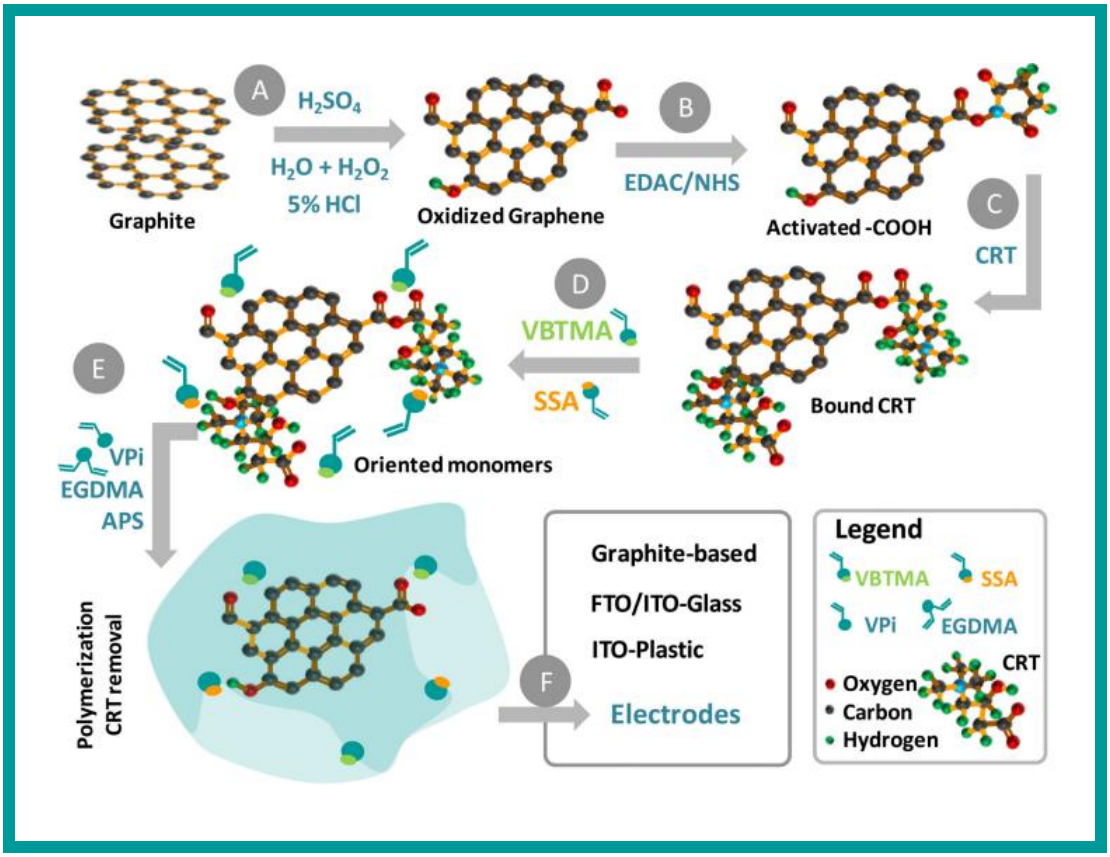

Figure 3.1. Design of synthesis of CRT selective sensor. A: Preparation of GO by graphite exfoliation; B: Activation of carboxylic acid functions; C: Physical/Chemical interaction with CRT; D: Charged monomer interaction with CRT; E: Polymerization around CRT with neutral material; F: application of the material in different conductive supports to prepared different CRT-selective electrodes.

3.2.3.2. Graphene oxide activation

The previous suspension (1 mg/mL) was centrifuged at 5000 rpm for 5 min to remove the unexfoliated graphite oxide particles. After this, GO was activated by adding of 1.0 mL NHS aqueous solution 50 mg/mL and 0.3 mL of fresh EDAC aqueous solution 10 mg/mL. This mixture was left stirring, continuously, at room temperature, for 30 min. After this, the activated GO particles flocculated and were separated by centrifugation, thoroughly washed with water and dried under a nitrogen atmosphere (brown powder).

3.2.3.3. CRT imprinting

The imprinted layer was produced by incubating 1.4 mg of activated GO particles in 0.050 mL CRT solution 8.0×10^{-4} mol/L prepared in 5.0×10^{-4} mol/L HEPES buffer, for 3 h. The solid fraction was isolated by centrifugation, washed with buffer solution, and incubated next in 0.050 mL TRIS solution 1.0 mol/L, also prepared in HEPES buffer, for about 30 min. The solid was again isolated by centrifugation, washed with buffer, and incubated next in charged functional monomers, 0.025 mL of VBTMA (1.6×10^{-3} mol/L) and 0.025 mL of SSA (1.6×10^{-3} mol/L), for 2.5 h. Once again, the solid was separated, washed and incubated, at room temperature, for 2.5 h, in 0.050 mL of a solution containing 8.0×10^{-3} mol/L EGDMA, 1.6×10^{-3} mol/L Vpi and 4.0×10^{-3} mol/L APS, prepared in buffer. The imprinted solid material was then washed with buffer and finally incubated in a solution of glacial acetic acid and SDS (1:1), at room temperature, for 12 h. The solid was finally thoroughly washed with buffer solution and dried under a nitrogen atmosphere.

Non-imprinted material (NIMs) was also prepared as control, following an equivalent procedure, where the CRT solution prepared in HEPES buffer was replaced by only buffer.

3.2.4. FTIR and Raman analysis

The FTIR analysis was conducted by placing the solid material on the ATR diamond surface. The spectra were collected under room temperature/humidity control, after background correction. The number of scans for sample and background was set to 32. The x-axis ranged from 525 to 4000 cm^{-1} and y-axis shown as % transmittance. The resolution was 4000.

The Raman spectra were measured with an objective 50× Zeiss (NA = 0.70) that in combination with this microscope lead to a laser spot at the sample of 500 nm. The laser power applied at the sample ranged between 0.5 mW and 3 mW. The confocal microscope operated in single spectrum mode, at wavelength of 532 nm, and the spectra were recorded as an extended scan.

3.2.5. Preparation of the electrodes

CRT selective membranes were obtained by preparing a cocktail solution of PVC with *o*NPOE (plasticizer, 1:3, w/w), together with 0.15 mg of ionophore (SPAM or NIM). Some membranes were also added of anionic or cationic additives (0.5 mg of TpClPB or pTOAB, respectively), according to the membrane composition indicated in **Table 3.1**.

The resulting mixture was mixed and dispersed in 2.0 mL of THF and casted over the conductive supports.

Table 3.1. Membrane composition of all CRT selective-membranes, prepared by including ionophore and lipophilic additive in PVC membranes plasticized with *o*NPOE.

No.	*"Active" Components*		*Membrane composition (mg)*			
	Ionophore	*Additive*	*Ionophore*	*Plasticizer*	*Additive*	*PVC*
I	SPAM	—	0.13	5.60	—	2.21
II	NIM	—	0.15	18.19	—	2.27
III	SPAM	TpClPB	0.12	6.39	0.52	2.39
IV	—	TpClPB	—	9.46	0.53	2.36
V	SPAM	*p*TOAB	0.15	7.13	0.49	2.34
VI	—	*p*TOAB	—	9.28	0.50	2.36
VII	NIM	*p*TOAB	0.15	2.20	0.08	3.50

All selective membranes were applied drop wise over graphite conductive supports. The graphite support was prepared by filling the smaller end of a plastic syringe with a mixture of graphite and Araldite/hardener, and introducing a copper wire though this graphite-paste at the inner side of the syringe body. A small cavity was drilled externally on the hardened graphite to create a 1mm-deep cavity for applying the membrane.

Some of the selective membranes were casted similarly over ITO or FTO/ITO conductive flat supports. These supports were used as commercially available, cut into small pieces, washed with ethanol and dried. An electrical wire was linked to it by holding a copper wire against the conductive surface by means of insulating glue.

The applied membranes were let dry at room temperature, for 24 h, and conditioned in a 1.0×10^{-3} mol/L CRT solution prior to emf readings.

3.2.6. Potentiometric assays

The electrodes were calibrated in HEPES buffer solution, 1.0×10^{-4} mol/L, by adding sample aliquots a standard 1.0×10^{-2} mol/L CRT solution, leading to CRT concentrations ranging from 1.0×10^{-6} to 1.7×10^{-3} mol/L. The emf was recorded after at stabilization to ±0.2 mV and plotted as a function of logarithm CRT concentration.

Selectivity studies followed the Matched Potential Method, where CRT concentrations were set to 1.0×10^{-5} mol/L and increased up to 4.5×10^{-5} mol/L. The potential change depended of the electrode, with the most sensitive ones leading to a ~25 mV decrease in *emf*. The interfering solutions tested were ascorbic acid (4.0 g/L), BSA (15 g/L), creatinine (30 g/L), glucose (1.5 g/L) and urea (2 g/L), adding in small aliquots into a primary ion solution of CRT of 1.0×10^{-5} mol/L and producing concentrations changes up to their physiological level (BSA (3.9-5.0 mg/L), creatinine (30 g/L), glucose (10-100 mg/L) and urea (<50 mg/L).

The analysis of CRT in urine samples was made in artificial urine solution spiked with CRT standard, diluted 1:10 diluted in HEPES buffer and analyzed by direct emf reading. The CRT concentrations so-obtained ranged from 2.0×10^{-6} to 2.8×10^{-3} mol/L.

3.3. Results and discussion

3.3.1. Design of SPAM material for CRT

The SPAM material was assembled on GO sheets obtained by graphite exfoliation (**Figure 3.1**). The analytical approach taken herein employed typical procedures described in the literature [36,37], yielding a yellow-brown colloidal suspension. This suspension was composed of oxidized graphene sheets as colloidal material and was destabilized after the chemical activation of the carboxylic acid laying on the GO surface. This was done by well-known EDAC/NHS chemistry, yielding a labile *O*-acylisourea intermediate that was made evident by an immediate flocculation of the activated GO sheets. This flocculation further allowed a physical separation of the graphene-based material from the solution, by centrifugation and filtration.

The imprinting stage started by the physical interaction between CRT and activated GO material. Simple electrostatic interaction was allowed by complementary electrical environment between the positive charge of the quaternary ammonium salt in CRT and the negative polarity of oxygen atoms in the GO layer (**Figure 3.1**).

Considering that CRT had a carboxylic function, anhydride bonding between CRT and the *O*-acylisourea intermediate become also possible (**Figure 3.1**). Since anhydride functions are quite unstable, this reaction allowed positioning the CRT over the receptor surface while allowing its easy removal after completing the imprinting stage. The inactivation of carboxylic acid functions that remained active was done by addition of TRIS, yielding amide bonds.

The GO/CRT material was incubated after in VBTMA (a positively charged monomer) and SSA (a negatively charged monomer). This incubation period had the purpose of establishing ionic pairs between opposite charges: $-COO^-$//VBTMA and $-NR_3^+$//SSA (**Figure 3.1**). The vinyl group in the monomer structure would allow their participation in the subsequent polymerization stage and, consequently, position the charged group at the imprinted binding site. The polymerization was initiated by radical species (APS) and conducted with neutral vinyl-based materials. VPi and EGDMA were selected for this purpose (**Figure 3.1**). These compounds had only ester functions and acted as monomer and cross-linker, respectively.

Finally, CRT biomolecules in the polymeric matrix had to be removed in order to generate the binding sites and the so-called plastic antibody material. This was made by treatment the imprinted material with SDS and acetic acid. The final material was named SPAM and should display rebinding positions for CRT. In order to identify if this rebinding was being made by the specifically designed binding sites and/or non-specific interactions with the polymeric network, a control material was prepared with no CRT (named NIM), where only non-specific interactions were allowed.

3.3.2. Surface analysis of the host-tailored polymers

The chemical assembly of the imprinted layer on GO was followed by Raman spectroscopy and FTIR. The corresponding spectra were indicated in **Figure 3.2A** and **Figure 3.2B**, respectively.
The Raman spectra of GO showed the typical G and D bands (**Figure 3.2A**), highlighting the hybridization of the carbon atoms as well as the electronic and geometrical carbon arrangement [38]. The G band is located at ~1580 cm^{-1} and corresponds to the stretching of the C–C bond in graphitic materials, common to all sp^2 carbon systems, while the D band appears at ~1370 cm^{-1}, assigning the presence of disorder in the sp^2-hybridized carbon system [38,39,40]. It is possible that the analyzed material also includes contaminant graphitic material from which GO was extracted.

The introduction of an additional polymeric imprinted layer at GO, when the SPAM material was assembled, was expected to introduce additional disorder into the sp^2 carbon system. This may be identified by analyzing the I_D/I_G intensity ratio between the disorder-induced D-band and the Raman allowed G band [38]. The direct comparison between GO and SPAM Raman spectra confirmed the presence of additional disorder, with I_D/I_G intensity ratios changing from 0.93 to 1.04.

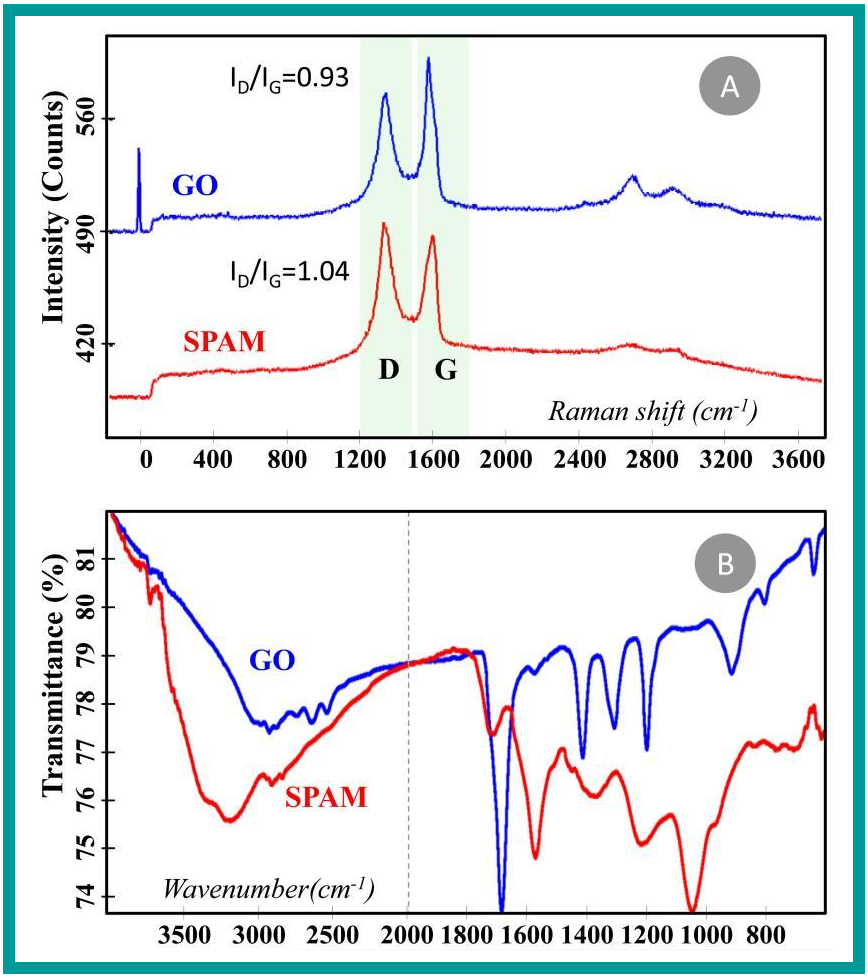

Figure 3.2. Spectra of GO, SPAM and NIM materials. (A) Raman spectra, with bands G, D and 2D identified. (B) FTIR spectra.

The FTIR spectra also confirmed significant chemical differences between GO and SPAM (**Figure 3.2B**). Regarding GO material, the oxidation of graphene leads to the occurrence of ether, hydroxyl, and carbonyl bonding on the aromatic carbon rings. The C=O stretching vibration is typically intense and was observed at 1689 cm^{-1}, a position accounting the presence of the aromatic rings from graphene. The typical C–O stretching vibration in carboxylic acid and ether functions range from 1300–1000 cm^{-1} [41] for which the medium intensity peak at 1200 cm^{-1} may be assigned to this event. The O–H stretching was evidenced by the broad adsorption below 2500 cm^{-1} and there was also evidence for a C=C stretching vibration in a small intensity peak at 1579 cm^{-1}. The addition of an imprinted material to GO introduced mostly saturated ester functions on the matrix, leading to significant changes in the FTIR spectra. In the SPAM material, the C=O stretching vibration was located at 1718 cm^{-1}, shifting the higher *x* values.

The band due to the C–O–C asymmetric stretching vibration occurred at 1219 $cm^{-1}$and that due to the symmetric stretching vibration was evident at 1050 cm^{-1}, as expected for aliphatic esters [41].

3.3.3. Effect of significant variables on the response of CRT selective electrodes

CRT selective electrodes were prepared with either SPAM (ISE I) or NIM (ISE II) materials acting as ionophore. These materials were dispersed in PVC dissolved in THF and plasticized by the addition of *o*NPOE, a high dielectric constant plasticizer solvent. Other membranes were prepared similarly, including a lipophilic ionic additive. Either positive (ISE III) or negatively (ISE V) charged additive was employed, considering that CRT has a constant positive charge at the nitrogen atom but may also bear a negative charge by acid/base ionization of the carboxylic acid function. Control membranes having these additives and no ionophore (ISE IV and VI) were also prepared to investigate the effect of the additive alone and identify the effect of the ionophore.

All these membranes were casted on electrode supports with graphite-based conductive material and the corresponding analytical features evaluated according to IUPAC recommendations (average results in **Table 3.2**). The best membrane compositions were used to prepare similar devices employing alternative conductive supports.

Table 3.2. Membrane composition of CRT sensors and the potentiometric features in 1.0×10^{-4} mol/L HEPES buffer, pH 5.2, with graphite-based electrodes.

Conductive support	Membrane system				Analytical features							
	No.	Ionophore	Plasticizer	Additive	Slope (mV/decade)	r^2(n=3)	σ		LOD		LLLR	
							mV	mol/L	mol/L	mg/L	mol/L	mg/L
Graphite	*I*	SPAM	*o*NPOE	—	−47.2±5.9	0.9975	± 1.0	8.9×10^{-4}	4.1×10^{-5}	6.61	7.6×10^{-5}	12.25
	II	NIM	*o*NPOE	—	−44.6±4.7	0.9954	± 0.6	8.9×10^{-4}	5.0×10^{-5}	8.06	9.6×10^{-5}	15.48
	III	SPAM	*o*NPOE	TpClPB	+47.3±11.1	0.9968	± 0.6	1.6×10^{-4}	3.6×10^{-6}	0.58	4.4×10^{-6}	0.71
	IV	—	*o*NPOE	TpClPB	—	—	—	—	—	—	—	—
	V	SPAM	*o*NPOE	*p*TOAB	−45.1±2.7	0.9923	± 0.1	2.7×10^{-4}	3.9×10^{-5}	6.29	5.6×10^{-5}	9.03
	VI	—	*o*NPOE	*p*TOAB	−46.2±6.3	0.9950	± 0.3	4.6×10^{-4}	3.6×10^{-5}	5.80	5.6×10^{-5}	9.03
FTO/ITO-Glass	*I*	SPAM	*o*NPOE	—	−22.6±19.2	0.9958	± 2.2	1.7×10^{-3}	8.9×10^{-5}	14.35	9.5×10^{-5}	15.31
	II	NIM	*o*NPOE	—	−42.4±8.7	0.9958	± 0.1	2.8×10^{-4}	5.0×10^{-5}	8.06	5.6×10^{-5}	9.03
	V	SPAM	*o*NPOE	*p*TOAB	−57.4±3.7	0.9994	± 0.6	9.0×10^{-4}	6.3×10^{-5}	10.16	9.5×10^{-5}	15.31
	VII	NIM	*o*NPOE	*p*TOAB	−32.1±10.8	0.9917	± 2.6	9.5×10^{-5}	6.8×10^{-5}	10.96	1.7×10^{-4}	27.40
ITO/PET	*I*	SPAM	*o*NPOE	—	+37.61±1.78	0.9944	± 0.2	5.6×10^{-5}	2.3×10^{-6}	0.37	4.4×10^{-6}	0.71
	II	NIM	*o*NPOE	—	+20.24±2.44	0.9981	± 0.6	4.4×10^{-6}	1.3×10^{-6}	0.21	2.4×10^{-6}	0.39
	V	SPAM	*o*NPOE	*p*TOAB	+41.50±10.2	0.9964	± 4.7	1.4×10^{-5}	1.8×10^{-6}	0.29	2.4×10^{-6}	0.39
	VII	NIM	*o*NPOE	*p*TOAB	+34.53±18.4	0.9921	± 2.0	4.4×10^{-6}	2.8×10^{-5}	4.51	4.4×10^{-6}	0.71

3.3.3.1. Effect of membrane composition

The typical potentiometric response of the ISEs prepared on graphite-based conductive supports may be seen in **Figure 3.3A**. The results indicated that SPAM ionophore improved the overall analytical performance of the device compared to NIM, decreasing the concentration level to which the electrode became responsive. This was evident by direct comparison of ISEs I and II, displaying linear responses down to 76 or 96 µmol/L CRT, with average anionic slopes of -47 and -45 mV/decade and LODs of 41 and 50 µmol/L, respectively.

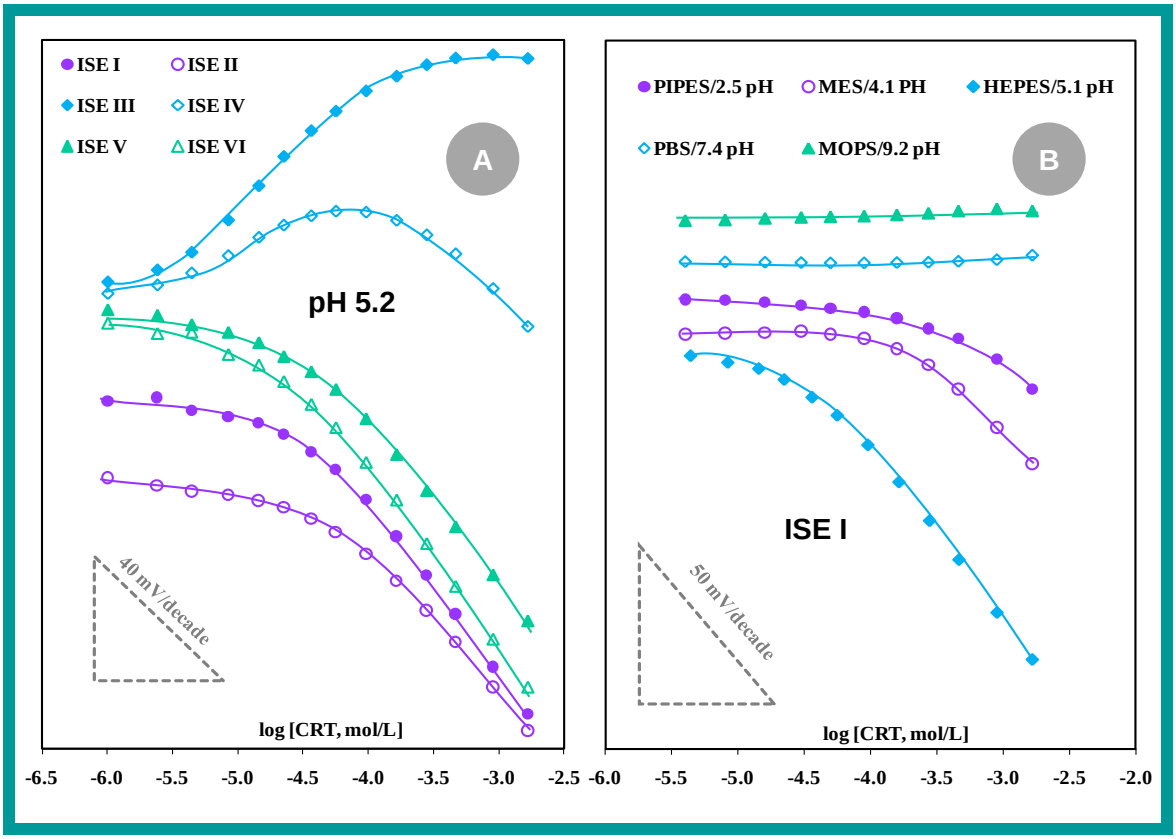

Figure 3.3. Calibration of CRT selective electrodes with graphite-based conductive material. (A) Different membrane compositions evaluated in HEPES buffer pH 5.1. (B) Different buffer/pH conditions using ISE I.

The addition of a lipophilic anionic additive gave rise to a potentiometric response with a positive slope (ISE III), meaning that the response of the electrode was now dominated by positive charges. The SPAM material was the one acting as ionophore in this condition (and not the additive), because the additive alone (ISE IV) was unable to produce a consistent behavior (**Figure 3.3A**).

The analytical response of ISE III also showed an unusual behavior by reaching early potential saturation, at ~1×10^{-4} mol/L. This response was considered a drawback at the future application of the device to the analysis of real samples. Contrasting to this behavior, the presence of the cationic lipophilic additive *p*TOBA improved the analytical performance of the electrodes, by decreasing the CRT concentration to which the electrode responded (ISE V). This effect was similar to that produced by the electrode having only additive (ISE VI), and therefore it was impossible to understand if this behavior resulted from the additive alone or the combination additive/SPAM ionophore.

Overall, the use of membranes composed by SPAM material favored the analytical response of the CRT selective electrodes and it was not clear if the presence of a lipophilic cationic additive would improve the performance of the devices.

3.3.3.2. Effect of pH

The pH of the analyzed solution may influence the potentiometric response. This is an outcome of the changes in the ionization degree of the carboxylate group of CRT under different pH conditions and the kind of ionic species present in the electrolyte acting as buffer. Considering this combined effect, this study was conducted for buffers of different compositions, prepared at a specific concentration and without adding external species (thereby ensuring a higher buffer capacity under practical conditions). The buffers selected for this study were PIPES, MES, HEPES, PBS and MOPS, corresponding to 2.5, 4.1, 5.1, 7.4 and 9.2 pH values when set to a 5.0×10^{-3} mol/L concentration.

Electrodes including membranes with SPAM (I and V) or NIM (II or VII), and with additive (V and VI) or without additive it (I and II) were tested for the different pH/buffer conditions. As an example, the calibrations obtained with electrodes ISE I are presented in **Figure 3.3B**. Overall, more acidic pH conditions hindered the electrode performance, which was most probably correlated to the decreased ionization of the carboxylic acid function. Neutral or alkaline pH gave rise to steady potentials. This behavior could be attributed to the prevailing double ionization of CRT (zwitterionic form), resulting in the interaction of the membrane with a zero net charge species and consequently to no potential variation. The best pH condition was indeed the buffer used to test the membrane composition (HEPES, 5.1).

3.3.3.3. Effect of conductive support

The effect of the conductive support on the potentiometric response was tested by casting the selective membranes on conductive materials placed on plastic (PET) or glass supports. The conductive layers consisted of flat ITO or FTO/ITO surfaces, used as commercially available. Selective membranes including SPAM (I and V) or NIM (II or VII) ionophore, with additive (V and VI) or no additive (I and II) were selected for this purpose. The typical calibration curves obtained are depicted in **Figure 3.4** and the corresponding features in **Table 3.2**.

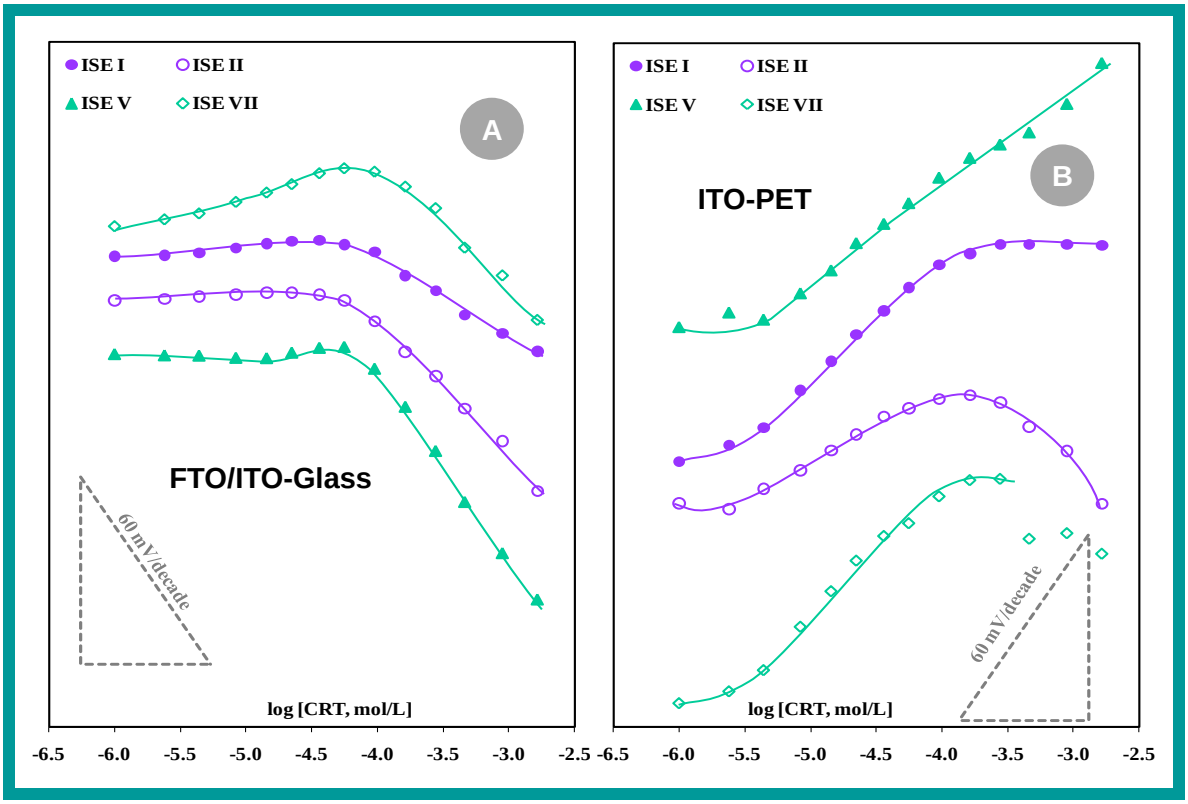

Figure 3.4. Calibration of CRT selective electrodes with different selective membranes casted on conductive glass (A) or PET (B), and tested in HEPES buffer pH 5.1.

In general, significant changes were observed in the performance of the electrodes by changing the conductive support, with electrodes composed of SPAM material and cationic lipophilic additive (ISE V) showing significant improvements in sensitivity. These electrodes were the only ones showing an expanded linear concentration range and an increased sensitivity, both in conductive glass (**Figure 3.4A**) and plastic supports (**Figure 3.4B**). Interestingly (and strangely at the same time) membranes assembled on the conductive PET shifted the emf changes from negative to positive slopes.

An upper limit of linear range was also identified, with limiting concentrations of 9.5×10^{-5}, 1.6×10^{-4} and 2.8×10^{-4} mol/L, for ISEs I, II and VII, respectively.

A disadvantageous feature associated to these new conductive supports was the decrease in stability of the emf readings and the worsened precision between consecutive calibrations (**Table 3.2**). These features could be attributed to the simple fact that the membrane on this new flat conductive surface was thinner, which could accelerate emf drifts driven by the direct interaction of the hydration water molecules with the conductive material. The lifetime of the electrodes was smaller than those employing graphite-based supports.

3.3.4. Selectivity of the electrodes

Selectivity assays used the Matched Potential Method and tested the effect of species that may co-exist with CRT in urine (ascorbic acid, BSA, Crea, glucose and urea, among other electrolytes), assessed up to their normal physiological concentration. For this purpose, several aliquots of standard solutions containing individual species were added to a solution of 1.0×10^{-5} or 4.6×10^{-4} mol/L in CRT, depending of the linear range of the electrode under study. The log values of the selectivity coefficients (K^{POT}) obtained are presented in **Figure 3.5**. The overall log K^{POT} values ranged −3.33/+0.25; −1.89/+0.52; and −1.71/+0.97 for conductive supports of graphite-based, FTO/ITO-glass and ITO-PET, respectively. When the interfering species was not able to introduce the necessary potential change, the log K^{POT} was calculated by using the maximum concentration of interfering species tested and co-existing with CRT in solution.

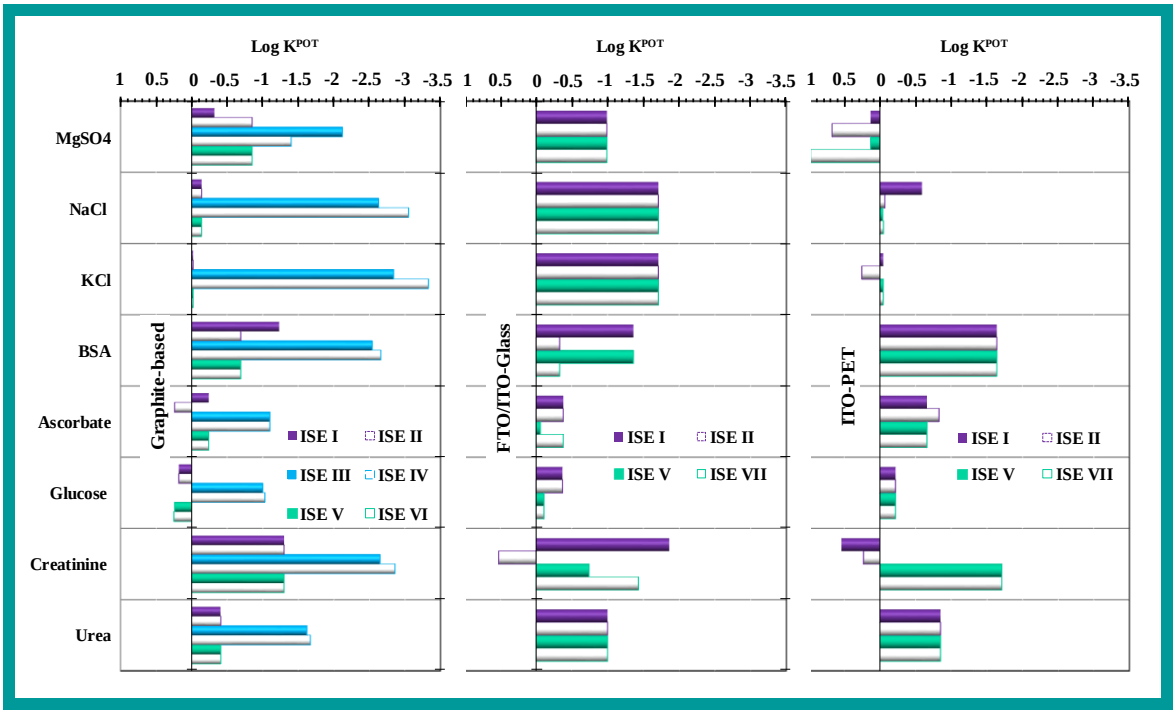

Figure 3.5. Potentiometric selectivity coefficients of all electrodes obtained by the matched potential method. (A) graphite-based; (B) FTO/ITO-glass; (C) ITO-PET.

Regarding the graphite-based electrodes, the most selective readings have been recorded with ISEs containing negative lipophilic additive (ISEs III and IV). This occurrence did not mean, however, that these electrodes were the most selective; the range of concentration tested for these devices was different (lower, due to the linear range of response) and the emf values of these electrodes became stable at higher concentrations, thereby hindering the detection of an interfering effect. The electrodes with SPAM/NIM or cationic lipophilic additive showed similar behavior, suggesting that the additive did not affect the selectivity features of the devices. Moreover, the apparent interference from glucose (a non-ionic species) was linked to the use of glucose concentrations lower than those of CRT present, rather than an emf change caused by the addition of glucose. In fact, the total changes in emf values after glucose addition varied from a minimum of 3.0 mV (ISE II) to a maximum of 5.0 mV (ISE I).

The use of FTO/ITO-glass seemed to improve the selectivity of the ISEs compared to graphite-based devices (**Figure 3.5B**), with several species tested to their maximum concentration without causing the necessary potential change. The opposite effect was observed for ITO-PET based electrodes, leading to more positive log K^{POT} values (**Figure 3.5C**). The overall behaviour pointed out better selectivity for ISEs I or V, especially when FTO/ITO-glass was used as conductive support.

3.3.4.1. Determination of CRT in urine

For the analytical application of the CRT selective electrodes, the ISEs V were selected because these were the ones combining the best selectivity and sensitivity. These electrodes also included a linear response within the average of normal carnitine concentration expected in urine. An average value of 18.8 and 9.3 mg/L in man and women, respectively, would be expected assuming reference values of carnitine in urine of 28.2 mg/day (175 micromol/day) in man or 13.9 mg/day (86 micromol/day) in women, and urine average output per individual each day of about 1.5 L.

The analysis was conducted after running a calibration of the ISEs in synthetic urine containing BSA and checking the analytical performance. The devices were applied to determine CRT in urine samples ranging from 3.4×10^{-4} to 1.3×10^{-4} mol/L. The response time of the electrodes was always below 30 seconds, independent of the concentration level used. The lifetime of the electrodes was three months. The obtained recoveries were of 91% (± 6.8%) to 118% (± 11.2%), respectively, with relative errors below −20% and a corresponding average relative standard deviation of 8.0%. A similar approach was taken for the same membrane casted on conductive glass, with similar results to those reported herein. An estimate about false positives or negatives within sample analysis cannot be provided because there are individuals that may have abnormal urine component that have not been tested herein.

3.4. Conclusions

Novel SPAM materials were tailored on GO supports with charged monomers. These materials were successfully introduced in plasticized PVC membranes for potentiometric transduction made with electrodes of different conductive materials. Overall, the use selective membranes containing SPAM as ionophore and a cationic lipophilic additive favored the overall analytical performance of the final devices, providing suitable selectivity features for practical application, with fast response and improved LODs for this potential biomarker of ovarian cancer. This effect was enhanced by casting the membrane over a conductive glass support. Moreover, the obtained analytical data showed that the CRT sensors could be applied with success to the analysis of synthetic urine samples. Other advantages of these devices include simplicity, low cost, quick responses, high analytical throughput, low LOD and good selectivity.

Overall, the combination of SPAM sensory material designed for CRT with a suitable selective membrane composition and electrode design produced devices with suitable analytical performance for point-of-care application.

References

[1] W. Pormsila, R. Morand, S. Kraehenbuehl, P.C. Hauser, 'Capillary electrophoresis with contactless conductivity detection for the determination of carnitine and acylcarnitines in clinical samples', *Journal of Chromatography B-Analytical Technologies in the Biomedical and Life Sciences*, vol. 879, pp. 921–926, 2011.

[2] M.Y. Fong, J. McDunn, S.S. Kakar, 'Identification of Metabolites in the Normal Ovary and Their Transformation in Primary and Metastatic Ovarian Cancer', *Plos One*, vol. 6, 2011.

[3] H.H. Ahmed, 'Modulatory effects of vitamin E, acetyl-L-carnitine and alpha-lipoic acid on new potential biomarkers for Alzheimer's disease in rat model', *Experimental and Toxicologic Pathology*, vol. 64, pp. 549–556, 2012.

[4] L.A. Calo, E. Pagnin, P.A. Davis, A. Semplicini, R. Nicolai, M. Calvani, A.C. Pessina, 'Antioxidant effect of L-carnitine and its short chain esters - Relevance for the protection from oxidative stress related cardiovascular damage', *International Journal of Cardiology*, vol. 107, pp. 54–60, 2006.

[5] J.L. Flanagan, P.A. Simmons, J. Vehige, M.D.P. Willcox, Q. Garrett, 'Role of carnitine in disease', *Nutrition & Metabolism*, vol. 7, 2010.

[6] B.J. Chang, M. Nishikawa, E. Sato, K. Utsumi, M. Inoue, 'L-Carnitine inhibits cisplatin-induced injury of the kidney and small intestine', *Archives of Biochemistry and Biophysics*, vol. 405, pp. 55–64, 2002.

[7] A. Marzo, G. Cardace, N. Monti, S. Muck, E.A. Martelli, 'Chromatographic and nonchromatographic assay of l-carnitine family components', *Journal of Chromatography-Biomedical Applications*, vol. 527, pp. 247–258, 1990.

[8] A. Marzo, N. Monti, M. Ripamonti, E.A. Martelli, 'Application of high-performance liquid-chromatography to the analysis of propionyl-l-carnitine by a stereospecific enzyme assay', *Journal of Chromatography*, vol. 459, pp. 313–317, 1988.

[9] M. Dabrowska, M. Starek, 'Analytical approaches to determination of carnitine in biological materials, foods and dietary supplements', *Food Chemistry*, vol. 142, pp. 220–232, 2014.

[10] M. Kivilompolo, L. Ohrnberg, M. Oresic, T. Hyotylainen, 'Rapid quantitative analysis of carnitine and acylcarnitines by ultra-high performance-hydrophilic interaction liquid chromatography-tandem mass spectrometry', *Journal of Chromatography A*, vol. 1292, pp. 189–194, 2013.

[11] A.C. Isaguirre, R.A. Olsina, L.D. Martinez, A.V. Lapierre, S. Cerutti, 'Rapid and sensitive HILIC-MS/MS analysis of carnitine and acetylcarnitine in biological fluids', *Analytical and Bioanalytical Chemistry*, vol. 405, pp. 7397–7404, 2013.

[12] Y.Z. Deng, J. Henion, J.J. Li, P. Thibault, C. Wang, D.J. Harrison, 'Chip-based capillary electrophoresis/mass spectrometry determination of carnitines in human urine', *Analytical Chemistry*, vol. 73, pp. 639–646, 2001.

[13] Y.Z. Deng, N.W. Zhang, J. Henion, 'Chip-based quantitative capillary electrophoresis/mass spectrometry determination of drugs in human plasma', *Analytical Chemistry*, vol. 73, pp. 1432–1439, 2001.

[14] L. Vernez, W. Thormann, S. Krahenbuhl, 'Analysis of carnitine and acylcarnitines in urine by capillary electrophoresis', *Journal of Chromatography A*, vol. 895, pp. 309–316, 2000.

[15] R.P. Hassett, E.L. Crockett, 'Endpoint fluorometric assays for determining activities of carnitine palmitoyltransferase and citrate synthase', *Analytical Biochemistry*, vol. 287, pp. 176–179, 2000.

[16] A. Galan, A. Padros, M. Arambarri, S. Martin, 'Automation of a spectrophotometric method for measuring L-carnitine in human blood serum', *Journal of Automatic Chemistry*, vol. 20, pp. 23–26, 1998.

[17] S. Yalkowsk, G. Zografi, 'Potentiometric titration of monomeric and micellar acylcarnitines', *Journal of Pharmaceutical Sciences*, vol. 59, no. 798, 1970.

[18] C. Botre, F. Botre, C. Pranzoni, 'A potentiometric approach to the study of the antagonism between acetazolamide and L-carnitine congeners on carbonic-anhydrase activity', *Electroanalysis*, vol. 3, pp. 567–572, 1991.

[19] A.A. Rat'Ko, R.I. Stefan, J.F. Van Staden, H.Y. Abould-Enein, 'Determination of l-carnitine using enantioselective, potentiometric membrane electrodes based on macrocyclic antibiotics', *Talanta*, vol. 63, pp. 515–519, 2004.

[20] R.L. Stefan, R.G. Bokretsion, J.F. Van Staden, H.Y. Aboul-Enein, 'Determination of L- and D-enantiomers of carnitine using amperometric biosensors', *Analytical Letters*, vol. 36, pp. 1091–1102, 2003.

[21] J. Zeravik, C. Teller, F.W. Scheller, 'Analysis of cholinesterase binding to a carnitine-modified EQCM sensor', *Biosens Bioelectron*, vol. 22, pp. 2244–2249, 2007.

[22] B. Lesnik, 'Immunoassay Techniques in Environmental Analyses', *Encyclopedia of Analytical Chemistry*, pp. 2653–2672, 2000.

[23] C.J. Tan, M.G. Chua, K.H. Ker, Y.W. Tong, 'Preparation of bovine serum albumin surface-imprinted submicrometer particles with magnetic susceptibility through core-shell miniemulsion polymerization', *Analytical Chemistry*, vol. 80, pp. 683–692, 2008.

[24] C.J. Tan, Y.W. Tong, 'Molecularly imprinted beads by surface imprinting', *Analytical and Bioanalytical Chemistry*, vol. 389, pp. 369–376, 2007.

[25] F.T.C. Moreira, S. Sharma, R.A.F. Dutra, J.P.C. Noronha, A.E.G. Cass, M.G.F. Sales, 'Smart plastic antibody material (SPAM) tailored on disposable screen printed electrodes for protein recognition: Application to myoglobin detection', *Biosens Bioelectron*, vol. 45, pp. 237–244, 2013.

[26] A.P.M. Tavares, F.T.C. Moreira, M.G.F.Sales, 'Haemoglobin smart plastic antibody material tailored with charged binding sites on silica nanoparticles: its application as an ionophore in potentiometric transduction', *RSC Advances*, vol. 3, pp. 26210–26219, 2013.

[27] J. Gauczinski, Z. Liu, X. Zhang, M. Schoenhoff, 'Surface Molecular Imprinting in Layer-by-Layer films on Silica Particles', *Langmuir*, vol. 28, pp. 4267–4273, 2012.

[28] G. Cabral-Miranda, M. Gidlund, M.G.F. Sales, 'Backside-surface imprinting as a new strategy to generate specific plastic antibody materials', *Journal of Materials Chemistry B*, vol. 2, pp. 3087–3095, 2014.

[29] P.Y. Chen, P.C. Nien, K.C. Ho, 'Highly Selective Dopamine Sensor based on an Imprinted SAM/Mediator Gold Electrode', *Proceedings of the Eurosensors XXIII Conference*, pp. 285–288, 2009.

[30] F.T.C. Moreira, R.B. Queiros, L.A.A. Truta, T.I. Silva, R.M. Castro, L.R. Amorim, M.G.Sales, 'Host-Tailored Sensors for Leucomalachite Green Potentiometric Measurements', *Journal of Chemistry*, 2013.

[31] X.L. Zhang, Y. Zhang, X.F. Yin, B.B. Du, C. Zheng, H.H. Yang, 'A facile approach for preparation of molecularly imprinted polymers layer on the surface of carbon nanotubes', *Talanta*, vol. 105, pp. 403–408, 2013.

[32] T. Kuila, S. Bose, A.K. Mishra, P. Khanra, N.H. Kim, J.H. Lee, 'Chemical functionalization of graphene and its applications', *Progress in Materials Science*, vol. 57, pp. 1061–1105 2012.

[33] X. Huang, Z. Yin, S. Wu, X. Qi, Q. He, Q. Zhang, Q. Yan, F. Boey, H. Zhang, 'Graphene-Based Materials: Synthesis, Characterization, Properties, and Applications', *Small*, vol. 7, pp. 1876–1902, 2011.

[34] A.H. Kamel, F.T. Coelho Moreira, T.S. Ribeiro Rebelo, M.G.Ferreira Sales, 'Molecularly-imprinted materials for potentiometric transduction: application to the antibiotic enrofloxacin', *Analytical Letters*, vol. 44, pp. 2107–2123, 2011.

[35] A.K. Singh, V.K. Gupta, B. Gupta, 'Chromium(III) selective membrane sensors based on Schiff bases as chelating ionophores', *Analytica Chimica Acta*, vol. 585, pp. 171–178, 2007.

[36] W.S. Hummers, R.E. Offeman, 'Preparation of grafhitic oxide', *Journal of the American Chemical Society*, vol. 80, no. 1339, 1958.

[37] S. Ge, M. Yan, J. Lu, M. Zhang, F. Yu, J. Yu, X. Song, S. Yu, 'Electrochemical biosensor based on graphene oxide-Au nanoclusters composites for L-cysteine analysis', *Biosens Bioelectron*, vol. 31, pp. 49–54, 2012.

[38] M.S. Dresselhaus, A. Jorio, M. Hofmann, G. Dresselhaus, R. Saito, 'Perspectives on Carbon Nanotubes and Graphene Raman Spectroscopy', *Nano Letters*, vol. 10, pp. 751–758, 2010.

[39] Y. Li, X. Li, C. Dong, J. Qi, X. Han, 'A graphene oxide-based molecularly imprinted polymer platform for detecting endocrine disrupting chemicals', *Carbon*, vol. 48, pp. 3427–3433, 2010.

[40] T. Tran Thanh, M. Castro, T.Y. Kim, K.S. Suh, J.F. Feller, 'Graphene quantum resistive sensing skin for the detection of alteration biomarkers', *Journal of Materials Chemistry*, vol. 22, pp. 21754–21766, 2012.

[41] G. Socrates, 'Infrared and Raman Characteristic Group Frequencies', *John Wiley & Sons, Ltd*; Chichester, UK, 2001.

CHAPTER 4

Sol-gel chemistry in biosensing devices for CEA biomarker detection

This chapter describes a work that employed a simple chemistry strategy to obtain a suitable orientation of the monoclonal Anti-CEA antibody (Ab-CEA) on top of a modified conductive glass. The present work is based on the paper *Sol-gel Chemistry in biosensing devices of electrical transduction: application to CEA cancer biomarker* published in the Journal Current Topics in Medicinal Chemistry, 15(3), 2015.

4.1. Introduction

Biosensors are compact analytical devices made with biorecognition and transducing elements. These devices are especially suitable for local applications when build with an appropriate size, and on a portable fashion, producing quick responses, with low cost. In this context, they also allow quick diagnosis and application over wide disease screening programs, being especially suitable for biomedical monitoring [1-5].

Biomedical monitoring with biosensors uses mostly biological materials as biorecognition elements, such as antibodies, transposing into a solid support the conventional antibody-based immunoassays currently employed as diagnostic tools in hospitals and clinical laboratories. An antibody is a protein molecule of the immune system that binds with a high degree of affinity and specificity to a target compound named antigen. Today, antibodies may also be targeted for almost any biomolecule.

The main difficulty of the application of an antibody on a biosensor device is to maintain its biological activity at the detection point. This requires their integration within biocompatible materials, among which sol-gel materials are included. Sol-gel materials offer several advantages, such as i) allowing mild preparation conditions; ii) electro-, photo- and chemical stability; iii) possible control of thickness, porosity and surface area [6,7]; iv) and physical and chemical robustness.

But the principal use of sol-gel materials in biomedical biosensing has been related to the encapsulation of biomolecules. In earlier stages, enzymes were entrapped in silica gel matrix and kept their catalytic activity [8,9]. Successful interaction of sol-gel with other biomolecules such as antibodies [10-14] has also been recognized. In all these, the main properties of the target biological compound are mainly preserved [15-22]. This successful combination of sol-gel and biomolecules was made solid over the years and evolved towards a 2D arrangement [23], where the biological recognition element of the biosensor device is bound to the receptor surface of the transducer. Thus, a practical application of such concept is presented herein, where an antibody is bound to a conductive glass acting as part of the electrical transducer element by means of simple sol-gel chemistry. This concept is applied to the detection of a cancer biomarker protein, CEA, responsible for clinical diagnosis of different cancers [24-28].

Recent data indicated that this glycoprotein is an important tumor marker responsible for clinical diagnosis of over 95% of all colon tumors, 50% of breast tumors, as well as tumors of the lung cancer, ovarian carcinoma [29].

The detection of CEA levels in biological samples, as serum, blood and urine, plays an important role in the pre-diagnosis evaluation and in the follow-up examination during therapy stage [26,27].

Numerous analytical methods have been described in the literature for CEA detection in different biological samples such as colorimetric enzyme immunoassay [29], radiometry immunoassays [25,28,30], chemiluminescence immunoassay [25,30,31], ELISA [25,28,30,32], colorimetry immunoassay [31], spectrophotometry [33], DLS immunoassay [31], fluoroimmunoassay and electrochemical immunoassay [24,25,28,29,31,32], electrochemical assays with potentiometry [34], and amperometry [29,32], and also some conventional methods as enzyme linked fluorescent assay (ELFA) and microparticle enzyme immunoassay (MEIA), which are less advantageous for being more expensive, complex and time consuming, requiring specially equipped laboratories and highly qualified personnel [24]. Overall, these methods are effective but unsuitable for point-of-care applications, once the response time, portability and cost are critical. Therefore, in alternative, novel approaches with simple, faster and low-cost procedures could be advantageous for immunosensor design [25,35,36].

In this paper, a different and simpler immunosensor design for CEA is proposed, by employing simple chemistry strategies that allow a suitable orientation of the monoclonal Anti-CEA antibody (Ab-CEA) on top of the modified conductive support (FTO glass). The concept was applied to electrochemical detection, because it provides a rapid, sensitive and low-cost diagnosis tool for the detection of protein biomarkers, as CEA.

4.2. Experimental

4.2.1. Apparatus

The electrochemical measurements were carried out using a Metrohm Autolab potentiostat/galvanostat, Autolab PGSTAT302N, interfaced to computer and controlled by NOVA 1.9 software.

Raman microscope DXR from Thermo Scientific was used for Raman spectrometry. The Raman spectra was recorded with a 532 nm laser, in the spectral range of 200-3500cm^{-1}, for 3.5 mW power and exposures of 60 seconds, in combination with a 50x objective magnification for focus and collection of Raman-scattered light. The confocal hole was set to 25 µm pinhole aperture.

4.2.2. Reagents and solutions

All chemicals were of analytical grade and water was deionized or ultrapure Milli-Q laboratory grade. CEA from human fluids was purchased to Fluka; Hydroxylammonium chloride was purchased from Merck; Ethanol (absolute) was obtained from Panreac; Potassium hexacyanoferrate III ($K_3[Fe(CN)_6]$) and Potassium hexacyanoferrate II ($K_4[Fe(CN)_6]$) trihydrate were obtained from Riedel-de-Häen; 3-Aminopropyltriethoxysilane (APTES), Bovine serum albumin (BSA), N-Hydroxysuccinimide (NHS), N-Ethyl-N′-(3-dimethylaminopropyl)carbodiimidehydrochloride (EDAC) and Monoclonal Anti-CEA antibody produced in mouse (Ab-CEA) were obtained from Sigma-Aldrich. The Ab-CEA solution was used after a 10x dilution of the commercial product. Phosphate buffered saline (PBS buffer obtained from Amresco, E404, Biotechnology grade), pH 7.4 was used throughout this work.

4.2.3. FTO electrode modification

A fluoride-doped tin oxide (FTO, sheet resistance 13.0 Ω/sq) glass was obtained from Sigma-Aldrich, and was cut into 2.0 cm × 1.5 cm size slices. The slices were ultrasonically cleaned for 15 min in acetone and for 15 min in deionized water, and then dried in nitrogen atmosphere. The cleaned FTO electrodes were pre-treated in 1% NH_4OH solution (pH 13.2) at room temperature, in the dark, for 1 h, leading to an active hydroxyl surface (-OH) layer [37-39]. The pretreated FTO electrodes were immersed in ethanol solution containing 2% APTES (v/v), at room temperature overnight, to form silanols monolayer (Si-O-H). Then, the APTES silanols started to condense with the surface hydroxyls. Self-assembling into a monolayer of APTES is therefore established, by a lateral siloxane (Si-O-Si) network, which are oriented to align the amine groups away from the underlying FTO substrate [39] (**Figure 4.1**, on top). After the reaction, the modified glasses were washed thoroughly with ethanol (three times) to remove unbounded silane molecules from the glass surface and dried at room temperature [40].

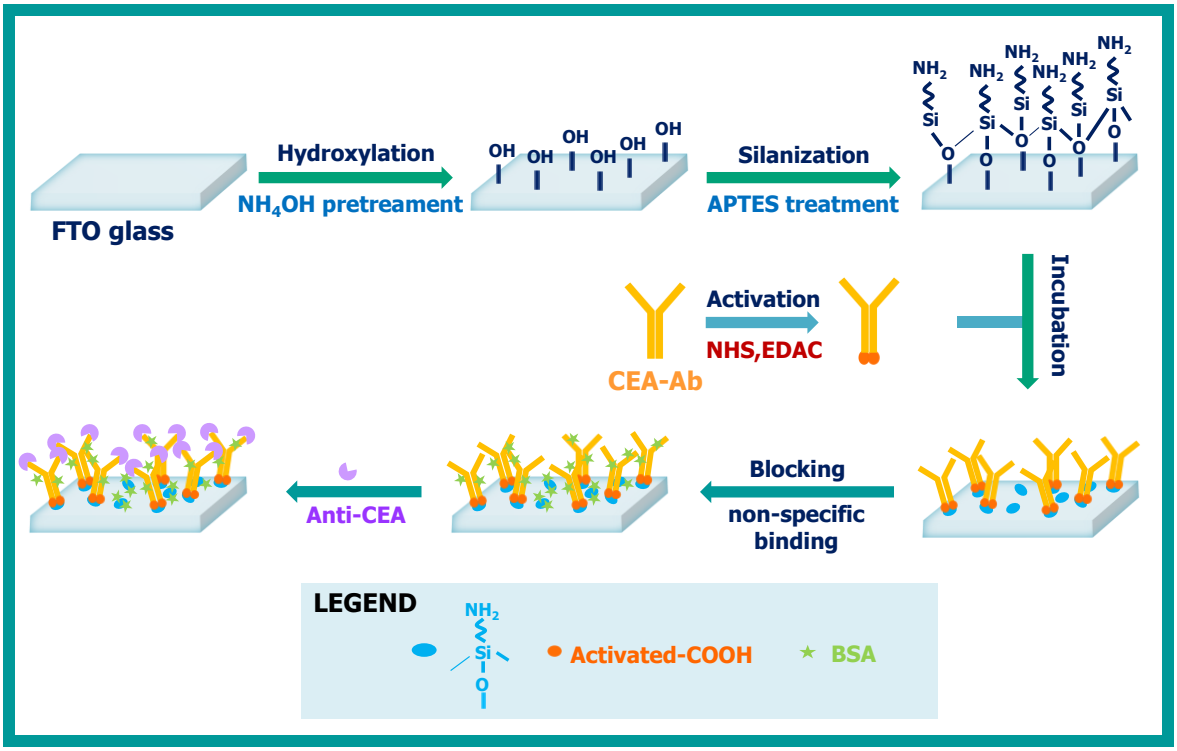

Figure 4.1. Schematic design of the immunosensor.

4.2.4. Building of the Immunosensor

The immunosensor was setup by self-assembling of the antibody/antigen (Ab-CEA/CEA) affinity reaction on the surface of the working electrode. Before binding the newly formed FTO-NH_2 layer, the Ab-CEA was left to react with NHS (50 mg/mL) and EDAC (10 mg/mL) prepared in PBS buffer (pH 7.4) for 10 minutes and 15 minutes, respectively. Subsequently, the modified Ab-CEA structure was added after to the FTO-NH_2 layer at 4 ºC, for 1 hour. After that, the modified electrode loaded with Ab-CEA was introduced into a BSA solution (0.5 M), for 2 h, at 4 ºC, to block the non-specific binding of the antibody. Then, the modified electrode was incubated with CEA for 30 min, to allow the affinity reaction between the Ab-CEA and CEA. The working CEA solutions had varying concentrations and were prepared in PBS buffer (pH 7.4) by accurate dilution of a stock solution of 25 µg/mL. **Figure 4.1** displays the stepwise building of the immunosensor.

4.2.5. Electrochemical Detection

A three-electrode system contained a silver chloride reference electrode (Ag/AgCl/0.6 mol/Kg KCl), a carbon counter electrode and a modified conductive glass was used as a working electrode.

The electrochemical behaviours of the modified electrodes were characterized by using EIS and SWV measurements, which were conducted with a redox probe of 5.0 mM $[Fe(CN)_6]^{4-/3-}$ (1:1) mixture solution, prepared in PBS buffer, pH 7.4. During the self-assembled process, EIS assays were performed at a standard potential of +0.14 V, using a sinusoidal potential perturbation with amplitude of 0.01 V and a number of frequencies equal to 100, logarithmically distributed over a frequency range of 0.01-10000 Hz. The recorded data was fitted to a Randles equivalent circuit using the implemented NOVA software from Autolab. In SWV measurements, the potentials were changed from -0.2 to +1.2 V, corresponding to a frequency of 25 Hz and a step height of 50 mV.

4.3. Results and discussion

4.3.1. Immunosensor Design

The immunosensor design consisted on creating a monolayer of free amine groups on the conductive glass support (FTO glass) by a silanization reaction with APTES. The presence of this layer on the FTO support could be confirmed by the transfer kinetics of the iron redox-probe, accounting the formation of a less resistive layer, and thus, a significant impedance decrease, as shown in **Figure 4.2A**. The function of this reaction was to allow the subsequent binding of the antibody through its Fc terminal, composed by –COOH functions, thereby allowing that the two paratope sites of the antibody remain free for antigen binding.

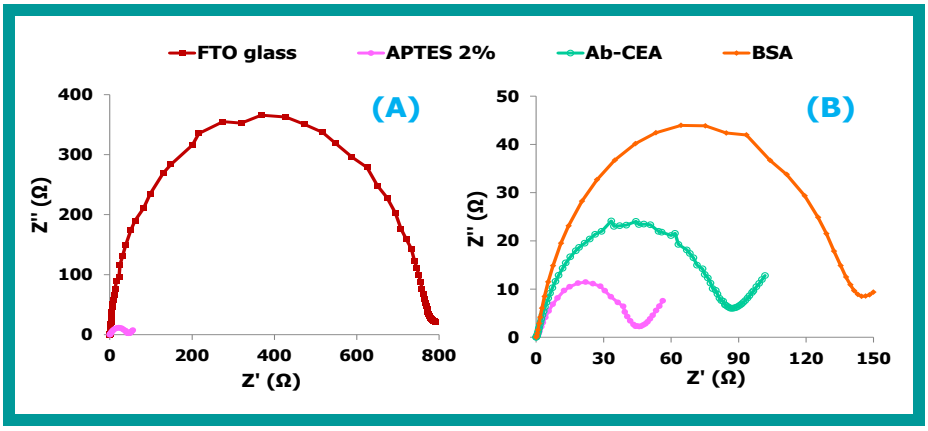

Figure 4.2. EIS spectra obtained on the assembly of the immunosensor, including (**A**) silanization of the FTO glass with APTES and (**B**) binding of the antibody (Ab-CEA) followed by BSA blocking.

The Ab-CEA was activated via a carbodiimide reaction that would allow its easy and mild covalent binding to the amine layer. Carbodiimide reaction occurred by EDAC/NHS chemistry, where the -COOH group formed a highly reactive *O*-acylisourea intermediate that reacted rapidly with NHS, to produce a stable succinimidyl ester intermediate [23,36,41]. Once activated, the Ab-CEA was connected to the support by covalent amide bonds. The electrical impedance of the FTO/NH_2/Ab-CEA was larger than that of the FTO/NH_2 material, because antibodies are huge proteins that hinder electrical signals passing through these (**Figure 4.2B**). Available regions on the FTO/NH_2/Ab-CEA support include antigen binding sites and other areas where binding of the other chemical species besides CEA is allowed. To block this unspecific binding, FTO/NH_2/Ab-CEA was incubated with a high amount of BSA. The resulting FTO/NH_2/Ab-CEA/BSA immunosensor promoted a significant increase in the R_{ct} value, comparing to the R_{ct} value obtained after the silanization with APTES on the FTO support (**Figure 4.2B**). This significant impedance increase confirmed the formation of a resistive barrier in the non-specific response sites.

4.3.2. Raman Spectroscopy

The chemical modification of the conductive surface was characterized by Raman spectroscopy measurements (**Figure 4.3**). The spectra of the control substrate (FTO glass, in **Figure 4.3A**) showed two bands, 556 and 788 cm^{-1} that were assigned to Sn-O and Sn-O-Sn stretching vibrations, respectively [42]. The band located at 1094 cm^{-1} can be associated with the asymmetric Si-O-Si stretching vibration and the ionic character of the Si-O group [19].

After the sol-gel chemistry on top of the conductive surface with APTES (**Figure 4.3B**), all of the Raman spectra, except in the **Figure 4.3D**, showed a distinct band at approximately 2900 cm^{-1}, which is most likely associated to the stretching vibration of the C-H bond of the N-C-H group [19]. The Raman intensity of this band increased with the addition of the antibody (**Figure 4.3C**) and after binding with CEA (**Figure 4.3E**). The disappearance of the intensity of the vibrational band at 2900 cm^{-1}, in **Figure 4.3Figure 4.3D**, should have been related to the presence of BSA, but there is no plausible explanation for this occurrence because BSA is composed by amino-acids, just as the antibody and CEA. Still, Raman spectra confirm the existence of chemical changes at each stage of the modification process, thereby confirming the successful design of the immunosensor.

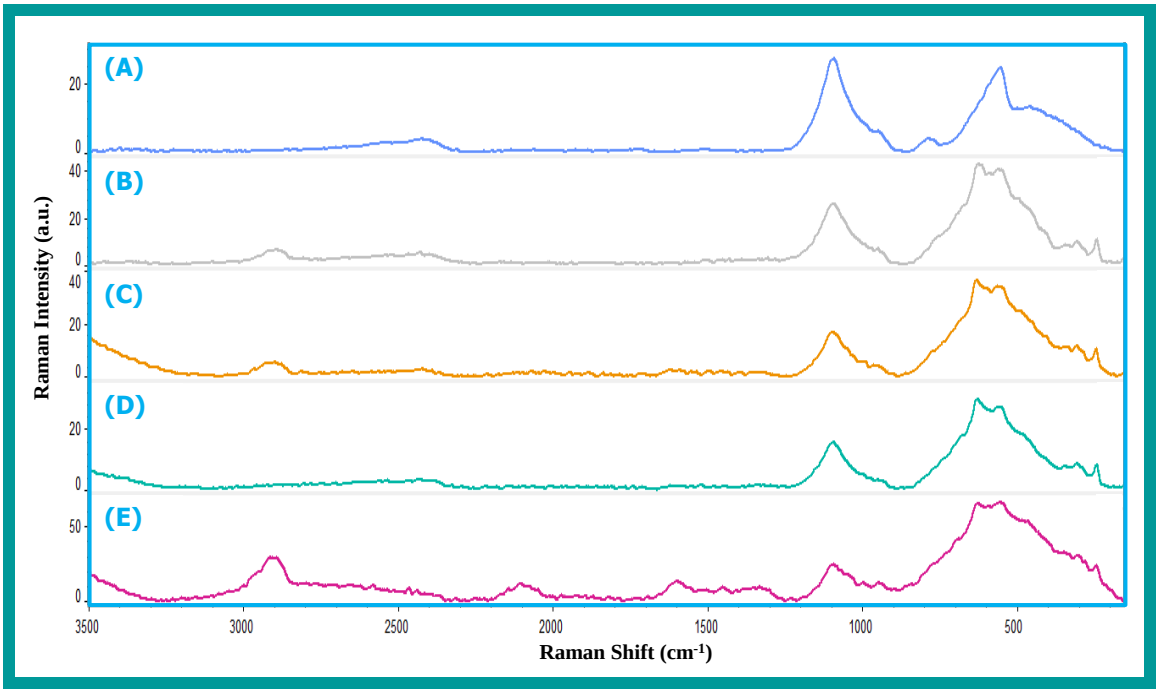

Figure 4.3. Raman spectra of several layers casted on glass: (**A**) FTO, (**B**) FTO/NH_2, (**C**) FTO/NH_2/Ab-CEA, (**D**) FTO/NH_2/Ab-CEA/BSA; and (**E**) FTO/NH_2/Ab-CEA/BSA/CEA.

4.3.3. Analytical Performance of the Biosensor

The calibration curves of the CEA immunosensor were evaluated by EIS and SWV studies. The main analytical features were evaluated by plotting the charge-transfer resistance (R_{ct}) and the current intensity, respectively, against logarithm CEA concentration (ranging from 0.0025-1.5 ng/mL), in PBS buffer, pH 7.4 (**Figure 4.4**).

According to EIS data, shown in **Figure 4.4A**, the R_{ct} values in the Nyquist plots, increased linearly with the increasing of the logarithm of CEA concentration after 0.50 ng/mL. The cationic slope was 241.9 Ω/decade log [CEA, ng/mL]. The limit of detection (LOD) and the lower limit of linear range (LLLR) were 0.42 ng/mL and 0.50 ng/mL, respectively. In SWV assays, the immunosensor showed linear behaviour from 0.25 ng/mL to 1.50 ng/mL, with a slope -6.2×10^{-3} mA/decade log [CEA, ng/mL]. The LOD was equal to 0.043 ng/mL and the LLLR was 0.25 ng/mL. The typical voltammograms obtained are presented in **Figure 4.4B**.

Overall, SWV electro-analytical readings showed quicker, more sensitive and extended linear range against CEA concentration, when compared to EIS assays. Therefore, this electrochemical approach can be selected for further evaluations and possible practical application to biological samples [43].

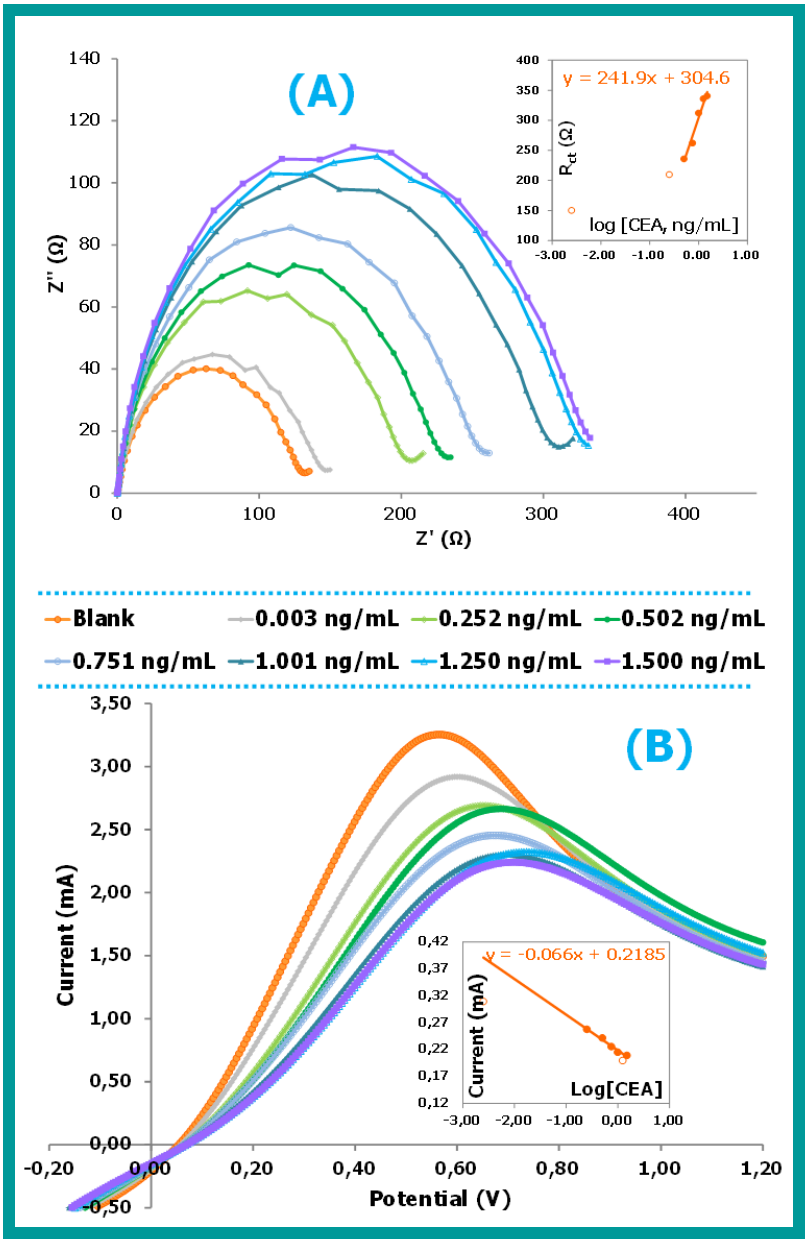

Figure 4.4. EIS (**A**) and SWV (**B**) measurements and the corresponding calibration curves obtained against CEA standard concentrations ranging from 0.0025-1.5 ng/mL.

4.4. Outlook and perspectives

A simple and sensitive immunosensor for CEA detection was developed. The successful analytical features presented by SWV studies suggest that a suitable orientation of the antibody over a conductive glass platform was successfully achieved. Overall, this works confirmed the successful application of simple silane chemistry in the assembly of an immunosensing device.

The final biosensor is also a potential device to be applied in the analysis of biological sample, at clinical context, since it allowed a good sensitivity when compared to other analytical techniques, such as ELISA assays. The use of conductive glass as physical support is also a simple approach towards its *on-site* application. Further studies and optimization procedures are however advised before real applications are tried out.

References

[1] M. Florescu, M. Barsan, R. Pauliukaite, C.M.A. Brett, 'Development and application of oxysilane sol-gel electrochemical glucose biosensors based on cobalt hexacyanoferrate modified carbon film electrodes', *Electroanal.*, vol. 19, no. 2-3, pp. 220-226, 2007.

[2] H. Ju, X. Zhang, J. Wang, 'Biosensors Based on Sol–Gel Nanoparticle Matrices', *Biol. Med. Phys. Biomed.*, pp. 305-332, 2011.

[3] J. Ponmozhi, C. Frias, T. Marques, O. Frazao, 'Smart sensors/actuators for biomedical applications: Review', *Measurement*, vol. 45, no. 7, pp. 1675-1688, 2012.

[4] J.P. Hart, A.K. Abass, K.C. Honeychurch, R.M. Pemberton, S.L. Ryan, R. Wedge, 'Sensors/biosensors, based on screen-printing technology for biomedical applications', *Indian J. Chem. A.*, vol. 42, no. 4, pp. 709-718, 2003.

[5] J. Wang, G. Chen, H. Jiang, Z. Li, X. Wang, 'Advances in nano-scaled biosensors for biomedical applications', *Analyst*, vol. 138, no. 16, pp. 4427-4435, 2013.

[6] S. Marx, Z. Liron, 'Molecular imprinting in thin films of organic-inorganic hybrid sol-gel and acrylic polymers', *Chem. Mater.*, vol. 13, no. 10, pp. 3624-3630, 2001.

[7] M. Lahav, A.B. Kharitonov, O. Katz, T. Kunitake, I. Willner, 'Tailored chemosensors for chloroaromatic acids using molecular imprinted TiO_2 thin films on ion-sensitive field-effect transistors', *Anal. Chem.*, vol. 73, no. 3, pp. 720-723, 2001.

[8] T. Coradin, M. Boissiere, J. Livage, 'Sol-gel chemistry in medicinal science', *Curr. Med. Chem.*, vol. 13, no. 1, pp. 99-108, 2006.

[9] L.M. Ellerby, C.R. Nishida, F. Nishida, S.A. Yamanaka, B. Dunn, J.S. Valentine, J.I. Zink, 'Encapsulation of proteins in transparent porous silicate-glasses prepared by the sol-gel method', *Science*, vol. 255, no. 5048, pp. 1113-1115, 1992.

[10] X. Sun, S. Du, X. Wang, B. Qi, 'A Novel Label-Free Impedance Immunosensor Based on Sol-Gel for Determination of Carbofuran', *Sensor Lett.*, vol. 10, no. 1-2, pp. 330-334, 2012.

[11] X.L. Sun, Z.Y. Wang, Y.J. Fang, P.P. Chen, Z.J. Li, 'Immunosensor Based on Immobilizing Antibody of Aflatoxin B-1 Using Silica Sol-Gel Technology', *Chinese J. Anal. Chem.*, vol. 38, no. 2, pp. 245-248, 2010.

[12] J.C. Zhou, M.H. Chuang, E.H. Lan, B. Dunn, P.L. Gillman, S.M. Smith, 'Immunoassays for cortisol using antibody-doped sol-gel silica', *J. Mater. Chem.*, vol. 14, no. 14, pp. 2311-2316, 2004.

[13] P. Pulido-Tofino, J.M. Barrero-Moreno, M.C. Perez-Conde, 'Sol-gel glass doped with isoproturon antibody as selective support for the development of a flow-through fluoroimmunosensor', *Anal. Chim. Acta*, vol. 429, no. 2, pp. 337-345, 2001.

[14] G.J. Copello, M.C. Marzi, M.F. Desimone, E.L. Malchiodi, L.E. Diaz, 'Antibody detection employing sol-gel immobilized parasites', *J. Immunol.Methods*, vol. 335, no. 1-2, pp. 65-70, 2008.

[15] X. Du, P. Zhan, N. Gan, Y. Cao, T. Li, W. Sang, L. Wang, 'Highly Selective Molecular Recognition and Ultrasensitive Detection of 3,4-dichloroaniline Based on Molecularly Imprinted Sol-Gel Film Combined with Multi-Walled Carbon Nanotubes', *J. Electrochem. Soc.*, vol. 160, no. 10, pp. H742-H748, 2013.

[16] R.B. Queiros, S.O. Silva, J.P. Noronha, O. Frazao, P. Jorge, G. Aguilar, P.V.S. Marques, M.G.F. Sales, 'Microcystin-LR detection in water by the Fabry-Perot interferometer using an optical fibre coated with a sol-gel imprinted sensing membrane', *Biosens. Bioelectron.*, vol. 26, no. 9, pp. 3932-3937, 2011.

[17] R. Gupta, A. Kumar, 'Synthesis and characterization of sol-gel-derived molecular imprinted polymeric materials for cholesterol recognition', *J. Sol-gel Sci. Techn.*, vol. 58, no. 1, pp. 182-194, 2011.

[18] Z. Lin, F. Yang, X. He, X. Zhao, Y. Zhang, 'Preparation and evaluation of a macroporous molecularly imprinted hybrid silica monolithic column for recognition of proteins by high performance liquid chromatography', *J. Chromatogr. A*, vol. 1216, no. 49, pp. 8612-8622, 2009.

[19] A.R. Khorrami, A. Rashidpur, 'Development of a fiber coating based on molecular sol-gel imprinting technology for selective solid-phase micro extraction of caffeine from human serum and determinatin by gas chromatography/mass spectrometry', *Anal. Chim. Acta*, vol. 727, pp. 20-25, 2012.

[20] M.E. Brown, D.A. Puleo, 'Protein binding to peptide-imprinted porous silica scaffolds', *Chem. Eng. J.*, vol. 137, no. 1, pp. 97-101, 2008.

[21] S. Dai, M.C. Burleigh, Y.H. Ju, S.D. Waezsada, Z.L. Xue, C.E. Barnes, 'Molecular imprinting on sol-gel materials', *Abstr. Pap. Am. Chem. S.*, vol. 218, pp. U1064-U1064, 1999.

[22] D.Y. Sasaki, T.M. Alam, R.A. Assink, B. Hart, K.J. Shea, 'Molecular imprinting in guanidine functionalized sol-gel materials', *Abstr. Pap. Am. Chem. S.*, vol. 217, pp. U339-U339, 1999.

[23] N.S. Ferreira, M.G.F. Sales, 'Disposable immunosensor using a simple method for oriented antibody immobilization for label-free real-time detection of an oxidative stress biomarker implicated in cancer diseases', *Biosens. Bioelectron.*, vol. 53, pp. 193-199, 2014.

[24] Y. Fu, R. Yaan, Y. Chai, Y. Zhang, Y. Peng, 'Electrochemical immunoanalysis for carcinoembryonic antigen based on multilayer architectures of gold nanoparticles and polycation biomimetic interface on glassy carbon electrode', *Electroanal.*, vol. 18, no. 24, pp. 2451-2457, 2006.

[25] F. Tan, F. Yan, H. Ju, 'A designer ormosil gel for preparation of sensitive immunosensor for carcinoembryonic antigen based on simple direct electron transfer', *Electrochem. Commun.*, vol. 8, no. 12, pp. 1835-1839, 2006.

[26] Tumor markers found in blood or urine. http://www.cancer.org/treatment/understandingyourdiagnosis/examsandtestdescriptions/tumormarkers/tumor-markers-t-m-blood-urine (Accessed in September, 2014).

[27] CEA: Proteins and Tumor Markers. http://breastcancer.answers.com/symptoms/cea-proteins-and-tumor-markers (Accessed in September, 2014).

[28] M. Liu, C. Jia, Q. Jin, X. Lou, S. Yao, J. Xiang, J. Zhao, 'Novel colorimetric enzyme immunoassay for the detection of carcinoembryonic antigen', *Talanta*, vol. 81, no. 4-5, pp. 1625-1629, 2010.

[29] J.C. Kemmegne-Mbouguen, E. Ngameni, P.G. Baker, T.T. Waryo, B. Kgarebe, E.I. Iwuoha, 'Carcinoembryonic Antigen Immunosensor Developed with Organoclay Nanogold Composite Film', *Int. J. Electrochem. Sc.*, vol. 9, no. 1, pp. 478-492, 2014.

[30] W. Shi, Z. Ma, 'A novel label-free amperometric immunosensor for carcinoembryonic antigen based on redox membrane', *Biosens. Bioelectron.*, vol. 26, no. 6, pp. 3068-3071, 2011.

[31] X. Miao, S. Zou, H. Zhang, L. Ling, 'Highly sensitive carcinoembryonic antigen detection using Ag@Au core-shell nanoparticles and dynamic light scattering', *Sensor Actuat. B-Chem.*, vol. 191, pp. 396-400, 2014.

[32] P. Lv, L. Min, R. Yuan, Y. Chai, S. Chen, 'A novel immunosensor for carcinoembryonic antigen based on poly(diallyldimethylammonium chloride) protected prussian blue nanoparticles and double-layer nanometer-sized gold particles', *Microchim. Acta*, vol. 171, no. 3-4, pp. 297-304, 2010.

[33] B.J. Casey, P. Kofinas, 'Selective binding of carcinoembryonic antigen using imprinted polymeric hydrogels', *J. Biomed. Mater. Res. A*, vol. 87, no. 2, pp. 359-363, 2008.

[34] Y. Wang, Z. Zhang, V. Jain, J. Yi, S. Mueller, J. Sokolov, Z. Liu, K. Levon, B. Rigas, M.H. Rafailovich, 'Potentiometric sensors based on surface molecular imprinting: Detection of cancer biomarkers and viruses', *Sensor Actuat. B-Chem.*, vol. 146, no. 1, pp. 381-387, 2010.

[35] H. Yu, F. Yan, Z. Dai, H. Ju, 'A disposable amperometric immunosensor for alpha-1-fetoprotein based on enzyme-labeled antibody/chitosan-membrane-modified screen-printed carbon electrode', *Anal Biochem.*, vol. 331, pp. 98-105, 2004.

[36] G. Cabral-Miranda, E.H.G. Yamashiro-Kanashiro, M. Gidlund, M.G.F. Sales, 'Specific label-free and real-time detection of oxidized low density lipoprotein (oxLDL) using an immunosensor with three monoclonal antibodies', *J. Mater. Chem. B*, vol. 2, no. 5, pp. 477-484, 2014.

[37] E. Zor, I.H. Patir, H. Bingol, M. Ersoz, 'An electrochemical biosensor based on human serum albumin/graphene oxide/3-aminopropyltriethoxysilane modified ITO electrode for the enantioselective discrimination of D- and L-tryptophan', *Biosens. Bioelectron.*, vol. 42, pp. 321-325, 2013.

[38] R. Huang, L.H. Guo, 'Lack of nano size effect on electrochemistry of dopamine at a gold nanoparticle modified indium tin oxide electrode', *Science China-Chemistry*, vol. 53, no. 8, pp. 1778-1783, 2010.

[39] A. Sarkar, T. Daniels-Race, 'Electrophoretic Deposition of Carbon Nanotubes on 3-Amino-Propyl-Triethoxysilane (APTES) Surface Functionalized Silicon Substrates', *Nanomaterials*, vol. 3, pp. 272-288, 2013.

[40] M.A. Aziz, S. Patra, H. Yang, 'A facile method of achieving low surface coverage of Au nanoparticles on an indium tin oxide electrode and its application to protein detection', *Chem. Commun.*, no. 38, pp. 4607-4609, 2008.

[41] S. Teixeira, R.S. Conlan, O.J. Guy, M.G.F. Sales, 'Label-free human chorionic gonadotropin detection at picogram levels using oriented antibodies bound to graphene screen-printed electrodes', *J. Mater. Chem. B*, vol. 2, no. 13, pp. 1852-1865, 2014.

[42] V. Kumar, A. Govind, R. Nagarajan, 'Optical and Photocatalytic Properties of Heavily F-Doped SnO_2 Nanocrystals by a Novel Single-Source Precursor Approach', *Inorg. Chem.*, vol. 50, no. 12, pp. 5637-5645, 2011.

[43] G. Socrates, 'Infrared and Raman Characteristic Group Frequencies', *John Wiley & Sons, Ltd*, 3rd Edition, 2001.

CHAPTER 5

Carcinoembryonic antigen imprinting on a conductive glass support

This chapter reports a new approach of designing protein plastic antibody for CEA biomarker detection created on a carbon ink film linked by sol-gel chemistry to a conductive glass support. This is based on the paper titled *Carcinoembryonic antigen imprinting by simple electropolymerization on a common conductive glass support and its determination in serum samples* submitted in a scientific journal.

5.1. Introduction

Cancer diseases are the main cause of death worldwide. According to the recent World Cancer Report 2014 published by the WHO, the most common causes of cancer death are lung, liver, stomach, colorectal and breast cancers [1,2][2,3]. Carcinogenesis consists in the abnormal transformation of cells within the body, which leads to their uncontrolled proliferation and, ultimately, to the invasion of nearby tissues [3,4]. Its detection in an initial state is fundamental and the detection of morphological alterations in the tissues need invasive procedures.

Under this scenario, the current discovery of circulating tumour markers has emerged as a key element in cancer diagnosis and follow-up, also playing an important role in the early analysis of cancer risk [1,2]. Tumour markers are defined as biomolecules that are produced by the body in response to or along with cancer growth, and that may be detected in biological samples, such as blood, urine or tissues [2]. Therefore, biomarkers are a dynamic and a powerful approach to reflect the stage of a disease, at a faster, non-invasive and low-cost way, useful for over wide screening programs and applications in POC context, and consequently suitable for early monitoring of cancer diseases [1,5].

CEA is an important tumour marker that has been employed in clinical diagnosis of over 90% colorectal cancers. This is the third most common type of cancer disease and the major cause of the death throughout the world. Such bad scenario accounts the complexity and heterogeneity through the multiple genetic mutations that occurs in the disease [6–8]. CEA is a marker that plays an important role for clinical diagnosis and prognosis evaluation of colorectal cancer, providing a follow-up examination during therapy stage of the disease and its monitoring through CEA levels that can be presented in different biological samples, including urine, serum or blood [2,9–13]. In 2011, Nielsen at co-authors determined that CEA marker was an important biomarker for early detection of colorectal cancer. The normal levels of CEA marker in healthy adults are <2.5 ng/mL, in case of an adult non-smoker, and <5.0 ng/mL in a smoker, and levels above 5.0 ng/mL may signal the presence of cancer [9].

Despite the effectiveness of the conventional methodologies [1,14–22] already described in the literature to monitor CEA in different biological samples, its complexity and high costs made these techniques unsuitable for POC applications [12,23,24,25]. In this typical scenario, biosensors are becoming an alternative to the conventional techniques usually used in clinical context, due to their simplicity fast response, low cost and easy miniaturization and portability [26,27].

In terms of CEA, there are many works reported so far [28]. The most recent ones employ mostly antibodies as biorecogntion elements, in which the detection system relies in surface plasmon resonance [29], electrochemiluminescence [30], or electrochemical [31,32] measurements, or else rely on a hybrid system that targets electrical autonomy for electrochemical sensing [33]. Aptamers are also a convenient choice, coupled to luminescence [34], electrochemical [35] or electrochemiluminescence signals [36]. Another alternative in terms of biorecognition element could be molecularly imprinted polymers (MIPs), as reported by Moreira et al., 2016 [37]. MIPs act as antibodies and are synthetic materials, tailored for the desired molecule, with low cost and rapid procedures. In this, a polypyrrol imprinted film was assembled on site for the production a 3-electrode system within few seconds. Moreover, this approach used print-circuit board technology, yielding suitable procedures for mass production. Yet, alternative and simple approaches to be established on-site with currently available material in analytical laboratories remains missing.

Thus, this work reports a novel and simple approach to monitor CEA biomarker with MIP technology on a simple conductive glass surface. For this purpose, the polymerization was achieved by electrical stimulus on an FTO-glass modified with a homemade carbon ink. The biomimetic material (assigned as MPAP) was assembled on top, by moulding CEA at the molecular level around a Polyaminophenol (PAP) polymeric matrix. In this, Aminophenol (AP) was electropolymerization on the FTO glass (the working electrode), previously incubated with CEA biomarker and Aminophenylboronic acid (APBA). Proteinase K was incubated next, for protein removal. A control non-imprinted material, NPAP, was prepared in parallel to assess the contribution of the imprinted sites in the overall analytical performance. MPAP and NPAP were evaluated by two different electrochemical techniques, namely, EIS and CV techniques, and their application feasibility in biological samples were, also, tested.

5.2. Experimental section

5.2.1. Reagents

All chemicals were of analytical grade and water was deionized or ultrapure Milli-Q laboratory grade. Acetone, 3-Aminopropyltriethoxysilane (APTES), Lithium iodide (LiI) and Sulphuric acid, 95-97% (H_2SO_4) were obtained from Sigma-Aldrich. 3-Aminophenylboronic acid monohydrate, 98% (APBA) and 3-Aminophenol, 99% (AP) were obtained from Acros Organics. Carcinoembryonic antigen from human fluids (CEA) and Poly(vinyl chloride) carboxylated (PVC-COOH) were purchased to Fluka.

Hydroxylammonium chloride was purchased from Merck; *N*,*N*-Dimethylformamide (DMF) was obtained from Analar Normapur; Ethanol absolute was obtained from Panreac and Sodium hydroxide was obtained from Scharlau. Iodine (I_2) and Sodium acetate were obtained from Riedel-de-Häen. Proteinase K and Phosphate buffered saline (PBS) tablets (pH 7.4) were purchased from Amresco.

5.2.2. Apparatus

The electrochemical measurements were carried out by a Methrom Autolab potentiostat/galvanostat, Autolab PGSTAT302N, interfaced to computer and controlled by NOVA 1.9 software. Solid materials were characterized by Fourier Transform Infrared Spectrometry (FTIR), using a Nicolet iS10 FTIR spectrometer, from Thermo Scientific, couple to the Attenuated Total Reflectance (ATR) sampling accessory of germanium contact crystal, also from Nicolet. The spectra were collected under room temperature/humidity control, after background correction. The number of scans for sample and background was set to 100. The *x*-axis ranged from 600 to 4000 cm^{-1} and *y*-axis shown as % transmittance. The resolution was 32. The same materials were also analyzed by Raman spectroscopy using a Raman microscope DXR from Thermo Scientific, equipped with a 532 nm laser. The Raman spectra was recorded in the range of 200-3500 cm^{-1}, with a 50× objective magnification for focus and collection of Raman-scattered light, at 3.5 mW laser power and 25 µm pinhole aperture. Scanning Electronic Microscopy (SEM) was performed using a High resolution (Schottky) Environmental Scanning Electron Microscope with X-Ray Microanalysis and Electron Backscattered Diffraction analysis, from Quanta 400 FEG ESEM/EDAX Genesis X4M. All measurements were carried out at room temperature.

5.2.3. Synthesis of MPAP material for CEA detection

5.2.3.1. Working electrode modification

The first stage of the preparation of the working electrode consisted in cutting the FTO (sheet resistance 13.0 Ω/sq) glass, from Sigma-Aldrich, into 2.0 cm × 1.3 cm slices. Afterwards, these substrates were cleaned by ultrasonication, for 15 minutes, in acetone, followed by 15 minutes in deionized water, and dried in nitrogen atmosphere. FTO electrodes were pre-treated with NH_4OH and APTES, in order to create a suitable surface for coupling other materials [13].

The APTES silanols were condensed with the surface hydroxyls, establishing the self-assembling into a monolayer of APTES through the lateral siloxane (Si-O-Si) network oriented to align the amine groups away from the underlying FTO electrode [13,38] (**Figure 5.1**.**A**, left). Afterwards, these pre-treated electrodes (pFTO) were modified with a homemade conductive carbon ink (hCCI) composed by a mixing of graphite powder spiked with 15% PVC-COOH in DMF, which was deposited on top of the pFTO surface by spin coater technique and thermally sintered in a Nabertherm GmbH P330 oven, for 1h, at 120ºC (**Figure 5.1A**, right) [39]. In order to remove unwanted-species that could be present in the deposited ink, this carbon layer was oxidized with H_2SO_4 solution 0.5 mol/L, before starting the construction of the plastic antibody [39]. This step was performed by CV in a potential range of –0.2 to 1.5 V, at a scan-rate of 50 mV/s, for 10 cycles.

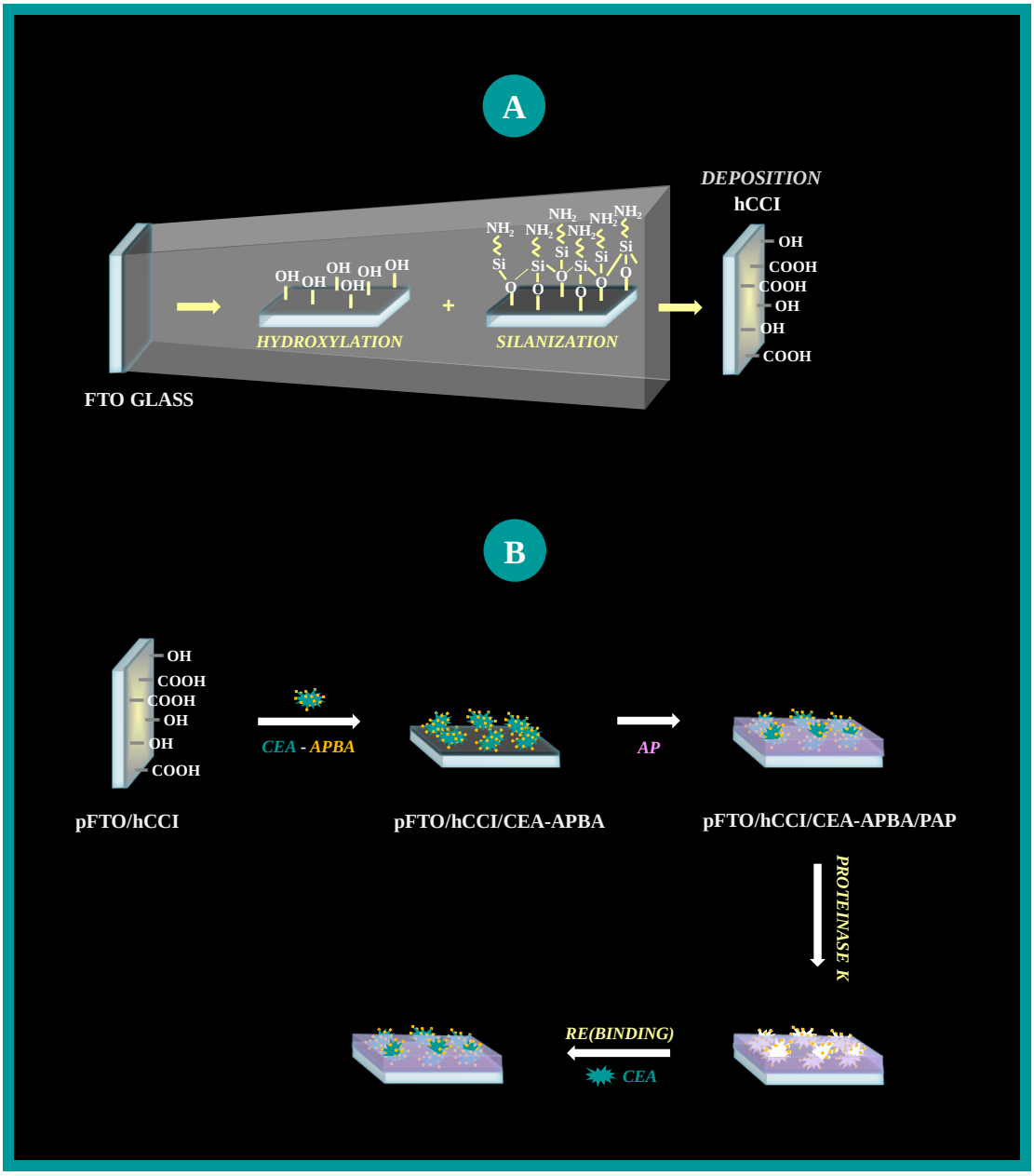

Figure 5.1. Assembling of the plastic antibody for CEA detection. (A) Modification of the working electrode based on the pre-treatment of the FTO glass surface and the deposition of the homemade carbon ink (hCCI) on top of it. (B) Schematic representation of the synthesis of the MPAP material, highlighting the modification of pre-treated FTO glass (pFTO) with hCCI (pFTO/hCCI); incubation of pFTO/hCCI with CEA and the monomer 3-Aminophenylboronic acid monohydrate (APBA), pFTO/hCCI/CEA-APBA; imprinting stage with formation of a Polyaminophenol (PAP) thin film; CEA removal with Proteinase K and re(binding) of protein, pFTO/hCCI/CEA-APBA/PAP.

5.2.3.2. Electrosynthesis of CEA imprinting

The MPAP films were produced by covering the modified working electrode area with a solution containing CEA 25 ng/mL and APBA 0.01 mol/L, prepared in acetate buffer pH 5.0. The incubation period was set to 1h30, at room temperature. Afterwards, the working electrode was thoroughly washed with PBS buffer, pH 7.4, in order to remove unbound protein and monomer residues from the surface, followed by an incubation of 5 minutes, in 0.01 mol/L AP solution, also prepared in acetate buffer (pH 5.0). Then, a polymerization of AP was performed by CV in a potential range between -0.2 and 0.8 V, at a scan rate of 50 mV/s, for 15 cycles [40]. The resulting film was washed with PBS buffer and incubated overnight in 500 µg/mL proteinase K solution (in PBS buffer, pH 7.4), at room temperature and in the dark. The MPAP film was finally thoroughly washed for several times in PBS buffer, followed by a cleaning with this buffer solution through CV consecutive scanning, between -0.5 and 1.0 V, at a scan rate of 50 mV/s, for 15 cycles, aiming to remove any protein fragments and proteinase K present on the electrode surface (**Figure 5.1B**).

In parallel, non-imprinted materials (NPAP) were produced, as control, following an equivalent procedure to MPAP materials but without the protein incubation step.

5.2.4. Rebinding studies

The adsorption dynamics of MPAP and NPAP films were measured by EIS assays. These measurements were conducted by incubating the electrodes with increasing concentrations of CEA standards, prepared in buffer, ranging from 2.5 ng/mL to 1.50 µg/mL. A 30 minutes period of incubation at room temperature was set before adding the redox probe for subsequent EIS measurements. A Langmuir isotherm model (**Equation 5.1**) was applied to the experimental data, where R_{ct} is the normalized charge transfer density (kΩ/cm^2), recognized by the charge-transfer resistance, S the concentration of CEA (in µg/mL), and $R_{ct}^{máx}$ is the maximum charge transfer density observed (kΩ/cm^2). The apparent dissociation constant (K_D, in µg/mL) that defines the protein concentration required to provide half of the maximum response produced by the device, and the maximum binding capacity ($R_{ct}^{máx}$) were calculated from the fitting of the experimental data to the model in **Equation 5.1**.

$$R_{ct} = \frac{R_{ct}^{máx}}{1 + K_D / [S]} \qquad \textbf{(Equation 5.1)}$$

5.2.5. Electrochemical biosensing

Electrochemical measurements were performed in a conventional three-electrode cell assembly composed by a silver chloride reference electrode (Ag/AgCl/0.6 mol/kg KCl), a carbon counter electrode and the modified FTO glass used as a working electrode.

The electrochemical behaviour of the modified electrodes was tested by CV and EIS assays, at room temperature, which an iodide redox probe of 10 mM I_2 and 20 mM LiI mixture solution, prepared in PBS buffer of pH 7.4. During the self-assembling process, the potentials of CV assays were scanned from –0.7 to 0.7 V, at 50 mV/s for 20 cycles. EIS assays were performed at open circuit potential, using a sinusoidal potential perturbation of 0.01 V amplitude and 50 frequency values, logarithmically distributed over a frequency range of 0.01-10000 Hz. The impedance data were fitted to a suitable Randles equivalent circuit through the implemented NOVA software.

The biosensor response to varying CEA concentrations was assessed by EIS measurements. Each working electrode was evaluated by incubations for a fixed period time of 30 minutes, at room temperature, in CEA concentration levels ranging from 2.5 ng/mL to 1.50 µg/mL. Sample analysis was made by spiking fetal bovine serum (FBS) with CEA, in the same concentration range, and diluting it 10× with PBS buffer.

5.3. Results and discussion

5.3.1. CEA plastic antibody assembly

The plastic antibody was assembled on top of the modified FTO glass, using CEA as a template molecule and CV was used to electropolymerize AP. The overall process consisted in 5 different steps: (1) preparation of a support containing a monolayer of free amine groups; (2) casting the carbon ink; (3) adsorption of CEA with charged monomers; (4) synthesis of the polymeric film PAP, around the protein; (5) removal of the protein; (6) and cleaning the sensing surface. Each of these steps was followed by measuring the corresponding electron transfer properties, evidenced by EIS and CV assays (**Figure 5.2**).

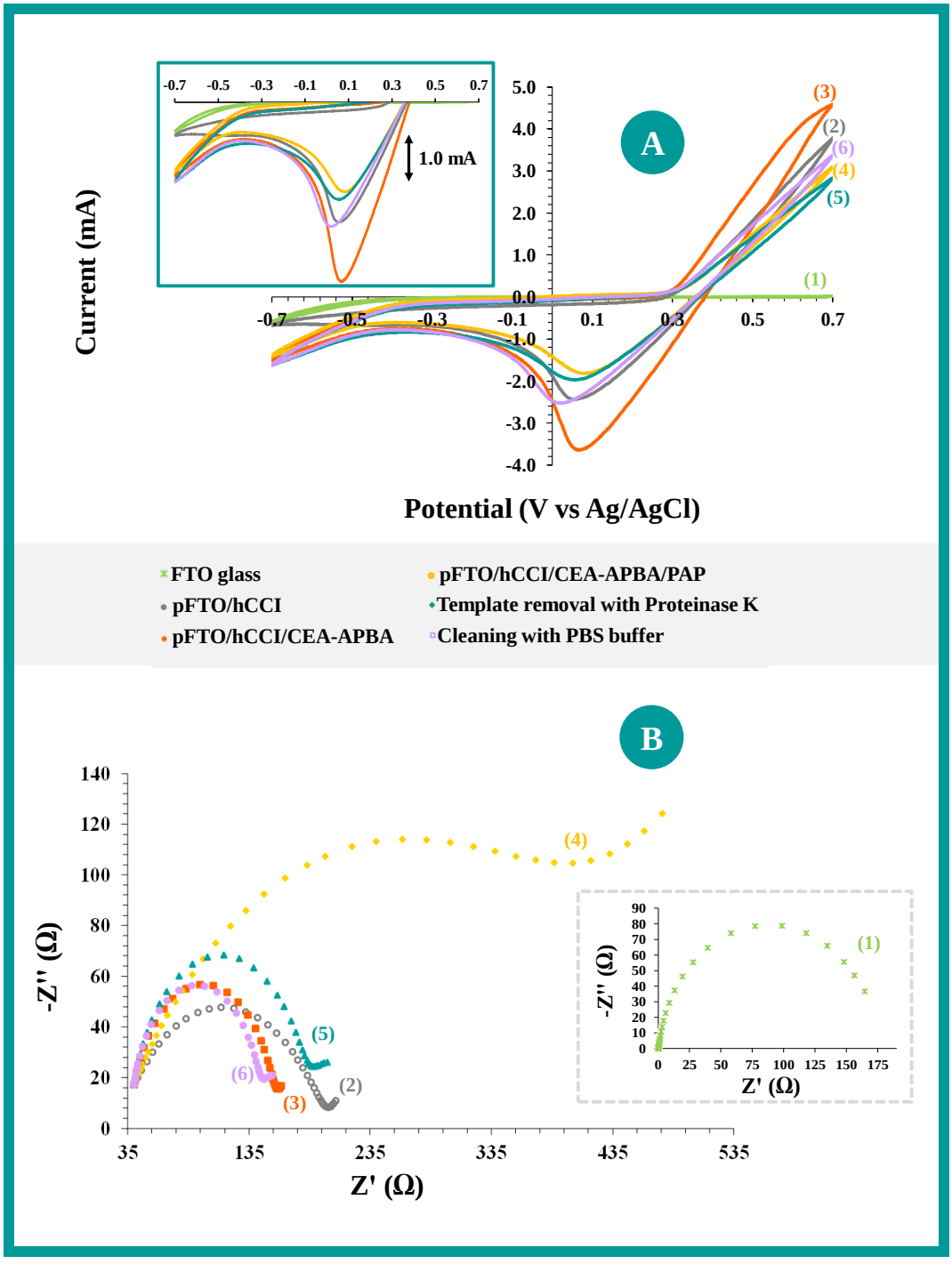

Figure 5.2. CV and EIS spectra (A and B, respectively) of the MPAP assembly, including different stages: (1) clean conductive glass support (FTO glass); (2) coating of the hCCI on top of the pFTO substrate; (3) incubation of the CEA-APBA mix solution; (4) electropolymerization of AP monomer; (5) template removal with Proteinase K; and (6) cleaning with PBS buffer (pH 7.4).

In step 1, the monolayer of free amine groups was formed on top of the conductive glass support, by means of a silanization reaction based in a 2% APTES solution [13]. This amine layer bridged the FTO glass to the carbon ink and was found essential, as different tests made initially by casting the carbon ink directly on the FTO revealed a little stability.

In step 2, the hCCI was casted directly on top of this amine film (pFTO/hCCI). This modification decreased the electrical resistance of the overall surface, signalled by a decrease in the charge transfer resistance of the iodide probe in EIS (**Figure 5.2B**). Consistently, the anodic peak current values increased significantly, as revealed by comparing the cyclic voltammograms of steps (1) and (2) in **Figure 5.2A**. The resulting carbon ink layer was further cleaned, to ensure a reproducible surface and the presence of oxidized carbons that would allow anchoring the protein in step 3 and the polymeric film in step 4.

In step 3, the CEA protein was first incubated with APBA to allow the formation of ionic interactions between the anionic carboxylate groups on the outer surface of the protein, and the cationic protonated amine groups of APBA [23]. This solution was then placed on top of the pFTO/hCCI, to allow the adsorption of the protein on this surface. Ionic interactions were also contributing to this adsorption. This modification decreased the R_{ct} signal of the support (~53.5 Ω), as shown in the EIS spectra in **Figure 5.2B**, and (consistently) decreased the anodic peak current represented in the CV assay (**Figure 5.2A**). This behaviour could be related to a positive charge arising at the surface of the electrode, increasing its attraction for the anionic redox probe of iodide.

In step 4, a polymeric layer was formed around the protein/APBA complex, pFTO/hCCI/CEA-APBA, by electropolymerizing AP (pH 5.0) on the modified substrate, by means of consecutive sweeps in CV mode. Polyaminophenol (PAP) films exhibit several advantages compared to other electrosynthesized polymers due to their self-limited growth (thicknesses within 10-50 nm and high degree of permselectivity, with an interfering-free effect from some electroactive species present in biological fluids [41]. Electrostatic interactions with the target protein at the rebinding event should have been established by the amine and hydroxyl functional groups linked to the aromatic ring of this monomer, contributing for its stability at the binding position [42]. The presence of PAP film contributed to an additional barrier for the redox probe access on the modified electrode surface, thereby promoting a significant increase of R_{ct} value (of ~264.0 Ω), and a decrease of the anodic peak current (**Figure 5.2A**).

Herein, CEA was removed enzymatically by incubating overnight the substrate pFTO/hCCI/CEA-APBA/PAP in proteinase K, 500 µg/mL of (step 5). This enzyme offered low specificity regarding the peptide bond environment and high efficiency for proteins denaturation and amide bond cleavage [43]. The removal of the protein was confirmed by a significant decrease in the R_{ct} value (of ~239.5 Ω, when compared to the R_{ct} values of pFTO/hCCI/CEA-APBA/PAP) and consistent increase of the anodic peak current (**Figure 5.2A**).

Finally, the resulting surface was cleaning in step 6, to ensure a reproducible surface. This was made by incubating the surface in PBS buffer. In this step, an additional decrease of the R_{ct} value (~39.0 Ω) was observed, along with a decrease of the anodic peak current, thereby confirming the removal of protein fragments or proteinase K that could be adsorbed on surface (**Figure 5.2A**).

5.3.2. Surface morphology and chemical structural analysis

The surface morphology of the pFTO/hCCI, pFTO/hCCI/CEA-APBA/PAP (MPAP) and pFTO/hCCI/PAP (NPAP) materials was analyzed by SEM and EDS. The chemical changes occurring by the modification of the conductive substrate were further characterized by FTIR and Raman spectroscopies.

53.2.1. SEM/EDS analysis

SEM analysis was conducted over the control (pFTO/hCCI), MPAP and NPAP films, in order to confirm the formation of a polymeric layer around the carbon ink substrate. The collected images are represented in **Figure 5.3**, along with the corresponding EDS spectra.

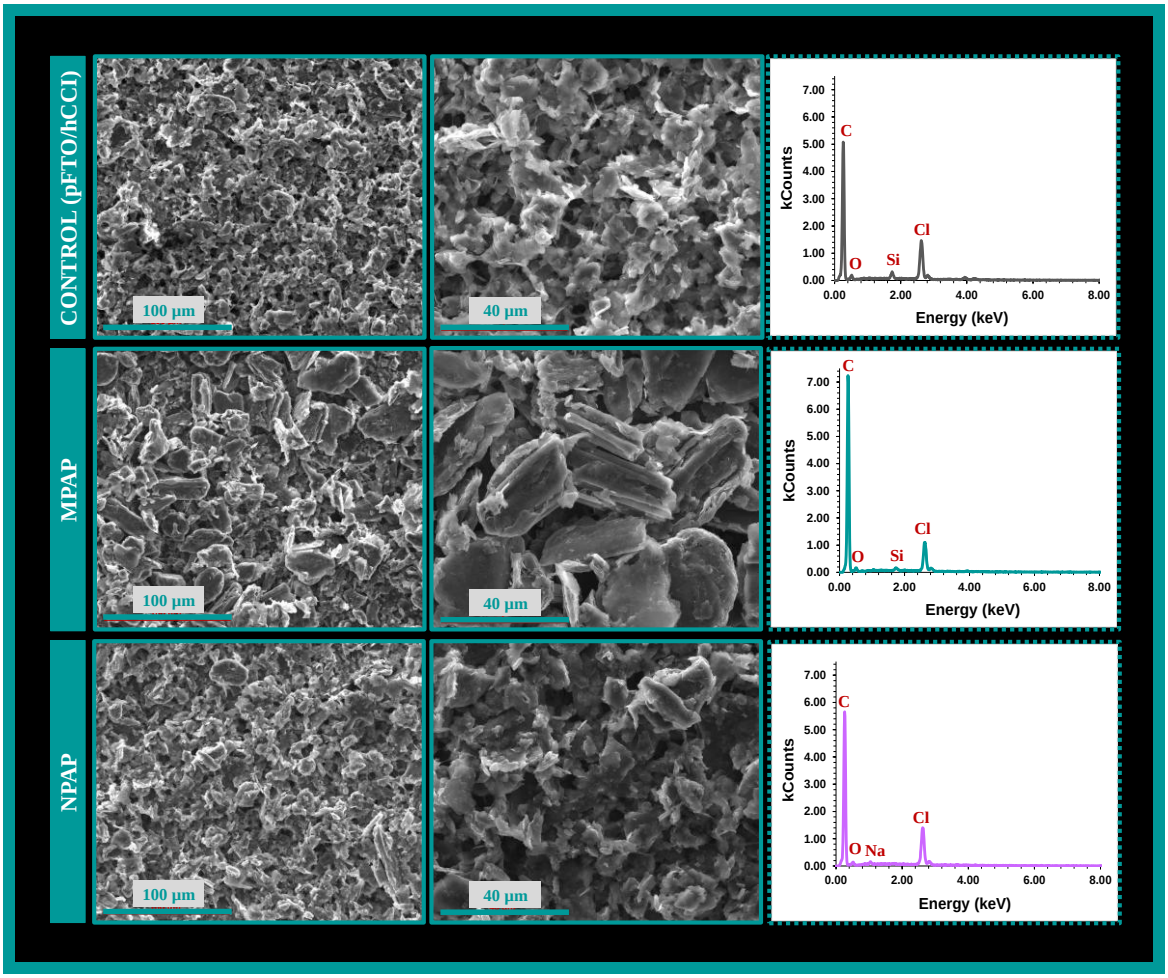

Figure 5.3. Scanning electron microscopy (left) and energy-dispersive X-ray spectroscopy (right) analysis of FTO glass modified with homemade conductive carbon ink (Control (pFTO/hCCI)); molecularly-imprinted material (MPAP); and non-imprinted material (NPAP).

The control substrate (pFTO/hCCI) evidenced the presence of carbon (C), oxygen (O), silicon (Si) and chlorine (Cl) in the EDS analysis. In addition, these elements were also found in MPAP and NPAP materials. In the EDS spectrum of NPAP, sodium (Na) was also present, possibly evidencing the entrapment of Na^+ species, coming from the PBS solution when the polymer was growing. In general, the non-imprinted materials are less porous than the corresponding imprinted materials, thereby justifying this observation.

In general, the SEM images showed morphological differences in all materials. The control materials displayed the smaller particles, related to the ink deposition. As expected, the formation of the PAP film on top and around these particles increased their size.

In general, the particles in the MPAP film were bigger than the ones in the NPAP film. This may be explained by the fact that the presence of CEA generates an increased porous polymeric structure and therefore of higher volume, a typical difference between imprinting and non-imprinted materials. Additional information from these images of little magnification is difficult to extract, but it is important to clarify that it would be unlikely to observe differences between MPAP and NPAP at higher magnification, as the target protein CEA is only few nanometers size.

5.3.2.2. FTIR analysis

FTIR spectra were recorded for FTO glass, pFTO/hCCI, MPAP and NPAP surfaces. The typical data obtained are shown in **Figure 5.4A**, and revealed the chemical differences within these materials.

In FTO glass, the IR peak at 645 cm^{-1} was assigned to Sn–O vibrations of the tin dioxide present in the glass substrate [44,45]. The C–C and C–O stretching vibrations coming from the PVC–COOH in the ink formulation were signalled by a small broad band centred at 1109 cm^{-1} [46]. Another intense peak at 1524 cm^{-1} could be assigned to vibrations of the ionized carboxylate groups within the PVC network. Moreover, the peaks at 1693 cm^{-1} are assigned to C=O from the hCCI layer (carboxylated PVC or oxidized carbon materials in the carbon ink). The bands located around 3500-3900 cm^{-1} could be attributed to the hydroxyl groups, mostly from the carbon support but also from the glass substrate [47].

The presence of the polymeric PAP films on the pFTO/hCCI supports (MPAP or NPAP) were evidenced by the weak bands at ~2900 cm^{-1}. These bands assigned the C=C stretching vibration characteristic from the phenyl ring, thereby confirming the presence of a polymeric layer [48]. The peaks ranging 1649-1743 cm^{-1} were assigned to the characteristic C=N stretching vibrations in the PAP film and the =C–C=O stretching vibrations in the specific 3-aminophenoxazone group [42]. The last one suggested the attack of nitrogen to the aromatic ring and subsequent formation of a quinonoid imine unit throughout the 3-AP polymerization [48,49]. In addition, the more intense broad band at 1083 cm^{-1} in the MPAP material revealed the presence of CEA inside the polymeric network. It was assigned to the C–O stretching vibrations, coming from the –COOH and –OH functions present in the several residues of the amino acids in CEA and in the glycosylated fraction of CEA. In addition, and as expected, the peaks signalling the Sn–O vibrations, at 647 (MPAP) and 650 (NPAP) cm^{-1}, were less intense than in the FTO glass, supporting the fact that this glass was modified with other compounds [45,50].

Overall, the combined information of the FTIR spectra confirmed the presence of the PAP film on the pFTO/hCCI support and the differences between the MPA and NPAP films.

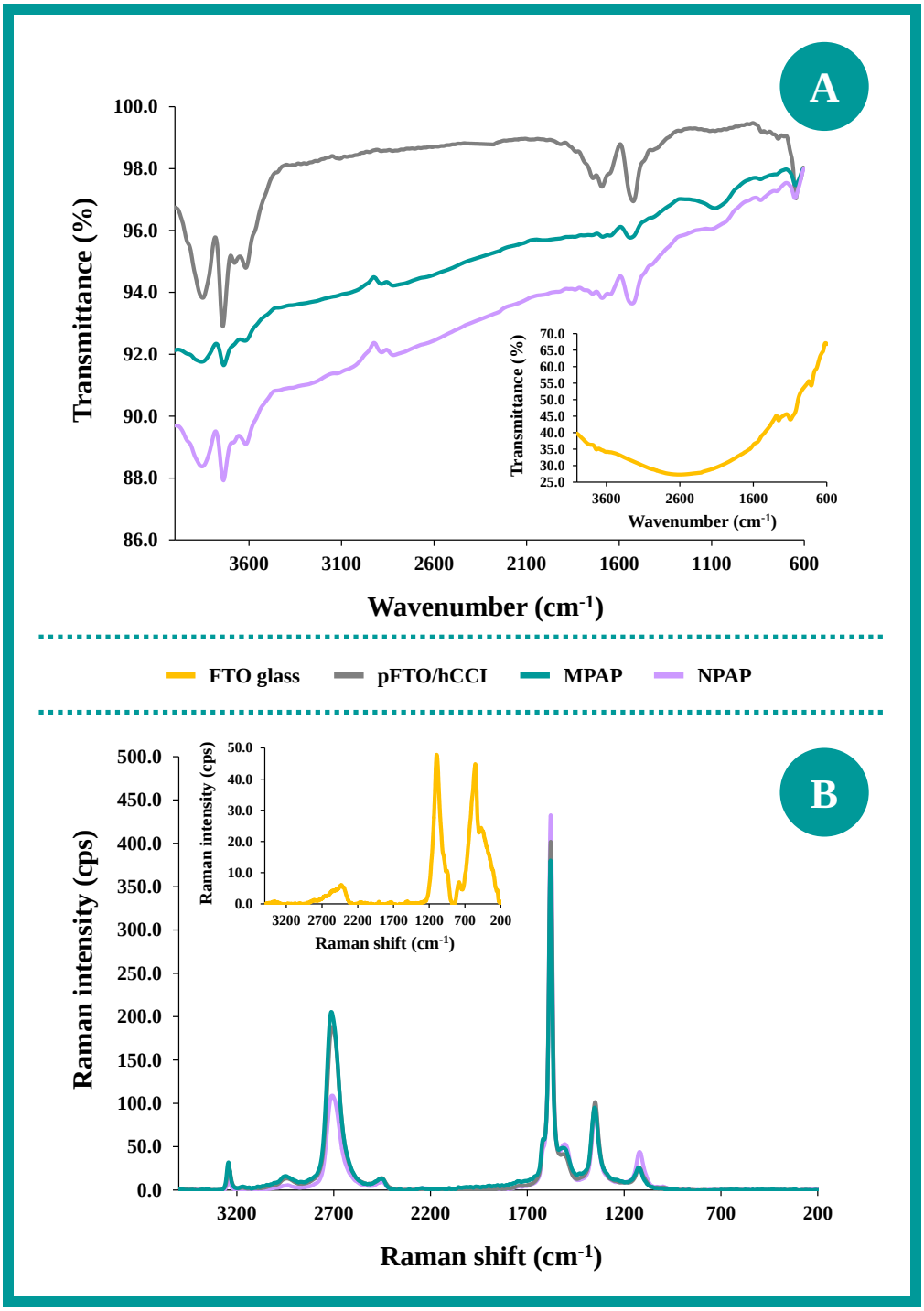

Figure 5.4. Characterization of the substrate (FTO glass), pFTO/hCCI, MPAP and NPAP by FTIR spectroscopy (A) and Raman spectroscopy (B).

5.3.2.3. Raman spectroscopy

The chemical modifications occurring on top of the conductive support (FTO glass) were also followed by Raman analysis (**Figure 5.4B**). According to the Raman spectrum of the control substrate, bands centred at 555 and 773 cm^{-1} were evidenced and suggest the presence of Sn–O and Sn–O–Sn stretching vibrations [51].

In general, all spectra presented a band around 1100 cm^{-1} that can be associated to the asymmetric Si–O–Si stretching vibration, the ionic character of the Si–O group and/or the C–F stretching vibration from the doping of tin oxide glass with fluorine [13]. Also, after the pre-treatment on top of the FTO surface with sol-gel chemistry, the Raman spectra, except the FTO glass spectrum, showed a distinct band near 2950 cm^{-1}, which could be attributed to the stretching vibration of C–H provided from APTES [13,33]. The Raman intensity of this band increased with the assembly of MPAP on the FTO surface covered with hCCI, which could be explained by the amino acids in the CEA protein [40]. Meanwhile, the NPAP Raman spectrum showed the decrease of the intensity comparing to the MPAP.

The Raman spectra of pFTO/hCCI showed the typical G, D and 2D bands, characteristic from the hybridization of the carbon atoms as well as the electronic and geometrical carbon arrangement presented by the hCCI composition [52]. Therefore, the fingerprints of carbon allotropes are mostly evidenced by D, G, and 2D bands around 1350 cm^{-1}, 1580 cm^{-1} and 2710 cm^{-1}, respectively [53]. The G band arises near to 1580 cm^{-1} due to the plane vibration of the sp^2 carbon systems and represents the C–C stretching of graphitic materials [52–54]. The D band appears at ~1350 cm^{-1}, assigning the presence of disorder of sp^2-hybridized carbon atoms, whereas the 2D band is originated from second order Raman scattering process and represented with almost the double frequency of D band [53,54]. This phenomenon may be explained by analyzing the I_D/I_G and I_{2D}/I_G intensities ratio between the disorder-induced D-band and, also, 2D band, with the G band. The I_D/I_G and I_{2D}/I_G ratios of the pFTO/hCCI were 0.253 and 0.468, respectively. After the polymerization without template (NPAP), the I_D/I_G ratio decreased to 0.208 and I_{2D}/I_G ratio to 0.252. Furthermore, after formation of MPAP the I_D/I_G ratio changed to 0.250 and I_{2D}/I_G ratio increased to 0.541, suggesting the modification on the pFTO/hCCI substrate. The I_D/I_G and I_{2D}/I_G ratios change was not the same in MPAP and in NPAP, which may be explained through the protein effect in the MPAP construction.

Overall, the Raman spectra confirmed the existence of chemical changes at each stage (FTO glass, pFTO/hCCI, MPAP and NPAP) on top of the substrate, certifying, thereby, the successful design of this biosensor for CEA detection.

5.3.3. Optimization of the MPAP and NPAP assembly

The assembly of the plastic antibody was optimized to ensure that an effective method to model and probe the interfacial properties of the surface modified electrode was being implemented [17]. The optimization was followed by Nyquist plots in EIS, where the R_{ct} occurring at the electrode surfaces corresponded to the diameter of the semicircle, when in contact with the electrolyte used in the study. The charge transfer behaviour was evaluated with an iodide redox couple, I^-/I_3^-.

5.3.3.1. Effect of different conditions for biosensor assembly

Several variables were tested herein, aiming to improve the CEA recognition by the imprinted layer. This study included the use of one (AP) or two (APBA) different monomers, and understanding their interaction with CEA. AP and APBA have been described in literature as electroactive monomers that can polymerize to form conducting and non-conducting polymers, depending on the experimental conditions [55]. All polymerizations were done in PBS, because this is close to the native environment of the protein and avoids its conformational change, which would be critical for protein recognition.

Herein, different combinations of AP and APBA were tested: (A) MIP: CEA/PAP and NIP: PAP; (B) MIP: CEA-APBA/PAP and NIP: APBA/PAP, and (C) MIP: CEA-APBA/PAPBA and NIP: APBA/PAPBA (**Figure 5.5**). Overall, the use of AP for protein imprinting has been proven successful, but additional discrimination between imprinted sites and surrounding environment is always favourable for the biosensor performance. Thus, APBA was included in the MIP process, to drive specific interactions between the polymeric network (thought the boronic group) and the glycosylated moieties in CEA. For this purpose, APBA was added first to the protein layer on the FTO glass, to form CEA/APBA interactions prior to polymerization. Then, the polymer network was generated by AP electropolymerization (CEA-APBA/PAP), thereby contributing to differentiate the rebinding site from the surrounding area. The tests with no APBA (CEA/PAP) and with only APBA (CEA-APBA/PAPBA) were meant to evaluate the effect of APBA only at the rebinding site.

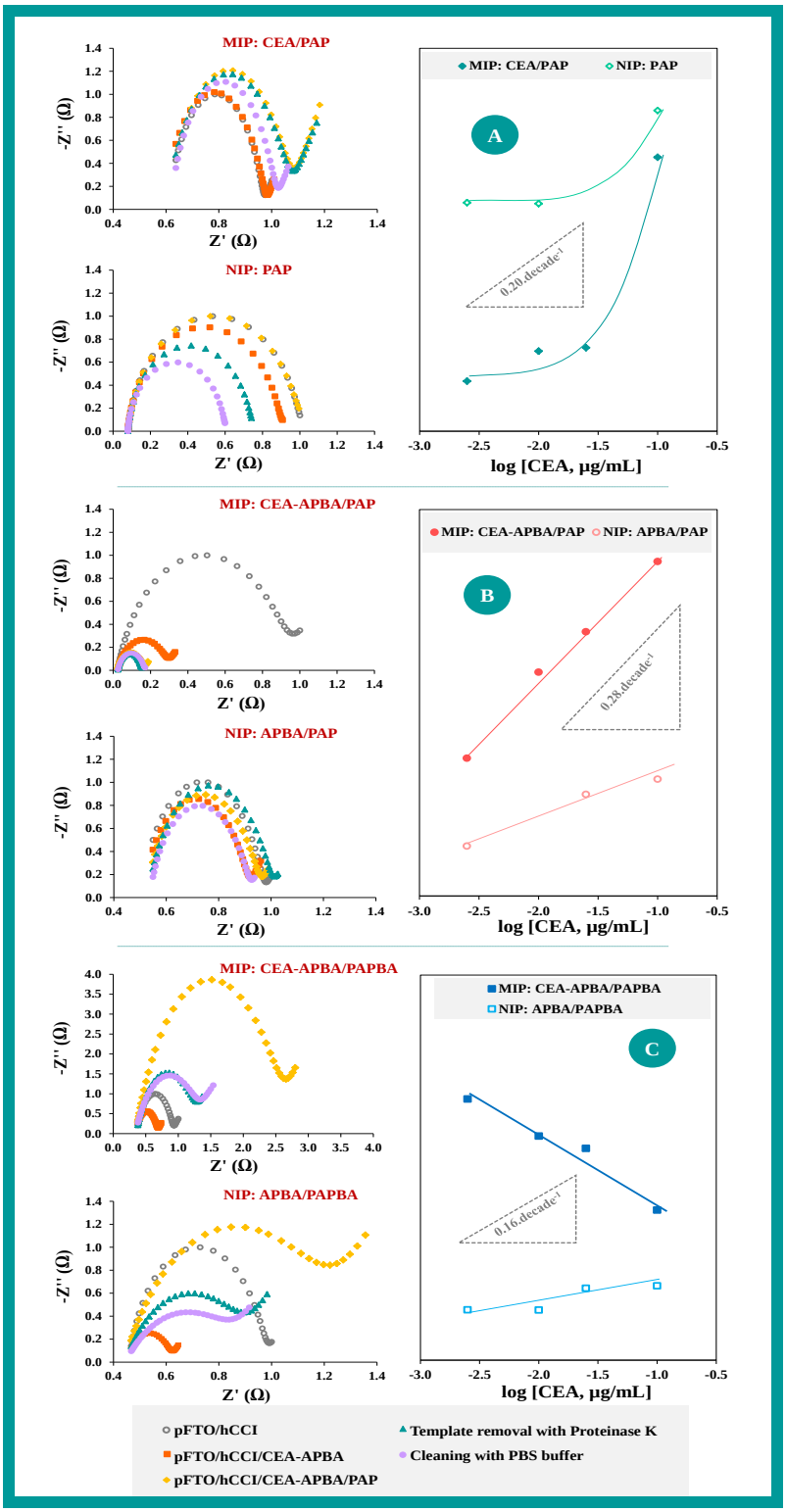

Figure 5.5. EIS measurements of the three approaches performed for MPAP and NPAP assembly for CEA detection: (A) MIP: CEA/PAP and NIP: PAP; (B) MIP: CEA-APBA/PAP and NIP: APBA/PAP, and (C) MIP: CEA-APBA/PAPBA and NIP: APBA/PAPBA, using an iodide redox probe.

Thus, the first approach consisted in understanding the performance of MPAP and NPAP materials without APBA (**Figure 5.5A**). According to the EIS assays, the incubation of the CEA protein before electropolymerization in the MPAP material caused a slight increase of the relative R_{ct} value (~1.08), while the incubation in buffer solution (PBS buffer, pH 7.4) in the control material (non-imprinted) promoted a decrease of the impedance signal (ΔR_{ct} ~ 0.88). This meant that the protein caused a more intense effect upon R_{ct}, opposed by the presence of PBS in solution. After electropolymerizing AP, the R_{ct} increased in both NPAP and MPAP sensors, thereby yielding a non-conductive polymer. In relative terms, the R_{ct} increase was more intense in the MPAP than in the NPAP, accounting the presence of the protein. The following step was the protein removal with proteinase K, which was performed in both NPAP and MPAP materials. Overall, a decrease in R_{ct} was expected, corresponding to the exit of protein (exclusive for MPAP films) and to the extraction of fragments of oligomeric structures easily removed (in both MPAP and NPAP films). While it was expected a significant decrease in R_{ct} after proteinase K action, the changes in resistance observed were much lower in the MPAP film (relative R_{ct} ~ 1.29) than in the NPAP film (~ 0.72) when compared to the previous polymeric layer. This behaviour could reveal the adsorption of proteinase K to the surface where CEA was present, which would increase the relative R_{ct}, in opposition to the decreased R_{ct} by removal of CEA. The subsequent electrochemical cleaning in PBS buffer yielded an additional resistance decrease, as expected Finally, the sensors were calibrated with CEA concentration levels ranging 2.5 to 100 ng/mL. In general, the MPAP sensor was much more sensitive than the NPAP one, both of these showing a proportional behaviour for CEA concentrations only above to 25 ng/mL (a concentration level above the cut-off level for CEA detection).

The parallel approach using APBA around the binding sites is shown in **Figure 5.5B**. In general, the Nyquist plots revealed a decrease of the relative resistance signal after the incubation with this mixing solution in the both sensors, which was more significant in the MPAP material (~ 70.9%) than in the control (~ 15.0%). In general, it was evident that the layer of APBA covering CEA decreased the charge transfer resistance of the iodide probe on this support. After electropolymerizing AP in the MPAP and NPAP sensors, a less resistive layer (relative R_{ct} ~ 0.15) and an increase of R_{ct} (relative R_{ct} ~ 0.92) were observed, respectively. This might be explained through the AP monomer charges that interacted with the mixing of CEA/APBA, hindering the polymer growth on the MPAP surface or yielding a conductive polymeric structure. After incubation with proteinase K, the control material yielded an additional barrier for the redox probe access while the MPAP material showed decreasing ΔR_{ct} values (~ 0.14). Yet, the electrochemical cleaning led these materials to an appositive behaviour, in which the control material decreased its resistance and the MPAP material increased.

The calibration curves of these sensors demonstrated a good linear response of the MPAP sensor in the CEA concentration range of 2.5 to 100 ng/mL, with a cationic slope of 0.28 per decade log[CEA, µg/mL] and a squared correlation coefficient >0.99. In contrast, the linear trend of the NPAP material was of low quality (squared correlation coefficient of ~0.97), with a slope of 0.10 per decade log[CEA, µg/mL].

The third approach (**Figure 5.5C**) consisted in applying the previous conditions for the electropolymerization of APBA, used as monomer. In general, the inclusion of CEA/APBA (in the MPAP) or PBS/APBA (in the NPAP), formed a less resistive layer, decreasing the relative R_{ct} to 0.61 or 0.33, respectively. The subsequent electropolymerization with APBA caused an increased significantly the relative R_{ct}, both in MPAP and NPAP materials. This effect was more intense in the MPAP film. After proteinase K incubation, and as expected, a less resistive layer was observed in both materials (relative R_{ct} of 1.60 and 0.88 in MPAP and NPAP, respectively). This decrease was more evident in the MPAP sensor, thereby accounting the exit of the protein, along with other oligomeric structures of the polymeric film. The subsequent electrochemical cleaning with PBS buffer did not change the overall behaviour of the MPAP film, but contributed to an additional decrease of the R_{ct} values in the NPAP (~ 0.82). The calibration curves obtained after this showed a random behaviour in the control material for the same CEA concentration range tested before and an anionic slope -0.16/decade log[CEA, µg/mL] with a squared correlation coefficient >0.96 in the MPAP.

Considering the previous information, it was interesting to observe that the presence of APBA was fundamental to generate a liner trend in the concentration range of CEA studied. In addition, the control and imprinted materials of polymeric APBA displayed opposite trends (negative and positive slopes) under the presence of CEA, highlighting that the imprinted rebinding positions were dominating the biosensor response. Yet, the more sensitive response was obtained by the mix solution of CEA/APBA and subsequent electropolymerization with AP monomer, for which it was selected for subsequent studies.

5.3.3.2. Effect of hCCI film thickness deposited on the FTO glass substrate

After identifying the best conditions for CEA rebinding, the effect of thickness of the hCCI films was tested. The obtained data is shown in **Figure 5.6A,B,C**. For this purpose, different angular velocities established by spin coating, at a constant time (60 s), were applied: (A) 500 rpm; (B) 750 rpm and (C) 1000 rpm.

This effect was evaluated by checking the response of the MPAP sensors under three CEA concentration levels ranging between 2.5 ng/mL and 833.0 ng/mL, and using an iodide redox probe (**Figure 5.6D**).

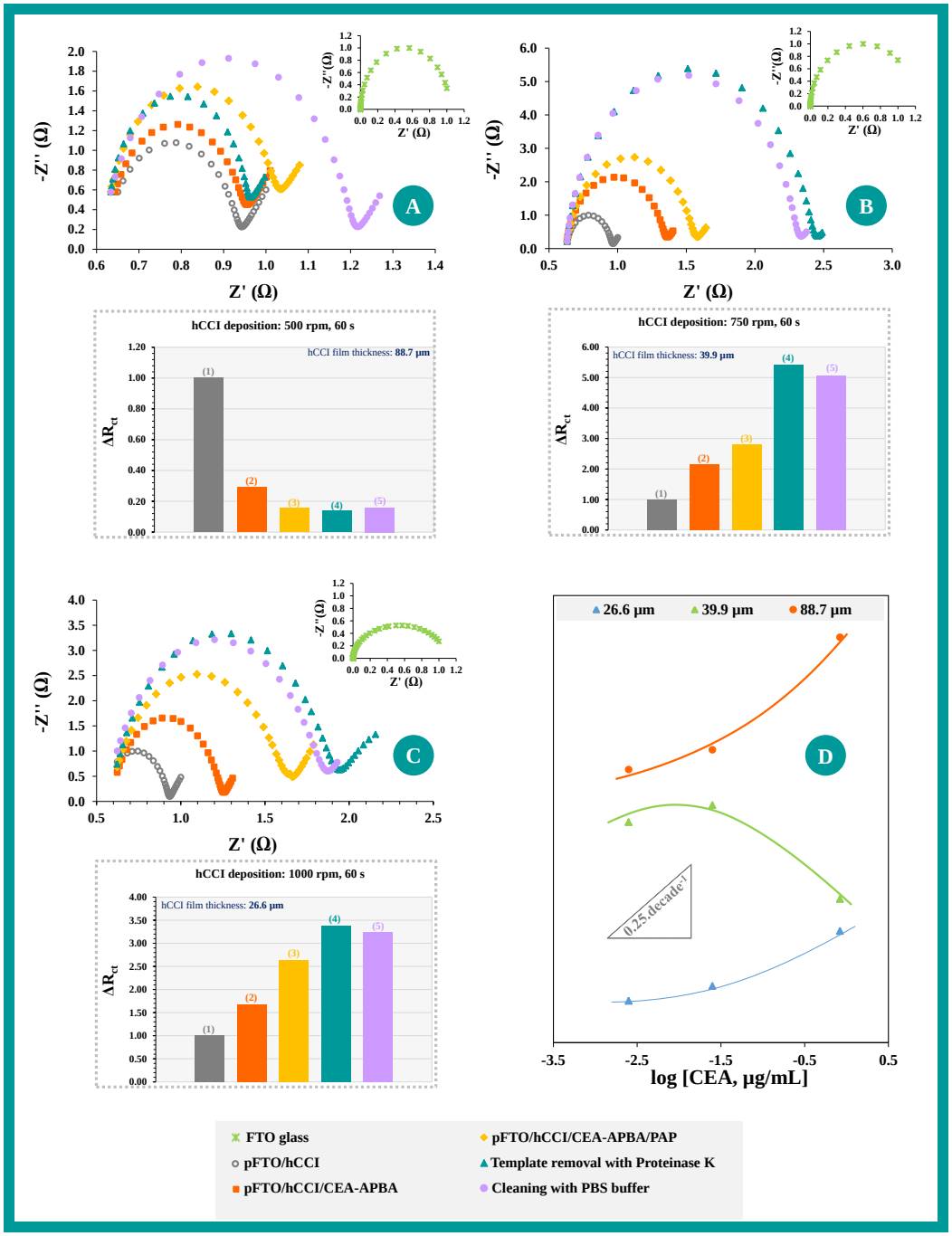

Figure 5.6. EIS data representative of the effect of hCCI films thickness deposited on the FTO glass substrates using different angular velocities by spin coating technique, at a constant time (60 s): (A) 500 rpm; (B) 750 rpm and (C) 1000 rpm; and analysing (D) the performance of the MPAP sensors under three CEA concentration levels ranging between 2.5 ng/mL and 833.0 ng/mL, in an iodide redox probe.

EIS assays (**Figure 5.6A,B,C**) demonstrated that the hCCI films deposited on top of an FTO glass substrate decreased its resistance to charge transfer. After the hCCI deposition, the films thickness was measured by an electronic micrometer, allowing to associate that 500 rpm casting corresponded to a 88.7 µm film, 750 rpm to 39.9 µm and 1000 rpm corresponds to 26.6 µm. In general, the substrates in which the ink was casted with higher angular velocity were thinner, yielding a lower impact of the film in terms of the overall resistance. The substrates with ~89 µm of hCCI films of thickness had the lower absolute R_{ct} values, when compared to the other films with ~40 µm and of ~27 µm thickness.

Among these materials, the biosensor with the thicker substrate was expected to have a completely different behaviour, because the subsequent formation of the polymeric film is electrically dependent. Indeed, the bar graphs shown in **Figure 5.6** revealed exactly this opposite trend. The modification of the substrate of higher absolute resistance (the thicker hCCI film) yielded decreasing the relative R_{ct} values after CEA/APBA incubation, electropolymerization and enzymatic protein removal, while the thinner substrates gave rise to a resistance increase along the same steps of modification. Accordingly, the final electrochemical cleaning of the surface yielded slight higher relative R_{ct} values for the thicker substrate and lower relative R_{ct} values for the thinner films.

Interestingly, the best calibration curve related to CEA binding in the range from 2.5 to 833 ng/mL was obtained for the MPAP sensor containing a thicker hCCI film (88.7 µm). The thinner material was less sensitive and the intermedium thickness was inconsistent with the others, questioning the feasibility of its generated data (**Figure 5.6D**). Overall, the sensor a carbon ink film of ~89 µm casted directly on the FTO glass showed a promising linear behaviour for CEA levels above 2.5 ng/mL, displaying a cationic slope of 0.25 per decade log[CEA, µg/mL] and a squared correlation coefficient >0.99.

5.3.3.3. Effect of the oxidation of the substrate coated with hCCI

An optimization of the pFTO/hCCI support was performed by electrochemical cleaning of the surface with 0.5 M H_2SO_4. This cleaning was made by CV scanning, ranging from -0.2 and +1.5 V, for 10 cycles, at a scan-rate of 50 mV/s. After this, a clean and reproducible surface was obtained, containing oxidized carbon functions at the substrate that would display a high electrostatic affinity for the amine groups in CEA [56].

Figure 5.7 shows the effect of the CV scanning in H_2SO_4 upon the electron transfer properties of the MPAP (**Figure 5.7A** and **Figure 5.7C**) and the control films (**Figure 5.7B** and **Figure 5.7D**), along with the corresponding calibration curves with CEA concentration levels, ranging 2.5 ng/mL to 1.5 µg/mL, using an iodide redox probe (**Figure 5.7E**). In general, a significant decrease of the pFTO/hCCI to pFTO/hCCI/CEA-APBA impedance signal was evidenced in the construction of both sensors, showing the formation of a less resistive layer in the higher decrease of ΔR_{ct} (ΔR_{ct} = $R_{ct(pFTO/hCCI/CEA\text{-}APBA)}/R_{ct(pFTO/hCCI)}$) value in the MPAP (~0.29) than in the control material (~0.85), as shown **Figure 5.7A** and **Figure 5.7B**. After the electropolymerization of AP, a decrease of 0.14 in ΔR_{ct} and a slight formation of a resistive layer (ΔR_{ct} = 0.92) was obtained in the MPAP and NPAP, respectively, which may can be explained through the charges of the AP monomer that was interacted with the CEA protein mixed with the monomer APBA, creating a blocking in the growth of the polymer in the MPAP, as show in **Figure 5.7A**. Conversely, an increment of in the ratio of R_{ct} value in the Nyquist plot of the NPAP was evidenced. Also, an additional barrier for the redox probe access of ~9% was produced on the modified electrode surface (pFTO/hCCI/PBS-APBA/PAP) of the control sensor, after the template removal step with proteinase K (**Figure 5.7B**). In case of the MPAP, a decrease of the ΔR_{ct} (~0.14) was obtained. However, electrochemical cleaning with PBS buffer (pH 7.4) by potential cycling from -0.5 and 1.0 V, for 15 cycles, at a scan-rate of 50 mV/s, revealed the formation of a resistive layer in MPAP (ΔR_{ct} ~ 0.16) and a decrease in the ratio of R_{ct} value in the control material (~ 0.19), which was explained by the influence of the charges on the surface of each sensor (**Figure 5.7A** and **Figure 5.7B**).

As previously mentioned in the section 4.3.3.1, an electrochemical cleaning with 0.5 M of H_2SO_4 was performed to remove possible unwanted-species that could be present on the hCCI surface. After this, the iodide redox probe evidenced an increased charged-transfer resistance. An additional electrical barrier was obtained after incubation of CEA-APBA in the plastic antibody (ΔR_{ct} ~ 0.69), while in the control material a slight decrease of ~5% in the ratio of R_{ct} value was obtained, as shown **Figure 5.7C** and **Figure 5.7D**, respectively. This phenomenon may be explained by the presence of CEA protein in the process of MPAP construction. Afterwards, a significant increase of relative R_{ct} values in the Nyquist plots of MPAP and NPAP was evidenced after the electropolymerization with AP monomer, being more evident in the NPAP (ΔR_{ct} ~ 2.30) than in the MPAP (ΔR_{ct} ~ 2.23), as expected, since the presence of CEA protein imprinted in the MPAP sensor surface may hinder polymer growth. The removal step, achieved by proteinase K and followed by the electrochemical cleaning with PBS buffer, promoted a higher decrease in the ratio of the resistive layer in MPAP (~ 12.5%) than in the control device (ΔR_{ct} ~ 1.4), which may correspond to the CEA protein removal and, also, to the removal of some proteinase K fragments that could be present in the substrate (**Figure 5.7C** and **Figure 5.7D**).

The calibration curves corresponding to the MPAP and NPAP materials, prepared with and without oxidation treatment, are shown in **Figure 5.7E**. These calibrations corresponded to consecutive incubations of increasing CEA concentrations, in the range of 2.5 ng/mL to 1.5 µg/mL, translated after each incubation by an iodide redox probe. Overall, the better linear response was obtained for the MPAP film including an oxidative treatment (ΔR_{ct} = 0.68×log[CEA, µg/mL] + 2.59), with a squared correlation coefficient >0.99. Without this acidic treatment, the MPAP presented a lower linear response than the previous one, with a slope 0.28 per decade log[CEA, µg/mL] and squared correlation coefficient >0.99. Similarly, but with a worst linear response than the plastic antibody, the NPAP material behaviour after oxidation treatment showed a low slope value (0.20 per decade log[CEA, µg/mL]) and a squared correlation coefficient >0.96. The control device without this acidic treatment demonstrated a slightly higher slope (0.23 per decade log[CEA, µg/mL]), but with a bad squared correlation coefficient, ~0.85. In addition, the greater difference in behaviour between imprinted and control material was obtained with surfaces containing an acidic treatment. Overall, the chemical modification of the sensing layer at the electrodes through the electrochemical cleaning with H_2SO_4 caused changes in the charge transfer of the electrode surfaces, thereby confirming the existence of such modifications in the MPAP and NPAP, while improving CEA binding response for imprinted surfaces.

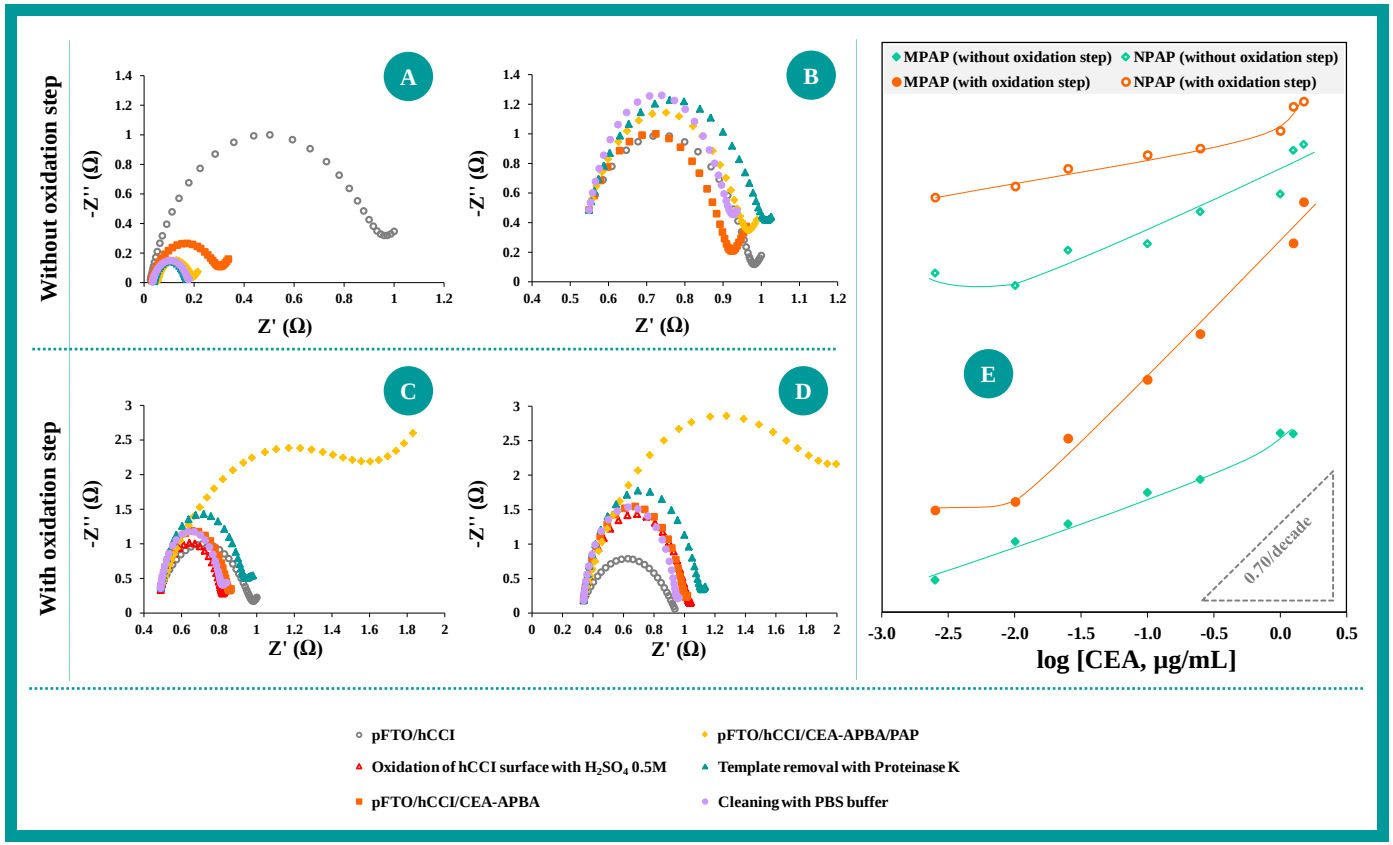

Figure 5.7. EIS spectra obtained through the effect/non-effect of the oxidation with H_2SO_4 0.5M of the substrate coated with hCCI in the assembly of the MPAP (A and C) and NPAP (B and D) materials and the corresponding CEA calibration curves (2.5 ng/mL to 1.5 µg/mL) using an iodide redox probe.

5.3.3.4. Analytical performance

The main analytical features of MPAP and NPAP electrodes were evaluated by means of calibrations plotting the charge-transfer resistance (R_{ct}, in EIS measurements) against logarithm CEA concentration, in the range of 2.5 ng/mL to 1.5 µg/mL, using an iodide redox probe, as shown in **Figure 5.8**.

The overall response showed that the MPAP biosensor responded well after 2.5 ng/mL CEA, being this concentration level included in the linear response range of the device. The linear response was observed up to 1.5 µg/mL, being express as $\log(\Delta R_{ct}) = 0.044 \times \log[\text{CEA, µg/mL}] + 1.111$, with a squared correlation coefficient >0.989 and LOD of 1.8 ng/mL. The average relative standard deviation of replicate measurements was below 5% (**Figure 5.8A**). In the control sensor (NPAP), the logarithm of R_{ct} values increased with the increasing of the logarithm of CEA concentration after 10.0 ng/mL. A cationic slope of 0.080 Ω/decade log[CEA, µg/mL] and a squared correlation coefficient >0.972 was obtained, coupled to an LOD of 7.6 ng/mL and a relative standard deviation of 18% (**Figure 5.8B**).

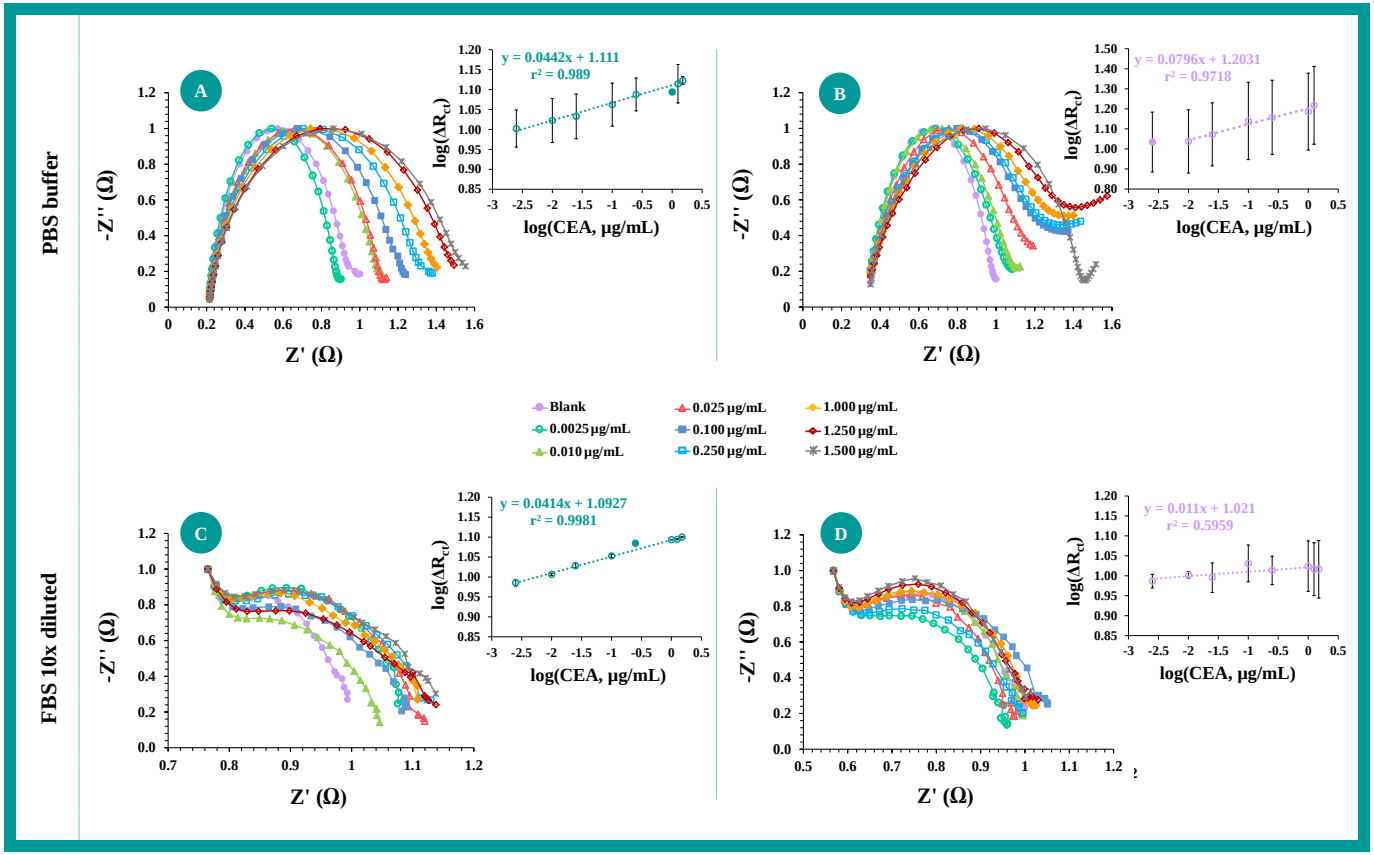

Figure 5.8. EIS measurements of MPAP (A and C) and NPAP (B and D) based hCCI-FTO glass biosensor and the corresponding calibrations with different concentrations of CEA protein in PBS buffer (A and B) and in spiked FBS samples (C and D).

Overall, EIS data of MPAP sensors displayed a good linear response to the increase CEA concentrations, with a lower LOD (1.8 ng/mL) and a stable response, when compared to NPAP EIS assays (LOD = 7.6 ng/mL), showing thus that the imprinted sites of CEA governed the electrical response in the MPAP electrode. Moreover, the NPAP surface displayed unacceptable linearity features and precision data.

5.3.4. Binding isotherm

The binding equilibrium studies were based on comparative EIS studies of MPAP, whose binding cavities obtained should correspond to the morphology and functionality of the CEA protein, and NPAP materials, as shown **Figure 5.9**. In order to assess the performance of the template rebinding of the sensor, the maximum response ($\Delta R_{ct}^{máx}$) and the dissociation constant (K_D) were fitted to the Langmuir equation (represented in **Equation 5.1**). These parameters reflected the differences of CEA amount bounded to the sensor surface ($\Delta R_{ct}^{máx}$) and the CEA concentration necessary to reach half of the maximum response (K_D), thereby indicating the effective amount of CEA bound to the film and, also, its affinity. A larger binding affinity of CEA bound to the film is typically shown by a low K_D value, once the $\Delta R_{ct}^{máx}$ of the sensor occurred more rapidly, while a high K_D indicated the non-efficient binding of protein to the sensor, as the ΔRctmáx is reached only for higher CEA concentrations.

Overall, the MPAP showed better kinetic features in terms of $\Delta R_{ct}^{máx}$ and K_D values, comparing with the control material. The value of $\Delta R_{ct}^{máx}$ after each addition of CEA concentration was 188.3 Ω for MPAP and 53.3 Ω for NPAP, thereby corresponding to a 3.5× increase in signal density for the MPAP material when comparing to the NPAP surface (**Figure 5.9A**). Likewise, the K_D for MPAP and NPAP was evaluated, showing a lower value in the MPAP (K_D = 0.08 µg/mL) than in NPAP material (K_D = 0.10 µg/mL); the NPAP layer presented a K_D value ~1.3× higher. Thus, the smaller K_D value of the MPAP may represent the its good binding affinity for CEA protein.

In the **Figure 5.9B**, the subtracted signal density for specific binding $\Delta R_{ct\ (SB)}$ ($\Delta R_{ct\ (SB)} = \Delta R_{ct\ (MPAP)} - \Delta R_{ct\ (NPAP)}$) is represented, where a hyperbolic response of the amount of specific binding in the MPAP without non-specific binding effect was obtained. Therefore, a dissociation constant for specific binding ($K_{D(SB)}$) of 0.02 µg/mL corresponding to a maximum specific binding ($\Delta R_{ct\ (SB)}$) of 135.0 Ω is shown by the sensing material, MPAP.

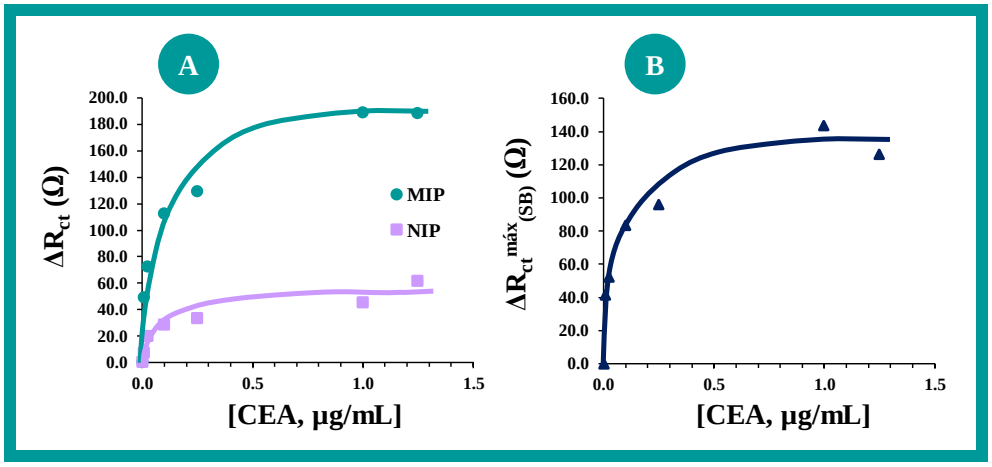

Figure 5.9. Graphical representation of the Langmuir isotherms: (A) equilibrium binding isotherm plot, $R_{ct}^{máx}$ and K_D values, for MPAP and NPAP materials; (B) specific binding isotherm representation of MPAP when the NPAP signal density is subtracted.

5.3.5. Application and reproducibility of the devices

Considering that the targeted biosensor meant to operate well in serum, it was important to check the performance of the device under close-to-real conditions, as demonstrated by the previously described sensors. For this purpose, the PBS buffer solution was replaced by a diluted FBS solution in order to simulate human's serum, once it displays great similarity. In general, this study also indicated the selectivity behaviour of the biosensor.

The calibrations of the MPAP and NPAP sensors were made in spiked FBS samples diluted 10×, using the same procedure as in section 4.3.3.3. The typical data is shown in **Figure 5.8C** and **Figure 5.8D**. The calibration curve of the MPAP sensor showed a linear dependency on log[CEA], from 2.5 ng/mL to 1.5 µg/mL, with a slope of 0.041 Ω/decade log[CEA, µg/mL], a squared correlation coefficient >0.998, and a LOD of 1.1 ng/mL. Although the sensitivity was lower than in PBS, the repeatability of this response in FBS was much better, with an average relative standard deviation below 0.3% (**Figure 5.8C**). The control material NPAP (**Figure 5.8D**) showed a non-linear response with the increase of CEA concentration in the same concentration range, corresponding to a cationic slope of 0.011 Ω/decade log[CEA, µg/mL], a squared correlation coefficient >0.596, a LOD of 1.7 ng/mL, and a relative standard deviation of ~ 4%.

Overall, the LOD value was slightly higher than when detecting CEA in pure PBS buffer pH 7.4, which may be explained by the presence of some ions in FBS composition that can have a little impact on the sensor performance through the electrostatic interaction with CEA protein or with the protein rebinding site. The repeatability of the results accounted relative errors ranging from 0.1 to 0.8%, with an average recovery factor of 90% and a corresponding average relative standard deviation of replicate measurements below 7%.

5.4. Conclusions and future perspectives

A novel plastic antibody for CEA was developed by molecularly-imprinting technique on a carbon ink film linked by sol-gel chemistry to a conductive FTO glass support, providing a suitable and promising tool for clinical applications. In general, the imprinted device described herein offered simplicity in designing, low-cost and a quick manufacturing, comparing to the conventional or concurrent methodologies described in the literature. The presence of an acidic pre-treatment on the surface was found essential to yield a stable and sensitive surface, with improved properties compared to the control materials. The MPAP device is a promising tool to monitor CEA in POC applications, presenting a good sensitivity and selectivity, once it can detect CEA concentration levels within the normal physiological values.

As future perspectives, this approach may be combines with DSSCs, in order to lead the production of self-sustained biosensors, once these cells are able to generate electrical current.

References

[1] Y. Wang, Z. Zhang, V. Jain, J. Yi, S. Mueller, J. Sokolov, Z. Liu, K. Levon, B. Rigas, M.H. Rafailovich, ‘Potentiometric sensors based on surface molecular imprinting: Detection of cancer biomarkers and viruses’, *Sensors and Actuators B: Chemical*, vol. 146, pp. 381–387, 2010.

[2] Y. Yin, Y. Cao, Y. Xu, G. Li, ‘Colorimetric immunoassay for detection of tumor markers’, *International Journal of Molecular Sciences*, vol. 11, pp. 5077–5094, 2010.

[3] G.M. Cooper, R.E. Hausman, ‘The Cell: A molecular approach’, fourth edition, 2007.

[4] S. Ramos, ‘Cancer chemoprevention and chemotherapy: Dietary polyphenols and signalling pathways’, *Molecular Nutrition and Food Research*, vol. 52, pp. 507–526, 2008.

[5] R. Mayeux, 'Biomarkers: potential uses and limitations', *NeuroRx: The Journal of the American Society for Experimental NeuroTherapeutics*, vol. 1, pp. 182–188, 2004.

[6] I. Ewing, J.J. Hurley, E. Josephides, A. Millar, 'The molecular genetics of colorectal cancer', *Frontline Gastroenterology*, vol. 5, pp. 26–30, 2014.

[7] J. Ferlay, I. Soerjomataram, R. Dikshit, S. Eser, C. Mathers, M. Rebelo, D.M. Parkin, D. Forman, F. Bray, 'Cancer incidence and mortality worldwide: Sources, methods and major patterns in GLOBOCAN 2012', *International Journal of Cancer*, vol. 136, pp. E359–E386, 2015.

[8] V. I., T. D., B. N.L., 'Cancer prevention: State of the art and future prospects', *Journal of Preventive Medicine and Hygiene*, vol. 56, pp. 21–27, 2015.

[9] I. Ghosh, D. Bhattacharjee, A.K. Das, G. Chakrabarti, A. Dasgupta, S.K. Dey, 'Diagnostic role of tumour markers CEA, CA15-3, CA19-9 and CA125 in lung cancer', *Indian Journal of Clinical Biochemistry*, vol. 28, pp. 24–29, 2013.

[10] M. Hall, S. Bryant, M. Jackson, J.T. Johnson, H. Schultze, W. Cooksey, S.D. Manceva, R. Crowell, S. Johnson, T. Sims-Davis, K.L. Beason, S.R. Clinton, D. Fortenberry, C. Bright, H. Hua, J. Ying, P. Sykes, 'A comparison of CA242 with twelve other tumor antigens for the serodiagnosis of pancreatic, gastric, and other gastrointestinal cancers', *Chemist*, vol. 86, pp. 1–16, 2013.

[11] M.A.A. Hamed, S.A.A. Ahmed, H.M. Khaled, 'Efficiency of diagnostic biomarkers among colonic schistosomiasis egyptian patients', *Memorias Do Instituto Oswaldo Cruz*, vol. 106, pp. 322–329, 2011.

[12] Y. Li, W.K. Yang, M.Q. Fan, A. Liu, 'A sensitive label-free amperometric CEA immunosensor based on graphene-nafion nanocomposite film as an enhanced sensing platform', *Analytical Sciences: The International Journal of the Japan Society for Analytical Chemistry*, vol. 27, no. 727, 2011.

[13] L.A.A.N.A. Truta, M.G.F. Sales, 'Sol-Gel Chemistry in Biosensing Devices of Electrical Transduction: Application to CEA Cancer Biomarker', *Current Topics in Medicinal Chemistry*, vol. 15, pp. 256–261, 2015.

[14] B.J. Casey, P. Kofinas, 'Selective binding of carcinoembryonic antigen using imprinted polymeric hydrogels', *Journal of Biomedical Materials Research - Part A*, vol. 87A, no. 359, 2008.

[15] Y. Fu, R. Yuan, Y. Chai, Y. Zhang, Y. Peng, 'Electrochemical immunoanalysis for carcinoembryonic antigen based on multilayer architectures of gold nanoparticles and polycation biomimetic interface on glassy carbon electrode', *Electroanalysis*, vol. 18, pp. 2451–2457, 2006.

[16] S. Hammarström, 'The carcinoembryonic antigen (CEA) family: structures, suggested functions and expression in normal and malignant tissues', *Seminars in Cancer Biology*, vol. 9, pp. 67–81, 1999.

[17] J.C. Kemmegne-Mbouguen, E. Ngameni, P.G. Baker, T.T. Waryo, B. Kgarebe, E.I. Iwuoha, 'Carcinoembryonic antigen immunosensor developed with organoclay nanogold composite film', *International Journal of Electrochemical Science*, vol. 9, pp. 478–492, 2014.

[18] M. Liu, C. Jia, Q. Jin, X. Lou, S. Yao, J. Xiang, J. Zhao, 'Novel colorimetric enzyme immunoassay for the detection of carcinoembryonic antigen', *Talanta*, vol. 81, pp. 1625–1629, 2010.

[19] P. Lv, L. Min, R. Yuan, Y. Chai, S. Chen, 'A novel immunosensor for carcinoembryonic antigen based on poly(diallyldimethylammonium chloride) protected prussian blue nanoparticles and double-layer nanometer-sized gold particles', *Microchimica Acta*, vol. 171, pp. 297–304, 2010.

[20] X. Miao, S. Zou, H. Zhang, L. Ling, 'Highly sensitive carcinoembryonic antigen detection using Ag@Au core-shell nanoparticles and dynamic light scattering', *Sensors and Actuators, B: Chemical*, vol. 191, pp. 396–400, 2014.

[21] W. Shi, Z. Ma, 'A novel label-free amperometric immunosensor for carcinoembryonic antigen based on redox membrane', *Biosensors and Bioelectronics*, vol. 26, pp. 3068–3071, 2011.

[22] F. Tan, F. Yan, H. Ju, 'A designer ormosil gel for preparation of sensitive immunosensor for carcinoembryonic antigen based on simple direct electron transfer', *Electrochemistry Communications*, vol. 8, pp. 1835–1839, 2006.

[23] D. Das, D.M. Kim, D.S. Park, Y.B. Shim, 'A glucose sensor based on an aminophenyl boronic acid bonded conducting polymer', *Electroanalysis*, vol. 23, pp. 2036–2041, 2011.

[24] W. Wang, G. Xu, X.T. Cui, G. Sheng, X. Luo, 'Enhanced catalytic and dopamine sensing properties of electrochemically reduced conducting polymer nanocomposite doped with pure graphene oxide', *Biosensors and Bioelectronics*, vol. 58, pp. 153–156, 2014.

[25] I. Zaccari, A.G. Davies, C. Walti, S.X. Laurenson, 'Label-free electrochemical biosensors for clinical diagnostic', in *7th Cairo International Biomedical Engineering Conference (CIBEC)*, pp. 15–18, 2014.

[26] D. Grieshaber, R. Mackenzie, J. Vörös, E. Reimhult, 'Electrochemical Biosensors -Sensor Principles and Architectures', *Sensors*, vol. 8, pp. 1400–1458, 2008.

[27] E. Burcu Bahadır, M. Kemal Sezgintürk, 'Applications of electrochemical immunosensors for early clinical diagnostics', *Talanta*, vol. 132, pp. 162–174, 2015.

[28] T. Pasinszki, M. Krebsz, T.T. Tung, D. Losic, 'Carbon Nanomaterial Based Biosensors for Non-Invasive Detection of Cancer and Disease Biomarkers for Clinical Diagnosis', *Sensors*, vol. 17, no. 1919, 2017.

[29] J.L. Liu, D. Raghu, G.P. Anderson, E.R. Goldman, J.A. Christodoulides, M.P. Raphael, 'Improving biosensing activity to carcinoembryonic antigen with orientated single domain antibodies', *Heliyon*, vol. 3, 2017.

[30] L. Xu, W. Zhang, L. Shang, R. Ma, L. Jia, W. Jia, H. Wang, L. Niu, 'Perylenetetracarboxylic acid and carbon quantum dots assembled synergistic electrochemiluminescence nanomaterial for ultra-sensitive carcinoembryonic antigen detection', *Biosensors and Bioelectronics*, vol. 103, pp. 6–11, 2018.

[31] Z. Qin, W. Xu, S. Chen, J. Chen, J.F. Qiu, C.R. Li, 'Electrochemical immunoassay for the carcinoembryonic antigen based on the use of a glassy carbon electrode modified with an octahedral Cu_2O-gold nanocomposite and staphylococcal protein for signal amplification', *Microchimica Acta*, vol. 185, no. 266, 2018.

[32] X. Gu, Z. She, T. Ma, S. Tian, H.-B. Kraatz, 'Electrochemical detection of carcinoembryonic antigen', *Biosensors and Bioelectronics*, vol. 102, pp. 610–616, 2018.

[33] L.A.A.N.A. Truta, F.T.C. Moreira, M.G.F. Sales, 'A dye-sensitized solar cell acting as the electrical reading box of an immunosensor: Application to CEA determination', *Biosensors and Bioelectronics*, vol. 107, pp. 94–102, 2018.

[34] N.M. Danesh, R. Yazdian-Robati, M. Ramezani, M. Alibolandi, K. Abnous, S.M. Taghdisi, 'A label-free aptasensor for carcinoembryonic antigen detection using three-way junction structure and ATMND as a fluorescent probe', *Sensors and Actuators B: Chemical*, vol. 256, pp. 408–412, 2018.

[35] T.S. Mohammad, D.N. Mohammad, R. Mohammad, E.A. Sarreshtehdar, A. Khalil, 'A Novel Electrochemical Aptasensor for Carcinoembryonic Antigen Detection Based on Target-induced Bridge Assembly', *Electroanalysis*, 2018.

[36] J.T. Cao, Y.L. Wang, J.B. Wang, Q.M. Zhou, S.H. Ma, Y.M. Liu, 'An electrochemiluminescence ratiometric self-calibrated biosensor for carcinoembryonic antigen detection', *Journal of Electroanalytical Chemistry*, vol. 814, pp. 111–117, 2018.

[37] F.T.C. Moreira, M.J.M.S. Ferreira, J.R.T. Puga, M.G.F. Sales, 'Screen-printed electrode produced by printed-circuit board technology. Application to cancer biomarker detection by means of plastic antibody as sensing material', *Sensors and Actuators B: Chemical*, vol. 223, pp. 927–935, 2016.

[38] A. Sarkar, T. Daniels-Race, 'Electrophoretic Deposition of Carbon Nanotubes on 3-Amino-Propyl-Triethoxysilane (APTES) Surface Functionalized Silicon Substrates', *Nanomaterials*, vol. 3, pp. 272–288, 2013.

[39] A.P.M. Tavares, N.S. Ferreira, L.A.A.N.A. Truta, M.G.F. Sales, 'Conductive Paper with Antibody-Like Film for Electrical Readings of Biomolecules', *Scientific Reports*, vol. 6, no. 26132, 2016.

[40] F.T.C. Moreira, S. Sharma, R.A.F. Dutra, J.P.C. Noronha, A.E.G. Cass, M.G.F. Sales, 'Protein-responsive polymers for point-of-care detection of cardiac biomarker', *Sensors and Actuators B: Chemical*, vol. 196, pp. 123–132, 2014.

[41] R. Tucceri, P. Arnal, A. Scian, 'Electrosynthesis and Spectroscopic Characterization of Poly(*o*-Aminophenol) Film Electrodes', *ISRN Polymer Science*, vol. 2012, pp. 1–26, 2012.

[42] M.A.R. Khan, F.T.C. Moreira, J. Riu, M.G.F. Sales, 'Plastic antibody for the electrochemical detection of bacterial surface proteins', *Sensors and Actuators B: Chemical*, vol. 233, pp. 697–704, 2016.

[43] M. Kats, M.E.S. Germain, 'Spectroscopic determination of protein concentrations from proteinase K digests', *Analytical Biochemistry*, vol. 307, pp. 212–218, 2002.

[44] A.N. Banerjee, S. Kundoo, P. Saha, K.K. Chattopadhyay, 'Synthesis and Characterization of Nano-Crystalline Fluorine-Doped Tin Oxide Thin Films by Sol-Gel Method', *Journal of Sol-Gel Science and Technology*, vol. 28, pp. 105–110, 2003.

[45] S. Chaisitsak, 'Nanocrystalline SnO_2:F thin films for liquid petroleum gas sensors', *Sensors*, vol. 11, pp. 7127–7140, 2011.

[46] M. Singh, S.K. Mahto, S. Das, A. Ranjan, S.K. Singh, P. Roy, N. Misra, 'Chemical modification of poly(vinyl chloride) for Blood and Cellular Biocompatibility', *RSC Adv.*, vol. 5, pp. 45231–45238, 2015.

[47] S.M. Anisuzzaman, C.G. Joseph, W.M.S.B.W. Daud, D. Krishnaiah, H.S. Yee, 'Preparation and characterization of activated carbon from Typha orientalis leaves', *International Journal of Industrial Chemistry*, vol. 6, pp. 9–21, 2015.

[48] G. Thenmozhi, P. Arockiasamy, R.J. Santhi, 'Isomers of Poly Aminophenol: Chemical Synthesis, Characterization, and Its Corrosion Protection Aspect on Mild Steel in 1M HCl', *International Journal of Electrochemistry*, 2014.

[49] D.L. Franco, A.S. Afonso, S.N. Vieira, L.F. Ferreira, R.A. Gonçalves, A.G. Brito-Madurro, J.M. Madurro, 'Electropolymerization of 3-aminophenol on carbon graphite surface: Electric and morphologic properties', *Materials Chemistry and Physics*, vol. 107, pp. 404–409, 2008.

[50] R. Scipioni, D. Gazzoli, F. Teocoli, O. Palumbo, A. Paolone, N. Ibris, S. Brutti, M.A. Navarra, 'Preparation and characterization of nanocomposite polymer membranes containing functionalized SnO_2 additives', *Membranes*, vol. 4, pp. 123–142, 2014.

[51] V. Kumar, A. Govind, R. Nagarajan, 'Optical and photocatalytic properties of heavily F-doped SnO_2 nanocrystals by a novel single-source precursor approach', *Inorganic Chemistry*, vol. 50, pp. 5637–5645, 2011.

[52] L.A.A.N.A. Truta, N.S. Ferreira, M.G.F. Sales, 'Graphene-based biomimetic materials targeting urine metabolite as potential cancer biomarker: Application over different conductive materials for potentiometric transduction', *Electrochimica Acta*, vol. 150, pp. 99–107, 2014.

[53] V. Singh, D. Joung, L. Zhai, S. Das, S.I. Khondaker, S. Seal, 'Graphene based materials: Past, present and future', *Progress in Materials Science*, vol. 56, pp. 1178–1271, 2011.

[54] G. V Martins, A.P.M. Tavares, E. Fortunato, M.G.F. Sales, 'Paper-Based Sensing Device for Electrochemical Detection of Oxidative Stress Biomarker (8-OHdG) in Point-of-Care', *Scientific Reports*, pp. 1–10, 2017.

[55] P.S. Sharma, A. Pietrzyk-Le, F. D'Souza, W. Kutner, 'Electrochemically synthesized polymers in molecular imprinting for chemical sensing', *Analytical and Bioanalytical Chemistry*, vol. 402, pp. 3177–3204, 2012.

[56] S. Teixeira, R.S. Conlan, O.J. Guy, M.G.F. Sales, 'Label-free human chorionic gonadotropin detection at picogram levels using oriented antibodies bound to graphene screen-printed electrodes', *Journal of Materials Chemistry B*, vol. 2, pp. 1852–1865, 2014.

CHAPTER 6

A dye-sensitized solar cell acting as the electrical reading box of an immunosensor

This chapter is based on the paper *A dye-sensitized solar cell acting as the electrical reading box of an immunosensor: Application to CEA determination* published to the journal Biosensors and Bioelectronics, 107:94-102, 2018. The integration of an immunosensor for CEA detection inside a photovoltaic cell that acts as electrical reading box is herein described.

6.1. Introduction

Biosensors are analytical devices that convert molecular recognition of a specific analyte into a measurable signal via a transducer, allowing quick responses, low cost and little requirements [1-3]. Among the different approaches in clinical analysis, electrochemical immunoassays hold a great impact in the literature [3]. Immunoassays involve antigen/antibody reactions, inspired in the immune response [3,4]. The use of antibody ensures appropriate selectivity towards a target compound, even when this compound is in very low concentrations. Electrochemical immunosensors are of special interest herein, due to their simplicity, easy miniaturization, specificity, selectivity, high sensitivity and rapid analysis [5]. Although using an enzymatic reaction, glucose meters are a public icon of electrochemical biosensors. In general, the combination of antibodies and electrochemical biosensors has been proven successful in many applications [3].

This works emerges a novel biosensor technology that consists on integrating an electrochemical immunosensor inside a photovoltaic (PV) cell. PV cells generate current from light with reasonable efficiency [6] and may therefore lead electrochemical-based biosensors towards an electrical-independent approach. The first step in this direction consists in evaluating the impact of an immunosensor on the PV and understanding if the electrical performance of such new system depends on the concentration of a given target compound. To pursue this target, two key elements are identified next: the type of the PV and the target compound to be tested in this proof-of-concept design.

There are different types of PV cells. DSSCs have attracted much attention due to their low cost, easy manufacture and high energy conversion efficiency [7,8]. DSSCs contain (a) a photoanode electrode, (b) a redox system electrolyte and (c) a cathode or CE [9,10]. Merging a biosensor and a DSSC could be as easy as using one of these two electrodes (photoanode or cathode) as the biosensor, provided that the biosensor itself would be constructed on a conductive glass support that could be interfaced within the final DSSC. Eventually, one could try to replace any of these two electrodes. From a practical perspective, the photoanode is more sensitive to water-content components, hindering its interaction with water-based samples. Replacing the CE would be simpler, if the sensing element displayed electrocatalytic properties towards the redox probe.

In alternative to the typical platinum-based CEs [10], carbon-based materials may be employed. These include graphite [11], graphene [12], carbon nanotubes [11]; conducting polymers [11,13]; or conductive inks [14,15] containing metal nanoparticles.

The most widely used materials are silver nanoparticles, due to their simple preparation, high-yielding, low viscosity and thus easy to flow under the conductive substrate surface, low resistivity and good electrical properties [15,16]. Thus, the CE is prepared herein with a conducting carbon-silver ink, which may be interfaced with antibodies.

As proof-of-concept, CEA was selected herein as target compound, once it is an important tumour marker employed in clinical diagnosis of colorectal cancer [17]. Overall, all these methods would benefit from the new approach proposed herein, which is simple in terms of device set-up and expects to yield suitable analytical features, while targeting electrical independency in a near future [4,18-25].

Therefore, this work proposes (1) a different and simple immunosensor design for CEA, employing simple chemistry strategies that allow suitable orientation of the Ab-CEA on top of the modified conductive support; and (2) merging this biosensor on a DSSC. The electrode design is optimized and the biosensor is tested in both formats: conventional modified glass and working as the CE of the DSSC. The system is further successfully calibrated in real urine samples spiked with the protein.

6.2. Experimental section

6.2.1. Reagents and solutions

All chemicals were of analytical grade and water was deionized or ultrapure Milli-Q laboratory grade. Ethanol absolute from Panreac (Spain); acetonitrile from Scharlau (Spain); acetic acid glacial (100% p.a.) and ethylene glycol(analytical reagent) from Analar Normapur (USA); phosphate buffered saline (PBS) pellets, E404, biotechnology grade, from Amresco (USA); ethylenediamine and silver nitrate ($AgNO_3$) from Merck (Germany); potassium hexacyanoferrate III ($K_3[Fe(CN)_6]$), potassium hexacyanoferrate II ($K_4[Fe(CN)_6]$) trihydrate and iodine (I_2) from Riedel-de-Häen; bovine serum albumin (BSA), CEA from human fluids (CEA); *cis*-bis(isothiocyanato)bis(2,2´-bipyridyl)−4,4´-dicarboxilate) ruthenium(II) (dye N3), *N*-ethyl-*N*′-(3-dimethylaminopropyl)carbodiimidehydrochloride (EDAC), 1-hexyl-3-methylimidazolium iodide (HMII), *N*-hydroxysuccinimide (NHS), lithium iodide, monoclonal anti-carcinoembryonic antigen antibody produced in mouse (Ab-CEA), 4-tert-butylpyridine (TBP) and titanium (IV) oxide (TiO_2) (> 99.7%, anatase, < 25 nm) from Sigma-Aldrich (USA). The Ab-CEA solution was used after a 10 × dilution of the commercial product in PBS buffer (pH 7.4), and was used throughout this work.

6.2.2. Equipment

The electrochemical measurements were made in a potentiostat/galvanostat, Autolab PGSTAT302N, from Methrom (United Kingdom), equipped with a Frequency Response Analysis (FRA) module, interfaced to computer and controlled by NOVA 1.9 software. DSSC measurements were made in the same equipment, coupled to a LED driver accessory, also from Methrom (United Kingdom). Electrochemical impedance analysis (EIS) was performed in a frequency range 0.01–10000 Hz. The photocurrent density-photovoltage (*J-V*) response of the solar cell was obtained using PV measurement system, under 77.7 mW/cm^2, having a LED driver operating with 450 mA output warm white LED. The cell area was fixed at 3.6 cm^2. Sintering was made in a Nabertherm GmbH P330 oven (Germany).

Solid materials were characterized by Fourier Transform Infrared Spectroscopy (FTIR), using a Nicolet iS10 FTIR spectrometer, from Thermo Scientific (USA), couple to the Attenuated Total Reflectance (ATR) sampling accessory of diamond contact crystal, also from Nicolet.

The spectra were collected under room temperature/humidity control, after background correction. The number of scans for sample and background was set to 100. The *x*-axis ranged from 650 to 4000 cm^{-1} and *y*-axis expressed in % transmittance. The resolution was 4000.

Solid materials were also analyzed by Raman spectrometry, using a DXR Raman spectroscope from Thermo Scientific (USA), equipped with a confocal microscope. The Raman spectra was collected with a 532 nm excitation laser, in the Raman shift from 200 to 3500 cm^{-1}, for 0.3 mW power and exposures of 90 s, in combination with a 50 × objective magnification for focus and collection of Raman-scattered light. The confocal aperture was set to 25 µm pinhole.

6.2.3. FTO electrode modification

A fluoride-doped tin oxide (FTO, sheet resistance 13.0 Ω/sq) glass was obtained from Sigma-Aldrich (USA), and was cut into 2.0 × 1.5 cm size slices. The slices were ultrasonically cleaned, first for 15 min in acetone and after for 15 min in deionized water, and then dried in nitrogen atmosphere. The cleaned FTO electrodes were modified with an organic silver conductive ink (OSC ink). For the synthesis of the OSC ink, silver nitrate (0.08 g/mL) was first dissolved completely with a reducing agent (1.11 g/mL, ethyleneglycol), under vigorous stirring, at room temperature. Then, a complexing agent (0.90 g/mL, ethylenediamine) was added dropwise, to the previous solution, over a few min. (~ 60 s), followed by 500 µL of deionised water [14,15,27,28].

The chemical reaction occurred slowly, changing from the pale yellow to a dark brown solution, revealing the formation of silver particles [14]. The synthesized OSC ink was deposited on the surface of the pre-treated FTO coated glass and thermally sintered, set to a temperature of 200 °C, along 10 h. Thus, a silver film formed onto the FTO layer (FTO/Ag-NH_2) and acted as support of the immunosensing layer.

6.2.4. Assembly of the immunosensing layer

The immunosensor (FTO/Ag-NH_2/Ab-CEA) was assembled as represented in **Figure 6.1A**. A solution of ethylenediamine (30 mg/mL) was placed first on the previous silver film for 2 h, at room temperature. Different conditions were tested to improve the efficiency of amine binding, in terms of time (during 30 min, and 1 and 2 h) and temperature (4, 25 and 60 °C).

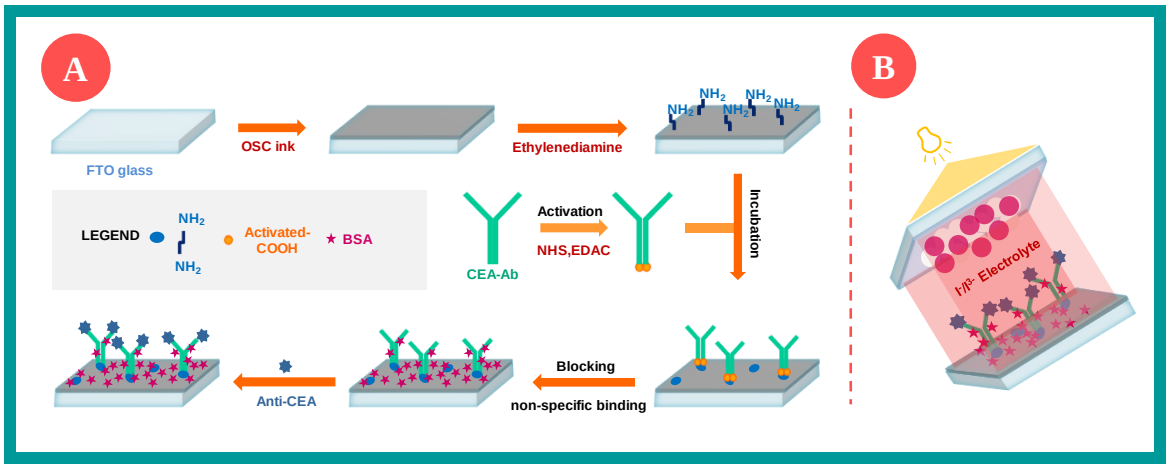

Figure 6.1. Schematic design of the immunosensor for CEA detection (A) and its application in a DSSC (B).

In parallel, a solution of Ab-CEA was activated to bind the amine support. This was done by reacting the Ab-CEA solution with NHS (50 mg/mL) and EDAC (10 mg/mL), prepared in PBS buffer (pH 7.4), for 10 and 15 min, respectively. Next, the activated Ab-CEA was added to the Ag-NH_2 layer, at 4 °C, for 1 h. The resulting surface was then loaded with BSA solution (33.2 mg/mL), for 2 h, at 4 °C, in order to block the non-specific binding areas of the antibody.

The antigen binding was made by incubating 25 µL of a CEA solution of increasing concentrations, for 30 min, to allow the affinity reaction between the Ab-CEA and CEA. The working CEA solutions were prepared in PBS buffer (pH 7.4) by accurate dilution of a stock solution of 25 µg/mL, and had varying concentrations: 1–25 ng/mL, 0.01–25 ng/mL and 0.005–15 ng/mL. CEA was also detected in real urine samples doped with this antigen, ranging from 1.0 to 25 ng/mL and 0.0050–15 ng/mL. After each incubation, the surface was washed with PBS prior to redox probe (iron or iodide based) measurements by EIS and cyclic voltammetry (CV), for all CEA concentration ranges tested.

6.2.4.1. Electrochemical biosensing

Electrochemical measurements were made in an electrochemical cell at room temperature by using CV and EIS assays, which were conducted with a redox probe of 5.0 mM $[Fe(CN)_6]^{3-/4-}$ (1:1) mixture solution or 10 mM I_2 and 20 mM LiI mixture, both prepared in PBS buffer, pH 7.4.

The immunosensor response to CEA concentration levels was tested by EIS at an open circuit potential (OCP), using a sinusoidal potential perturbation with amplitude of 0.01 V and a number of frequencies equal to 100, logarithmically distributed over a frequency range of 0.01 − 10000 Hz. EIS data were fitted to a Randles equivalent circuit using the implemented NOVA software from Autolab. In CV measurements, the potential was scanned from − 1.0 to + 1.0 V, at a sweep 50 mV/s, for 10 cycles.

Measurements of the conventional set-up of the biosensor were performed in a conventional three-electrode system assembly, consisting of a silver chloride reference electrode (Ag/AgCl//0.6 mol/Kg KCl), a carbon CE and the immunosensor FTO/Ag-NH_2/Ab-CEA.

6.2.5. DSSC assembly and performance

A typical DSSC contains (a) a photoanode electrode, (b) a cathode, and (c) a redox system electrolyte [9,10]. Each element is described next.

6.2.5.1. Preparation of the electrodes

The (a) photoanode combines (i) a transparent conductive material, which allows light to pass through; (ii) a mesoporous oxide layer (typically TiO_2) deposited on the conductive transparent layer to activate electronic conduction; (iii) and a monolayer of dye (usually ruthenium complexes) at the surface of the mesoporous oxide layer to enhance light adsorption. Herein, the photoanode consisted of a TiO_2 paste, prepared by dispersing 6.0 g of TiO_2 anatase nanopowder in 8.0 mL of ethanol, 1.0 mL of acetic acid and in 1.0 mL of ultrapure water. This mixture was stirred for 1 h, at room temperature and the resulting paste was printed on the FTO coated glass by using the doctor blade method. Next, the photoanodes were annealed at 450 °C for 1 h [29,30], cooled down to 80 °C and finally immersed in a dye bath solution, at room temperature, in the dark [30]. This dye solution was composed by an ethanolic solution of dye N3 (0.5 mM). The photoanode electrode was removed after 24 h from the dye solution, washed with ethanol and dried.

The (b) cathode or CE consisted of an FTO conductive glass sheet, coated with a catalyst, catalysing the redox couple regeneration and the electron collection from the external circuit [30-32]. Herein, the CE was made as described in section 6.2.4.

6.2.5.2. Set-up of the DSSCs

The PV cells were assembled with the photoanode (FTO/TiO_2 paste/dye) and the cathode (immunosensor, FTO/Ag-NH_2/Ab-CEA). These electrodes were separated by a redox system consisting of an electrolyte (normally an organic solvent containing a redox mediator, such as I^-/I^{3-} couple, iodide/triiodide), which is in contact with the dye and restores it during operation.

Herein, two different electrolyte solutions were employed: (1) an electrolyte solution commonly used in DSSCs, containing 5.0 mM I_2, 100 mM LiI, 600 mM HMII and 500 mM TBP in acetonitrile; (2) and another electrolyte containing 10 mM I_2 and 20 mM LiI in PBS buffer (called herein as the *new electrolyte*). Each electrolyte was casted between the electrodes (photoanode and cathode). The schematic representation is shown in **Figure 6.1B**, corresponding to a cell area of 3.6 cm^2.

6.2.5.3. Electrochemical measurements of the DSSCs

DSSC measurements were evaluated by EIS analysis, performed with the FRA module in a frequency range 0.01–10000 Hz, and by *J-V* response, using a LED driver operating under 450 mA output warm white LED, with 77.7 mW/cm^2. This is a 2-electrode set-up system.

6.3. Results and discussion

6.3.1. Preparation of the immunosensor support

The schematic representation of the stepwise functionalization process to assemble the immunosensor is shown in **Figure 6.1A**. The first stage consisted on cleaning and controlling the FTO glass support. The next stage consisted on the modification of the conductive glass support (FTO glass) with a layer of silver-based ink, aiming to cast silver nanoparticles on the FTO. Silver nanoparticles hold electrocatalytic features against the iodide probe, ensuring a suitable performance of the DSSC.

Before binding the Ab-CEA, the FTO/Ag surface was modified with amine groups. The antibodies had been first casted directly on this silver support, but binding to the antigen was not effective and the electrochemical signals offered little reproducibility. This modification consisted in the addition of ethylenediamine to the silver-based material, allowing a reaction between silver and the amine groups in ethylenediamine. The resulting layer was identified as FTO/Ag-NH_2.

Overall, amine groups are capable of interacting with proteins while preventing significant conformation changes. The presence of such conductive ink was evidenced by naked eye and was followed by FTIR and Raman spectra, compared to the non-modified FTO-glass.

The FTIR spectra are shown in **Figure 6.2A**. The spectrum of FTO glass showed broad bands due to the vibrational modes of the Sn-O-Sn oxide lattice, below 800 cm^{-1}. These Sn−O−Sn groups were evidenced, abundantly, at ~800 cm^{-1}. This band was shifted to lower wavenumbers in the FTO glass modified with OSC ink [33]. The FTIR spectrum of the OSC ink film also revealed a weak band around 2950 and 2850 cm^{-1}, assigned to the presence of asymmetric and symmetric C−H stretching. The broad peak around 1575 cm^{-1} and the weak band between 1000 and 1100 cm^{-1} were assigned, respectively, to the C−N and C−O stretching vibrations.

The presence of a peak around 692 cm^{-1} may correspond to the O−C−C in plane bending vibration, which means that the ethylenediamine was coordinated to silver nitrate, in which an electron of the amino group was donated to the silver atom, thus decreasing the electron density of the amino group and resulting in a weaker NH group peak [15].

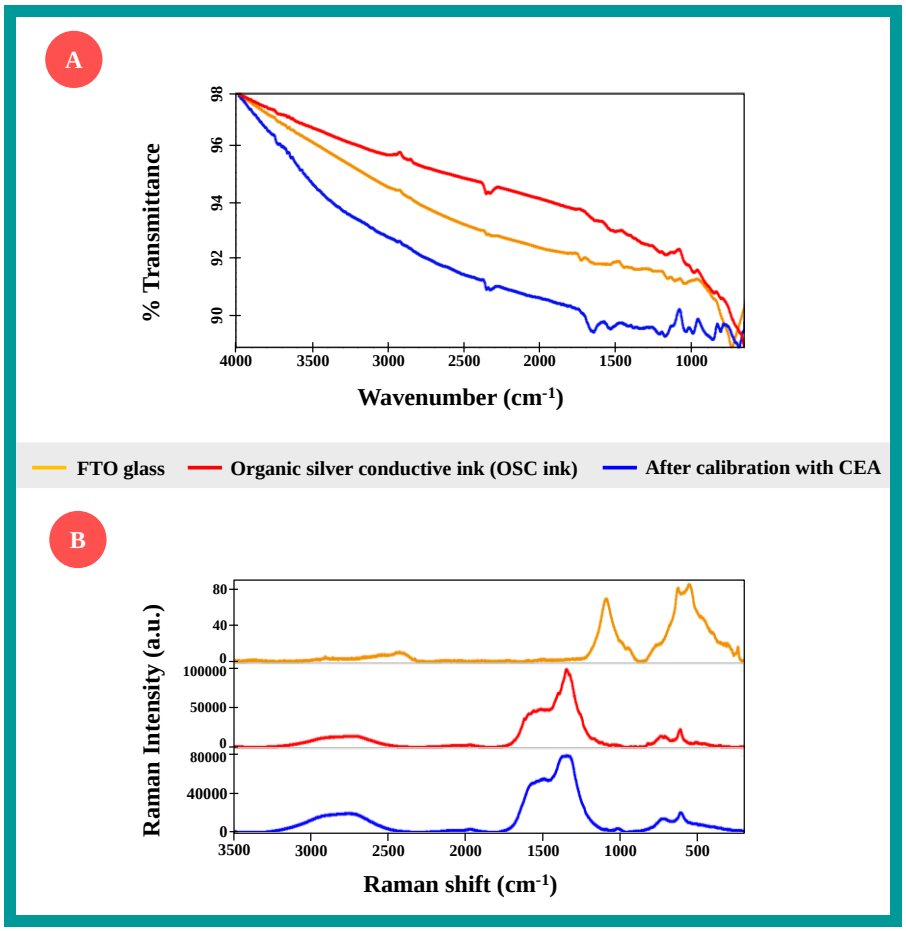

Figure 6.2. Characterization of several layers casted on glass by **(A)** FTIR and **(B)** Raman spectroscopy.

The Raman spectra of the same materials are shown in **Figure 6.2B**. The spectrum of bare FTO glass evidenced a broad band between 400 and 900 cm^{-1}. This region evidenced two small peaks, at 563 and 628 cm^{-1} that could be assigned to Sn−O and Sn−O−Sn stretching vibrations, respectively [34,35]. The band at 1088 cm^{-1} could be assigned to the asymmetric Si−O−Si stretching vibration and the ionic character of the Si−O group [35,36]. This band at 1088 cm^{-1} could also be related to the doping of tin oxide glass with fluorine, compound that has a strong band at 1100 − 1000 cm^{-1}, due to the C−F stretching vibration [31].

The silver-based carbon ink on the FTO shifted the bands assigned to Sn−O and Sn−O−Sn stretching vibrations to higher Raman shift values (to 618 and 742 cm^{-1}, respectively). The presence of carbon in the ink was revealed by two intense bands, at 1350 cm^{-1} and 1540 cm^{-1}, related to the $-CH_2$ deformation vibration and to the C=C vibration [35,36]. Around 2500 − 3100 cm^{-1}, this spectrum showed a broad band, which could be associated to the stretching vibration of C−H bond in the N−C−H group [35,36].

The changes in the electrical features out coming from the presence of the ink were also followed by EIS. The corresponding Nyquist plots are shown in **Figure 6.3**. In these plots, the resistances to charge transfer (R_{ct}) corresponded to the diameter of each semicircle observed. Accordingly, the FTO-glass (**Figure 6.3A**) was the material of higher R_{ct} (~667 kΩ), followed by FTO-glass modified with the OSC ink, with an R_{ct} of ~1806 Ω (**Figure 6.3B**). The presence of the amine groups (**Figure 6.3C**) also enhanced significantly the base level of resistance (up to ~8073 Ω).

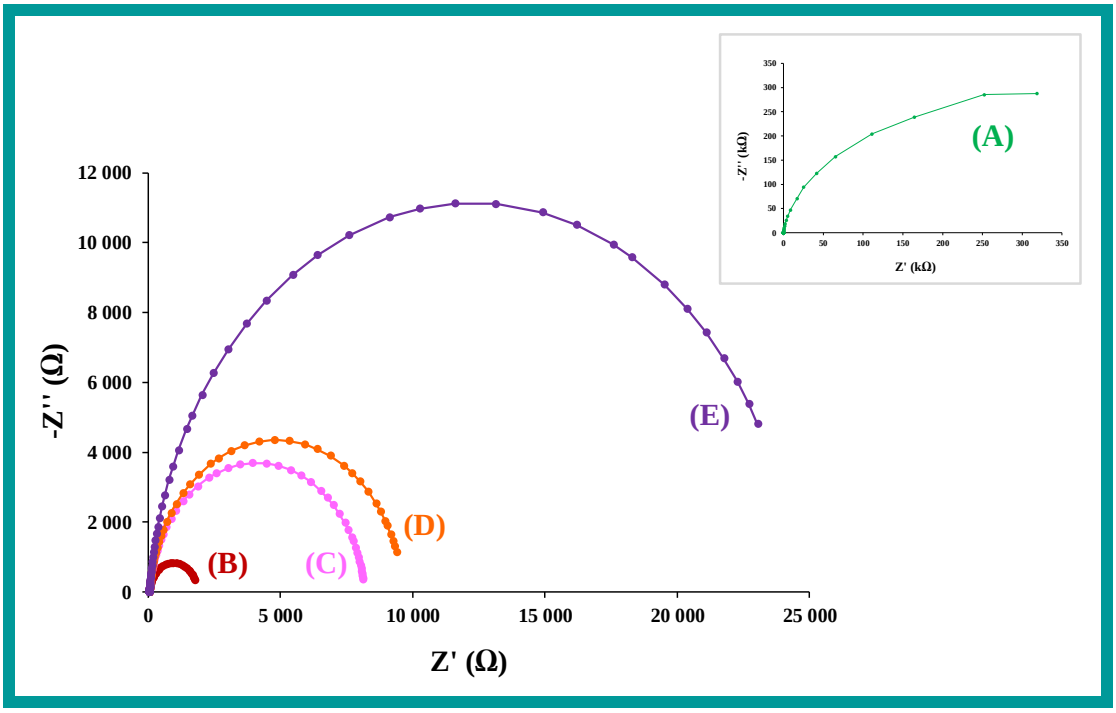

Figure 6.3. EIS spectra obtained on the assembly of the immunosensor through an iodide redox probe, including (**A**) bare FTO electrode; (**B**) FTO/Ag: modification of FTO support with an OSC ink layer; (**C**) FTO/Ag-NH_2: addition of amine groups on top of the conductive layer with ethylenediamine; (**D**) FTO/Ag-NH_2/Ab-CEA: binding of the antibody to the amine surface, and (**E**) FTO/Ag-NH_2/Ab-CEA/BSA: blocking of non-specific binding sites with BSA.

6.3.2. Binding the antibody to the support

Antibodies may bind to a given support in numerous ways, among which different chemistries may be employed. Herein, a simple approach developed by us in the past was used, consisting of a simple activation of the –COOH groups within the Ab-CEA [37]. The activation of this group allows a mild reaction with the amine groups on the FTO support to form amide products, and contributes to a suitable orientation of the antibody on the support. As the Fc terminal of an antibody is composed by –COOH groups, it is expected that the antibody binds to the FTO/Ag-NH_2 support through this point, thereby allowing that both paratope sites remain free for subsequent antigen binding [32].

The –COOH groups of the Ab-CEA were activated via a carbodiimide reaction by EDAC/NHS. In this, the –COOH group formed a highly reactive *O*-acylisourea intermediate that reacted rapidly with NHS, to produce a succinimide ester intermediate [35]. This intermediate is expected to react with the free amine groups on the FTO/Ag-NH_2, yielding a covalent binding of the antibody on this surface. This reaction is favoured under mild conditions and no significant conformation changes are expected to occur in the antibodies.

The incubation of the activated Ab-CEA on the FTO/Ag-NH_2 is expected to bind the antibodies to the platform, in a covalent way and with a suitable orientation. The resulting material is the immunosensor FTO/Ag-NH_2/Ab-CEA. The EIS data collected with FTO/Ag-NH_2/Ab-CEA supports confirmed the presence of Ab-CEA in the immunosensor. In general, antibodies are huge proteins with non-conductive features that hinder the electrical signals passing through the materials. Thus, the electrical effect yields an increase in the observed R_{ct} up to ~9600 Ω (**Figure 6.3D**), when compared to the FTO/Ag-NH_2 (**Figure 6.3C**).

Following the typical immunoassays, the last final stage of the immunosensor assembly consisted in blocking free peptide region on the support that could otherwise allow unspecific binding. For this purpose, the FTO/Ag-NH_2/Ab-CEA support was incubated in a high amount of BSA, a simple and low-cost protein commonly used as blocking of the non-specific sites in immunosensors. The resulting FTO/Ag-NH_2/Ab-CEA(-BSA) support (**Figure 6.3E**) yielded the most significant increase in the R_{ct} value observed throughout the assembly of the immunosensor (up to ~24.5 kΩ) and confirmed the presence of bound BSA.

6.3.3. Optimization of CEA binding

CEA is a glycoprotein [38] involved in cell adhesion, directly linked to different cancer conditions besides colorectal cancer, such as breast, ovarian, lung, gastric, pancreatic, liver, and medullary thyroid cancers [39]. CEA levels may be detected in different biological samples, as serum, blood and urine, playing therefore an important role in the pre-diagnosis evaluation and in the follow-up examination during therapy. The normal levels of CEA biomarker in healthy adults is about 3.0–5.0 ng/mL, and higher levels of this biomarker can signal the presence of cancer [19]. The binding of CEA into the FTO/Ag-NH_2/Ab-CEA(-BSA) support was made by incubating the protein for a fixed time, washing with buffer and reading the response of the same support under a standard redox probe.

A change in the R_{ct} yielded by this probe was directly linked to changes in the electrical properties of the surface. In general, the presence of bound CEA on the surface was detected by an R_{ct} increase. This feature was used to optimize the response of the immunosensor against different conditions.

The first study consisted in understanding how changing the temperature and time of incubation of ethylenediamine could improve the linkage of the activated Ab-CEA to silver-based carbon ink film. For this purpose, the incubation of amine groups was evaluated at different temperatures (4, 25 and 60 °C), along different times (30 min, 1 h and 2 h), for each temperature described, and against an iron redox probe. EIS assays (**Figure 6.4**) demonstrated that when the CEA immunosensor did not contain ethylenediamine, the R_{ct} increased by the addition of Ab-CEA but the blocking effect of the BSA was negligible, which was not consistent with the presence of the antibody on the surface. In addition, the repeatability of this procedure was poor, suggesting that the antibody binding was not stable, due to the week interactions established with the carbon/silver material. The subsequent tests included always ethylenediamine. From all variables tested, only the 25 °C incubation for 2 h was able to produce consistent results. Overall, the other conditions indicated that the temperature (lower or higher than 25 °C) affected the behaviour of the FTO/Ag surface alone, thereby changing all subsequent data. Thus, the condition that ensured a good linkage between Ab-CEA and the silver film formed onto the FTO layer was the incubation at 25 °C for 2 h.

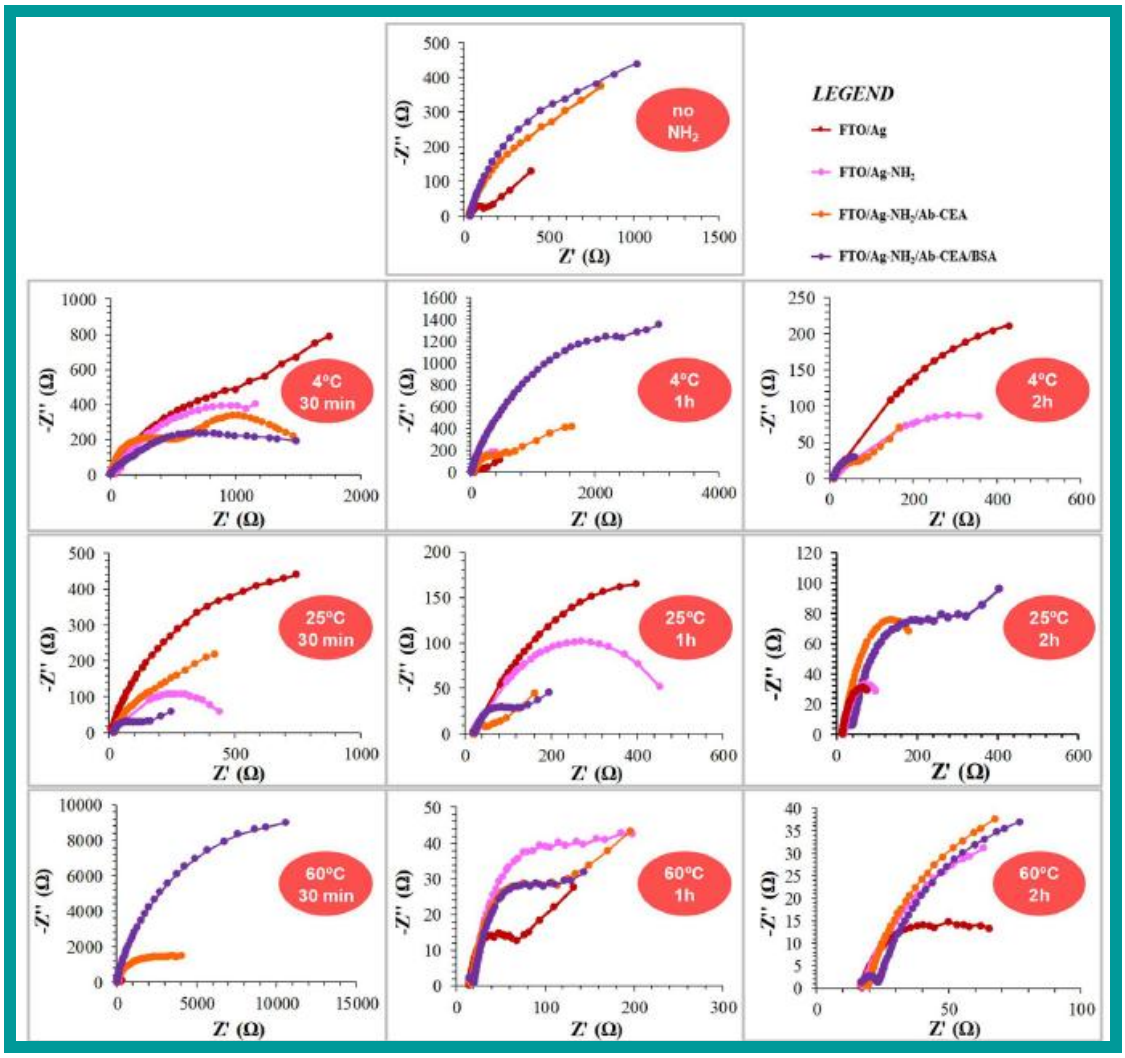

Figure 6.4. EIS spectra representative of immunosensor assembly, with different operational conditions of ethylenediamine incubation: no incubation with amine groups, at 4ºC, 25ºC and 60ºC during 30 min, 1 h and 2 h for each temperature.

The impact of the CEA binding on the surface was also followed by FTIR and Raman spectroscopy. The FTIR spectra after incubating CEA of high concentration are shown in **Figure 6.2**. The major transmittance peak is centred at 1680 cm^{-1}, which represents C=O stretching vibrations, arriving from the several functional groups containing this bond. Also, other major peaks at 1516, 1179 and 1039 cm^{-1} were identified and assigned to the C−N stretching vibrations (secondary amides), N−H bending (tertiary amides) and C−O vibrations in carbohydrate moieties [40,41].

Regarding Raman spectra, the most representative peaks are similar to those of the ink film, but their Raman shift changed: around 613 cm^{-1} (− 0.10 a.u.); 716 cm^{-1} (+ 0.22 a.u.); 1345 cm^{-1} (− 0.20 a.u.); 1564 cm^{-1} (+ 0.13 a.u.) and, around 2500–3100 cm^{-1} (+ 0.35 a.u.).

6.3.4. Electrochemical performance of the immunosensor in a 3-electrode system

The analytical features of the biosensor were obtained by calibrating the system for increasing concentrations of CEA. This was done first by having PBS buffer as background of the calibrating solution and after in diluted blank urine. This study was complemented by checking the effect of having an iron or iodide-based redox probe. EIS and CV data was obtained for CEA concentrations ranging 0.005 − 15 ng/mL.

The typical data obtained with standard solutions prepared in PBS buffer and iron redox probe is shown in **Figure 6.5A**. Overall, the Nyquits plots evidenced linear behaviour for $1/\Delta R_{ct}$ (which $\Delta R_{ct} = R_{ct(sample)}/R_{ct(blank)}$) against log(concentration) from 0.005 ng/mL up to 15 ng/mL CEA in buffer. The anionic slope was − 0.17 Ω/decade concentration and the squared correlation coefficient > 0.98. The CV data was consistent with these results, also showing linear behaviour in the range of 0.005–15.0 ng/mL, with a slope − 0.15 A/decade concentration and squared correlation coefficient > 0.99, under PBS buffer solution and iron redox probe conditions (inset of **Figure 6.5A**).

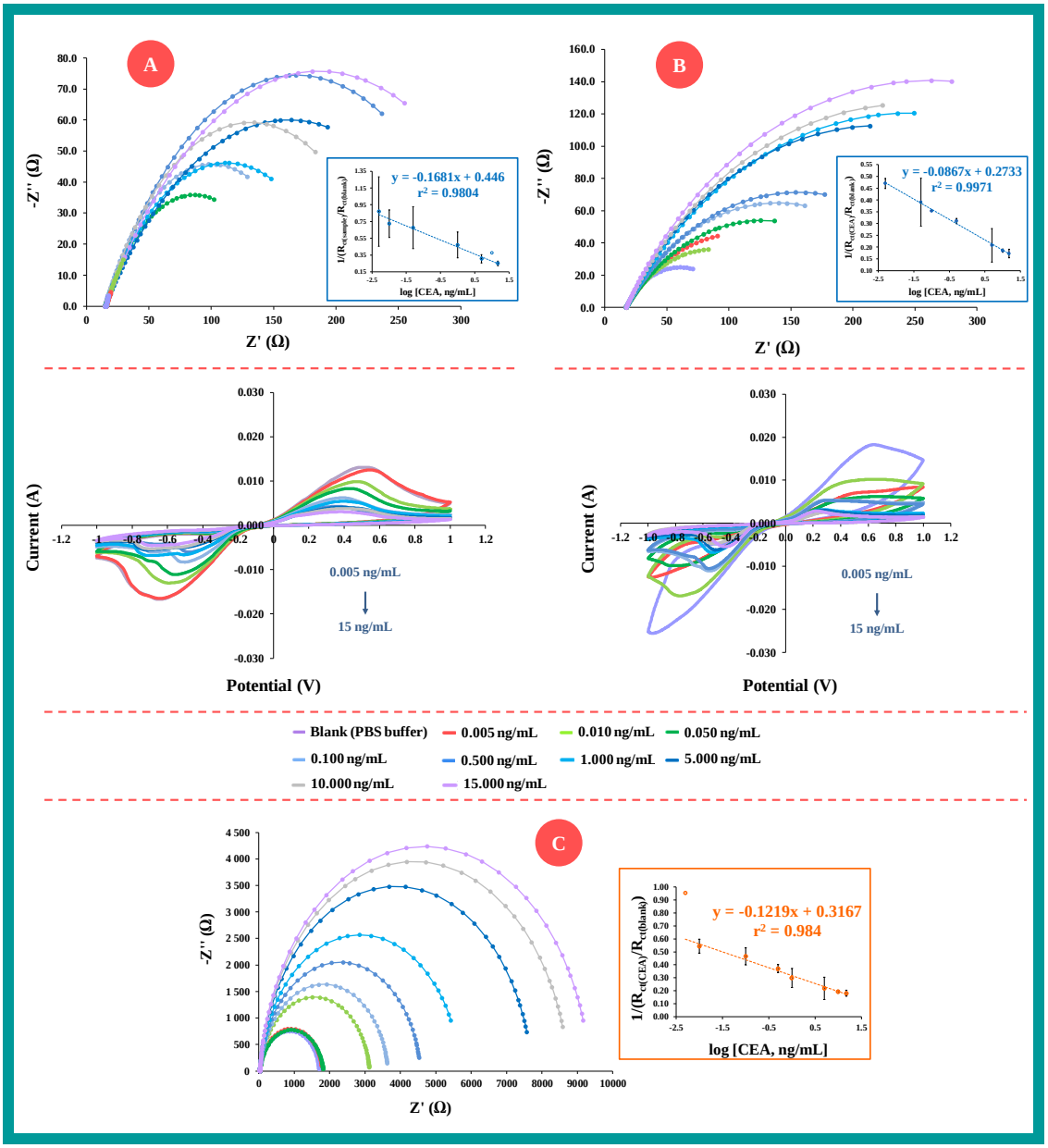

Figure 6.5. Typical EIS data of the CEA immunosensor behaviour with different ranges of CEA concentrations, in (**A**) PBS solution or (**B**) spiked blank urine (diluted 10×) using an iron redox probe or (**C**) spiked blank urine (diluted 10×) using an iodide redox probe. The CV data related to the same conditions in (**A**) and (**B**) is shown below.

For calibrating in conditions close to urine samples, blank urine was collected from healthy volunteer and diluted 10 ×. Then, standard solutions were prepared in this diluted urine and the typical Nyquist plots obtained shown in **Figure 6.5B**, in which an iron redox probe was used to follow-up the changes in the electrical properties.

Under this condition, the linear response of the immunosensor was within the same concentration range as in buffer, having an anionic slope of − 0.087 and a squared correlation coefficient > 0.99; the linear behaviour was observed down to 0.005 ng/mL. The response under CV measurements was also consistent with the previous data, showing the same linear range, for an anionic slope of − 0.18 and squared correlation coefficient of > 0.99.

Considering that the DSSC operates with an iodide redox probe, the analytical features of the immunosensor were also evaluated against this redox probe. This was done for the same concentration range tested before and the iodide redox solution was prepared in PBS. The EIS data was collected at the OCP of this probe. Overall, the EIS calibration was linear from 0.010 ng/mL, with a slope of − 0.12 Ω/decade concentration, an LOD of 0.010 ng/mL and a squared correlation coefficient of ~0.99 (**Figure 6.5C**). Moreover, repeated calibrations indicated that the response was precise, with standard deviations below than 10%.

Overall, these results showed a similar behaviour of the immunosensor, when evaluated by EIS assays in the same CEA concentration range against an iron redox probe or an iodide redox probe. This meant that the electrical features of FTO/Ag-NH_2/Ab-CEA(-BSA) remained concentration dependent, when in the presence of iodide. Therefore, this suggested that the immunosensor could be employed as the CE of the DSSC.

6.3.5. Electrochemical performance of the immunosensor as counter electrode of the DSSC

As previously explained, a DSSC was employed as the electrical reading box of the biosensor by using the FTO/Ag-NH_2/Ab-CEA(-BSA) as the CE within the PV cell set-up. To evaluate the potential of the analytical application of this novel approach, the device was calibrated against CEA increasing concentrations, prepared in real urine, diluted in buffer. The levels of CEA spiked into this urine blank solution ranged from 0.25 to 183.50 ng/mL and the electrochemical behaviour was evaluated by EIS and J-V measurements, having a redox electrolyte that was PBS- or acetonitrile-based. In general, the interfacial charge transfer process within the fabricated DSSC was first fitted into an appropriate equivalent circuit (**Figure 6.6**), obtained by the NOVA software, and the analytical data collected under illumination.

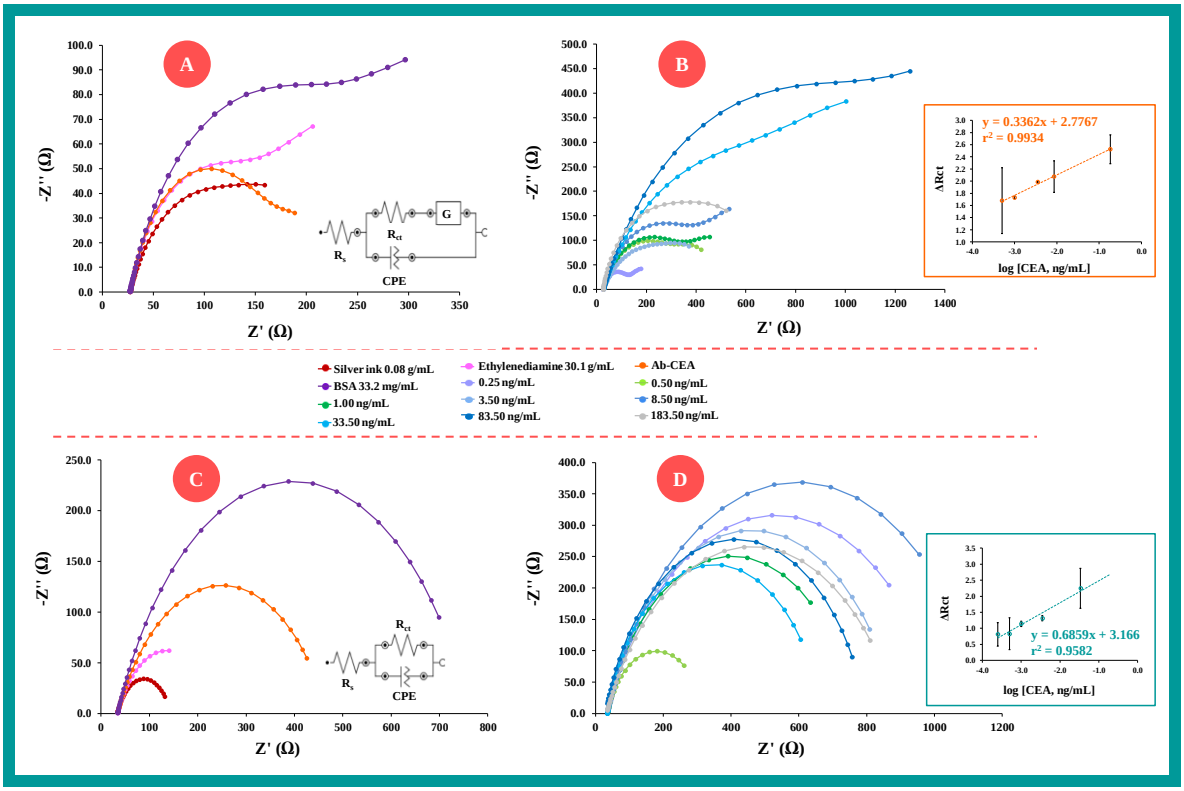

Figure 6.6. EIS measurements of the assembly of the immunosensor designed and the corresponding calibration curves in real urine samples spiked with different CEA standard concentrations (0.25 to 183.50 ng/mL) obtained in a DSSC set-up. The measurements were made in the presence of different electrolytes: (**A**) and (**B**) were obtained with new electrolyte and (**C**) and (**D**) with the conventional electrolyte used for the DSSCs evaluation.

The set-up and calibration of the device in PBS-based electrolyte are shown in **Figure 6.6A-B**. In general, the electrochemical relative features of the assembly of this new set-up (**Figure 6.6A**) were consistent with the previous data of the immunosensor outside the DSSC. The calibration obtained by the Nyquist plots (**Figure 6.6B**), also confirmed a linear increase of ΔR_{ct} ($\Delta R_{ct} = R_{ct(sample)}/R_{ct(blank)}$) against the increasing of the logarithm CEA concentration. Linear behaviour was observed down to 0.25 ng/mL, with typical cationic slopes of 0.34 per decade concentration and squared correlation coefficients > 0.99 (inset in **Figure 6.6B**). Linear responses were observed within a higher concentration range than with the immunosensor conventional set-up, but this range was within the CEA levels of clinical interest.

The evaluation of the set-up and calibration of the device in acetonitrile-based electrolyte is shown in **Figure 6.6C-D**. As previously, the electrochemical relative features of the assembly of this new set-up (**Figure 6.6C**) were consistent with the previous data of the immunosensor outside the DSSC, apart from the elimination of diffusion-limited process (no W element, and the Randle's circuit applied herein). The Nyquist plots (**Figure 6.6D**) gave rise to a linear increase of ΔR_{ct} ($\Delta R_{ct} = R_{ct(sample)}/R_{ct(blank)}$) against the increasing of the logarithm CEA concentration down to 0.50 ng/mL, with typical cationic slopes of 0.69 per decade concentration and squared correlation coefficients > 0.96 (inset in **Figure 6.6D**).

Overall, the immunosensor response inside a DSSC was concentration dependent. The linear CEA concentration range with the acetonitrile-based electrolyte was narrower than with the PBS-based electrolyte. This was a reasonable result, as proteins tend to denature in acetonitrile medium, limiting the response of the biosensor. This is especially evident for higher concentration levels, in which the antibodies and protein suffer from a cumulative effect of consecutive incubations.

6.3.6. Photovoltaic data of the immunosensor/DSSC set-up

Besides the Nyquist plots, it was possible to extract data related to the usual characterization of PV cells and to understand the impact of the immunosensor upon these cells. For this purpose, *J-V* curves were recorded for each stage of the set-up of the immunosensor, followed by its subsequent calibration in diluted urine. The results obtained are summarized in **Table 6.1**, displaying the values of the short-circuit current density (J_{sc}), the open-circuit potential (V_{oc}) and the fill factor (*FF*).

The *FF* of the PV cell with FTO/Ag as cathode was of similar amplitude in both cells, containing different electrolytes. The PBS-based electrolyte displayed a ~21% FF, while the acetonitrile-based electrolyte had an *FF* value of ~25%. However, the subsequent modifications of the immunosensor until the CE FTO/Ag-NH_2/Ab-CEA(-BSA) was ready, contributed to significant variations in this value, ending in 22% when the new electrolyte was used and in ~12% when in the presence of conventional electrolyte. Thus, the overall impact of the antibodies on the CE of the cell was contained by using a PBS-based electrolyte.

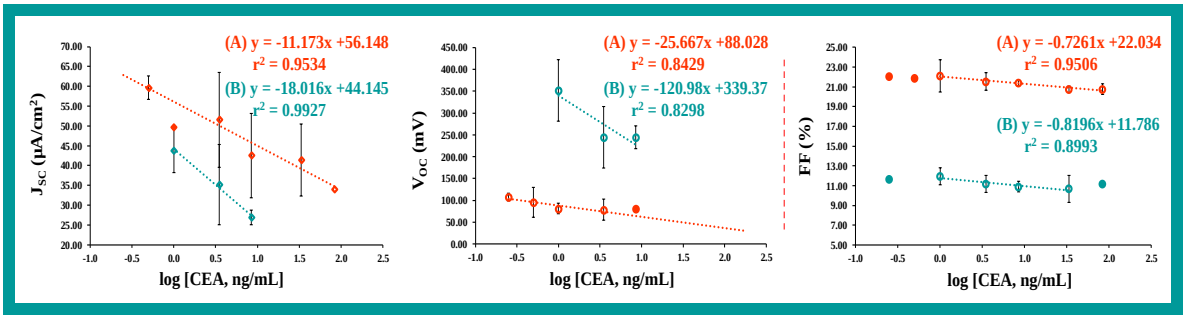

Figure 6.7. Representative calibration curves of J_{sc}, V_{oc} and *FF* of the modified DSSCs evaluated for (**A**) new electrolyte and (**B**) conventional electrolyte with the increase of the CEA concentration levels. The DSSC performance was evaluated under 77.7 mW/cm^2 (LED driver was operating with 450 mA output warm white LED). J_{sc}: Short-circuit current density; V_{oc}: Open-circuit potential; *FF*: Fill factor. Area of the cell electrode was 3.6 cm^2.

The calibration procedure of the immunosensor using the PV cell as an electrical reading box was the same as in section 6.3.5. It started by incubating the sensor in 0.25 ng/mL for the same period of time as in the previous studies, washing this surface and setting-up the PV cell with this material as CE; this procedure was repeated for increasing concentrations, and the resulting electrical output of the cell is listed in **Table 6.1**. These values were also plotted in **Figure 6.7**. In general, the overall tendency of J_{sc}, V_{oc} and *FF* was to decrease for increasing concentrations of CEA, thereby presenting anionic slopes. This behaviour was supported by the blocking effect of the protein upon the conductivity features of the CE. In terms of concentration dependency, the variable J_{sc} seemed to be the most reliable one among the photovoltaic properties. J_{sc} decreased with the increasing CEA concentrations and attained a maximum value of 59.65 µA/cm^2, in the new electrolyte assays, and 43.80 µA/cm^2 in the conventional electrolyte.

Table 6.1. Photovoltaic parameters of the assembly of the immunosensor/DSSC device for the CEA biomarker detection, in the presence of different electrolyte: (A) new electrolyte and (B) conventional electrolyte. The DSSC performance was evaluated under 77.7 mW/cm^2 (LED driver was operating with 450 mA output warm white LED). J_{SC}: Short-circuit current density; V_{OC}: Open-circuit potential; *FF*: Fill factor; *PCE*: Power conversion efficiency. Area of the cell electrode was 3.6 cm^2.

	Cathode modifications	J_{SC} (µA/cm^2)		V_{OC} (mV)		*FF* (%)	
		A	B	A	B	A	B
	FTO/Ag	152.50	243.38	95.21	163.57	21.3	24.9
	FTO/Ag-NH$_2$	109.04	98.19	78.13	183.11	23.6	24.4
	FTO/Ag-NH$_2$/Ab-CEA	96.45	51.81	75.68	185.55	26.2	14.7
	FTO/Ag-NH$_2$/Ab-CEA(-BSA)	64.89	41.99	73.24	263.67	22.2	11.8
FTO@Ag-NH$_2$@Ab-CEA/BSA/CEA	**0.50 ng/mL**	59.65	169.71	95.21	483.40	21.9	15.2
	1.00 ng/mL	49.70	43.80	80.57	351.56	22.1	11.9
	3.50 ng/mL	51.55	35.17	78.13	244.14	21.5	11.2
	8.50 ng/mL	42.50	26.91	80.57	244.14	21.4	10.9
	33.50 ng/mL	41.37	45.67	139.16	341.80	20.8	10.7
	83.50 ng/mL	34.06	36.35	100.10	261.23	20.8	11.2

Overall, it seemed clear that the response of J_{sc} seemed to be dominated by concentration and that the new electrolyte displayed wider tendencies for a linear range than the conventional acetonitrile-based electrolyte. The quality of the linear range could be improved, because there are many other new variables that need to be controlled under this new set-up, e.g., whether to recover the photoanode or to use a new electrode for each concentration reading.

Still, the anionic response of the immunosensor obtained in the DSSC assays along the calibration in biological samples was similar to the response obtained in the calibration curves in spiked blank urine samples, evaluated against an iodide redox probe.

6.4. Conclusions and future perspectives

Overall, our new platform describes the disruptive integration of biosensors inside PV, trying to employ these as the electrical reading box of a biosensor. In detail, an immunosensor for CEA prepared on FTO glass displayed suitable features, when integrated inside a DSSC and after being evaluated by conventional EIS and CV electrochemical techniques. The resulting biosensor was sensitive for CEA, considering that it displayed linear responses within the concentration range of clinical interest, and it was selective for CEA in diluted urine samples, used as background medium in the preparation of standard solutions. Moreover, the CEA-immunosensor revealed a stable response, with standard deviations below 3% when evaluated in the DSSC configuration.

The future perspectives for this disruptive approach are marvellous. This apparently strange interaction between PV cells and biosensors may lead to the production of self-sustained biosensors, because a PV cell is itself an electrical energy generator. Thus, no electrical power, nor battery, may turn out necessary to have this biosensor working in the field.

As its performance is concentration dependent, its electrical output may be translated into a concentration value. Eventually, this concept may be extended to any other biomolecules and to many other biorecognition elements besides antibodies. Moreover, once the system is calibrated in a blank sample, it is highly likely that it will operate well in the analysis of real samples.

Further studies are currently ongoing to make the device completely self-sustained, not only regarding electrical source, but also in terms of reading box. As the PV cell provides an electrical output, this output may be also translated by numerous ways, avoiding the need for complex or portable potentiostat devices. This work is currently undergoing in BioMark sensor research.

References

[1] M. Florescu, M. Barsan, R. Pauliukaite, C.M.A. Brett, ‘Development and application of oxysilane sol–gel electrochemical glucose biosensors based on cobalt hexacyanoferrate modified carbon film electrodes’, *Electroanalysis*, vol. 19, pp. 220–226, 2007.

[2] M.L.Y. Sin, K.E. Mach, P.K. Wong, J.C. Liao, 'Advances and challenges in biosensor-based diagnosis of infectious diseases', *Expert Rev. Mol. Diagn.*, vol. 14, pp. 225–244, 2014.

[3] A.P.F. Turner, 'Biosensors: sense and sensibility', *Chem. Soc. Rev.*, vol. 42, pp. 3184-3196, 2013.

[4] J.M.V. Emon, 'Immunoassay and other bioanalytical techniques', *CRC press*, Taylor and Francis Group, 2007.

[5] S. Teixeira, R.S. Conlan, O.J. Guy, M.G.F. Sales, 'Label-free human chorionic gonadotropin detection at picogram levels using oriented antibodies bound to graphene screen-printed electrodes', *J. Mater. Chem. B*, vol. 2, pp. 1852–1865, 2014.

[6] D. Wei, P. Andrew, T. Ryhanen, 'Electrochemical photovoltaic cells-review of recent developments', *J. Chem. Technol. Biotechnol.*, vol. 85, pp. 1547-1552, 2010.

[7] M. Grätzel, 'Photoelectrochemical cells', *Nature*, vol. 414, pp. 338–344, 2001.

[8] B. O'Regan, M. Grätzel, 'A low-cost high efficiency solar cell based on dye-sensitized colloidal TiO_2 films', *Nature*, vol. 353, pp. 737–740, 1991.

[9] B.S. Shirke, P.V. Korake, P.P. Hankare, S.R. Bamane, K.M. Garadkar, 'Synthesis and characterization of pure anatase TiO_2 nanoparticles', *J. Mater. Sci.-Mater. Electron.*, vol. 22, pp. 821–824, 2011.

[10] A. Hagfeldt, G. Boschloo, L. Sun, L. Kloo, H. Pettersson, 'Dye-Sensitized Solar Cells', *Chem. Rev.*, vol. 110, pp. 6595–6663, 2010.

[11] M. Yen, C. Yen, S. Liao, M. Hsiao, C. Weng, Y. Lin, C.M. Ma, M. Tsai, A. Su, K. Ho, P. Liu, 'A novel carbon-based nanocomposite plate as a counter electrode for dye-sensitized solar cells', *Compos. Sci. Technol.*, vol. 69, pp. 2193–2197, 2009.

[12] S.B. Bon, L. Valentini, J.M. Kenny, L. Peponi, R. Verdejo, M.A. Lopez-Manchado, 'Electrodeposition of transparent and conducting graphene/carbon nanotube thin films', *Physic. Status Solidi a-Appl. Mater. Sci.*, vol. 207, pp. 2461–2466, 2010.

[13] B. Gholamkhass, S. Holdcroft, 'Enhancing the durability of polymer solar cells using gold nano-dots', *Sol. Energy Mater. Sol. Cells*, vol. 95, pp. 3106–3113, 2011.

[14] M.C. Dang, T.M. Dung Dang, E. Fribourg-Blanc, 'Silver nanoparticles ink synthesis for conductive patterns fabrication using inkjet printing technology', *Advances in Natural Sciences: Nanoscience and Nanotechnology*, vol. 6, 2015.

[15] W. Yang, C. Liu, Z. Zhang, Y. Liu, S. Nie, 'One step synthesis of uniform organic silver ink drawing directly on paper substrates', *J. Mater. Chem.*, vol. 22, pp. 23012–23016, 2012.

[16] A.R. Gliga, S. Skoglund, I.O. Wallinder, B. Fadeel, H.L. Karlsson, 'Size-dependent cytotoxicity of silver nanoparticles in human lung cells: the role of cellular uptake, agglomeration and Ag release', *Particle and Fibre Toxicology*, vol. 11, pp. 1–17, 2014.

[17] G. Lech, R. Słotwiński, M. Słodkowski, I.W. Krasnodębski, 'Colorectal cancer tumour markers and biomarkers: recent therapeutic advances', *World J. Gastroenterol.*, vol. 22, pp. 1745–1755, 2016.

[18] B.J. Casey, P. Kofinas, 'Selective binding of carcinoembryonic antigen using imprinted polymeric hydrogels', *J. Biomed. Mater. Res. - Part A 87A*, vol. 359, 2008.

[19] S. Hammarström, 'The carcinoembryonic antigen (CEA) family: structures, suggested functions and expression in normal and malignant tissues', *Semin. Cancer Biol.*, vol. 9, pp. 67–81, 1999.

[20] M. Liu, C. Jia, Q. Jin, X. Lou, S. Yao, J. Xiang, J. Zhao, 'Novel colorimetric enzyme immunoassay for the detection of carcinoembryonic antigen', *Talanta*, vol. 81, pp. 1625–1629, 2010.

[21] P. Lv, L. Min, R. Yuan, Y. Chai, S. Chen, 'A novel immunosensor for carcinoembryonic antigen based on poly(diallyldimethylammonium chloride) protected prussian blue nanoparticles and double-layer nanometer-sized gold particles', *Microchim. Acta*, vol. 171, pp. 297–304, 2010.

[22] X. Miao, S. Zou, H. Zhang, L. Ling, 'Highly sensitive carcinoembryonic antigen detection using Ag@Au core-shell nanoparticles and dynamic light scattering', *Sens. Actuators, B: Chem.*, vol. 191, pp. 396–400, 2014.

[23] W. Shi, Z. Ma, 'A novel label-free amperometric immunosensor for carcinoembryonic antigen based on redox membrane', *Biosens. Bioelectron.*, vol. 26, pp. 3068–3071, 2011.

[24] F. Tan, F. Yan, H. Ju, 'A designer ormosil gel for preparation of sensitive immunosensor for carcinoembryonic antigen based on simple direct electron transfer', *Electrochem. Commun.*, vol. 8, pp. 1835–1839, 2006.

[25] Y. Wang, Z. Zhang, V. Jain, J. Yi, S. Mueller, J. Sokolov, Z. Liu, K. Levon, B. Rigas, M.H. Rafailovich, 'Potentiometric sensors based on surface molecular imprinting: Detection of cancer biomarkers and viruses', *Sens. Actuators B: Chem.*, vol. 146, pp. 381–387, 2010.

[26] J.C. Kemmegne-Mbouguen, E. Ngameni, P.G. Baker, T.T. Waryo, B. Kgarebe, E.I. Iwuoha, 'Carcinoembryonic antigen immunosensor developed with organoclay nanogold composite film,' *Int. J. Electrochem. Sci.*, vol. 9, pp. 478–492, 2014.

[27] Y. Chang, D. Wang, Y. Tai, Z. Yang, 'Preparation, characterization and reaction mechanism of a novel silver-organic conductive ink', *J. Mater. Chem.*, vol. 22, pp. 25296–25301, 2012.

[28] Y. Tao, Y. Tao, B. Wang, L. Wang, Y. Tai, 'A facile approach to a silver conductive ink with high performance for macroelectronics', *Nanoscale Res. Lett.*, vol. 8, pp. 1–6, 2013.

[29] K.T. Dembele, R. Nechache, L. Nikolova, A. Vomiero, C. Santato, S. Licoccia, F. Rosei, 'Effect of multi-walled carbon nanotubes on the stability of dye sensitized solar cells', *J. Power Sources*, vol. 233, pp. 93–97, 2013.

[30] U. Mehmood, S. Rahman, K. Harrabi, I. Hussein, B.V. Reddy, 'Recent Advances in Dye Sensitized Solar Cells', *Adv. Mater. Sci. Eng.*, pp. 1–12, 2014.

[31] J. Gong, J. Liang, K. Sumathy, 'Review on dye-sensitized solar cells (DSSCs): Fundamental concepts and novel materials', *Renewable & Sustainable Energy Reviews*, vol. 16, pp. 5848–5860, 2012.

[32] J. Wu, Z. Lan, J. Lin, M. Huang, Y. Huang, L. Fan, G. Luo, 'Electrolytes in dye-sensitized solar cells', *Chem. Rev.*, vol. 115, pp. 2136–2173, 2015.

[33] R. Scipioni, D. Gazzoli, F. Teocoli, O. Palumbo, A. Paolone, N. Ibris, S. Brutti, M.A. Navarra, 'Preparation and characterization of nanocomposite polymer membranes containing functionalized SnO_2 additives', *Membranes*, vol. 4, pp. 123–142, 2014.

[34] V. Kumar, A. Govind, R. Nagarajan, 'Optical and photocatalytic properties of heavily F-doped SnO_2 nanocrystals by a novel single-source precursor approach', *Inorg. Chem.*, vol. 50, pp. 5637–5645, 2011.

[35] L.A. Truta, M.G. Sales, 'Sol-gel chemistry in biosensing devices of electrical transduction: application to CEA cancer biomarker', *Curr. Top. Med. Chem.*, vol. 15, 2015.

[36] G. Socrates, 'Infrared and Raman characteristic group frequencies', third edition, *John Wiley & Sons, Ltd*, London, United Kingdom, 2004.

[37] N.S. Ferreira, M.G. Sales, 'Disposable immunosensor using a simple method for oriented antibody immobilization for label-free real-time detection of an oxidative stress biomarker implicated in cancer diseases', *Biosens. Bioelectron.*, vol.53, pp. 193–199, 2014.

[38] S.S. Pinho, C. Reis, 'Glycosylation in cancer: mechanisms and clinical implications', *Nat. Rev. Cancer*, vol. 15, pp. 540–555, 2015.

[39] S.R. Stowell, T. Ju, R.D. Cummings, 'Protein Glycosylation in Cancer', *Ann. Rev. Pathol.*, vol. 10, pp. 473–510, 2015.

[40] P.R. Bahn, A. Pappelis, 'IR spectra of protein, thermal protein', *thermal glycoprotein*, pp. 73–74, 2001.

[41] S.P. Lewis, A.T. Lewis, P.D. Lewis, 'Prediction of glycoprotein secondary structure using ATR-FTIR', *Vib. Spectrosc.*, vol. 69, pp. 21–29, 2013.

CHAPTER 7

Coupling gold nanoparticles to dye-sensitized solar cells

In this chapter, a work based on the paper titled *Coupling gold nanoparticles to Dye-Sensitized Solar Cells for an increased efficiency*, under submission, is presented. Herein, a new approach for establishing a suitable and environmental safe interface between DSSCs and AuNPs is demonstrated.

7.1. Introduction

DSSCs are photovoltaic devices inspired in the respiration of plants and its system of converting light energy into an electron flow that sustains the cell operation [1]. Their great advantages, as easy manufacturing at low fabrication cost, and eco-friendly approach in their fabrication [2-8], make them suitable to be implemented in different research areas. In the literature, several studies have described the importance of the incorporation of metals in DSSCs. Au NPs have attracted more attention due to strong absorption in the visible associated to LSPR in the optical spectra [4,6,9–14]. Au NPs allow the improvement of the overall performance of photovoltaic devices by altering electron charging effects, thereby increasing the photocurrent and photovoltage features of the photovoltaic cells [15–17].

The present work aims to present a new approach for establishing a suitable and environmentally safe interface between DSSCs and Au NPs was purposed in this work. Colloidal Au NPs were chemically synthesized and then attached to titanium dioxide (TiO_2) and, also, to TiO_2 surface modified with siliceous shells enriched in dithiocarbamate moieties (SiO_2/SiDTC) [11,18–25]. Photoanodes composed of a conductive glass covered by fluorine doped tin oxide (FTO glass) were used and modified with films of TiO_2 anatase, TiO_2@Au NPs (diameters ~4 nm and ~22nm), and TiO_2 chemically functionalized with SiO_2/SiDTC and loaded with colloidal Au NPs, in order to improve the typical energy conversion efficiency of DSSCs. A sandwich configuration was made using the photoanode, a platinum counter electrode, and an iodide electrolyte solution (I^-/I_3^-) [3,5,6,26,27]. This assembly allowed the photoexcitation of the sensitizer dye adsorbed on the TiO_2 surface, promoting the transfer of electrons injected into the conduction band of the TiO_2 and reaching the counter electrode through the outer circuit. By electron donation from the I^-/I_3^- redox couple, the photosensitizer dye is regenerated and the circuit is completed via electron migration through the external load [2,5].

The final cell showed good stability and reproducibility due to electrostatic repulsion minimization between the Au NPs and their attachment to the TiO_2 surfaces [11,19,20]. In general, a simple approach to incorporate Au NPs in the construction of a new photoanode for a DSSC was established, showing thus the beneficial influence of these NPs to the photovoltaic cell performance.

7.2. Experimental Section

7.2.1. Materials

The following chemicals were used as purchased: acetic acid glacial (CH_3CO_2H, 100% p.a., Analar Normapur); acetonitrile (CH_3CN, 99.9%, Scharlau); 3-aminopropyltriethoxysilane ($H_2N(CH_2)_3Si(OC_2H_5)_3$, APTES, > 99%, Sigma-Aldrich); ammonia solution (25% NH_4OH, Riedel-de-Häen); carbon disulfide (CS_2, > 99%, Panreac); ethanol absolute (C_2H_5OH, ≥ 99.9%, Panreac); hexachloroplatinic (IV) acid hexahydrate ($H_2PtCl_6 \cdot 6H_2O$, ~40% Pt for synthesis, Merck); 1-hexyl-3-methylimidazolium iodide ($C_{10}H_{19}IN_2$, HMII, 98%, Alfa Aesar); hydrogen tetrachloroaurate(III) trihydrate ($HAuCl_4.3H_2O$, ≥ 99.9% trace metals basis, Sigma-Aldrich); iodine (I_2, Riedel-de-Häen); lithium iodide (LiI, anhydrous, beads, ~10 mesh, 99.999% trace metals basis, Sigma-Aldrich); sodium borohydride ($NaBH_4$, 95%, Riedel-de-Häen); sodium hydroxide (NaOH, > 98%, Pronolab); 4-tert-butylpyridine ($C_9H_{13}N$, TBP, >96.0%, TCI); tetraethyl orthosilicate ($Si(OC_2H_5)_4$, TEOS, > 99%, Sigma-Aldrich); titanium(IV) oxide, anatase nanopowder (TiO_2, 99.7% trace metals basis, < 25nm, Sigma-Aldrich); di-tetrabutylammonium cis-bis(isothiocyanato)bis(2,2'-bipyridyl-4,4'-dicarboxylato)ruthenium(II) ($C_{58}H_{86}N_8O_8RuS_2$, N719 dye, 95% (NMR), Sigma-Aldrich); and trisodium citrate dihydrate ($Na_3C_6H_5O_7.2H_2O$, ≥ 99.0%, Sigma-Aldrich). All chemicals were of analytical grade. The water used throughout the experiments was deionized or ultrapure Milli-Q laboratory grade.

7.2.2. Characterization techniques

The particle size distribution of the colloidal particles was estimated by Dynamic Light Scattering (DLS) that was conducted using a ZetaSizer Nano series. The optical absorption and reflectance spectra of the materials were accomplished using an Ultraviolet-Visible (UV/Vis) GBC Scientific and an UV-Visible Jasco V-560 spectrophotometers, respectively.

Infrared spectra were recorded using a Fourier Transformed Infrared Spectrometer (FTIR, Thermo Scientific Nicolet iS10) equipped with an Attenuated Total Reflectance (ATR) accessory of diamond crystal. The photoanodes spectra were collected under room temperature/humidity control, after background correction. The number of scans for sample and background was set to 250. The x-axis ranged from 400 to 4000 cm^{-1} and y-axis shown as % transmittance. The resolution was 8. The same materials were also analyzed by Raman spectroscopy using a Raman microscope DXR from Thermo Scientific. The Raman spectra was recorded with a 532 nm laser, in the spectral range of 38-1500 cm^{-1}, for 3.0 mW power, in combination with a 10× objective magnification for focus and collection of Raman-scattered light. The confocal hole was set to 50 µm slit aperture.

Transmission electron microscopy (TEM) was carried out using a Hitachi H-9000 TEM microscope operating at 300 kV. The TEM samples were prepared by placing a drop of the colloidal sample on a carbon-coated copper grid and the solvent was left to evaporate at room temperature. The images were acquired with a magnification of 30000× and 300 kV (scale bar 100 nm).

The photoanodes were further characterized by using a High resolution (Schottky) Environmental Scanning Electron Microscope (SEM) with X-Ray Microanalysis and Electron Backscattered Diffraction analysis using a Quanta 400 FEG ESEM/EDAX Genesis X4M. Thickness of the films composed with TiO_2 anatase nanoparticles and TiO_2@Au modified nanocomposites was measured by SEM analysis. The images were obtained with 15 kV and different magnifications: 1000× (100 µm) and 10000× (10 µm) for a top view of the films surface, and 2500× (40 µm) for the cross section of the photoanodes. The gold content in the final nanocomposites was determined by inductively coupled plasma spectroscopy (ICP) using a Jobin-Yvon JY70 Plus spectrometer. Elemental analysis of carbon, nitrogen, hydrogen and sulfur was obtained on a Truspec 630-200-200 equipment.

DSSC measurements were accomplished by a Methrom Autolab potentiostat/galvanostat, Autolab PGSTAT302N, interfaced to computer and controlled by NOVA 1.10 software. These measurements were composed with a Frequency Response Analysis (FRA) module and a LED driver accessory. Electrochemical impedance spectroscopy (EIS) analysis was performed using the FRA module in a frequency range 0.01-100000 Hz, and the photocurrent density-photovoltage (*J-V*) response of the solar cell was obtained using PV measurement system, under 100 mW/cm^2, from a white LED, at room temperature.

7.2.3. Synthesis of colloidal Au NPs

Colloidal Au NPs were synthesized by the citrate reduction method [12,23–25]. Briefly, 5 mL of trisodium citrate solution (38.8 mM) were added to 50 mL of aqueous solution of $HAuCl_4 \cdot 3H_2O$ 1 mM, previously brought to a rolling boil with vigorous stirring. The solution turned from light yellow to ruby-red, indicating the formation of Au NPs and after one hour the heating was switched off and the agitation was kept overnight. Before using, this colloid was centrifuged for 30 minutes at 15400 g, and the supernatant was removed and replaced by 2-fold the initial volume of ultrapure water. Finally, the colloid with a particle size ~22 nm formed was stored in clean flask and protected from direct sunlight, in order to extend the stability and shelf life of the colloidal solution [6,19,28].

A different synthetic route, based on Martin method, was employed to synthesize Au NPs of size ~4 nm, using $NaBH_4$ as the reducing agent. A 10 mL of an aqueous solution containing 1 mM $HAuCl_4.3H_2O$ was added dropwise to a 30 mL of 2 mM $NaBH_4$ solution, under vigorous stirring and using an ice bath. The color of solution immediately changed to reddish pink indicating particle formation [22–24].

7.2.4. Synthesis of the siloxydithiocarbamate precursor (SiO_2/SiDTC)

The synthesis of the SiO_2/SiDTC precursor was accomplished according to the protocol described in the literature [25]. Briefly, this compound (-SiDTC) was obtained through the conversion of APTES into the corresponding dithiocarbamate in alkaline medium [25,29]. This medium was composed by a sodium ethoxide solution obtained from the reaction of 0.2 g of NaOH in 25 mL of dry ethanol over a nitrogen atmosphere, for 6 hours. The mixture was cooled in an ice bath, followed by a dropwise addition of 0.30 mL CS_2 and 1.17 mL APTES and stirring for 30 minutes. Then, the resultant yellow solution was heated at 40 ºC and left under vigorous stirring for 24 hours. After this period of time, the mixture was cooled to room temperature, and the volatile compounds were evaporated under a dynamic vacuum, in order to obtain a yellow solid [25].

7.2.5. Surface modification of TiO_2 NPs

7.2.5.1. TiO_2-SiO_2/SiDTC NPs

The surface modification of the commercial TiO_2 NPs was accomplished via a hydrolytic condensation of TEOS with the SiDTC precursor (**Figure 7.1B**) [22,25]. First, a dispersion of TiO_2 NPs (200 mg) in 150 mL of ethanol was prepared, which was left immersed in an ice bath, over 15 minutes under sonication (Sonics, Vibracell), to achieve homogenization. Afterwards, 12 mL of an ammonia solution and a mixture SiDTC and TEOS at 1:3 molar ratio was added and the resulting suspension was left in an ice bath for 2 hours, under sonication. Finally, the TiO_2-SiO_2/SiDTC NPs was washed thoroughly with ethanol [22,25], and characterized by elemental microanalysis. As expected, sulfur (S) content in the samples increased with the addition of SiDTC precursor in the TiO_2 NPs, confirming, thus, the formation of a siliceous framework incorporating SiDTC moieties bound firmly to the TiO_2 NPs.

The analysis of N/S molar ratios showed to stay in the same order of magnitude as the expected value (0.5), indicating thus the presence of dithiocarbamate groups in these materials (TiO_2-SiO_2/SiDTC) comparing to the pure TiO_2 sample [25].

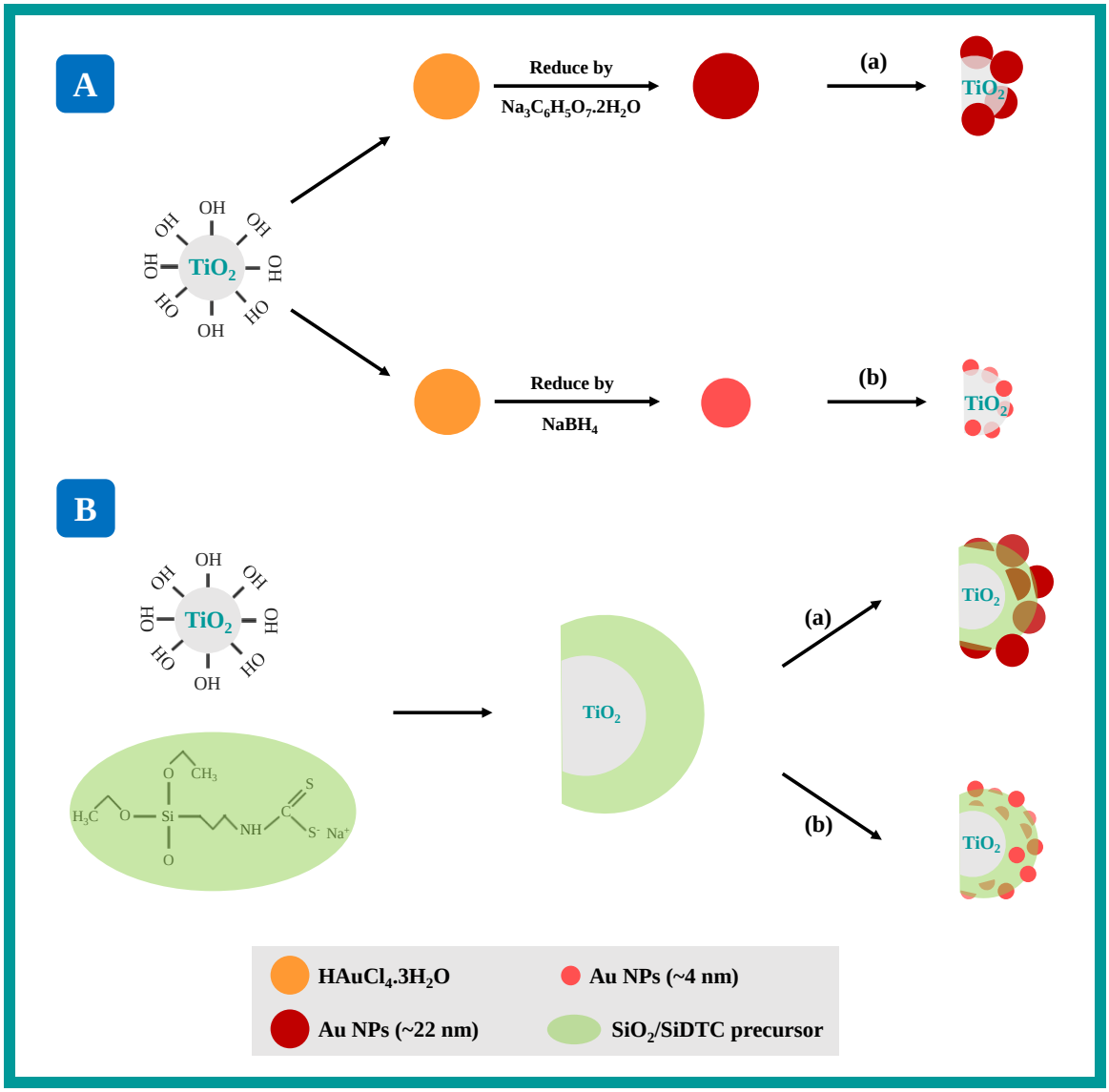

Figure 7.1. Schematic representation of the surface modification of TiO_2 NPs based in a (A) direct absorption of colloidal Au NPs obtained from citrate (a) and borohydride (b) reduction methods; and (B) chemical functionalization with a SiO_2/SiDTC precursor, followed by the attachment of the colloidal Au NPs with different particle sizes (a and b).

7.2.5.2. TiO_2@Au and TiO_2-SiO_2/SiDTC@Au nanocomposites

Different pastes were prepared for depositing films on top of a conductive glass (**Figure 7.1**). One paste was composed by TiO_2 anatase nanoparticles, dispersed in ethanol absolute, acetic acid and ultrapure water, in a v/v% ratio of 76.7:11.6:11.6, respectively. Other four pastes were prepared by loading TiO_2 NPs with colloidal Au NPs, synthesized from citrate and borohydride reduction methods (particle sizes ~22 nm and ~4 nm, respectively). Three pastes were prepared by mixing different weight ratios of colloidal Au NPs (size ~22 nm) with TiO_2 nanoparticles: 0.023%, 0.027% and 0.048%, and the other paste was made using the Au NPs with lower particle size (~4 nm), in the same proportion of higher weight ratio used in the previous paste (~0.048%) (**Figure 7.1A**). Moreover, three approaches were also accomplished, where TiO_2 NPs were chemically functionalized with dithiocarbamate groups and then loaded with colloidal Au NPs, at the same proportion weight ratio (**Figure 7.1B**).

All pastes were stirred for one hour, approximately, to achieve homogeneous solutions. These solutions were then employed next as thin-films, produced via the doctor blade method on top of fluoride-doped tin oxide (FTO, sheet resistance 13.0 Ω/sq, Sigma-Aldrich) glass. This glass was previously cleaned by ultrasonication in ethanol for 15 minutes, followed by 15 minutes in deionized water, and a drying in nitrogen atmosphere. The resulting photoanodes contained different gold contents and were characterized by ICP analysis.

7.2.5.3. Fabrication of DSSCs with TiO_2@Au modified photoanodes and evaluation of their performances

The compact film composed by different pastes was deposited on top of the FTO glass, to prevent the recombination of electrons and ions within the electrolyte solution at the FTO-electrolyte interface. The compact layers were deposited by the doctor blade method, keeping a constant area of 0.20 cm^2.

All the films were annealed at 450ºC for 30 minutes [30], cooled down to 80°C and immersed in a dye bath solution for 18 hours, in dark, at room temperature [6]. This dye solution was composed by an ethanolic solution of 0.5 mM in the N719 dye. After adsorption of dye, the photoanode was withdrawn from the solution, cleaned with ethanol to remove non-adsorbed dye, and dried at room temperature.

The counter electrodes (CEs) were prepared in parallel, by depositing an ethanolic solution of 10 mM platinum salt by spin coating at 2000 rpm for 20 seconds. Afterwards, the CEs were annealed in the oven at 450ºC for 15 minutes. The construction of the DSSCs was completed by preparing the electrolyte solution, herein composed of 0.05 M I_2, 0.1 M LiI, 0.6 M HMII and 0.5 M TBP in acetonitrile.

A sandwich configuration was made using the photoelectrode and the counter electrode, sealing the cell with a scotch magic tape (thickness 19 mm) that acts as a spacer layer between the two electrodes (**Figure 7.2**).

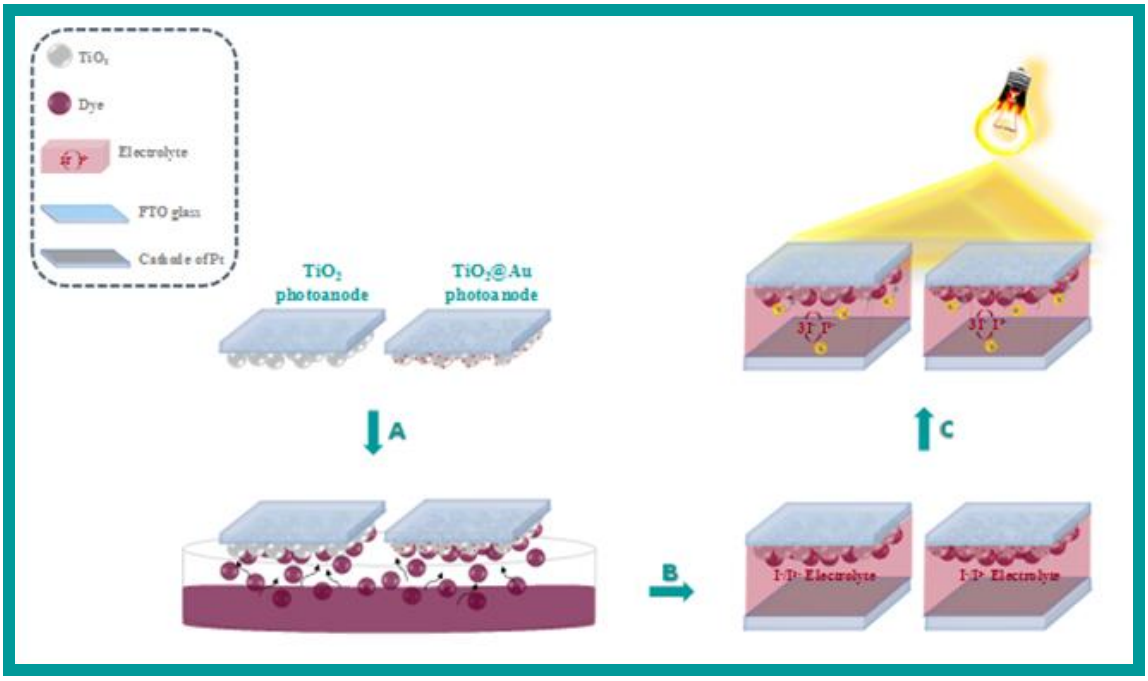

Figure 7.2. Schematic representation of a DSSC composed by TiO_2 and TiO_2@Au (~22 nm) photoanodes: (A) adsorption process of N719 dye in the thin films prepared through doctor blade method; (B) construction of sandwich configuration (photoanode/electrolyte/counter electrode) typical in a DSSC; and (C) electron flow through the DSSC under illumination.

The operation principle of these DSSCs was based in two main stages, including the thin films (TiO_2 and TiO_2@Au NPs) deposition on the FTO glass, through doctor blade method, in order to activate electronic conduction, followed by a covalent bonding process of a N719 dye solution to enhance light adsorption in the device (**Figure 7.2A**).

Then, the electrolyte (I^-/I_3^- redox couple) was introduced in the system to contact with a coloured dye able to absorb light and excite electrons, which will be injecting into the valence band of a semiconductor and travelling outside towards another electrode system to reach the dye and regenerate until its initial form. The typical sandwich configuration (photoanode/electrolyte/counter electrode) of DSSCs was completed with the insertion of the Pt counter electrode that will allow the catalysis of the redox couple regeneration reaction and the electron collection from the external circuit (**Figure 7.2B,C**) [20,21,31].

7.3. Results and Discussion

7.3.1. Characterization of materials

7.3.1.1. Optical properties of colloidal Au NPs

The visible absorption spectrum of the Au NPs colloid obtained from the citrate reduction method is shown in **Figure 7.3A** and shows the characteristic LSPR band peaked at 520 nm, which is in agreement with Au NPs whose sizes range 15-25 nm [32,33]. The size of the Au NPs was further assessed by DLS assays (**Figure 7.3B**); the average hydrodynamic diameter obtained by this technique was 22.68 ± 5.79 nm. The zeta potential of the colloidal NPs, at pH 5.6, was determined as -45.7 ± 0.6 mV, which is consistent with the presence of citrate anions coming from the reducing agent employed (trisodium citrate) at the NPs surfaces.

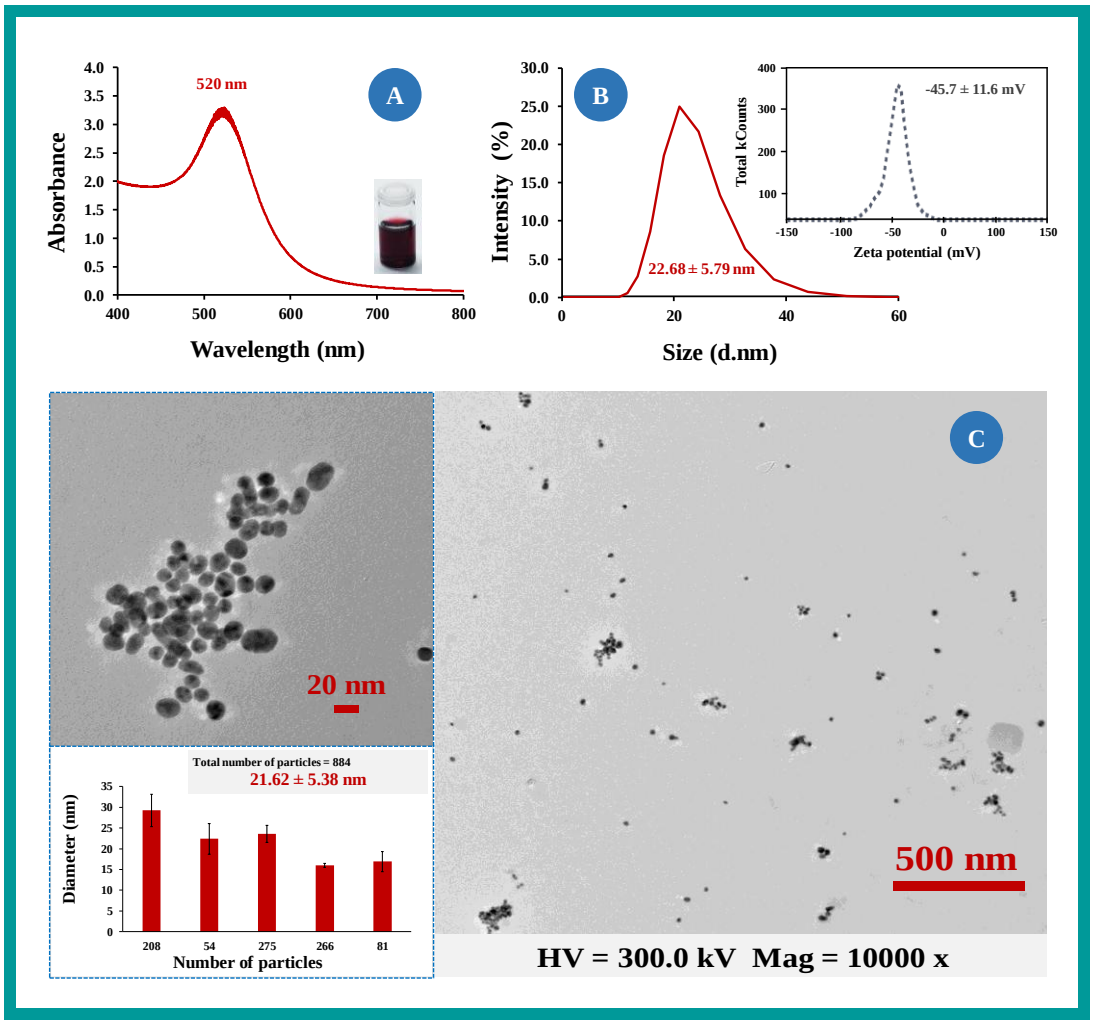

Figure 7.3. Representation of optical properties of colloidal Au NPs obtained from a citrate reduction: (A) UV-Vis spectra, (B) DLS with zeta potential analysis and (C) TEM image and the representative graph of Au NPs with average size ~22 nm.

Figure 7.3C shows the TEM images of the Au NPs, revealing a spherical morphology with some aggregates that are probably related to the sample preparation during the deposition of the colloid on the grid. The average size of the Au NPs as estimated by analysing the TEM images was 22 nm [30–34], which is consistent with the average size mentioned above. Similarly, the colloidal Au NPs obtained from the borohydride reduction were characterized by UV/Vis spectroscopy, DLS and TEM microscopy (**Figure 7.4**). The LSPR band peaked at 509 nm, corresponding to Au NPs with sizes range 3.2-5.2 nm [23,24]. Further assessments by DLS assays were performed, showing an average hydrodynamic diameter of 5.8 ± 1.3 nm, and a zeta potential, at pH 7.8, of -43.1 ± 0.6 mV.

The TEM microscopy showed Au NPs with spherical shape of an estimate average size of 4.3 ± 0.6 nm, similar to the particle size dimensions obtained in the previous techniques.

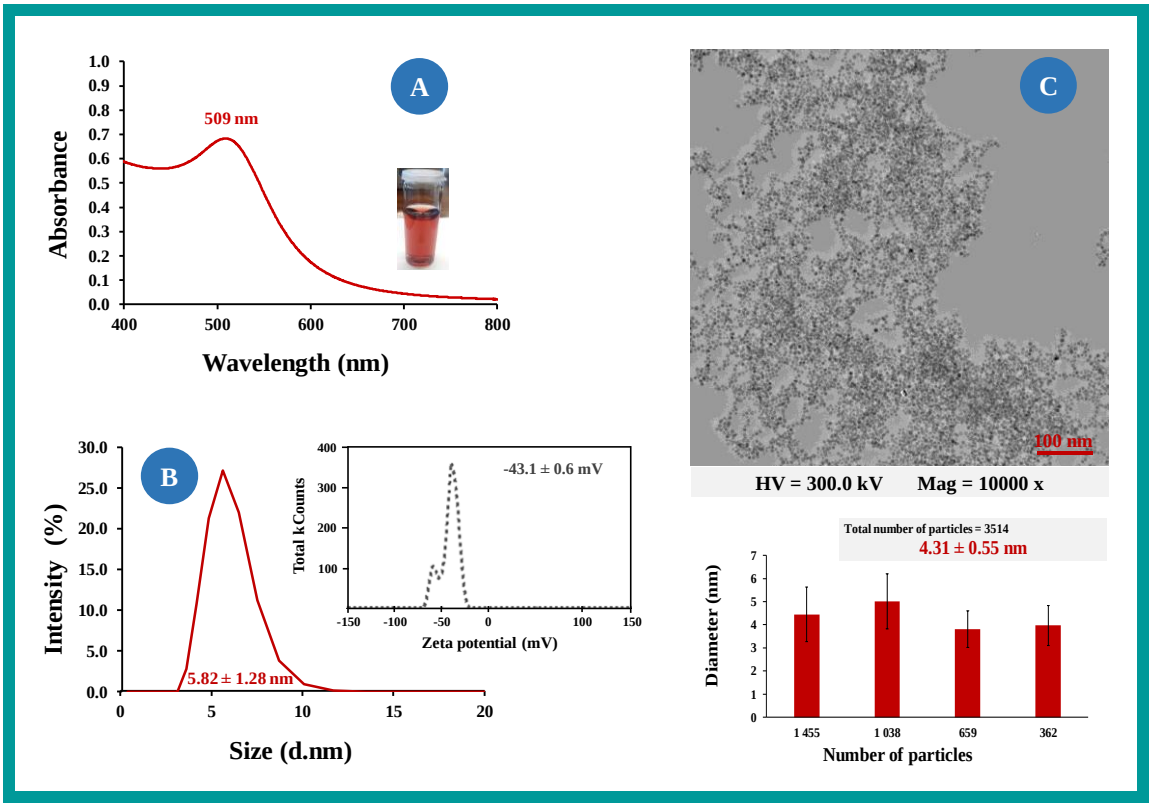

Figure 7.4. Representation of optical properties of colloidal Au NPs obtained by the borohydride reduction method: (A) UV-Vis spectrum, (B) DLS with zeta potential analysis and (C) TEM image and the representative graph of Au NPs with average size ~4 nm.

7.3.1.2. Optical characterization of photoanodes

The photoanodes of the DSSC were characterized by normalize absorbance spectra obtained from the Kubelka-Munk analysis of the measured reflectance spectra (**Figure 7.5**). This characterization was conducted only for TiO_2 photoanodes deposited on FTO-glass substrates either, with and without the N719 dye and, with and without Au NPs (size ~22 nm). The absorbance spectrum of the blank TiO_2 photoanode material displayed a flat line across the visible, just as expected (**Figure 7.5A**), with an absorbance that varies around 0.08. The presence of the dye on the photoanodes led to a broad increment of the absorbance signal within 400-600 nm, as compared to the neat TiO_2 substrates. For the substrates containing Au NPs, this increment displayed a blue shift and was much more pronounced (**Figure 7.5A**).

As expected, the absorbance observed at 400-600 nm, for the TiO_2 substrates loaded with Au NPs, depended strongly on the amount of metal added to the substrates, increasing for higher load of Au NPs, as shown **Figure 7.5B** [10,35]. The incorporation of these nanoparticles at the surface of TiO_2 films reduce the surface area available for dye absorption, and, also, high loadings of Au NPs in the TiO_2 photoanodes can affect the dye regeneration and, consequently, the collection efficiency [35].

Overall, the Au NPs were linked to the dye-TiO_2 films, causing a significant effect upon absorption spectra. This effect was more pornounced in the absorbance data and for weight ratios of Au NPs loadings between 0.023% and 0.027%.

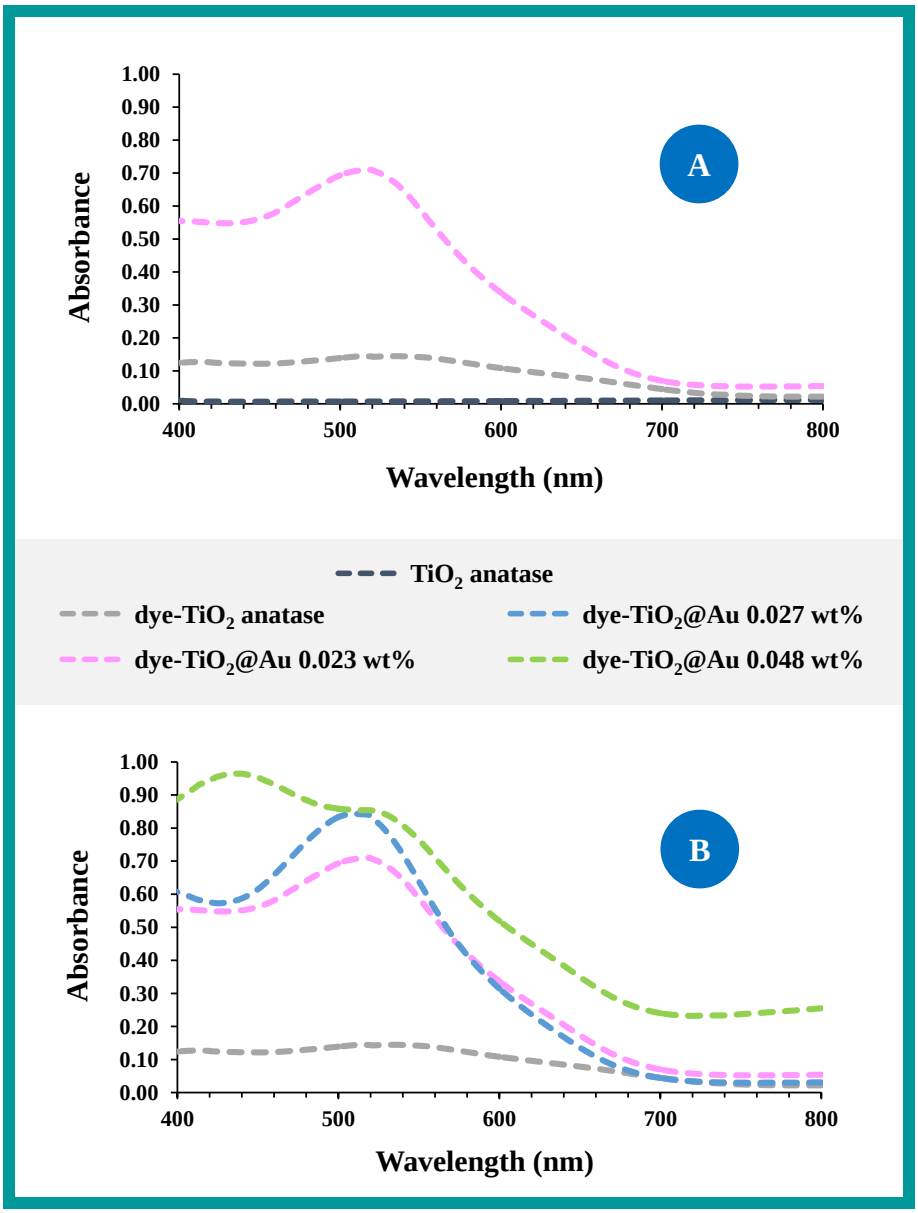

Figure 7.5. Absorbance of TiO_2 films and TiO_2@Au photoanodes containing different weight ratios of Au NPs (~22 nm) deposited on FTO substrate: (A) absorbance of TiO_2 photoanode without N719 dye absorption and dye-TiO_2 films without and with Au 0.023 wt%; and (B) absorbance of bare dye-TiO_2 film, and dye-TiO_2 photoanodes loaded with 0.023 wt%; 0.027 wt% and 0.048 wt% of Au NPs.

7.3.1.3. Vibrational spectroscopy

All samples representative of the TiO_2 photoanode and TiO_2@Au (~22 nm) modified photoanodes with different weight ratios of AuNPs: 0.023 wt%, 0.027 wt% and 0.048 wt% were analyzed through Raman and FTIR spectroscopies.

The Raman spectra of the samples have been collected in the 38-1500 cm^{-1} range (**Figure 7.6**-top). The bands peaked at 139.5, 195.1, 394.2, 515.0 and 635.9 cm^{-1} are ascribed to the anatase phase of TiO_2 [36–38]. The ratio between Raman intensity indicate the bands under analysis after the addition of 0.023 wt% and 0.027 wt% of Au loaded TiO_2 nanoparticles and pure TiO_2, collected at ~138.6 cm^{-1}, have decreased. However, the intensity ratio increased after the addition of 0.048 wt% Au. This effect may be explained by the possibility for the formation of agglomerates when high weight ratios of Au loaded TiO_2 nanoparticles are used, contributing thus for a slight increase in the relative Raman intensity [39]. In general, no significant increase of signal influenced be metal particles were identified in the samples due its low weight ratios loaded onto TiO_2 and, consequently, its weak Raman scattering power [23,36,40,41].

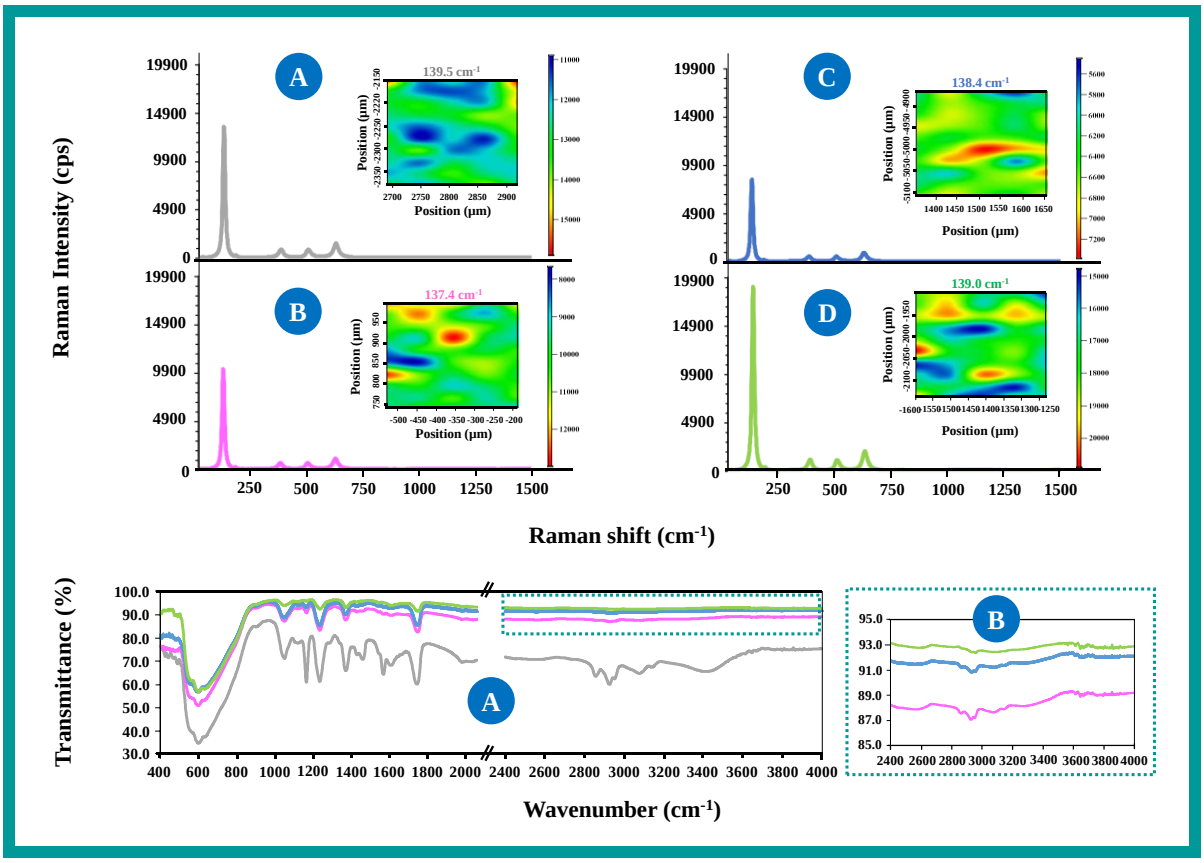

Figure 7.6. Raman and FTIR spectra of (A) TiO_2 photoanode and TiO_2 and TiO_2@Au modified photoanodes with different weight ratios of Au NPs (~22 nm): (B) 0.023 wt%, (C) 0.027 wt% and (D) 0.048 wt%, and the respective spatial maps obtained at the wavelength correspondent to the most intense Raman band.

Moreover, the overall surface of the prepared films was assessed by mapping a 5×10 µm area of the photoanodes using this spectrometer coupled to a confocal Raman microscope and an automated XY stage. Spatial maps of the Raman intensity for the band of anatase at ~140 cm^{-1} are represented for samples having different weight ratios of Au NPs/TiO_2. The mapped area is shown as an inset in each **Figure 7.6**-top, showing the colour coverage distribution map in the different photoanodes: TiO_2 anatase (A), TiO_2@Au 0.023 wt% (B), TiO_2@Au 0.027 wt% (C) and TiO_2@Au 0.048 wt% (D). Overall, it is possible to observe the differences caused in the surface of the plasmonic DSSCs when comparing with the control DSSCs. The presence of the Au NPs with ~22 nm yielded a more heterogeneous surface, with several spots showing quite distinct Raman intensity values.

The same materials were characterized by FTIR spectroscopy within the 400-4000 cm^{-1} wavenumber range. The vibrational spectra obtained are shown in **Figure 7.6A**-bottom. All samples showed a broad band at 500-800 cm^{-1}, which is assigned to the Ti-O-Ti vibrational mode in the TiO_2 lattice [39,41,42].

The FTIR spectra of TiO_2 anatase sample (**Figure 7.6A**-bottom) show bands peaked at 2857 cm^{-1}, 2927 cm^{-1} and 2853 cm^{-1} that correspond to the C-H stretching vibrations, and bands presented in a range of 3300-3500 cm^{-1} can be allocated to the stretching vibration of O-H groups [41,42].

FTIR spectra obtained of the photoanodes modified with different weight ratios of Au NPs, shown in **Figure 7.6A,B**-bottom, show absorption bands located at the same region of the TiO_2 anatase between 400-4000 cm^{-1}. However, the bands in the 3300-3500 cm^{-1} range observed in the TiO_2 anatase spectrum (**Figure 7.6B**-bottom) have disappeared with the addition of different amounts of Au NPs (~22 nm) in the photoanodes composition. The blocking of these peaks can be assigned to the stretching vibration of O-H bonds provided from the citrate species used to stabilize electrostatically the Au NPs [43].

7.3.1.4. TEM and SEM analysis of photoanodes

The TiO_2 and TiO_2@Au (~22 nm) modified nanocomposite films prepared by the doctor blade method on FTO glass surface were characterized by TEM and SEM analysis (**Figure 7.8**).

The TEM images revealed the presence of Au loaded TiO_2 nanoparticles, with sizes ranging 15-22 nm. **Figure 7.8B** clearly shows small spherical shaped Au NPs within larger TiO_2 nanoparticles, and its random distribution around the nanoparticles [11]. The scattering of the Au NPs on the surface of the semiconductor particles is highly relevant for the DSSCs performance, because the close proximity of metal NPs supress its LSPR properties. Therefore, it is desirable to have an optimum weight ratio of Au loaded TiO_2 nanoparticles in the DSSC photoanodes composition [4,10].

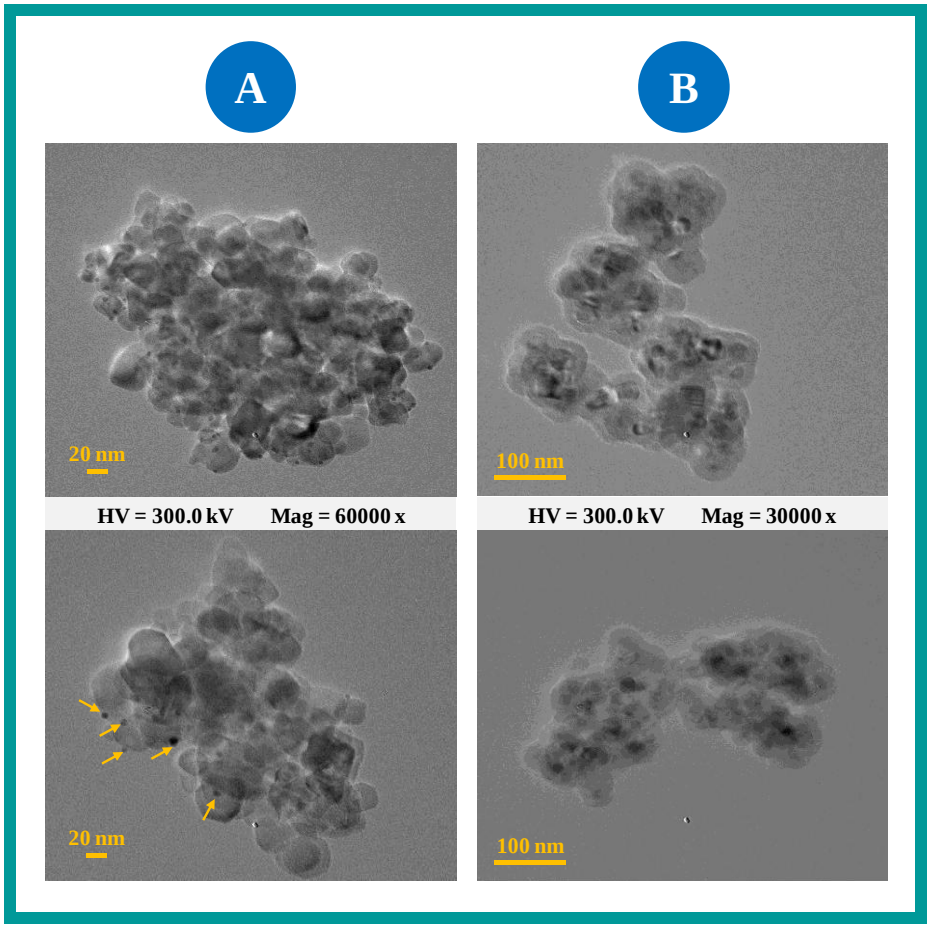

Figure 7.7. TEM images of photoanodes composed by TiO_2@Au NPs synthesized by borohydride method (~4 nm) and TiO_2 NPs chemically functionalized with siloxydithiocarbamate compound (TiO_2-SiO_2/SiDTC).

Likewise, the TiO_2@Au (~4 nm) and TiO_2-SiO_2/SiDTC modified films were characterized by TEM microscopy (**Figure 7.7A** and **B**, respectively). The TEM images (**Figure 7.7A**) revealed that the Au NPs synthesized by borohydride reduction method have been distributed around TiO_2 nanoparticles, with sizes ranging 3-7 nm. **Figure 7.7B** shows that the SiO_2/SiDTC precursor used to functionalize TiO_2 affords the appearance of amorphous capping around the TiO_2 NPs [22,25].

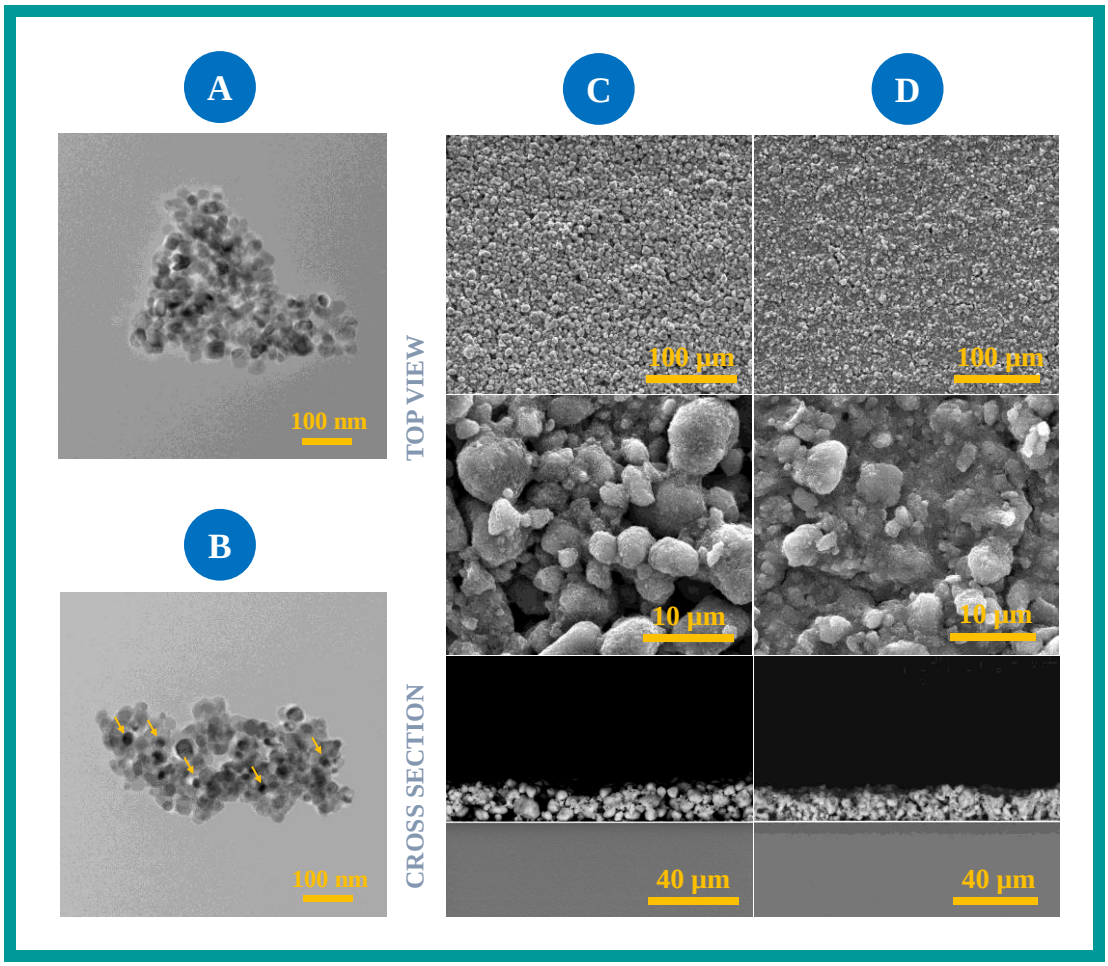

Figure 7.8. Characterization of photoanodes composed with TiO_2 nanoparticles and TiO_2@Au (~22 nm) 0.023 wt% by TEM and SEM analysis. (A) TEM images of TiO_2 nanoparticles; (B) TEM images of TiO_2@Au 0.023 wt%; (C) SEM images of TiO_2 nanoparticles and (D) SEM images of TiO_2@Au 0.023 wt%.

Further analysis to assess size and morphology was carried out by SEM observation. TiO_2 alone showed a rough morphology structure, with agglomerates ranging 2-6 µm diameter (**Figure 7.8C**). TiO_2@AuNPs (~22 nm) evidenced a more compact and less heterogeneous morphology, evidencing also agglomerated NPs ranging 3-5 µm (**Figure 7.8D**) [10]. The resulting films of TiO_2 and TiO_2@Au 0.023 wt% presented thicknesses of ~11.0 µm and ~8.0 µm, respectively, as shown by the cross-section images in **Figure 7.8C,D**.

Overall, the addition of Au NPs, with particle size ~22 nm, promoted little changes in the original morphology of TiO_2 nanoparticles. The material became more compact with particles of intermediate size, which may contribute to enhance the electrical properties of the photoanode [20].

7.3.2. Plasmonic DSSCs

7.3.2.1. Photovoltaic performance of TiO_2@Au and TiO_2-SiO_2/SiDTC@Au photoanodes-modified DSSCs

The obtained solar cells were assessed by monitoring the photocurrent density-photovoltage (*J-V*) under an incident light power of 100 mW/cm^2, at room temperature. The photovoltaic performance of DSSCs prepared with regular TiO_2 photoanodes and photoanodes of TiO_2 modified with different colloidal Au NPs (~4 nm and ~22 nm), TiO_2 doped with different amount of Au NPs with a particle size ~22 nm (0.023wt%, 0.027wt% and 0.048wt%), TiO_2 functionalized with the SiO_2/SiDTC precursor photoanodes and these type of photoanodes doped with both colloidal Au NPs (~4 nm and ~22 nm). All photoanodes previously described for the DSSCs performance are summarized in **Table 7.1** and shown in **Figure 7.9A**.

Table 7.1. Photovoltaic-characterization data of DSSCs based in different photoanodes.

Photoanode	V_{OC} (mV)	J_{SC} (mA/cm^2)	*FF* (%)	*PCE* (%)
Control - TiO_2 anatase	774.2 ± 3.5	21.5 ± 0.7	68.4 ± 0.4	11.42 ± 0.17
TiO_2@Au(~22 nm)-0.023 wt%	758.7 ± 7.2	24.6 ± 0.4	68.1 ± 0.6	12.70 ± 0.16
TiO_2@Au(~22 nm)-0.027 wt%	757.7 ± 12.7	24.4 ± 0.9	67.6 ± 0.5	12.56 ± 0.15
TiO_2@Au(~22 nm)-0.048 wt%	777.4 ± 4.9	22.2 ± 1.1	69.9 ± 0.2	12.03 ± 0.41
TiO_2@Au(~4 nm)	739.3 ± 9.4	25.2 ± 0.2	63.3 ± 0.8	11.80 ± 0.29
TiO_2-SiO_2/SiDTC	733.1 ± 2.2	25.2 ± 0.3	66.3 ± 0.6	12.24 ± 0.25
TiO_2-SiO_2/SiDTC@Au(~22 nm)	752.5 ± 9.5	24.8 ± 0.4	64.3 ± 0.1	12.02 ± 0.01
TiO_2-SiO_2/SiDTC@Au(~4 nm)	732.7 ± 10.7	25.6 ± 0.6	63.0 ± 0.2	11.84 ± 0.13

***V_{OC}*:** open-circuit potential; ***J_{SC}*:** short-circuit current density; ***FF*:** fill factor; ***PCE*:** power conversion efficiency.

A significant boost in the short-circuit current up to 24.6 mA/cm^2 was observed from the *J-V* curve of TiO_2@Au(~22 nm) 0.023wt% compared to those of the DSSCs based on TiO_2 (21.5 mA/cm^2). The TiO_2@Au(~22 nm) 0.023wt% based DSSC displaying an efficiency (η=12.70%), exhibiting an increment of 14.4% in photocurrent and 11.2% in overall power conversion efficiency (**Figure 7.9A**). This significant improvement in the photovoltaic performance may be explained through the Au NPs near-field excitations along with the incident light far-fields, providing a photocurrent enhancement [6,44].

Further studies were performed using colloidal Au NPs with lower particle sizes (~4 nm). These photoanodes provided an increment of 17.2% in photocurrent and 3.3% in overall power conversion efficiency, when compared with the conventional DSSC photoanodes (η=11.42%). However, relating to the TiO_2@Au(~22 nm) 0.048wt% based DSSC, which presents a short-circuit current up to 22.2 mA/cm^2 and a power conversion efficiency of 12.03%, it is verified that smaller Au NPs caused an improvement of 13.5% in photocurrent, but a decrease of 1.9% in overall power conversion efficiency (**Table 7.1** and **Figure 7.9**).

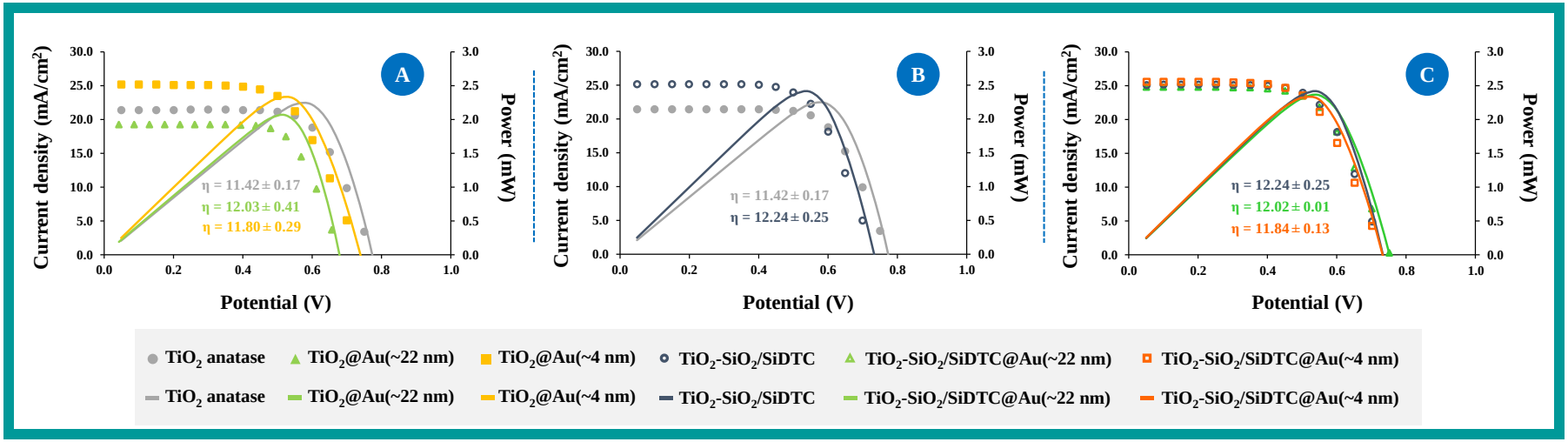

Figure 7.9. Graphical representation of photocurrent density-photovoltage (*J-V*) curves obtained for: (A) control (TiO_2) photoanode, TiO_2@Au (~4 nm) and TiO_2@Au (~22 nm) photoanodes modified DSSCs; (B) conventional DSSC photoanode composed by TiO_2, and the photoanode modified with siliceous shells enriched in SiDTC moieties (TiO_2-SiO_2/SiDTC); and (C) photoanodes composed by TiO_2-SiO_2/SiDTC and these photoanodes loaded with both colloidal Au NPs (~4 nm and 22 nm).

The chemical functionalization of the TiO_2 NPs with SiO_2/SiDTC precursor has shown an improvement of overall power conversion efficiency, as shown in **Table 7.1**. However, the significant boost was caused by the effect of hybrid material composed of siliceous domains terminated with dithiocarbamate groups in the composition of the conventional photoanodes, once it is evidenced an improvement of the photocurrent in 17.2% and, also, 7.2% in overall power conversion efficiency (**Figure 7.9B**). The loaded of both Au NPs sizes (~4 nm and ~22 nm) in these modified TiO_2-SiO_2/SiDTC photoanodes revealed a decrease of 3.3% and 1.8% in the power conversion efficiency of Au NPs with ~4 nm and ~22 nm, respectively. Indeed, the formation of Au-S linkages were achieved, as expected, due to the stronger chemical bonds formed between the soft character of both gold (acid) and sulfur (donor base) [22]. This fact was observed in the DSSCs performance, once a decrease effect in the power conversion efficiency and photocurrent parameters was evidenced, which may have resulting from the difficulty of molecular dye injects charges into this hybrid framework composed siliceous shells enriched in dithiocarbamate groups, influencing thus the plasmonic effect of Au NPs that were loaded in these photoanodes [45]. Despite this behavior, the loaded of Au NPs in the modified photoanodes (TiO_2-SiO_2/SiDTC) exhibited an increment of 11.7% in photocurrent of Au NPs with ~22 nm and 1.6% in photocurrent of Au NPs with ~4 nm, although a non-significant improvement of the overall power conversion efficiency was obtained regarding to TiO_2@Au (~4 nm and ~22 nm) photoanodes (**Figure 7.9C**).

The intensity of the near-field effect, which affects the Au NPs performance, depends on the size/shape of NPs and also on the surrounding environment. Concerning size, there is an optimum value for the diameter of the Au NPs to promote the near-field intensity effects and, consequently, enhance the DSSC performance [6]. Also, due to the LSPR effect of Au NPs, the large number of electrons accumulated on its surface are excited and transferred to the conduction band of the TiO_2, being collected by the current collector (FTO) and improving the photocurrent under irradiation in the visible region [11]. Herein, a diameter of ~22 nm was found better in terms of DSSC performance (**Figure 7.10A,B**).

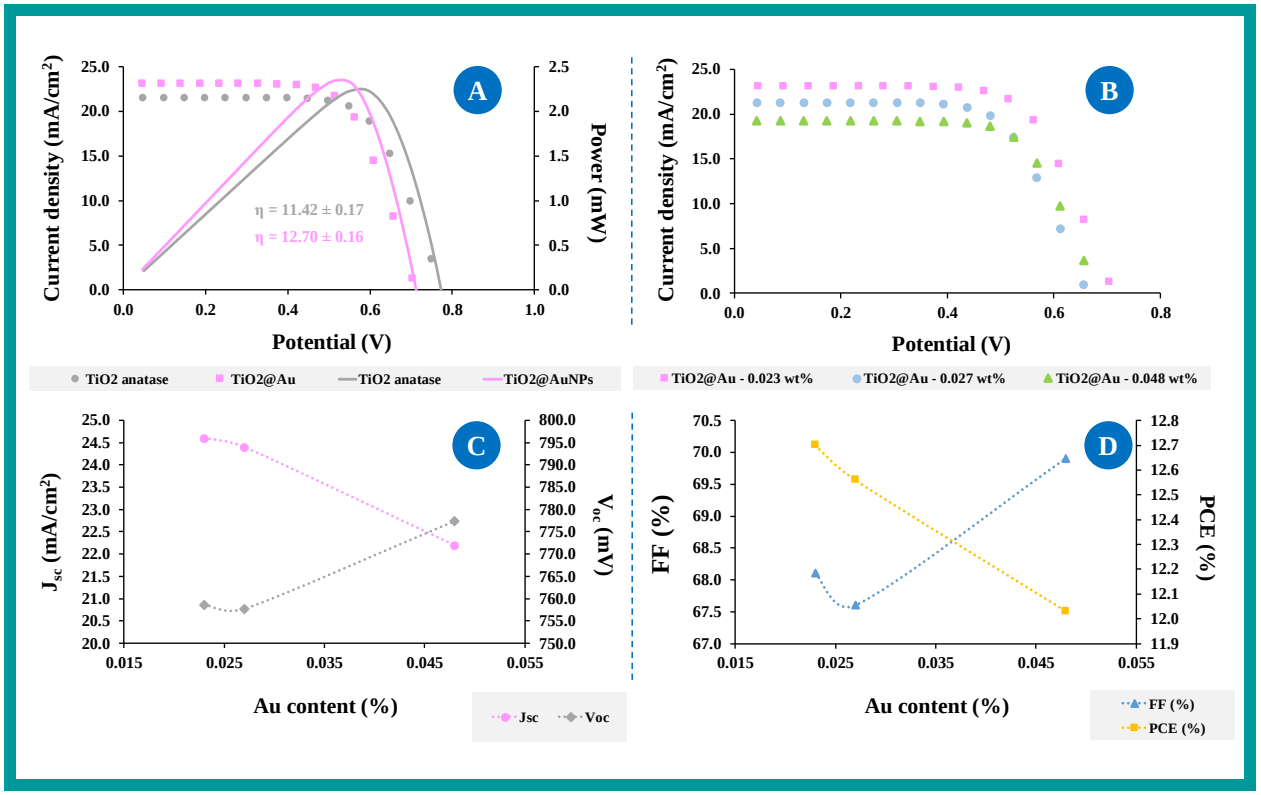

Figure 7.10. Plots of photocurrent density-photovoltage (*J-V*) curves (A and B) and DSSC parameters (C and D) obtained for: (A) *J-V* curves of control (TiO_2) and TiO_2@Au (~22 nm) photoanode modified DSSCs with 0.023w% of Au NPs; and (B) *J-V* curves, (C) short-circuit current density (J_{SC}) and open-circuit potential (V_{OC}), and (D) fill factor (*FF*) and power conversion efficiency (*PCE*) of TiO_2@Au nanocomposite modified photoanodes with different Au content, respectively.

In addition to size, the Au load amount in the TiO_2-based photoanodes also varied, which could also impact upon the DSSC performance. The photocurrent density-photovoltage (*J-V*) curves recorded for the TiO_2@Au nanocomposites modified photoanodes with different Au contents (**Figure 7.10B**) have been used to calculate the corresponding photovoltaic performance data (**Table 7.1**) and plotted according to the Au load in **Figure 7.10C,D**.

In general, additional increments in Au content showed a decrease in the power conversion efficiency. Such decrease may reflect the saturation effect of localized surface plasmon that induces enhancement of DSSC performance, due to the increase in impurities and recombination losses brought by incorporation of these nanoparticles into the TiO_2 matrix. This recombination can result from the excess of Au present in the composite, which may lead to reduce the number of charge carriers that will affect the dye regeneration and promote the decrease of J_{SC} and the increase of V_{OC}, and consequently provide the decrease of overall conversion efficiency of the DSSCs [3,23,35]. The J_{SC} was increased by a decrease in the Au content and attained a maximum of 24.6 mA/cm^2 with 0.023% (**Figure 7.10C**). The J_{SC} decreased to 24.4 mA/cm^2 and 22.2 mA/cm^2 with 0.027% and 0.048% Au loading in the photoanode of the DSSC. On the other hand, the V_{OC} trend increased with higher amounts of Au, from ~757.7 to 777.7 mV (**Figure 7.10D**).

The slight decrease of the performance of the plasmonic DSSCs with higher Au (~22 nm) loading in TiO_2 nanoparticles could be due to the increase recombination within the cell, being this phenomenon also observed through electrochemical impedance spectroscopy (EIS) results [4].

7.3.2.2. Electrochemical behaviour of TiO_2@Au(~22 nm) photoanodes-modified DSSCs

For the interfacial charge transfer process within the conventional and plasmonic DSSCs produced, the EIS measurements were performed in the frequency range between 0.01 and 100000 Hz, under illumination and open circuit conditions for N719 dye. The impedance data of the DSSC samples are summarized in **Table 7.2** while their Nyquist plots are shown in **Figure 7.11**. All the cells were evaluated at 0.7 V potential, under dark conditions.

Table 7.2. EIS fitted parameters obtained from Nyquist plots of the fabricated DSSC devices with and without Au NPs.

Photoanode	R_s (Ω)	R_{ct2} (Ω)	CPE_2 (µF)	τ_s (µs)	τ_n (µs)	η_c (%)
Control - TiO_2 anatase	16.51	7.54	4.60	75.91	34.66	43.05
TiO_2@Au - 0.023 wt%	17.58	5.85	5.19	91.31	30.38	31.48
TiO_2@Au - 0.027 wt%	17.95	6.46	4.51	81.03	29.16	34.09
TiO_2@Au - 0.048 wt%	17.03	6.19	5.39	91.79	33.37	34.33

***R_s*:** series resistance; ***R_{ct}*:** charge transfer resistance; ***CPE*:** chemical capacitance; ***τ_s*:** electron transport time; ***τ_n*:** electron lifetime; ***η_c*:** charge collection efficiency.

The EIS parameters shown in **Table 7.2** were further fitted through an equivalent circuit (in the center of **Figure 7.11**). The circuit in a conductive state was represented by a combination of a series resistance and charge transfer resistance (R_s and R_{ct}, respectively), a constant phase element (*CPE*) and Gerischer impedance (*G*). The impedance related to the dye-adsorbed photoanode and electrolyte interface is represented by R_{ct2} while the impedance between counter electrode and electrolyte interface was denoted by R_{ct1}. Moreover, the equivalent circuit contains a Gerischer impedance (symbol *G*) that transduces the recombination rate corresponding to the conductivity observed in the system under illumination, between the electron transport resistance and the charge transfer resistance that occurs at the photoanode/electrolyte interface [37,46].

Comparing to the Nyquist plots of control DSSCs (no Au loaded), an increment of 6.48% in the R_s value was observed for a 0.023 wt% Au NPs load (**Figure 7.11A**), thereby improving the charge transportation (τ_s) and decreasing the electron lifetime (τ_n) of the DSSC [46]. The electron lifetime, calculated by means of **equation 7.1**.

$$\tau_n = R_{ct} \times CPE \qquad \textbf{(equation 7.1)}$$

The values 34.66 and 30.38 µs have been obtained for τ_n, for conventional and plasmonic DSSC with 0.023 wt% of Au, respectively, showing a decrease of 12.35% in the τn value, which indicates an increase of the carrier recombination, and thus the enhancement of J_{SC} [37,44].

Well-defined semicircles in the middle frequency region of the Nyquist plots (**Figure 7.11A**), correspondent to the electron transport and recombination process within the photoanode interface was analyzed. The highest recombination resistance promoted by control DSSC comparatively with the plasmonic DSSC with 0.023 wt% of Au NPs was, thus, evidenced. Therefore, an interface charge resistance (R_{ct2}) of 7.54 and 5.85 Ω for TiO_2 and TiO_2@Au(~22 nm) 0.023wt% DSSCs, respectively, were obtained, with 4.60 and 5.19 μF of chemical capacitance (CPE_2). The increasing of the CPE_2 values can be explained by its contribution to ensure that charge carriers exist for a longer time, reflected by an enhancement of 20.29% in τs when 0.023 wt% of Au NPs are present [37,44]. This value was obtained by **equation 7.2**.

$$\tau_s = R_s \times CPE \qquad \textbf{(equation 7.2)}$$

In addition, the photovoltaic performance of the DSSC was also evaluated by the charge collection efficiency (η_c), obtained by **equation 7.3**.

$$\eta_c = \frac{1}{(1+\frac{R_s}{R_{ct}})} \times 100 \qquad \textbf{(equation 7.3)}$$

A decrease of 26.88% in the η_c was obtained upon the addition of Au NPs [40]. As the result, it can be remarked that the shorter R_{ct} in the system upon the addition of 0.023 wt% of Au NPs may provide an increment of up to 14% in the photocurrent and up to 11% in overall *PCE* as previously described [46].

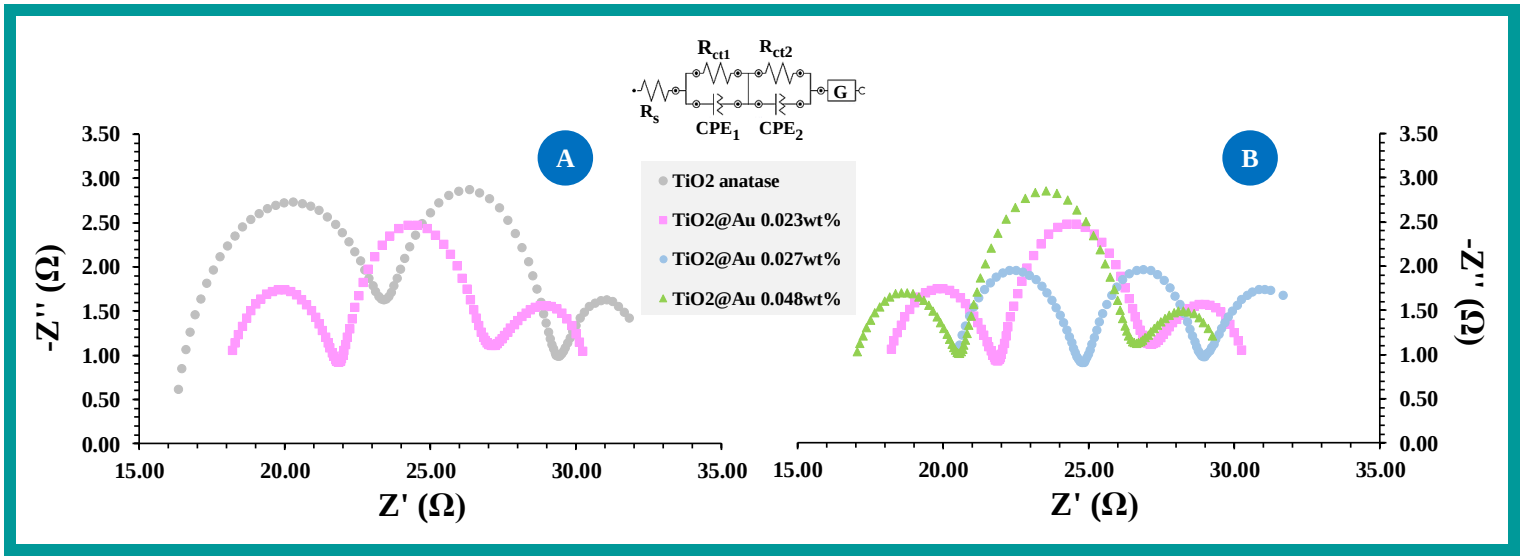

Figure 7.11. EIS data of four different DSSCs composed by (A) TiO_2 anatase and TiO_2@Au 0.023 wt%, and (B) TiO_2 with different weight ratios of Au NPs (~22 nm): 0.023; 0.027 and 0.048 wt%.

A similar study was performed to compare the cells with different weight ratios between 0.023-0.048wt% of Au NPs (**Figure 7.11A**). A variation in the R_s values was evidenced upon the addition of different Au NPs ratios (0.023wt%, 0.027wt% and 0.048wt%) used in the photoanode composition. An increment of 2.10% and 8.72% in R_s values were obtained comparing to the lower weight ratio of Au introduced into the system (TiO_2@Au(~22 nm) 0.023 wt%) and to the control DSSC, respectively. However, the addition of higher amount of Au NPs (TiO_2@Au(~22 nm) 0.048 wt%) yielded a decrease of 3.13% in R_s values, comparing to the TiO_2@Au(~22 nm) 0.023 wt% DSSC, but an enhancement of 3.15% to R_s values for the blank DSSC. This may be explained by the improvement of τ_s and the decrease of τ_n in this plasmonic DSSC [46]. In general, the R_{ct} value increased in the order of TiO_2@Au(~22 nm) 0.023 wt% < TiO_2@Au(~22 nm) 0.048 wt% < TiO_2@Au(~22 nm) 0.027 wt% < TiO_2 anatase (**Figure 7.11A,B**), showing the crucial dependence of the charge transport in a plasmonic DSSC [27,37,44]. As a result, the photoanodes with higher amount of Au NPs demonstrated an ineffective electron transfer process between the photoanode and electrolyte interface. This was further confirmed by a decrease in the J_{SC} and *PCEs* values, obtained in the plasmonic cells composed by TiO_2@Au(~22 nm) 0.027 wt% and TiO_2@Au(~22 nm) 0.048 wt%, and also in the conventional DSSC, as shown in **Table 7.2**.

7.4. Conclusions

Simple approaches to incorporate Au NPs, with different particles sizes (~4 nm and ~22 nm) in the DSSCs photoanodes were established and characterized, as well as, a more complex strategy was performed, functionalising, first, the TiO_2 NPs with a SiDTC precursor, followed by the loading of colloidal Au NPs with particle sizes of ~4 nm and ~22 nm.

Overall, the DSSCs fabricated with TiO_2@Au(~22 nm) photoanodes were evidenced better improvement in the photovoltaic properties, resulting from a synergistic effect between this colloidal Au and TiO_2 NPs, comparing with the research already described in the literature. Furthermore, the TiO_2@Au(~22 nm) photoanodes applying a very low amount of Au NPs, 0.023 wt%, showed the higher power conversion efficiency, up to 12.70%, when compared to the control photoanode composed with only TiO_2 (11.42%) under simulated solar irradiation conditions (100 mW/cm^2). Therefore, this work showed the beneficial influence of plasmonic Au nanoparticles to the photovoltaic performance with a simple strategy, allowing the improvement of the visible light adsorption, due its surface plasmon effect resultant of light harvesting property in the visible region and its scattering properties.

Moreover, the strategies that presented the modification of TiO_2 NPs chemically with dithiocarbamate groups showed that can be a promising tool to be employed in the plasmonics DSSCs. However, further studies will have to be done.

References

[1] B. O'Regan, M. Grätzel, 'A low-cost high efficiency solar cell based on dye-sensitized colloidal TiO_2 films', *Nature*, vol. 353, no. 6346, pp. 737–740, 1991.

[2] A. Yella, H.W. Lee, H.N. Tsao, C. Yi, A.K. Chandiran, M.K. Nazeeruddin, E.W.G. Diau, C.Y. Yeh, S.M. Zakeeruddin, M. Gratzel, 'Porphyrin-Sensitized Solar Cells with Cobalt (II/III)-Based Redox Electrolyte Exceed 12 Percent Efficiency', *Science*, vol. 334, no. 6056, pp. 629–634, 2011.

[3] C.C. Chou, K.Y. Tsao, C.C. Wu, H. Yang, C.M. Chen, 'Improved power conversion efficiency for dye-sensitized solar cells using a subwavelength-structured antireflective coating', *Applied Surface Science*, vol. 328, pp. 198–204, 2015.

[4] H.K. Jun, M.A. Careem, A.K. Arof, 'Plasmonic Effects of Quantum Size Gold Nanoparticles on Dye-sensitized Solar Cell', *Materials Today: Proceedings*, vol. 3, pp. S73–S79, 2016.

[5] T. Asano, T. Kubo, Y. Nishikitani, 'Electrochemical properties of dye-sensitized solar cells fabricated with PVDF-type polymeric solid electrolytes', *Journal of Photochemistry and Photobiology A: Chemistry*, vol. 164, no. 1–3, pp. 111–115, 2004.

[6] Chander, N., Khan, A.F., Thouti, E., Sardana, S.K., Chandrasekhar, P.S., Dutta, V., and Komarala, V.K. (2014) Size and concentration effects of gold nanoparticles on optical and electrical properties of plasmonic dye sensitized solar cells. Solar Energy, 109, 11–23.

[7] D.W. Zhang, M. Wang, A.G. Brolo, J. Shen, X.D. Li, S.M. Huang, 'Enhanced performance of dye-sensitized solar cells using gold nanoparticles modified fluorine tin oxide electrodes', *Journal of Physics D: Applied Physics*, vol. 46, no. 8, 2013.

[8] D. Kozanoglu, D.H. Apaydin, A. Cirpan, E.N. Esenturk, 'Power conversion efficiency enhancement of organic solar cells by addition of gold nanostars, nanorods, and nanospheres', *Organic Electronics: physics, materials, applications*, vol. 14, no.7, pp. 1720–1727, 2013.

[9] A. Pandikumar, S.P. Lim, S. Jayabal, N.M. Huang, H.N. Lim, R. Ramaraj, 'Titania@gold plasmonic nanoarchitectures: An ideal photoanode for dye-sensitized solar cells', *Renewable and Sustainable Energy Reviews*, vol. 60, pp. 408–420, 2016.

[10] H. Ninsonti, W. Chomkitichai, A. Baba, N. Wetchakun, W. Kangwansupamonkon, S. Phanichphant, K. Shinbo, K. Kato, F. Kaneko, 'Au-Loaded Titanium Dioxide Nanoparticles Synthesized by Modified Sol-Gel/Impregnation Methods and Their Application to Dye-Sensitized Solar Cells', *International Journal of Photoenergy*, pp. 1–8, 2014.

[11] S.P. Lim, A. Pandikumar, H.N. Lim, R. Ramaraj, N.M. Huang, 'Boosting Photovoltaic Performance of Dye-Sensitized Solar Cells Using Silver Nanoparticle-Decorated N,S-Co-Doped-TiO_2 Photoanode', *Scientific reports*, vol. 5, no. 11922, 2015.

[12] V.D. Dao, H.S. Choi, 'Highly-Efficient Plasmon-Enhanced Dye-Sensitized Solar Cells Created by Means of Dry Plasma Reduction', *Nanomaterials*, vol. 6, no. 4, 2016.

[13] J.T. Park, W.S. Chi, H. Jeon, J.H. Kim, 'Improved electron transfer and plasmonic effect in dye-sensitized solar cells with bi-functional Nb-doped TiO_2/Ag ternary nanostructures', *Nanoscale*, vol. 6, no. 5, pp. 2718–2729, 2014.

[14] A. Brolo, 'Plasmonics for future biosensors', *Nature Photonics*, vol. 6, pp. 709–713, 2012.

[15] Y.H. Jang, Y.J. Jang, S.T. Kochuveedu, M. Byun, Z. Lin, D.H. Kim, 'Plasmonic dye-sensitized solar cells incorporated with Au-TiO_2 nanostructures with tailored configurations', *Nanoscale*, vol. 6, no. 3, pp. 1823–1832, 2014.

[16] X. Wang, C.E. Egan, M. Zhou, K. Prince, D.R.G. Mitchell, R.A. Caruso, 'Effective gel for gold nanoparticle formation, support and metal oxide templating', *Chemical Communications*, vol. 104, no. 29, pp. 3060-3062, 2007.

[17] A. Kudo, T. Fujita, X.Y. Lang, L.Y. Chen, M.W. Chen, 'Enhanced Electrochemical Performances of Nanoporous Gold by Surface Modification of Titanium Dioxide Nanoparticles', *Materials Transactions*, vol. 51, no. 9, pp. 1566–1569, 2010.

[18] H. Choi, W.T. Chen, P.V. Kamat, 'Know Thy Nano Neighbor. Plasmonic versus Electron Charging Effects of Metal Nanoparticles in Dye-Sensitized Solar Cells', *ACS nano*, vol. 6, no. 5, pp. 4418–4427, 2012.

[19] S.K. Ghosh, T. Pal, 'Interparticle coupling effect on the surface plasmon resonance of gold nanoparticles: From theory to applications', *Chemical Reviews*, vol. 107, no. 11, pp. 4797–4862, 2007.

[20] S.P. Lim, Y.S. Lim, A. Pandikumar, H.N. Lim, Y.H. Ng, R. Ramaraj, D.C.S. Bien, O.K.A.Z. Huang, N. Ming, 'Gold–silver@TiO_2 nanocomposite-modified plasmonic photoanodes for higher efficiency dye-sensitized solar cells', *Physical Chemistry Chemical Physics*, vol. 19, pp. 1395–1407, 2016.

[21] J. Kimling, M. Maier, B. Okenve, V. Kotaidis, H. Ballot, A. Plech, 'Turkevich method for gold nanoparticle synthesis revisited', *Journal of Physical Chemistry B*, vol. 110, no. 32, pp. 15700–15707, 2006.

[22] J.L. Lopes, K.L. Marques, A.V. Girão, E. Pereira, T. Trindade, 'Functionalized magnetite particles for adsorption of colloidal noble metal nanoparticles', *Journal of Colloid and Interface Science*, vol. 475, pp. 96–103, 2016.

[23] C. Deraedt, L. Salmon, S. Gatard, R. Ciganda, R. Hernandez, J. Ruiz, D. Astruc, 'Sodium borohydride stabilizes very active gold nanoparticle catalysts', *Chemical Communications*, vol. 50, pp. 14194–14196, 2014.

[24] E.M. Rico, 'Multi-functional gold nanoparticles for drug delivery', *Advances in Experimental Medicine and Biology*, vol. 620, pp. 48-56, 2012.

[25] D.S. Tavares, A.L. Daniel-da-Silva, C.B. Lopes, N.J.O. Silva, V.S. Amaral, J. Rocha, E. Pereira, T. Trindade, 'Efficient sorbents based on magnetite coated with siliceous hybrid shells for removal of mercury ions', *Journal of Materials Chemistry A*, vol. 1, no. 28, pp. 8134–8143, 2013.

[26] J.R. Durrant, S.A. Haque, 'Solar Cells: a solid compromise', *Nature Materials*, vol. 2, no. 6, pp. 362-363, 2003.

[27] M.A.K.L. Dissanayake, J.M.K.W. Kumari, G.K.R. Senadeera, C.A. Thotawatthage, 'Efficiency enhancement in plasmonic dye-sensitized solar cells with TiO_2 photoanodes incorporating gold and silver nanoparticles', *Journal of Applied Electrochemistry*, vol. 46, no. 1, pp. 47–58, 2016.

[28] C.D. Keating, M.D. Musick, M.H. Keefe, M.J. Natan, 'Kinetics and Thermodynamics of Au Colloid Monolayer Self-Assembly', *Journal of Chemical Education*, vol. 76, no. 7, pp. 949–955, 1999.

[29] S. Goubert-Renaudin, R. Schneider, A. Walcarius, 'Synthesis of new dithiocarbamate-based organosilanes for grafting on silica', *Tetrahedron Letters*, vol. 48, no. 12, pp. 2113–2116, 2007.

[30] K.T. Dembele, R. Nechache, L. Nikolova, A. Vomiero, C. Santato, S. Licoccia, F. Rosei, 'Effect of multi-walled carbon nanotubes on the stability of dye sensitized solar cells', *Journal of Power Sources*, vol. 233, pp. 93–97, 2013.

[31] Frens, G. (1973) Controlled Nucleation for the Regulation of the Particle Size in Monodisperse Gold Suspensions. Nature Physical Science, 241, 20–22.

[32] J. Turkevich, 'Colloidal gold. Part I - Historical and preparative aspects, morphology and structure', *Gold Bulletin*, vol. 18, no. 3, pp. 86–91, 1985.

[33] J. Turkevich, 'Colloidal gold. Part II - Colour, coagulation, adhesion, alloying and catalytic properties', *Gold Bulletin*, vol. 18, no. 4, pp. 125–131, 1985.

[34] S.O. Pereira, A. Barros-Timmons, T. Trindade, 'Biofunctionalisation of colloidal gold nanoparticles via polyelectrolytes assemblies', *Colloid and Polymer Science*, vol. 292, no. 1, pp. 33–50, 2014.

[35] J. Villanueva-Cab, J.L. Montaño-Priede, U. Pal, 'Effects of Plasmonic Nanoparticle Incorporation on Electrodynamics and Photovoltaic Performance of Dye Sensitized Solar Cells', *The Journal of Physical Chemistry C*, vol. 120, no. 19, pp. 10129-10136, 2016.

[36] J. Wu, Z. Lan, J. Lin, M. Huang, Y. Huang, L. Fan, G. Luo, 'Electrolytes in dye-sensitized solar cells', *Chemical Reviews*, vol. 115, no. 5, pp. 2136–2173, 2015.

[37] U. Mehmood, S. Rahman, K. Harrabi, I. Hussein, B.V. Reddy, 'Recent Advances in Dye Sensitized Solar Cells', *Advances in Materials Science and Engineering*, pp. 1–12, 2014.

[38] S. Mayumi, Y. Ikeguchi, D. Nakane, Y. Ishikawa, Y. Uraoka, 'Effect of Gold Nanoparticle Distribution in TiO_2 on the Optical and Electrical Characteristics of Dye-Sensitized Solar Cells', *Nanoscale Res. Lett.*, vol. 12, no. 1, 2017.

[39] S. Kurien, 'Chapter 4: analysis of FTIR spectra of nanoparticles of $MgAl_2O_4$, $SrAl_2O_4$, and $NiAl_2O_4$', 2005.

[40] W. Haiss, N.T.K. Thanh, J. Aveyard, D.G. Fernig, 'Determination of Size and Concentration of Gold Nanoparticles from UV/Vis Spectra', *Analytical Chemistry*, vol. 79, no. 11, pp. 4215-4221, 2007.

[41] G. Socrates, 'Infrared and Raman characteristic group frequencies', third edition, *John Wiley & Sons, Ltd*, London, United Kingdom, 2004.

[42] J. Huang, Q. Li, D. Sun, Y. Lu, 'Biosynthesis of silver and gold nanoparticles by novel sundried Cinnamomum camphora leaf', *Nanotechnology*, vol. 18, no. 10, 2007.

[43] J.W. Park, J.S. Shumaker-Parry, 'Structural study of citrate layers on gold nanoparticles: Role of intermolecular interactions in stabilizing nanoparticles', *Journal of the American Chemical Society*, vol. 136, no. 5, pp. 1907–1921, 2014.

[44] J. Gong, J. Liang, K. Sumathy, 'Review on dye-sensitized solar cells (DSSCs): Fundamental concepts and novel materials', *Renewable & Sustainable Energy Reviews*, vol. 16, no. 8, pp. 5848–5860, 2012.

[45] S.W. Sheehan, H. Noh, G.W. Brudvig, H. Cao, C.A. Schmuttenmaer, 'Plasmonic Enhancement of Dye-Sensitized Solar Cells Using Core−Shell−Shell Nanostructures', *Journal of Physical Chemistry C*, vol. 117, pp. 927–934, 2013.

[46] A.A. Shah, A.A. Umar, M.M. Salleh, 'Efficient quantum capacitance enhancement in DSSC by gold nanoparticles plasmonic effect', *Electrochimica Acta*, vol. 195, pp. 134–142, 2016.

CHAPTER 8

CONCLUSIONS AND FUTURE WORK

This chapter will address the main conclusions of the research work developed along this thesis and some future prespectives that can be adopted in the proposed approaches.

8.1. General conclusions

This thesis describes new approaches for biosensing materials and platforms, aiming to create non-invasive clinical methodologies to be applied in the early diagnosis and screening of cancer diseases. Different cancer biomarkers were tested, and new synthetic receptors with high affinity for these biomarkers were successfully obtained, using electrochemical techniques that enable monitoring the target analyte at low concentrations and in low sample volumes.

For this purpose, different biorecognition elements were developed herein, including natural antibodies and plastic antibodies, making use of molecular imprinting techniques and specific nanomaterials, in order to improve the cancer biomarker binding and mimic these events in real and complex environments.

Regarding the transduction employed herein, potentiometry could be a suitable strategy for an early diagnosis of cancer biomarkers, due to its low-cost manufacturing using cheap materials, and its feasibility for the portability of the devices. However, this technique presents a strong a limitation in terms of reproducibility regarding the changes in the baseline potential among different electrodes of the same batch. This is an outcome of casting different amounts of selective membrane in each electrode body, because the mixture contains a volatile component. Thus, accurate results need a previous calibration of the electrode carrying out the analysis. Other electroanalytical techniques, such as EIS, CV and SWV, have demonstrated to be rapid and sensitive techniques, able to achieve lower detection capability in good agreement, or better, with other methodologies reported in the literature and within the normal physiological values referenced for the detection of cancer biomarkers, as CEA. Overall, these devices may also offer portable versions to carry out tests on-site, when combining biosensors technology with photovoltaic cells.

The first biosensor developed mainly focused on the development of a simple analytical strategy to monitoring the CRT metabolite in urine samples, a potential biomarker for an early diagnosis of ovarian cancer. Thus, an artificial antibody was created on a graphene oxide support, imprinting sites with charged monomers, followed by its incorporation in a PVC membrane. Electrodes of different solid conductive platforms, as graphite, FTO glass and ITO coated PET slides were coated with the PVC membranes and evaluated by potentiometry. The final devices provided suitable features, showing good sensitivity and selectivity, fast response and good detection capability to detect CRT in biological samples of ovarian cancer individuals, in a clinical context.

As a non-invasive cancer biomarker directly used in a clinical context, it was selected CEA protein. It is a glycoprotein of great importance for an early diagnosis and screening of colorectal cancer. Herein, two sensitive immunosensors and an artificial antibody for CEA detection were developed using different strategies on top of a conductive glass support, as FTO glass, and analytically evaluated by electrochemical techniques (EIS, CV and SWV). Both immunosensors showed to be a potential method for screening CEA towards on-site application, mainly due to its simplicity, short response time and LODs below to the normal physiological values referenced for this target detection. Regarding the biomimetic material for CEA, a simplicity in designing, low-cost and quick manufacturing, comparing to the conventional or concurrent methodologies described in the literature was achieved. This device was, also, proved to be a promising tool to monitor CEA for clinical applications, presenting a good sensitivity and selectivity, once it can detect CEA concentration levels within the normal physiological values.

In order to offer easy access and portability features for a given biosensor, able to monitor cancer biomarkers in biological fluids, a new approach was presented herein, combining biosensoring technology with photovoltaic cells, as DSSCs. DSSCs are an electrical energy generator inspired in photosynthesis, and, thus, may lead to the production of self-sustained biosensors. For this purpose, an electrochemical immunosensing system for CEA was implemented in a DSSC set-up that acted as an electrical reading box. As previously mentioned, the resulting CEA immunosensor, acting as counter electrode of the DSSC, displayed suitable and sensitive features for monitoring different concentrations of CEA, in real samples, in a clinical context. In general, this approach may open new horizons towards autonomous electrochemical biosensing through the employment of the photovoltaic cells as an electrical reading system.

Finally, new strategies were proposed to improve the overall performance of electrical reading box (DSSCs) of the biosensor for CEA diagnosis when an environmentally safe interface between DSSCs and Au NPs was established. Accordingly, colloidal Au NPs, with different particle sizes, were chemically synthesized, and incorporated in the DSSCs photoanodes. Also, more complex strategies were presented, modifying chemically the semiconductor used in the conventional DSSCs (TiO_2 nanoparticles) with surface dithiocarbamate groups (SiO_2/SiDTC), aiming to promote a strong and uniform loading of these colloidal Au NPs. In general, the beneficial influence of plasmonic Au NPs to the photovoltaic performances was obtained through the exhibition of the improvement of the visible light adsorption caused by the Au NPs surface plasmon effects, resulting from the scattering and light harvesting properties in the visible region.

Overall, this work introduced original approaches to create biosensing devices for cancer biomarker monitoring, which showed great advantages, including simplicity, easy manufacturing, low sample volume comsuption, and its suitability to be a portable and an autonomous device for POC applications.

8.2. Future work

Concerning the multidisciplinarity of the scope of this thesis, new approaches may be explored as future work.

The molecularly imprinted polymers could be synthesized under mild chemical conditions, analogous to the biological environment or through the imprinting of natural materials compatible with physiological conditions to preserve the original protein conformation that may contribute for the enhancement of the selectivity and the sensitivity of these artificial antibodies.

The screening of other cancer biomarkers, such as CA15-3, CA125, CA19-9, among others, could be, also, implemented in the described biosensing devices set-up, individually, or combining in a multi-sensorial platform to screening a set of cancer biomarkers, with an important role for a clinical context.

Focusing on the portability and easy access of these biosensing devices to monitor cancer biomarkers in real samples anywhere in the world, emerged the new goal to acquire an autonomous device through the interface of this technology with the photovoltaic cells (DSSCs) that acts as an electrical reading box. Several improvements could be accomplished by testing different conditions, including the construction of cell itself (different photoanode areas, sensitizer dyes, photoanodes thickness, paste recipe), the use of other metallic nanoparticles that contribute for the variation of electron charging effects (with different shapes and sizes), or, also, introducing an electrochromic cell couple to the photovoltaic system, which uses the electrical energy generated by DSSCs as a power source, and with the current decay, the color of electrochromic material changes, being this changing proportional to the concentration of target analyte used in the analysis. Thereby, a device completely self-sustained and autonomous, without dependence of an electrical source or battery, may be achieved and apllied in point-of-care, anywhere in the world.